

國立交通大學  
機械工程研究所

碩士論文

**Effect of Molecular Weight on Nanoscale Droplet  
Collisions Using Molecular Dynamics Simulation**

應用分子動力學模擬探討不同分子量對奈米尺寸液滴



研究生：王柏勝

指導教授：吳宗信 博士

中華民國九十六年七月

應用分子動力學模擬探討不同分子量對奈米尺寸液滴碰撞之影響

Effect of Molecular Weight on Nanoscale Droplet Collisions Using

Molecular Dynamics Simulation

研究生：王柏勝

Student : Po-Sheng Wang

指導教授：吳宗信 博士

Advisor : Dr. Jong-Shinn Wu

國立交通大學  
機械工程學系  
碩士論文



Submitted to Institute of Mechanical Engineering

Collage of Engineering

National Chiao Tung University

In Partial Fulfillment of the Requirements

for the degree of

Master of Science

In

Mechanical Engineering

July 2007

Hsinchu, Taiwan

中華民國九十六年七月

## 致謝

首先要感謝我的指導老師，吳宗信教授，不僅在每週的會議上訂正我研究的錯誤及方向，更在每天都會定時的討論我研究的進度，使我在學習的態度上有更正確的認知。同時也要感謝遠從義守大學來的江仲驊教授，中原大學的趙修武教授，成功大學的陳政宏教授願意來當我的口試委員，並對於我論文內容的批評與建議，使我的論文更佳的充實完善。同時感謝交通大學給了我求知的環境，讓我在這兩年內的碩士生涯有更多相同領域、相同的學生互相砥礪，學習。

在這 700 多天的 APPL 實驗室裡，總是充滿了一股溫馨的氣氛。由衷地感謝 李允民 學長，在我對程式上有所不了解時，總會及時的給予我解答，並提醒我更多應該要注意的部份，已畢業的 邵雲龍 學長，增進了不少我在電腦硬體領域的相關知識。周欣芸 學姐及 洪捷祭 學長，從你們身上我學習到對事物處理該有的守則及信條，尤其是祭哥，建立的學習方式使整個實驗室能更有規劃的朝研究之路大筆的邁進。李富利、鄭凱文、邱沅明、江明鴻 及 胡孟樺 學長姐、還有已畢業的 許國賢、陳百彥、梁偉豪 及 陳育進 學長們，在我剛進入碩一時不時的提醒我在學校的學習課程中要注意的細節。還有我的同學們，謝昇汎、陳又寧、洪維呈 及 盧勁全，有了你們的協助，讓我在這兩年內學習有了更加寬廣的空間。此外，吳玟琪、鄭丞志、林士傑、蘇正勤、呂政霖、柳志良 及 劉育宗 學弟妹，幫助我在研究時討論了許多有關未來領域方向的準備。並感謝在我準備最後論文階段時，時常關心我的朋友，科科王、走不出、祥世、國文將軍、蝗蟲 及 天兵顏，使得我的論文在我預想不到的情況下完成。更要提到的是博班念了七年的 許祐寧，在我每次有問題時從不會告訴我正確答案，並在每次詢問時都會不斷的提醒我學習上的怠慢，但從我比較他在實驗室中及畢業後對老師的負責任的態度，更讓我對社會上形形色色的人有了更一深刻的體認。

最後，我想感謝我的家人，我的父親 王明亮 先生，我的母親 黃月珠 女士，及我的弟弟 王翎羽，不僅在生活上給予我全力的支柱，更在我從小至今跌跌撞撞的成績裡，不停的鼓勵我支持我，使我能一步一步的越過人生不同的里程碑。還要感謝我的女友，秣丞，這兩年有了妳時時刻刻的陪伴我協助我，使我最後完成了這篇論文，我也會以更積極的態度去面對之後的人生。

王柏勝 謹誌  
九六年七月于風城

# 應用分子動力學模擬探討不同分子量對奈米尺寸液滴

## 碰撞之影響

學生：王柏勝

指導教授：吳宗信 博士

國立交通大學機械工程學系

### 摘要

本文使用平行化分子動力學程式(Parallelized cellular molecular dynamics. PCMD)來模擬兩顆在奈米尺度下(~10 nm)由氦(Helium)或氙(Xenon)原子所構成的液滴，並採用L-J (12-6)的勢能模型來探討兩顆液滴於真空環境時相互撞擊的行為及影響。在模擬中影響液滴碰撞時的行為參數主要分為液滴間的相對速度、碰撞參數(Impact Parameter)及材質。本文模擬氦原子的相對速度範圍為250 m/s~750 m/s，氙原子的相對速度範圍為250 m/s~2250 m/s，碰撞參數則皆為0~8.75 nm。利用可視化程式模擬觀察到的行為有：液滴結合(Direct Coalescence)、液滴變形結合(Stretching Coalescence)、液滴拉伸破裂(Stretching Separation)以及液滴碎裂(Shattering)。當相對速度和碰撞參數越高時，碰撞後的液滴其破裂和旋轉的現象會較為明顯，而材質的

不同則會影響液滴碰撞時碎裂的程度，並與之前的文獻做比較來判斷  
不同分子量下，奈米尺寸的液滴相互撞擊後的行為及能量變化。



**Effect of Molecular Weight on Nanoscale Droplet Collisions Using  
Molecular Dynamics Simulation**

**Student: Po-Sheng Wang**

**Advisor: Dr. Jong-Shinn Wu**

**Department of Mechanical Engineering**

**National Chiao-Tung University**

**Abstract**

In this thesis, Parallelized cellular molecular dynamics (PCMD) to simulate two droplets consist of Helium or Xenon in nanoscale and adopt the L-J (12-6) potential to discuss the behavior and effects when two droplets collide in vacuum. In the simulation, parameters which influence the behavior of collision primarily involve the relative velocity between droplets, the impact parameter and the material we use. The simulation in this context sets the relative velocity of helium atom range from 250 m/s to 750 m/s, the relative velocity of xenon atom range from 250 m/s to 2250 m/s, and the impact parameters all range from 0 to 8.75 *nm*. By the way of visualization program “pvwin” we can observe several behavior of simulation as follow: Direct Coalescence, Stretching Coalescence, Stretching Separation, and

Shattering. The greater the relative velocity and impact parameters are, the more obvious separation and rotation the droplets display after collision. Furthermore differences in material will affect the degree of shattering after collision. And we can compare the results with literature before to study the behavior and the change of energy in different molecular weights after the collision of droplets in the collision of droplets in nanoscale.



# Table of Contents

摘要.....	I
Abstract.....	III
Table of Contents.....	V
List of Tables.....	VII
List of Figures.....	VIII
Nomenclature.....	XV
Chapter 1 Introduction.....	1
1.1 Motivation.....	1
1.1.1 Nanoscale droplet collision dynamics.....	1
1.2 Background.....	2
1.2.1 Droplet collision dynamics.....	2
1.2.1.1 Droplet coalescence.....	3
1.2.1.2 Disruption and fragmentation.....	3
1.2.2 Governing parameters.....	3
1.2.2.1 Impact parameter ( $b$ ).....	4
1.2.2.2 Kinetic energy of collision.....	4
1.3 Literature reviews.....	4
1.4 Specific objectives of the proposed study.....	6
Chapter 2 Molecular Dynamics Simulation.....	8
2.1 Basic simulations of molecular dynamics.....	8
2.2 Equations of motion.....	11
2.3 Potential model.....	12
2.3.1 Lennard-Jones potential.....	13
2.4 Force computations.....	14
2.4.1 All pairs.....	14
2.4.2 Cell-link.....	14
2.4.3 Neighbor Lists.....	16
2.4.4 Cell link + Neighbor Lists.....	17
2.5 Boundary conditions.....	17
2.5.1 Periodic boundary conditions.....	17
2.5.2 Wall boundary conditions.....	17
2.6 Parallel molecular dynamics method.....	18
2.6.1 Atomic-decomposition algorithm.....	19
2.6.2 Force-decomposition algorithm.....	20



2.6.3 Spatial-decomposition algorithm .....	20
2.6.4 PCMD (Parallel Cellular Molecular Dynamics) algorithm .....	21
Chapter 3 Simulation of xnone and helium droplet-droplet collision dynamics .....	24
3.1 Simulation conditions .....	24
3.1.1 Test conditions .....	25
3.2 Results and discussion .....	26
3.2.1 The Xenon droplets collision .....	26
3.2.2 The Helium droplets collision.....	27
3.2.3 Data analysis .....	28
3.2.4 Distribution map of various regimes.....	32
Chapter 4 Concluding Remarks .....	34
4.1 Summary .....	34
4.2 Recommendation for the future work.....	35
References.....	36
Tables .....	38
Figures.....	39



## List of Tables

Table 1.1 System of units used in soft-sphere molecular dynamics programs .....38



## List of Figures

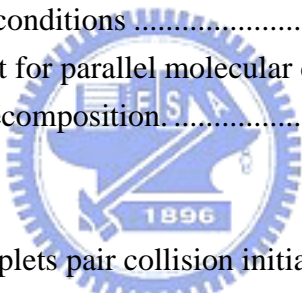
Fig. 1. 1	Terminology of possible droplet-droplet collision outcome. (a)coalescence, (b) disruption and (c) fragmentation.....	39
Fig. 1. 2	Impact parameter ( <i>b</i> ).....	39
Fig. 2. 1	Cartesian frame .....	40
Fig. 2. 2	Lennard-Jones (LJ) pair wise intermolecular potential .....	41
Fig. 2. 3	Xenon and Helium Lennard-Jones (LJ) pair wise intermolecular potential 41	41
Fig. 2. 4	All pairs, (b) Cell-link, and (c) Neighbor Lists methods .....	42
Fig. 2. 5	Neighbor Lists method.....	43
Fig. 2. 6	Cell-link + Neighbor Lists .....	43
Fig. 2. 7	Periodic boundary conditions .....	44
Fig. 2. 8	Proposed flow chart for parallel molecular dynamics simulation using dynamic domain decomposition.....	45
		
Fig. 3. 1	Head-on ( $b= 0$ ) droplets pair collision initial setup on y-z plane. ....	46
Fig. 3. 2	Non-head-on (ex: $b= 5nm$ ) droplets pair collision initial setup on x-y plane. 46	46
Fig. 3. 3	Distribution map of various regimes of Xenon droplet-collision. ....	47
Fig. 3. 4	Distribution map of various regimes of Helium droplet-collision.....	48
Fig. 3. 5	Snapshot of Xenon droplet pair collision under vacuum, at (a) $b=0$ , $V=250m/s$ , (b) $b=0, V=500m/s$ .....	49
Fig. 3. 6	Snapshot of Xenon droplet pair collision under vacuum, at (a) $b=0$ , $V=750m/s$ , (b) $b=0, V=1250m/s$ .....	50
Fig. 3. 7	Snapshot of Xenon droplet pair collision under vacuum, at (a) $b=0$ , $V=1500m/s$ , (b) $b=0, V=1750m/s$ .....	51
Fig. 3. 8	Snapshot of Xenon droplet pair collision under vacuum, at (a) $b=0$ , $V=2000m/s$ , (b) $b=0, V=2250m/s$ .....	52
Fig. 3. 9	Snapshot of xenon droplet pair collision under vacuum, at (a) $b=1.25nm$ , $V=750m/s$ , (b) $b=1.25nm, V=1000m/s$ .....	53
Fig. 3. 10	Snapshot of xenon droplet pair collision under vacuum, at (a) $b=1.25nm$ , $V=1250m/s$ , (b) $b=1.25nm, V=1500m/s$ .....	54

Fig. 3. 11	Snapshot of xenon droplet pair collision under vacuum, at (a) $b=1.25nm$ , $V=1750m/s$ , (b) $b=1.25nm$ , $V=2000m/s$ .	55
Fig. 3. 12	Snapshot of xenon droplet pair collision under vacuum, at (a) $b=1.25nm$ , $V=2250m/s$ , (b) $b=2.5nm$ , $V=750m/s$ .	56
Fig. 3. 13	Snapshot of xenon droplet pair collision under vacuum, at (a) $b=2.5nm$ , $V=1000m/s$ , (b) $b=2.5nm$ , $V=1250m/s$ .	57
Fig. 3. 14	Snapshot of xenon droplet pair collision under vacuum, at (a) $b=2.5nm$ , $V=1500m/s$ , (b) $b=2.5nm$ , $V=1750m/s$ .	58
Fig. 3. 15	Snapshot of xenon droplet pair collision under vacuum, at (a) $b=2.5nm$ , $V=2000m/s$ , (b) $b=2.5nm$ , $V=2250m/s$ .	59
Fig. 3. 16	Snapshot of xenon droplet pair collision under vacuum, at (a) $b=3.75nm$ , $V=250m/s$ , (b) $b=3.75nm$ , $V=500m/s$ .	60
Fig. 3. 17	Snapshot of xenon droplet pair collision under vacuum, at (a) $b=3.75nm$ , $V=750m/s$ , (b) $b=3.75nm$ , $V=1000m/s$ .	61
Fig. 3. 18	Snapshot of xenon droplet pair collision under vacuum, at (a) $b=3.75nm$ , $V=1250m/s$ , (b) $b=3.75nm$ , $V=1500m/s$ .	62
Fig. 3. 19	Snapshot of xenon droplet pair collision under vacuum, at (a) $b=3.75nm$ , $V=1750m/s$ , (b) $b=3.75nm$ , $V=2000m/s$ .	63
Fig. 3. 20	Snapshot of xenon droplet pair collision under vacuum, at (a) $b=3.75nm$ , $V=2250m/s$ , (b) $b=5nm$ , $V=250m/s$ .	64
Fig. 3. 21	Snapshot of xenon droplet pair collision under vacuum, at (a) $b=5nm$ , $V=500m/s$ , (b) $b=5nm$ , $V=750m/s$ .	65
Fig. 3. 22	Snapshot of xenon droplet pair collision under vacuum, at (a) $b=5nm$ , $V=1000m/s$ , (b) $b=5nm$ , $V=1250m/s$ .	66
Fig. 3. 23	Snapshot of xenon droplet pair collision under vacuum, at (a) $b=5nm$ , $V=1500m/s$ , (b) $b=5nm$ , $V=1750m/s$ .	67
Fig. 3. 24	Snapshot of xenon droplet pair collision under vacuum, at (a) $b=5nm$ , $V=2000m/s$ , (b) $b=5nm$ , $V=2250m/s$ .	68
Fig. 3. 25	Snapshot of xenon droplet pair collision under vacuum, at (a) $b=6.25nm$ , $V=250m/s$ , (b) $b=6.25nm$ , $V=500m/s$ .	69
Fig. 3. 26	Snapshot of xenon droplet pair collision under vacuum, at (a) $b=6.25nm$ , $V=750m/s$ , (b) $b=6.25nm$ , $V=1000m/s$ .	70
Fig. 3. 27	Snapshot of xenon droplet pair collision under vacuum, at (a) $b=6.25nm$ , $V=1250m/s$ , (b) $b=6.25nm$ , $V=1500m/s$ .	71
Fig. 3. 28	Snapshot of xenon droplet pair collision under vacuum, at (a) $b=6.25nm$ , $V=1750m/s$ , (b) $b=6.25nm$ , $V=2000m/s$ .	72
Fig. 3. 29	Snapshot of xenon droplet pair collision under vacuum, at (a) $b=6.25nm$ , $V=2250m/s$ , (b) $b=7.5nm$ , $V=250m/s$ .	73

Fig. 3. 30	Snapshot of xenon droplet pair collision under vacuum, at (a) $b=7.5nm$ , $V=500m/s$ , (b) $b=7.5nm$ , $V=750m/s$ .	74
Fig. 3. 31	Snapshot of xenon droplet pair collision under vacuum, at (a) $b=7.5nm$ , $V=1000m/s$ , (b) $b=7.5nm$ , $V=1250m/s$ .	75
Fig. 3. 32	Snapshot of xenon droplet pair collision under vacuum, at (a) $b=7.5nm$ , $V=1500m/s$ , (b) $b=7.5nm$ , $V=1750m/s$ .	76
Fig. 3. 33	Snapshot of xenon droplet pair collision under vacuum, at (a) $b=7.5nm$ , $V=2000m/s$ , (b) $b=7.5nm$ , $V=2250m/s$ .	77
Fig. 3. 34	Snapshot of xenon droplet pair collision under vacuum, at (a) $b=8.75nm$ , $V=250m/s$ , (b) $b=8.75$ , $V=500m/s$ .	78
Fig. 3. 35	Snapshot of xenon droplet pair collision under vacuum, at (a) $b=8.75nm$ , $V=750m/s$ , (b) $b=8.75$ , $V=1000m/s$ .	79
Fig. 3. 36	Snapshot of xenon droplet pair collision under vacuum, at (a) $b=8.75nm$ , $V=1250m/s$ , (b) $b=8.75$ , $V=1500m/s$ .	80
Fig. 3. 37	Snapshot of xenon droplet pair collision under vacuum, at (a) $b=8.75nm$ , $V=1750m/s$ , (b) $b=8.75nm$ , $V=2000m/s$ .	81
Fig. 3. 38	Snapshot of xenon droplet pair collision under vacuum, at (a) $b=8.75nm$ , $V=2550m/s$ .	82
Fig. 3. 39	Snapshot of helium droplet pair collision under vacuum, at (a) $b=0$ , $V=250m/s$ , (b) $b=0$ , $V=500m/s$ .	83
Fig. 3. 40	Snapshot of helium droplet pair collision under vacuum, at (a) $b=0$ , $V=750m/s$ .	84
Fig. 3. 41	Snapshot of helium droplet pair collision under vacuum, at (a) $b=1.25nm$ , $V=250m/s$ , (b) $b=1.25nm$ , $V=500m/s$ .	85
Fig. 3. 42	Snapshot of helium droplet pair collision under vacuum, at (a) $b=1.25nm$ , $V=750m/s$ , (b) $b=2.5nm$ , $V=250m/s$ .	86
Fig. 3. 43	Snapshot of helium droplet pair collision under vacuum, at (a) $b=1.25nm$ , $V=500m/s$ , (b) $b=1.25nm$ , $V=750m/s$ .	87
Fig. 3. 44	Snapshot of helium droplet pair collision under vacuum, at (a) $b=2.5nm$ , $V=250m/s$ , (b) $b=2.5nm$ , $V=500m/s$ .	88
Fig. 3. 45	Snapshot of helium droplet pair collision under vacuum, at (a) $b=2.5nm$ , $V=750m/s$ , (b) $b=3.75nm$ , $V=250m/s$ .	89
Fig. 3. 46	Snapshot of helium droplet pair collision under vacuum, at (a) $b=3.75nm$ , $V=500m/s$ , (b) $b=3.75nm$ , $V=750m/s$ .	90
Fig. 3. 47	Snapshot of helium droplet pair collision under vacuum, at (a) $b=5nm$ , $V=250m/s$ , (b) $b=5nm$ , $V=500m/s$ .	91
Fig. 3. 48	Snapshot of helium droplet pair collision under vacuum, at (a) $b=5nm$ , $V=750m/s$ , (b) $b=6.25nm$ , $V=250m/s$ .	92

Fig. 3. 49	Snapshot of helium droplet pair collision under vacuum, at (a) $b=6.25nm$ , $V=500m/s$ , (b) $b=6.25nm$ , $V=750m/s$ . .....	93
Fig. 3. 50	Snapshot of helium droplet pair collision under vacuum, at (a) $b=7.5nm$ , $V=250m/s$ , (b) $b=7.5nm$ , $V=500m/s$ . .....	94
Fig. 3. 51	Snapshot of helium droplet pair collision under vacuum, at (a) $b=7.5nm$ , $V=750m/s$ , (b) $b=8.75nm$ , $V=250m/s$ . .....	95
Fig. 3. 52	Snapshot of helium droplet pair collision under vacuum, at (a) $b=8.75nm$ , $V=500m/s$ , (b) $b=8.75nm$ , $V=750m/s$ . .....	96
Fig. 3. 53	Snapshot of density contour and clusters size distribution of Xenon droplets collision, $b=0$ , $V=250m/s$ , at (a) $25ps$ , (b) $75ps$ , (c) $150ps$ .....	97
Fig. 3. 54	Snapshot of density contour and clusters size distribution of Xenon droplets collision, $b=0$ , $V=500m/s$ , at (a) $25ps$ , (b) $75ps$ , (c) $150ps$ .....	98
Fig. 3. 55	Snapshot of density contour and clusters size distribution of Xenon droplets collision, $b=0$ , $V=750m/s$ , at (a) $25ps$ , (b) $75ps$ , (c) $150ps$ .....	99
Fig. 3. 56	Snapshot of density contour and clusters size distribution of Xenon droplets collision, $b=0$ , $V=1250m/s$ , at (a) $25ps$ , (b) $75ps$ , (c) $150ps$ .....	100
Fig. 3. 57	Snapshot of density contour and clusters size distribution of Xenon droplets collision, $b=0$ , $V=1500m/s$ , at (a) $25ps$ , (b) $75ps$ , (c) $150ps$ .....	101
Fig. 3. 58	Snapshot of density contour and clusters size distribution of Xenon droplets collision, $b=0$ , $V=1750m/s$ , at (a) $25ps$ , (b) $75ps$ , (c) $150ps$ .....	102
Fig. 3. 59	Snapshot of density contour and clusters size distribution of Xenon droplets collision, $b=0$ , $V=2000m/s$ , at (a) $25ps$ , (b) $75ps$ , (c) $150ps$ .....	103
Fig. 3. 60	Snapshot of density contour and clusters size distribution of Xenon droplets collision, $b=0$ , $V=2250m/s$ , at (a) $25ps$ , (b) $75ps$ , (c) $150ps$ .....	104
Fig. 3. 61	Snapshot of density contour and clusters size distribution of Helium droplets collision, $b=0$ , $V=250m/s$ , at (a) $25ps$ , (b) $75ps$ , (c) $150ps$ .....	105
Fig. 3. 62	Snapshot of density contour and clusters size distribution of Helium droplets collision, $b=0$ , $V=500m/s$ , at (a) $25ps$ , (b) $75ps$ , (c) $150ps$ .....	106
Fig. 3. 63	Snapshot of density contour and clusters size distribution of Helium droplets collision, $b=0$ , $V=750m/s$ , at (a) $25ps$ , (b) $75ps$ , (c) $150ps$ .....	107
Fig. 3. 64	Measurements of largest fragment of Xenon droplet pair collision, $b=0$ , $V=250m/s$ , (a) Number of atoms, (b) Vibration temperature (k), (c) Rotation energy, (d) Angular momentum, respectively. ....	108
Fig. 3. 65	Measurements of largest fragment of Xenon droplet pair collision, $b=0$ , $V=500m/s$ , (a) Number of atoms, (b) Vibration temperature (k), (c) Rotation energy, (d) Angular momentum, respectively. ....	109

Fig. 3. 66	Measurements of largest fragment of Xenon droplet pair collision, $b=0$ , $V=750m/s$ , (a) Number of atoms, (b) Vibration temperature (k), (c) Rotation energy, (d) Angular momentum, respectively. ....	110
Fig. 3. 67	Measurements of largest fragment of Xenon droplet pair collision, $b=2.5nm$ , $V=250m/s$ , (a) Number of atoms, (b) Vibration temperature (k), (c) Rotation energy, (d) Angular momentum, respectively. ....	111
Fig. 3. 68	Measurements of largest fragment of Xenon droplet pair collision, $b=2.5nm$ , $V=500m/s$ , (a) Number of atoms, (b) Vibration temperature (k), (c) Rotation energy, (d) Angular momentum, respectively. ....	112
Fig. 3. 69	Measurements of largest fragment of Xenon droplet pair collision, $b=2.5nm$ , $V=750m/s$ , (a) Number of atoms, (b) Vibration temperature (k), (c) Rotation energy, (d) Angular momentum, respectively. ....	113
Fig. 3. 70	Measurements of largest fragment of Xenon droplet pair collision, $b=5nm$ , $V=250 m/s$ , (a) Number of atoms, (b) Vibration temperature (k), (c) Rotation energy, (d) Angular momentum, respectively. ....	114
Fig. 3. 71	Measurements of largest fragment of Xenon droplet pair collision, $b=5nm$ , $V=500m/s$ , (a) Number of atoms, (b) Vibration temperature (k), (c) Rotation energy, (d) Angular momentum, respectively. ....	115
Fig. 3. 72	Measurements of largest fragment of Xenon droplet pair collision, $b=5nm$ , $V=750m/s$ , (a) Number of atoms, (b) Vibration temperature (k), (c) Rotation energy, (d) Angular momentum, respectively. ....	116
Fig. 3. 73	Measurements of largest fragment of Xenon droplet pair collision, $b=7.5nm$ , $V=250m/s$ , (a) Number of atoms, (b) Vibration temperature (k), (c) Rotation energy, (d) Angular momentum, respectively. ....	117
Fig. 3. 74	Measurements of largest fragment of Xenon droplet pair collision, $b=7.5nm$ , $V=500m/s$ , (a) Number of atoms, (b) Vibration temperature (k), (c) Rotation energy, (d) Angular momentum, respectively. ....	118
Fig. 3. 75	Measurements of largest fragment of Xenon droplet pair collision, $b=7.5nm$ , $V=750m/s$ , (a) Number of atoms, (b) Vibration temperature (k), (c) Rotation energy, (d) Angular momentum, respectively. ....	119
Fig. 3. 76	Measurements of largest fragment of Helium droplet pair collision, $b=0$ , $V=250m/s$ , (a) Number of atoms, (b) Vibration temperature (k), (c) Rotation energy, (d) Angular momentum, respectively. ....	120
Fig. 3. 77	Measurements of largest fragment of Helium droplet pair collision, $b=0$ , $V=500m/s$ , (a) Number of atoms, (b) Vibration temperature (k), (c) Rotation energy, (d) Angular momentum, respectively. ....	121

Fig. 3. 78	Measurements of largest fragment of Helium droplet pair collision, $b=0$ , $V=750m/s$ , (a) Number of atoms, (b) Vibration temperature (k), (c) Rotation energy, (d) Angular momentum, respectively. ....	122
Fig. 3. 79	Measurements of largest fragment of Helium droplet pair collision, $b=2.5nm$ , $V=250m/s$ , (a) Number of atoms, (b) Vibration temperature (k), (c) Rotation energy, (d) Angular momentum, respectively. ....	123
Fig. 3. 80	Measurements of largest fragment of Helium droplet pair collision, $b=2.5nm$ , $V=500m/s$ , (a) Number of atoms, (b) Vibration temperature (k), (c) Rotation energy, (d) Angular momentum, respectively. ....	124
Fig. 3. 81	Measurements of largest fragment of Helium droplet pair collision, $b=2.5nm$ , $V=750m/s$ , (a) Number of atoms, (b) Vibration temperature (k), (c) Rotation energy, (d) Angular momentum, respectively. ....	125
Fig. 3. 82	Measurements of largest fragment of Helium droplet pair collision, $b=5nm$ , $V=250m/s$ , (a) Number of atoms, (b) Vibration temperature (k), (c) Rotation energy, (d) Angular momentum, respectively. ....	126
Fig. 3. 83	Measurements of largest fragment of Helium droplet pair collision, $b=5nm$ , $V=500m/s$ , (a) Number of atoms, (b) Vibration temperature (k), (c) Rotation energy, (d) Angular momentum, respectively. ....	127
Fig. 3. 84	Measurements of largest fragment of Helium droplet pair collision, $b=5nm$ , $V=750m/s$ , (a) Number of atoms, (b) Vibration temperature (k), (c) Rotation energy, (d) Angular momentum, respectively. ....	128
Fig. 3. 85	Measurements of largest fragment of Helium droplet pair collision, $b=7.5nm$ , $V=250m/s$ , (a) Number of atoms, (b) Vibration temperature (k), (c) Rotation energy, (d) Angular momentum, respectively. ....	129
Fig. 3. 86	Measurements of largest fragment of Helium droplet pair collision, $b=7.5nm$ , $V=500m/s$ , (a) Number of atoms, (b) Vibration temperature (k), (c) Rotation energy, (d) Angular momentum, respectively. ....	130
Fig. 3. 87	Measurements of largest fragment of Helium droplet pair collision, $b=7.5nm$ , $V=750m/s$ , (a) Number of atoms, (b) Vibration temperature (k), (c) Rotation energy, (d) Angular momentum, respectively. ....	131
Fig. 3. 88	Measurements of largest fragment of Helium droplet pair collision, $b=2.5nm$ , $V=250m/s$ , (a) Number of atoms, (b) Vibration temperature (k), (c) Rotation energy, (d) Angular momentum, respectively. ....	132
Fig. 3. 89	Measurements of largest fragment of Helium droplet pair collision, $b=5nm$ , $V=250m/s$ , (a) Number of atoms, (b) Vibration temperature (k), (c) Rotation energy, (d) Angular momentum, respectively. ....	133



- Fig. 3. 90 Measurements of largest fragment of Helium droplet pair collision,  $b=5nm$ ,  $V=500m/s$ , (a) Number of atoms, (b) Vibration temperature (k), (c) Rotation energy, (d) Angular momentum, respectively. .... 134
- Fig. 3. 91 Measurements of largest fragment of Helium droplet pair collision,  $b=7.5nm$ ,  $V=750m/s$ , (a) Number of atoms, (b) Vibration temperature (k), (c) Rotation energy, (d) Angular momentum, respectively. .... 135
- Fig. 3. 92 Distribution map of various regimes of Xenon, Argon, and Helium droplet pair collision..... 136



## Nomenclature

$D$  : the diameter of droplet

$E$  : the energy

$E_{rot}$  : the rotational energy

$F_i$  : the force vector of molecular  $i$

$N$  : number of the density

$T$  : the temperature

$T_{vib}$  : the vibrational temperature

$k_B$  : Boltzmann constant

$m_i$  : the mass of atom  $i$

$n$  : number of the atoms

$r_i$  : the position vector of molecular  $i$

$\bar{r}_i$  : the position vector of  $m_i$

$\bar{v}_i$  : the velocity vector of  $m_i$

$\varepsilon$  : the strength of the interaction

$\rho$  : the density

$\sigma$  : the length scale



# Chapter 1 Introduction

## 1.1 Motivation

### 1.1.1 Nanoscale droplet collision dynamics

Nanoscale droplet collision dynamics plays an important role in various technologies such as spray forming, ink-jet printing, rain drop formation, spray scrubbing, spray cooling, surface coating, etc. In addition, the collision between two droplets becomes the most common event in these applications. Thus, the understanding of the fundamental collision dynamics between two droplets becomes crucial to optimize their applications. Depending on the size of the droplets, descriptions of the collision dynamics can be generally classified into continuum-scale.

The normal impact of two droplets is a complicated fluid mechanics phenomenon. The major physical processes are the conservation among energy, momentum and angular momentum. In a collision, the droplet loses kinetic energy while it strains and deforms. The strains lead to viscous dissipation, accounting for some conversion of mechanical energy to heat. In advanced, surface of the droplet increases while the original droplet breakdowns into smaller ones and surface energy increases accordingly. The surface energy can be viewed as a potential energy and the

conversion of kinetic energy to surface energy can be viewed as a conservative process. To continue, the droplet surface increases and surface energy increases as well. The surface energy can be regarded as a potential energy and conservation of kinetic energy to surface energy can be regarded as a conservative process. The increase of surface energy during the early part of a collision will result in recoiling and rebounding later through the conversion of surface energy back to kinetic energy. The momentum balance occurs through a force imposed on the droplet by the wall in a collision as the droplet loses velocity.

Restricted by the development of nanoscale technology, nowadays it is unable to utilize the macro-vision of continuum model to explain the nanoscale phenomenon. In order to understand the nanoscale physical mechanism, molecular dynamics (MD) simulation is the most widespread and useful method to solve the nanoscale problem.

When discuss the behaviors of the collision dynamics between two nanoscale droplets, the MD method can be applied to all phases of gas, liquid and solid and to interfaces of these three phases.

## **1.2 Background**

### **1.2.1 Droplet collision dynamics**

In this theory, we focus on the collision dynamics between two nanoscale droplets.

Based on the understanding in the continuum scale, droplet collision can be generally classified into several different types of collision depending on some critical parameters, as shown in Fig. 1.1. These different types of collision process will be introduced in the next two paragraphs.

### **1.2.1.1 Droplet coalescence**

Droplet coalescence, which forms an integrated post-collision droplet whose mass is equal to the sum of the mass of the pre-collision droplets, follows after the droplet contacts. The colliding droplets coalesce when the air film thickness reaches a critical value ( $\sim 10^2 \text{ \AA}$ , [Mackay, *et al.*, 1963]). The droplets may coalesce temporarily or permanently, depending on the CKE and impact parameter ( $b$ ).

### **1.2.1.2 Disruption and fragmentation**

Temporary coalescence occurs when the CKE exceeds the value for stable coalescence and eventually results in either disruption or fragmentation. Disruption is means that the collision product separates into the same number of droplets which exists prior to the collision. As for fragmentation, the coalesced droplet undergoes catastrophic break-up to form numerous small droplets.

### **1.2.2 Governing parameters**

The character of the two droplets collision process is controlled by the Webber number ( $We$ ), the impact parameter ( $b$ ) and Kinetic energy of collision. Physical

meaning of impact parameter is described in the following.

### 1.2.2.1 Impact parameter (*b*)

In fig. 1.2, if we set a line (which passes through the center of ball B) to be the x axis and the x axis parallels the direction of incident velocity vector of ball A. The distance from the incident path of ball A to the x axis is defined as the impact parameter (*b*).

### 1.2.2.2 Kinetic energy of collision

The kinetic energy of collision of the droplet pair with the same droplet fluid is given by [Julius and Li, 1989]:

$$\sum_i \frac{p_i^2(t)}{2m_i} = E_L^{\text{"rb"}}(t) + E^{\text{int}}(t) \quad (1.2)$$

and

$$T_{\text{vib}} = \frac{2E^{\text{int}}}{(3N - 6)k_B} \quad (1.3)$$

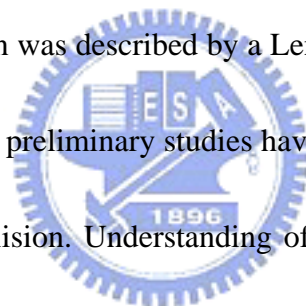
where *R* is the droplet size ratio  $r_L / r_S$ . Where  $r_L$  and  $r_S$  is radius of droplet large and droplet small, respectively.

## 1.3 Literature reviews

In the past, to recognize detailed fluid mechanisms happened between the liquid phase and the solid phase, numerous studies concerning impact of droplet on a solid surface have been carried out a variety of methods, and various models have been

developed. Hu propose the stochastic growth of cloud droplet distributions due to collection processes is studied using a detailed microphysical parcel model [Hu, *et al.*, 1998]. The results indicate that the van der Waals forces are effective in enhancing droplet collision when the droplets are small and the distributions are narrow. Ashgriz and Poo carried out collision experiments with water drops in the range from micrometer size to millimeter size [Ashgriz, *et al.*, 1990]. The two different types of separating collisions above were identified, reflexive and stretching separating, Harlow and Shannon are the first to simulate droplet impacting on the solid surface [Halow, *et al.*, 1967]. They used “marker-and-cell” (MAC) finite-difference method to solve the fluid mass and momentum conservation equations. Tsurutani enhanced the MAC model to include surface tension and viscosity effects, and furthermore considered the heat transferring from a hot surface to a cold liquid droplet when it spread on the surface [Tsuruani, *et al.*, 1990]. Trapaga and Szekely used “volume of fluid” (VOF) method to study impact of molten particles in a thermal spray process [Trapaga, *et al.*, 1990]. Fukai, Shiiba, Yamamoto, Miyatake, Poulikakos, and Megaridis Zhao formulated a finite-element model to study the effects on the spreading of a liquid droplet colliding with a flat surface [Fukai, *et al.*, 1995]. Lattice Boltzmann method excels in modeling flow problems involving multiphase materials and complicated geometry [Succi, 2001]. Inamuro presented a lattice Boltzmann

method for two-phase fluid flows with large density ratios and applied the method to the simulations of binary droplet collisions for various Weber numbers and impact parameters [Inamuro, *et al.*, 2004]. They simulated the other types of binary droplet collisions under certain conditions, bouncing collision for low Weber numbers and shattering collision (Disruption or fragmentation) for high Weber numbers and discussed the mixing processes in that two different conditions. Greenspan and Heath studied the collision dynamics of nanometer-sized particles [Greenspan, *et al.*, 1991]. The individual molecules were modeled as single mass particles and the molecule–molecule interaction was described by a Lennard–Jones potential. Based on the reviews in the above, only preliminary studies have been done in the simulation of nanoscale droplet-droplet collision. Understanding of the droplet collision dynamics may become important in the fast-growing nano science and technology.



#### **1.4 Specific objectives of the proposed study**

In the past, it is rare to utilize molecular dynamics method to discuss the behavior of the liquid droplets impacting. In this work, we use molecular dynamics simulations to compare the effect of different molecular weight on droplets, including the argon (the molecular weight is 39.95), xenon (131.4), and helium (4.05) molecular. We use neighbor-list combine with Cell link + Neighbor Lists methods to calculate force, and



choose Lennard-Jones (L.J.) potential to deal with interactions between xenon droplets and helium droplets and then we apply the completed parallel MD code to investigate the phenomena of the droplet collision.



# Chapter 2 Molecular Dynamics Simulation

## 2.1 Basic simulations of molecular dynamics

Molecular dynamic (MD) has generally used in simulating the structure of liquids, solids, and droplets. We will introduce briefly the molecular dynamic simulation and how to define the model applied to simulate the behavior of a droplet impacting a solid substrate or another droplet.

First of all in a simulation, we should consider the location of all atoms. By the location and the time derivative, all atoms can be defined their point masses in molecular dynamic simulation. Each atom as a particle interacts with the other particle through interaction forces derived from interaction potentials in the system, and time evolution is governed by Newtonian mechanics. At each time step, the acceleration of a particle used to update the position of the particle would be calculated by Newton's second law of motion as follows (2.1).

$$F_i = m\ddot{r}_i = m_i \frac{d^2 r_i}{dt^2} \quad (2.1)$$

Where  $r_i$  is the position vector of molecule  $i$  as show in Fig. 2.1 .

Since Newton's second law is time independent or equivalently  $F_i = m\ddot{r}_i = m_i \frac{d^2 r_i}{dt^2}$  is invariant under time translations. Consequently, we expect there to be some function of the positions and velocities whose value is constant in time; this function

is called the Hamiltonian,  $H$ ,

$$H(r^N, p^N) = \text{const} \quad (2.2)$$

Here, the momentum  $p_i$  of molecule  $i$  is defined in terms of its velocity by  $p_i = m\dot{r}_i$ . For an isolated system, total energy  $E$  is conserved, where  $E$  is equal to the sum of kinetic energy and potential energy. Thus, for an isolated system, we identify total energy as the Hamiltonian; then for  $N$  spherical molecules,  $H$  can be

$$\text{written as } H(r^N, p^N) = \frac{1}{2m} \sum_i p_i^2 + U(r^N) = E \quad (2.3)$$

where the potential energy  $U(r^N)$  results from the intermolecular interactions. First

consider the total time derivative of the general Hamiltonian (2.2),

$$\frac{dH}{dt} = \sum_i \frac{\partial H}{\partial p_i} \cdot \dot{p}_i + \sum_i \frac{\partial H}{\partial r_i} \cdot \dot{r}_i + \frac{\partial H}{\partial t} \quad (2.4)$$

If, as is (2.3),  $H$  has no explicit time dependence, then the last term on the RHS

of (2.4) vanishes and we are left with

$$\frac{dH}{dt} = \sum_i \frac{\partial H}{\partial p_i} \cdot \dot{p}_i + \sum_i \frac{\partial H}{\partial r_i} \cdot \dot{r}_i = 0 \quad (2.5)$$

Now consider the total time derivative of the isolated-system Hamiltonian given in

(2.3),

$$\frac{dH}{dt} = \frac{1}{m} \sum_i p_i \cdot \dot{p}_i + \sum_i \frac{\partial U}{\partial r_i} \cdot \dot{r}_i = 0 \quad (2.6)$$

On comparing (2.5) and (2.6), we find for each molecule  $i$ .

$$\frac{\partial H}{\partial p_i} = \frac{p_i}{m} = \dot{r}_i \quad (2.7)$$

$$\text{and } \frac{\partial H}{\partial r_i} = \frac{\partial U}{\partial r_i} \quad (2.8)$$

Substituting (2.7) into (2.5) gives

$$\sum_i \dot{\mathbf{r}}_i \cdot \dot{\mathbf{p}}_i + \sum_i \frac{\partial H}{\partial \mathbf{r}_i} \cdot \dot{\mathbf{r}}_i = 0 \quad (2.9)$$

$$\sum_i \left( \dot{\mathbf{p}}_i + \frac{\partial H}{\partial \mathbf{r}_i} \right) \cdot \dot{\mathbf{r}}_i = 0 \quad (2.10)$$

Since the velocities are all independent of one another, (2.10) can be satisfied only,

for each molecule  $i$ , we have

$$\frac{\partial H}{\partial \mathbf{r}_i} = -\dot{\mathbf{p}}_i \quad (2.11)$$

Equations (2.7) and (2.11) are Hamilton's equation of motion. For a system of  $N$  particles, (2.7) and (2.11) represent  $6N$  first-order differential equations that are equivalent to Newton's  $3N$  second-order differential equations (2.1).

In the Newtonian view, motion is a response to an applied force. However, in the Hamiltonian view, motion occurs in such a way as to preserve the Hamiltonian function, where the force does not appear explicitly.

For an isolated system, the particles move in accordance with Newton's second law, tracing our trajectories that can be represented by time-dependent position vectors  $\mathbf{r}_i(t)$ . Similarly, we also have time-dependent momentum  $\mathbf{p}_i(t)$ . At one instant, there are positions and moment of the  $N$  particles in a  $6N$ -dimensional hyperspace. Such a space, called phase space, is composed of two parts: a  $3N$ -dimensional configuration space, in which the coordinates are the components of position vectors  $\mathbf{r}_i(t)$ , and a  $3N$ -dimensional momentum space (or velocity space), in which the coordinates are

the components of the momentum vectors  $p_i(t)$ . As time evolves, the points defined by positions and momentum in the 6N phase space moves, describing a trajectory in phase space.

## 2.2 Equations of motion

Potential energy represents the functions of all atoms in the system. Because of the complexity of these functions, there is no analytical solution to the equations of motion, therefore we must use numerical theorems in the operation. There are many numerical algorithms has developed to calculate the integrating equations of motion.

One of them is Leapfrog method [Frenkel, *et al.*, 1996]. Leapfrog method is the most general method applied in MD simulation and there are some reasons for it. When we put the leapfrog method in the integrating equations of motion, the values of calculation will be accurate to third order. From the viewpoint of energy conservation, it tends to be considerably better than higher-order methods. Furthermore, its requirement of the memory storage of the computer calculation is lower than other methods.

The introductions of Leapfrog method are as follows :

The Leap-Frog method use the velocity at  $t - \frac{dt}{2}$  and  $t$  to compile the interaction force of atoms. Use the calculated force to compute the velocity at  $t + \frac{dt}{2}$  after a

time step, as (2.12) equation. And then apply the velocity at  $t + \frac{dt}{2}$  to get the location of the atom at  $t + \frac{dt}{2}$ , as (2.13). The process of operation above is relatively simple because the method we use has no need of modification.

$$V_i\left(t + \frac{dt}{2}\right) = V_i\left(t - \frac{dt}{2}\right) + dt * \frac{F_i(t)}{m_i} \quad (2.12)$$

$$r_i(t + dt) = r_i(t) + dt * V_i\left(t + \frac{dt}{2}\right) \quad (2.13)$$

To diminish the arithmetic error, we adopt the velocity at  $t + \frac{dt}{2}$  to solve the location at next time step rather than the velocity at  $t$ . In other words, the computed solutions of the time average velocity between the velocity at  $t$  and  $t + dt$  would have better accuracy than which only applied the velocity at  $t$ . The calculating processes as Fig. 2.1.



### 2.3 Potential model

It is very important to choose an appropriate potential energy model in MD simulation when we want to approach some different realistic materials. The force derived from the potential on an atom is due to the interaction with surroundings. Lennard-Jones potential, one of potential methods derived from complicated computation, will be used in the two droplets upon a solid wall model. Why we choose Lennard-Jones potential as our main method will be explained and discussed in the next section.

### 2.3.1 Lennard-Jones potential

Lennard-Jones potential is proposed by J.E. [Lennard Jones, 1924]. The potential energy of a pair of atoms,  $i$  and  $j$ , locates at  $r_i$  and  $r_j$  as follows eq.(2.14).

$$u(r_{ij}) = 4\varepsilon \left[ \left( \frac{\sigma}{r_{ij}} \right)^{12} - \left( \frac{\sigma}{r_{ij}} \right)^6 \right], \quad r_{ij} \leq r_c \quad (2.14)$$

The functional forms of the LJ and soft-sphere potentials in MD units are shown in Fig. 2.2 (a). Where  $r_{ij} = r_i - r_j$ , and the parameter  $\varepsilon$  govern the strength of the interaction and  $\sigma$  defines a length scale. Fig. 2.2 (b) is a relative curve of the xenon and helium in argon Fig. 2.2 (a). The interaction repels at close range, then attract, and is eventually cut off at some limiting separation  $r_c$ . While the strongly repulsive core arising from the nonbonded overlap between the electron clouds has a rather arbitrary form, the attractive tail actually represents the van der Waals interaction. For the interactions involve individual pairs of atoms, each pair is treated independently, with other atoms in the neighborhood having no effect on the force between them.

The force corresponding to  $u(r)$  is  $f = -\nabla u(r)$ , so the force that atom  $j$  exerts on atom  $i$  is (2.15)

$$f_{ij} = \left( \frac{48\varepsilon}{\sigma^2} \right) \left[ \left( \frac{\sigma}{r_{ij}} \right)^{14} - \frac{1}{2} \left( \frac{\sigma}{r_{ij}} \right)^8 \right] r_{ij} \quad (2.15)$$

Provide  $r_{ij} \leq r_c$ , and zero otherwise. As  $r$  increases towards  $r_c$  the force drops

to zero, so that there is no discontinuity at  $r_c$  ;  $f$  and higher derivatives are discontinuous, though this has no real impact on the numerical solution.

In addition, these units of equation are usually expressed in dimensionless format in MD simulation. The advantage of using dimensionless format is that the equation of motion becomes simpler because some parameters defined in the model will be absorbed by dimensionless units. Another advantage from the viewpoint of a particle is that transferring these units into dimensionless format can avoid some calculating errors in computer hardware while the atoms are over-ranged.

## 2.4 Force computations



### 2.4.1 All pairs

All pairs is the simplest method to implement, but extremely inefficient when the interaction range  $r_c$  is relatively small compared to linear size of simulation region.

In the simulation domain, all pairs of atoms must be examined in computing process as Fig. 2.3 (a). In fact that the amount of computation needed grows as  $O(N^2)$  rules out the method for all but the smallest value of  $N$ .  $N$  is the number of particles.

There are two techniques which can reduce the growth rate  $O(N^2)$  and they will be discussed in next two section.

### 2.4.2 Cell-link



Cell-link which can avoid most of unnecessary compute and improve the computational effects provides a means of organizing the information about atom positions into a form. This method is to divide the simulation region into a lattice of small cells, and the cells should exceed  $r_c$  in width. Then if particles are assigned to cells on the basis of their current positions, interactions are only possible between particles which are either in the same cells or in adjacent cells. Because of symmetry only half the neighboring cells need to be considered. For example, a total of 14 neighboring cells must be examined in three dimensions (include the cell itself).

The wraparound effects are readily incorporated into the scheme. Distinctly the region size must be at least  $4r_c$  long for this method to be useful. There are several ways for implementing this cell-link list method to connect the relation between particles and cells. In the current demonstration code, it utilizes the concept of the pointers for particles and cells. Each cell stores a particle number, which may be zero or nonzero. Nonzero value represents a true particle number, while the zero value represents either the last atom in the cell or an empty cell. In addition, only one array cell List is used to represent the particles and the cells. An obvious advantage of doing this is that we could know exactly the size of this array in advance if periodic boundary conditions are used. Of course, there are several other methods to implement this idea of cell-link list technique. Ideas depicted above can be clearly

illustrated by Fig. 2.3 (b).

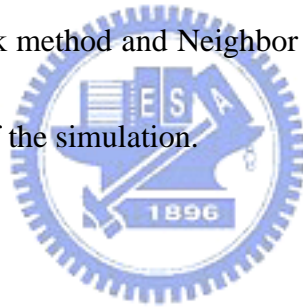
### 2.4.3 Neighbor Lists

During MD simulation, in order to consider the distance between each atom is all in the  $r_c$  range or not, we spend most of time in calculating the force between each atom. Adopting Neighbor Lists can cut down the time we spend in calculating [Lambrakos, *et al.*, 1986 and Verlet, *et al.*, 1967]. Neighbor List theory builds the relationship between each atom and its surrounding atoms in a particular interval of time steps as Fig. 2.3 (c), likes ten to twenty steps. Picking the atom  $i$  as the center,  $r_L$  is the radius of Neighbor List like Fig. 2.4 and  $r_L = r_c + \sigma$ . In the particular interval of time steps, when we calculate the force on the atom  $i$ , only use the atoms within  $r_L$  range to determine which atom exists in the  $r_c$  range. And then calculate the force of atom  $i$  without calculating the distance from whole atoms between each other at each time step in the system. For example, in the system containing  $N$  atoms, build a Neighbor List every ten time step in a simulation to establish the relationship of distance between each two atom. The number of calculating time is  $\frac{N*(N-1)}{2}$ . After every atom in the region  $r_L$  being confirmed among all atoms in the simulation, the calculation in forces or energy of the following ten time steps only need to estimate which atom is in the  $r_c$  region by the atom within  $r_L$  region. And then, update the distributing information of itself in each atom after passing through

the next ten time steps. When we use Neighbor Lists, we should especially notice the choose of  $\sigma$  whose value should not be too less, avoiding the calculation of forces or energy being affected by the atoms which is not within  $r_L$  range originally but gets into  $r_c$  range during the ten time steps above. On the contrary, if we choose a large value of  $\sigma$ , the number of atoms in  $r_L$  range will increase. Estimating which atom increases its calculating frequency in the  $r_c$  range simultaneously increases the requirement of time in calculation.

#### **2.4.4 Cell link + Neighbor Lists**

We could combine Cell link method and Neighbor List method likes Fig. 2.5 so as to promote the performance of the simulation.



## **2.5 Boundary conditions**

### **2.5.1 Periodic boundary conditions**

Unless the purpose of the MD simulation is to imitate a real walls having physical meaning, walls in simulation had better be eliminated by using Periodic boundary conditions (PBC). The introducing of PBC is equivalent to considering an infinite space-filling array of identical copies of simulation region. Physical meaning of periodic boundary conditions is shown in Fig. 2.6.

### **2.5.2 Wall boundary conditions**

Simulating in the MD system, we would like to keep the wall isothermal, so we define a corrected layer on wall. In the study, we use the Rescaling method to modify corrected layer. Rescaling method keeps the wall isothermal by modifying total kinetic energy. In microcosmic point of view, the temperature is related to kinetic energy. When we set a temperature for corrected layer, it means to set an average kinetic energy of atoms on the corrected layer. In a word, we must keep the kinetic energy fixed (2.16), therefore we should have a reference value. Continually, with the use of (2.17), we compute the total kinetic energy of atoms. Finally, we start rescaling by using (2.18) to make the total kinetic energy in the corrected layer be the same as the reference value which we use in (2.17).

$$E_{kd} = \frac{3}{2} Nk_B T_d \quad (2.16)$$

$$E_{ka} = \frac{1}{2} m \sum_{i=1}^N V_i^{old^2} = \frac{3}{2} Nk_B T_a \quad (2.17)$$

$$V_i^{new} = V_i^{old} \sqrt{\frac{E_{kd}}{E_{ka}}} = V_i^* \sqrt{\frac{T_d}{T_a}} \quad (2.18)$$

## 2.6 Parallel molecular dynamics method

There is no doubt about that MD simulation is a useful and valuable tool. But MD simulation is very time-consuming due to large number of time steps and possibly large number of atoms required to complete a meaningful simulation. In liquids and solids, MD simulation is required to resolve the vibration of the atoms, which limits

the time step to be on the order of femtosecond. Many hundreds of thousand or even millions of time steps are needed to simulate a nanosecond in “real” time scale. In addition, up to hundreds of thousand or millions of atoms are needed in the MD simulation, even for a system size in the nanometer scale. In the past, there have been considerable effort [Plimpton, 1995] that concentrated on parallelizing MD simulation on the memory-distributed machine by taking the inherently parallelism e.g., [Boghossian, *et al.*, 1990] and [Fox, *et al.*, 1998]. Generally, parallel implementation of the MD method can be divided into three categories, including the atom decomposition, the force decomposition and the spatial decomposition among processors.



### **2.6.1 Atomic-decomposition algorithm**

In the atom decomposition method, each processor, which owns nearly the same number of atoms as other processors and in which atoms are not necessarily geometrically nearby, integrates the Newton’s equation for all atoms and moves the atoms of their owns. However, this method requires global communication at each time step, which becomes unacceptably expensive as compared with the “useful” MD computation when the number of atoms increases to a certain amount, since each processor has to know all information (position and velocities) of all atoms at each time step. Or equivalently, the communication is  $O(N)$ , where  $N$  is the number of

atoms in the system that is independent of the number of the processors,  $P$ . Thus, the atom decomposition method is generally suitable for small-scale problem

### **2.6.2 Force-decomposition algorithm**

In the force decomposition method, it is based on a block-decomposition of the force matrix rather than a row-wise decomposition in the atom-decomposition method. It improves the  $O(N)$  scaling to be  $O(N/P)$ . It generally performs much better than the atom decomposition method; however, there exist some disadvantages. First, the number of processors has to be square of an integer. Second, load imbalance may become an issue. From previous experience [Plimpton, 1995], it is suitable for small- and intermediate-size problems.



### **2.6.3 Spatial-decomposition algorithm**

In the spatially static domain decomposition method, simulation domains are physically divided and distributed among processors. This method so far represents the best parallel algorithm for large-scale problem in MD simulation for short-ranged interaction [Karypi *et. al.*, 1998]; however, it only works well for a system, in which the atoms move only a very short distance during simulation or possibly distribute uniformly in space. MD simulation of solids represents one of the typical examples. In contrast, if the distribution of the atoms tends to vary very often in the configuration space, then the load imbalance among processors develops very fast

during simulation, which detracts the parallel performance. Thus, a parallel MD method capable of adaptive domain decomposition may represent a better solution for resolving this difficulty.

#### **2.6.4 PCMD (Parallel Cellular Molecular Dynamics) algorithm**

A new parallel algorithm for MD simulation, named parallel cellular molecular dynamics (PCMD), is developed by MuST (Multiscale Science & Technology) laboratory in NCTU in Taiwan, employing dynamic domain decomposition to address the issue of load imbalance among processors in the spatially static domain-decomposition method. We focus on developing a parallel MD method using dynamic domain decomposition by taking advantage of the existing link-cells as mentioned earlier. In this proposed method, not only are the cells used to reduce the cost for building up neighbor list, but also are used to serve as the basic partitioning units. Similar idea has been applied in the parallel implementation of direct simulation Monte Carlo (DSMC) method [Nicol *et. al.*, 1988], which is a particle simulation technique often used in rarefied gas dynamics. Note that in the following IPB stands for interprocessor boundary. General procedures as Fig. 2.7 in sequence include:

1. initialize the positions and velocities of all atoms and equally distribute the atoms among processors;
2. Check if load balancing is required. If required, then first repartition the domain,

followed by communicate cell/atom data between processors, renumber the local cell and atom numbers, and update the neighbor list for each atom due to the data migration;

3. Receive positions and velocities of other atoms in the neighbor list for all cells near the IPB;
4. Compute force for all atoms;
5. Send force data to other atoms in the neighbor list for all cells near the IPB;
6. Integrate the acceleration to update positions and velocities for all atoms;
7. Apply boundary conditions to correct the particle positions if necessary;
8. Check if preset total runtime is exceeded. If exceeded, then output the data and stop the simulation. If not, check if it is necessary to rebuild the neighbor list of all atoms using the most update atom information.
9. If it is necessary to rebuild the neighbor list ( $N=8$  in the current study), then communicate atom data near the IPB and repeated the steps 2-8. If not necessary, then repeat steps 3-8.

In the above, in addition to the necessary data communication when atoms cross the IPB and particle/cell data near the IPB, there are two more important steps in the proposed parallel MD method as compared with the serial MD implementation. One is how to repartition the domain effectively and the other is the decision policy for



repartitioning. These two steps are described next, respectively.



# Chapter 3 Simulation of xenon and helium droplet-droplet collision dynamics

## 3.1 Simulation conditions

This content mainly concerned the simulation of the behavior of xenon or helium droplet pair collision. In order to compare the influence of crucial parameter, impact parameter and the relative velocity between two droplets in the collision, the diameter of single droplet was set to be similar about  $10.5nm$  in both xenon and helium. In detail, in the composition of xenon droplet, we arranged the L-J potential atom in FCC crystal structure at first, which density was 0.2 and maintained equilibrium at  $166.73K$ , and then used the PCMD to simulate the variation in a hundred thousand time steps, and eventually obtained a xenon droplet which contained 2800 atoms. By the same approach, the density of helium crystal structure was 1.0 and it maintained equilibrium at  $0.55K$ . After using PCMD in a hundred thousand time steps, we would obtain a droplet containing 2700 atoms. To establish the simulation model of droplet pair collision, we copied the relative coordinates of droplets and adjusted the relative velocities between them. In addition, if the test case was head-on collision, the system dimension should be  $200\sigma * 500\sigma * 500\sigma$  (Fig. 3.1). For detailed observation of the behavior of disruption or fragmentation, otherwise the system dimension was usually

$600\sigma * 300\sigma * 300\sigma$  (Fig. 3.2).

### 3.1.1 Test conditions

When simulating a collision of xenon droplet, the impact parameter was 0 and the relative velocity ranged from  $1250m/s$  to  $2250m/s$  in a head-on condition, but in a non-head-on condition, the impact parameter was  $1.25nm$  to  $8.75nm$  and the relative velocity ranged from  $250 m/s$  to  $2250m/s$ . In simulating a collision of helium droplets, the impact parameter was 0, but in a non-head-on condition, the impact parameter was  $1.25nm$  to  $8.75nm$ . And both of two conditions had a relative velocity ranging from  $250m/s$  to  $750m/s$ . In all of these cases above, the original distance between droplets were about  $140\text{\AA}$  which was shown in Fig. 3.3 to Fig. 3.4.

To identify the droplet pair behavior easily and in objectivity, we classify each collision behavior in following manner [Svanberg, *et al.*, 1998]:

- i. Coalescence: The largest fragment contains  $> 80\%$  of the molecules.
- ii. Stretching Coalescence: The largest fragment contains  $> 80\%$  of the molecules, the droplet shape transform from a ball to a rotational bar, and never breakup.
- iii. Stretching Separation: The largest fragment contains  $< 60\%$  of the molecules, while the sum of the two largest fragments consists of  $> 90\%$  of the molecules.
- iv. Shattering: The largest fragment contains  $< 40\%$  of the molecules, and the sum of the two largest fragments consists of  $< 65\%$  of the molecules.

- v. Bounce: The droplet pair never touch each other in simulation, while the two largest fragments consists of  $> 80\%$  of the molecules.

## 3.2 Results and discussion

### 3.2.1 The Xenon droplets collision

By the way of visualization program “pvwin”, we could observe the behavior of collision in  $500ps$  in head-on cases (Fig. 3.5 to Fig. 3.8) and nonhead-on cases (Fig. 3.9 to Fig. 3.38). In head-on cases, the relative velocity was set from  $1250m/s$  to  $2250m/s$  and we found that the impacting time became earlier and the “disk” resulting from collision became larger while the relative velocity increased. On account of the high molecular weight of xenon, the attraction of L-J potential was strong which caused the “disk” coalesce to a larger droplet. When the relative velocity reached  $2250m/s$ , the “disk” appeared shattering resulting in lots of small droplets.

However, in the nonhead-on cases, the relative velocity was set from  $250m/s$  to  $2250m/s$ . Through Fig. 3.9 to Fig. 3.12 (a), with the increasing of the relative velocity, we observed several different events: When the impact parameter was  $1.25nm$  and the relative velocity was  $1500m/s$ , it resulted in stretching coalescence, but when the relative velocity reached  $2000m/s$ , although shattering happened after collision, it resulted in stretching separation eventually because of the strength of potential. When the relative velocity reached  $2250m/s$ , it resulted in shattering finally. In Fig. 3.12 (b)

to Fig. 3.20 (a), the same as above, direct coalescence, stretching coalescence, stretching separation, and shattering occurred in succession with the increase of relative velocity. Besides, the greater the impact parameter was, the earlier the stretching coalescence happened. Nevertheless, if the impact parameter was greater than  $5nm$  (Fig. 3.20 (b) to Fig. 3.38), shattering would not happen in  $2250m/s$  relative velocity. When the impact parameter increased to  $8.75nm$ , coalescence still occurred in  $250m/s$  relative velocity and stretching coalescence still occurred in  $500m/s$  relative velocity.

### 3.2.2 The Helium droplets collision

Due to the tendency not to coalesce of the low-molecular weight atom, we used up to 27000 helium droplets in low temperature MD simulation. In head-on cases (Fig. 3.39 to Fig. 3.40), when the relative velocity was  $250m/s$ , droplet area increased and then coalesce to a larger droplet as time went by. If the relative velocity was  $500m/s$  and  $750m/s$ , a phenomenon like "net" occurred and then shattered in to pieces consist of many small droplets as time went by. Besides, if the impact velocity was higher, the droplets which composed small shattering became smaller and dispersed evenly.

In nonhead-on cases (Fig. 3.41 to Fig. 3.52), when the impact parameter was  $1.25nm$  and the relative velocity was  $250m/s$ , the droplet occurred coalescence and rotated slowly. Nevertheless, when the relative velocity was  $500m/s$  and  $750m/s$ , the droplet

became stick-like at first and then shattered in to pieces consist of many small droplets as time went by. This kind of phenomenon called stretching coalescence would stretch and rotate when the impact parameter increased to  $3.75nm$  and  $5nm$  and the relative velocity was  $250m/s$ . In advanced, if the relative velocity reached to  $500m/s$  and  $750m/s$ , the stick-like phenomenon would become horizontal. As the impact parameter was  $6.25nm$  and the relative velocity was  $250m/s$  and  $500m/s$ , stretching separation occurred, but at  $750m/s$  shattering remained occurred. Finally, when the impact parameter was  $7.5nm$  and  $8.75nm$ , the relative velocity was  $250m/s$ ,  $500m/s$  and  $750m/s$ , stretching separation occurred.

### 3.2.3 Data analysis

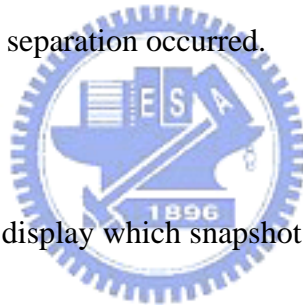


Fig. 3.53 to Fig. 3.60 was a display which snapshot the density contour and clusters size distribution at  $25ps$ ,  $50ps$  and  $150ps$  from y-z plane of xenon droplet pair collision in head-on cases. At relative velocity  $250m/s$ , the droplet distribution had no obvious changes after collision and only few pieces formed. Until the relative velocity reached  $750m/s$ , while the droplets collided and the coalesced, the surface area tended to be larger and density of the area close to the droplet surface was smaller, but no more pieces formed nevertheless. When the relative velocity was  $1250m/s$  to  $1750m/s$ , the number of the pieces tended to increase as the velocity increases and we could apparently observe from the density contour at  $75ps$  that the surface area of the

droplets increased and the density of the center of the droplets decreased after collision. But at 150ps, the droplet which stretched because of collision shrank to a smaller one and its density of the center increased also. When the relative velocity was 2000m/s, although a phenomenon like net occurred, the number of pieces increased substantially. But at 150ps, we could observe that the droplets coalesced gradually and some of the pieces became larger ones because of coalescence. When the relative velocity was 2250m/s, the pieces formed by the droplets after collision distributed evenly along the center of collision and the size of fragment was more average at 150ps than at 75ps. Fig. 3.61 to Fig. 3.63 was a display which snapshot the density contour and clusters size distribution at 25ps, 50ps and 150ps from y-z plane of helium droplet pair collision in head-on cases. At relative velocity 250m/s, although coalescence occurred, the helium droplet had more average density from the center to the surface in density contour at 150ps compared with the xenon droplet coalescence and also had larger entirely surface area, but fewer fragments formed. However, when the relative velocity was 500m/s and 750m/s, the surface area of droplet was apparently larger as relative velocity was higher at 75ps and fragments formed more easily. In Density contour at 150ps, we could observe that along the center of the droplet, the size of the fragments became smaller and the number of the fragments became larger while the radius of the droplets increased.

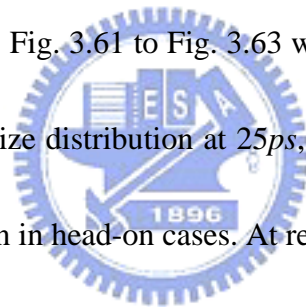
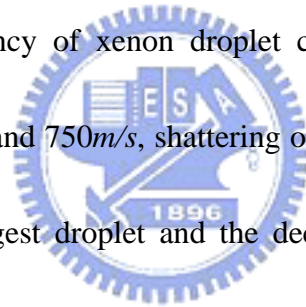


Fig. 3.64 to Fig. 3.75 were the data analysis of xenon droplet pair collision at relative velocity 250m/s, 500m/s , and 750m/s and impact parameter 0, 25nm, 50nm, and 75nm[Liu, et al., 1997 and marcus, *et al.*, 1998]. Fig. 3.64 (a) was the atom variation of the biggest fragment from droplet and through this figure we could find that the atom number was raise by the droplet coalescence. Fig. 3.64 (b) was the variation of temperature (K) and through it we could find that at 25ps, it was the collision between xenon atoms that made the temperature increase, but in 25ps to 100ps, it was coalescence that made the temperature descend substantially, however the evaporation made the temperature tend to be raise. Fig. 3.64 (c) was the rotation energy change of the biggest droplet as the time increased. And Fig. 3.64 (d) was the angular momentum distribution of different direction as the time increased. Compared Fig. 3.64 to Fig. 3.66, we could find out that as the velocity increased, the temperature was raised apparently at collision and both the rotation energy and angular momentum of every direction increased. Fig. 3.67 to Fig. 3.69 was the data analysis at impact parameter 25nm. Both of them were coalescence cases, therefore the atom number of the biggest droplet tended to decrease because of evaporation and the temperature increased as the relative velocity of collision increased. Moreover, on account of non-head cases, the rotation energy increased substantially after collision and the angular momentum of y-direction tended to be raise as the velocity increased.



Compared Fig. 3.70 to Fig. 3.75, we could find that the rotation energy and the angular momentum of y-direction also rose as the impact parameter increased. And Fig. 3.76 shown that at  $275ps$ , the rotation energy descended on account of stretching separation and followed by the substantially decreasing of the angular momentum of y-direction. Fig 3.76 to Fig 3.87 shown the data analysis of helium droplet pair collision when the relative velocities were  $250m/s$ ,  $500m/s$ , and  $750m/s$  and the impact parameters were  $0$ ,  $25nm$ ,  $50nm$ , and  $75nm$ . In head-on case, the variation tendency of temperature, rotation energy and angular momentum result in coalescence were the same as the variation tendency of xenon droplet coalescence at relative velocity  $250m/s$ . However, at  $500m/s$  and  $750m/s$ , shattering occurred result in the decrease of the atom number of the biggest droplet and the decrease of temperature, and that rotation energy and angular momentum had diversified variation result from the collision between the biggest droplet and other fragment. In non-head on cases, Fig. 3.79 and Fig. 3.82 had the same variation tendency as stretching coalescence cases of xenon droplet. Fig. 3.84 to Fig. 3.87 shown the stretching separation of droplets including the quickly decrease of temperature after the droplets separated, the decrease of rotation energy and the trend which the angular momentum became gentle on y-direction. On the contrary, in the other cases which result coalescence, when the impact parameter or relative velocity increased, the temperature, rotation energy and



angular momentum of collision all increase substantially.

Fig. 3.88 to Fig. 3.91 were the data analysis at the same relative velocity and impact parameter. According to Fig. 3.88 and Fig. 3.89, we could observe that in the same coalescence case, the helium droplet had the greatest number of atom, the faster decrease of rotation energy and the greatest angular momentum and in conclusion the variations tendency of helium droplet were generally similar. Fig. 3.90 shown that helium atom occurred shattering and then the rotation energy and angular momentum of it had substantially changes by the separation of the droplet. In Fig. 3.91, the helium droplets and xenon droplets were both had stretching separation, but the argon droplets had coalescence. We could clearly find that the separation time of xenon droplets was later than of helium droplet, decrease range of the rotation energy of xenon was not larger than of helium and the angular momentum of both xenon and helium became minimized after separation.

### **3.2.4 Distribution map of various regimes**

Fig. 3.92 was the distribution of various regimes in droplet collision of several different molecular weights. According to the distribution region of the figure, we could apparently observe that when the molecular weight was greater, the range of coalescence after droplet collision became larger and the shattering would occur as the higher relative velocity. Stretching coalescence often occurred in high molecular

weight and as the relative velocity increased, the stretching coalescence appeared more easily at low impact parameter. And stretching separations appeared at higher relative velocity as the molecular weight increased.



## Chapter 4 Concluding Remarks

### 4.1 Summary

In this paper, we mainly used the Parallel MD simulation to simulate the collision of helium droplets and xenon droplets, changed the impact parameter and relative velocity to simulate different cases, and discussed the influence cause by different molecular weights in droplets collision. And then we got some conclusion as following:

1. The collision of two droplets in nanoscale was very complicate, and it included direct coalescence, stretching coalescence, stretching separation and shattering. All these phenomena were also influenced by relative velocity, impact parameter, and molecular weights.
2. The greater the molecular weight of the atom was, the higher the relative velocity was needed to cause shattering after collision in nanoscale. And those atoms had low molecular weights occurred direct coalescence only in lower relative velocity.
3. Stretching coalescence often occurred between direct coalescence and stretching separation and we could observe this phenomenon in the collision of atoms with high molecular weight and this phenomenon present linear distribution in the distribution map of various regimes because of the increase of relative velocity

and the decrease of the impact parameter.

4. By analyzing the energy variation in droplets collision, we could decidedly infer which kind of phenomenon would occur and the conclusion was very practical in discussing dynamics of two droplets collision in nanoscale.

## 4.2 Recommendation for the future work

According to the study of this paper, several important future works were outlined as follows:

1. In order to study the helium droplets and xenon droplets pair collision in depth, we could improve the accuracy of simulation by changing the size of droplets and the relative velocity and distance between droplets and using the droplets rotated in the simulation.
2. In order to distinguish the behavior of collision under different molecular weights in detail, we could choose the other atoms of high or low molecular weight to simulate droplets pair collision.
3. In addition to vacuum circumstance, we could put the droplets in low or high pressure circumstances and consider the behaviour of multi-droplet collision.
4. Using droplets with different molecular weights, like Xe and He, to collide to each other to observe the phenomenon occurring after collision.

## References

- [1] Ashgriz, N. and Poo, J. Y., “Coalescence and separation in binary collisions of liquid drops”, *Journal of Fluid Mechanics*, 221, pp.183-204, 1990.
- [2] Bertagnolli, M., Marchese, M., Jacuci, G. St., Doltsinis, I. and Noelting, S., “Thermo-mechanical simulation of the splashing of ceramic droplets on a rigid substract”, *Journal of Computational Physics*, 133, pp.205, 1997.
- [3] Frenkel, D. and Smit, B., “Understanding Molecular Simulation, Academic”, Press, San Diego, 1996.
- [4] Fox, G. C., Johnson, M. A., Lyzenga, G. A., Otto, S. W., Salmon, J. K. and Walker, D. W., “Solving Problems on Concurrent Processors: Volume 1”, Prentice Hall, Englewood Cliffs, NJ, 1988.
- [5] Fukai, J., Shiiba, Y., Yamamoto, T., Miyatake, O., Poulidakos, D., Megaridis, C. M. and Zhao, Z., “Wetting effects on the spreading of a liquid droplet colliding with a flat surface: experiment and modeling”, *Physics Fluids*, 7, pp.236-247, 1995.
- [6] Greenspan, D. and Heath, L. F., “Supercomputer simulation of the modes of colliding microdrops of water”, *Journal of Physics D*, 24, pp.2121-2123, 1991.
- [7] Harlow, F. H. and Shannon, J. P., “The splash of a liquid droplet, *Journal of Applied Physics*”, 38, pp.3855, 1967.
- [8] Hsu, Y.-L., “Parallel MD Simulation of Droplet-Droplet Collision Dynamics”, Ph. D. Thesis, 2006.
- [9] Hu, Z. L., Bruintjes, R. T. and Betterton, E.A., “Sensitivity of cloud droplet growth to collision and coalescence efficiencies in a parcel model”, *Journal of Atmospheric Sciences*, 15, pp.2502-2515, 1998.
- [10] Inamuro, T., Ogata, T., Tajimas, S., Konoshi, N., “A lattice Boltzmann method for incompressible two-phase flows with large density difference, *Journal of Computational Physics*”, 198, pp.628–644, 2004.
- [11] Julius, J., Li, D. H., “Separation of the Energy of Overall Rotation in Any N-Body System”, *Physical review letters*, 62, pp.241-244, 1989
- [12] Karypi, G. s, Schloegel, K. and Kumar, V., “ParMetis, University of Minnesota, Department of computer Science”, September, 1998.
- [13] Lambrakos, S. G, Boris, J. P., Chandrasekhar, I., and Gaber, B., “A Vectorized Near-Neighbors Algorithm of Order N for Molecular Dynamics Simulations” *Ann. NY Acad. Sci.*, 482, pp.85, 1986.
- [14] Lennard, J. E., “The determination of molecular fields. I. from the variation of

- the viscosity of gas with temperature”, Proc. Roy. Soc. (Lond), 106A, pp.441, 1924.
- [15] Liu, M., Nikola, M., Marcus, S., and Jan, B. C. P., “Collision dynamics of Large Argon Clusters” J. Phys. Chem. A, 101, pp.4011-4018, 1997.
- [16] Mackay, G. D. M. and Mason, S. G., “The gravity approach and coalescence of fluid droplets and liquid interfaces”, Canadian Journal of Chemical Engineering, 41, pp.203, 1963.
- [17] Marcus, S., Liu, M., Nikola, M., and Jan, B. C. P., “Collision dynamics of large water clusters”, journal of chemical physics, 108, pp.5888-5897, 1998.
- [18] Nicol, D. M. and J, Saltz. H., “Dynamic Remapping of Parallel Computations with Varying Resource Demands”, IEEE Transactions on Computer, 37, pp.1073-1087, 1988.
- [19] Plimpton, S., “Fast Parallel Algorithms for Short-Range Molecular Dynamics”, J. of Computational Physics, 117, pp.1-19, 1995.
- [20] Succi, S., “The lattice Boltzmann equation for fluid dynamics and beyond”, Oxford University Press, 2001.
- [21] Svanberg, M., and Pettersson, J.B.C. and, “Collision dynamic of large argon clusters”, Journal of Physics and Chemistry, 101, pp.4011-4018, 1997.
- [22] Trapaga, G. and Szekely, J., “Mathematical modeling of the isothermal impingement of liquid droplets in spraying processes”, Metall. Trans. B, 22, pp.901, 1991.
- [23] Tsurutani. K. , Yao. M., Senda. J. and Fujimoto. H., Numerical analysis of the deformation process of a droplet impinging upon a wall., , JSME Int. Ser., pp.555, 1990.
- [24] Verlet L., “Computer ‘Experiments’ on Classical Fluids. I. Thermodynamical Properties of Lennard-Jones Molecules,” *Phys. Rev.*, Vol.159, 98-103, 1967.

## Tables

---

### *Fundamental Quantities*

Mass	$m = \text{mass of one atom}$
Length	$\sigma$
Energy	$\epsilon$
Time	$\sigma\sqrt{m/\epsilon}$

### *Derived Quantities*

Adiabatic compressibility	$\kappa_s^* = \kappa_s \epsilon / \sigma^3$
Configurational internal energy	$U_c^* = U_c / N\epsilon = \langle \mathcal{U}^* \rangle = \langle \mathcal{U} / N\epsilon \rangle$
Density	$\rho^* = N\sigma^3 / V$
Force	$F^* = F\sigma / \epsilon$
Heat capacity	$C_v^* = C_v / Nk$
Radial position	$r^* = r / \sigma$
Pressure	$P^* = P\sigma^3 / \epsilon$
Temperature	$T^* = kT / \epsilon \quad \epsilon/k = 170\text{K}$
Thermal pressure coefficient	$\gamma_v^* = \gamma_v \sigma^3 / k$
Total energy	$E^* = E / N\epsilon$
Velocity	$v^* = v\sqrt{m/\epsilon}$

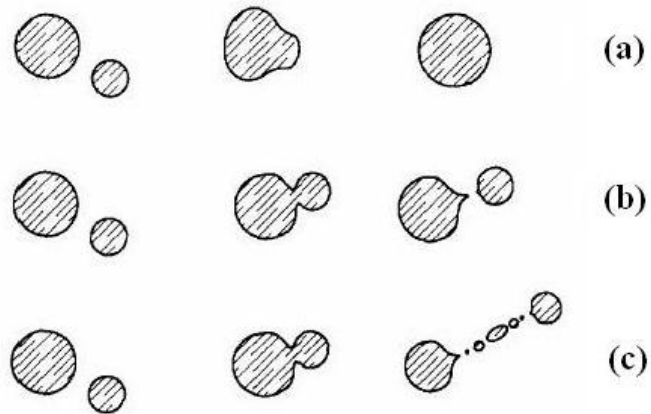
---



Table 1.1 System of units used in soft-sphere molecular dynamics programs



## Figures



**Fig. 1. 1 Terminology of possible droplet-droplet collision outcome.**  
(a)coalescence, (b) disruption and (c) fragmentation.

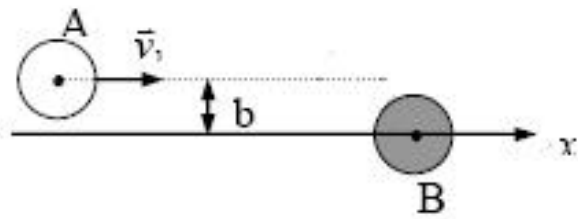


**Fig. 1. 2 Impact parameter ( $b$ ).**

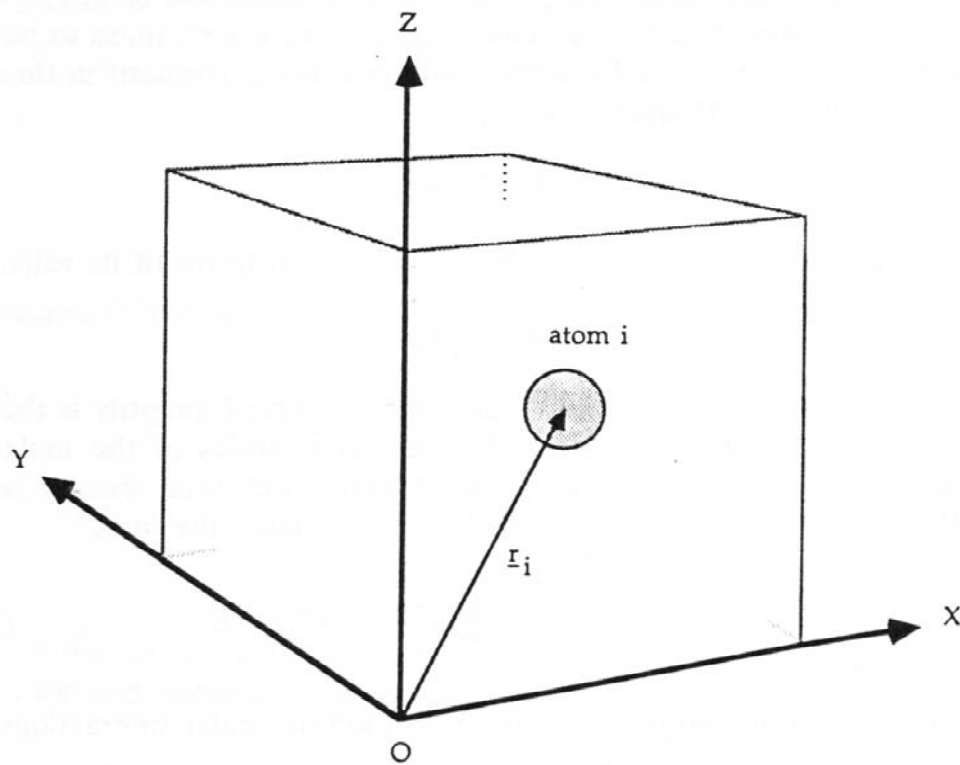


**Fig. 2. 1 Cartesian frame**

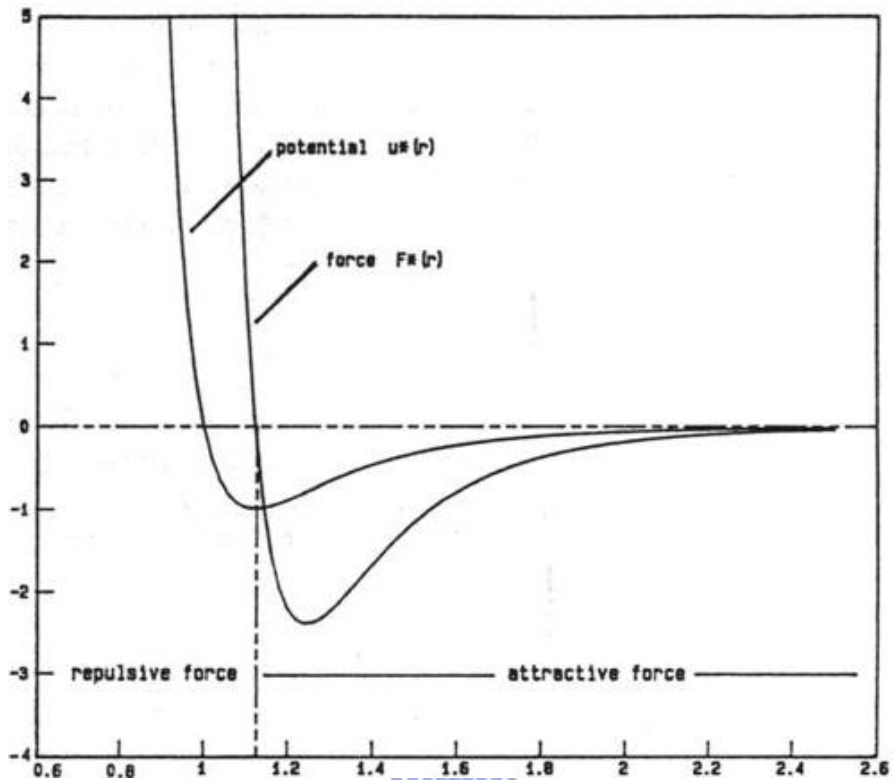


Fig. 2. 2 Lennard-Jones (LJ) pair wise intermolecular potential

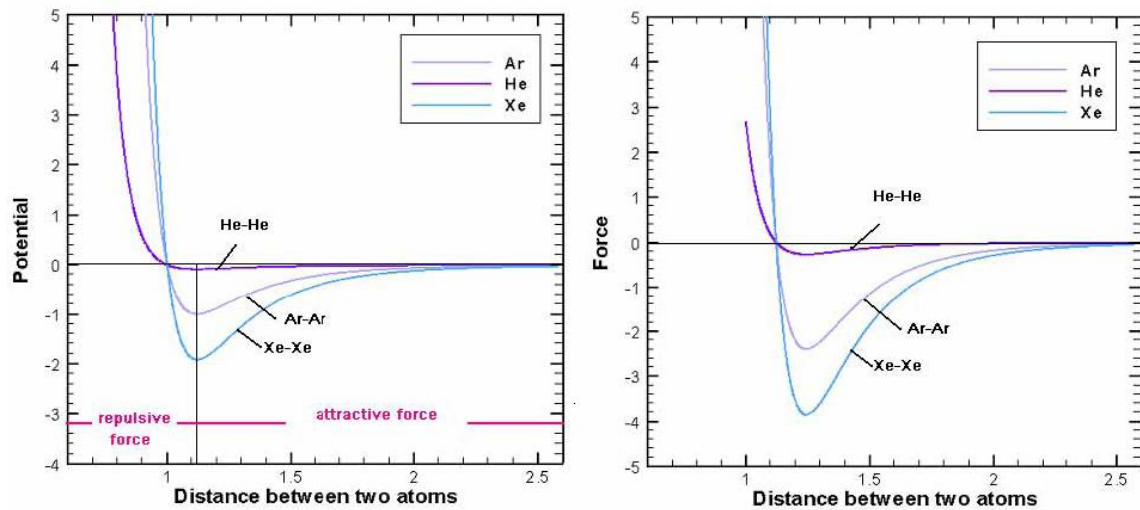
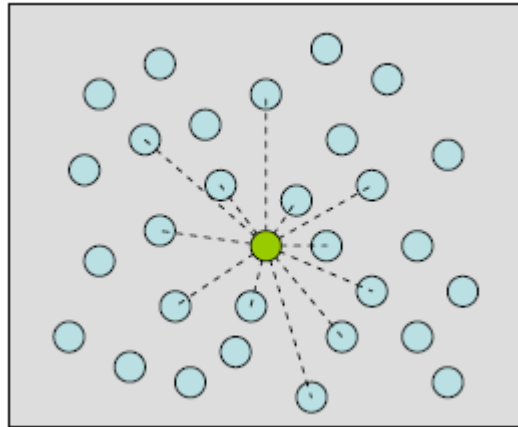
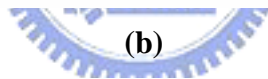
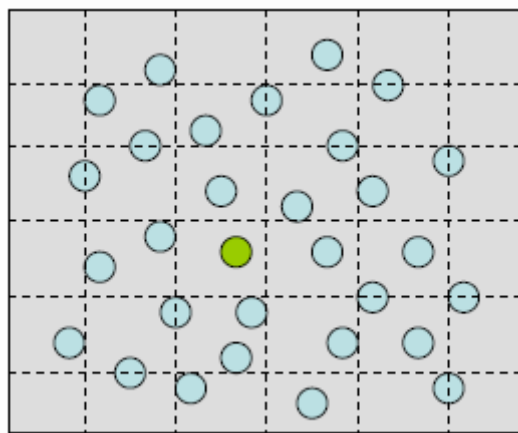


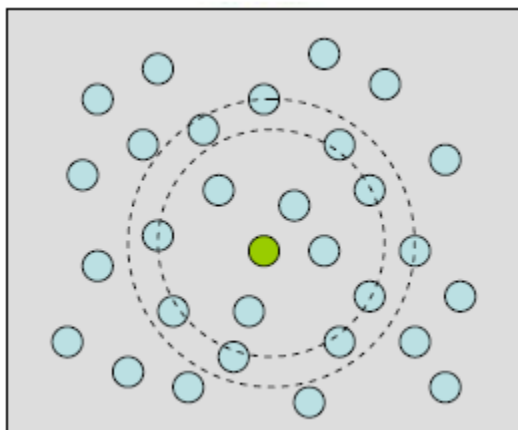
Fig. 2. 3 Xenon and Helium Lennard-Jones (LJ) pair wise intermolecular potential



(a)



(b)



(c)

**Fig. 2. 4 All pairs, (b) Cell-link, and (c) Neighbor Lists methods**

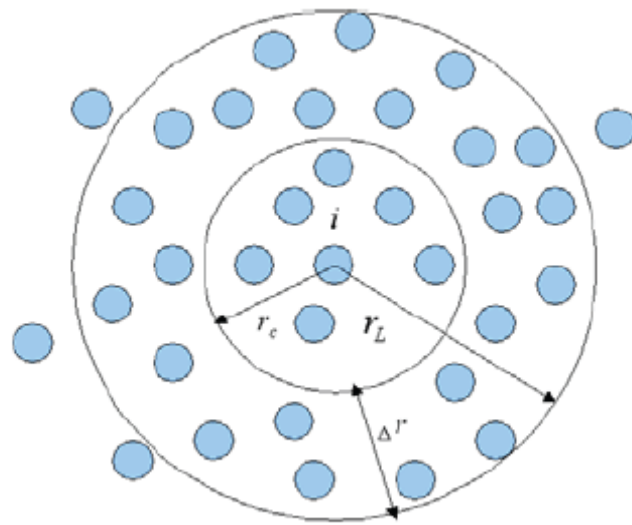


**Fig. 2. 5 Neighbor Lists method**

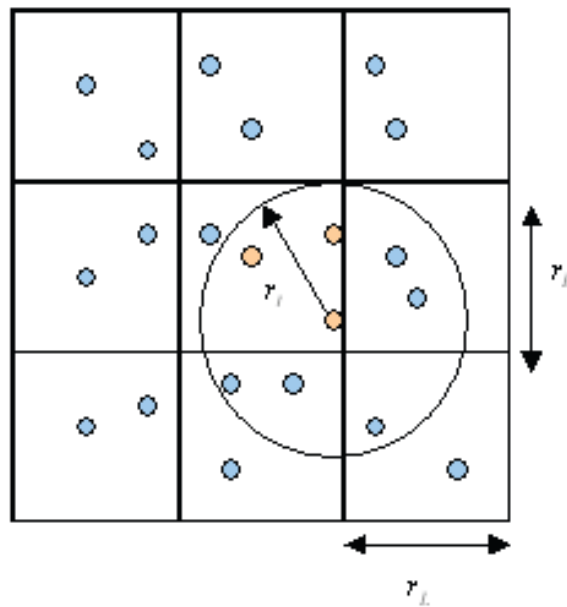


**Fig. 2. 6 Cell-link + Neighbor Lists**

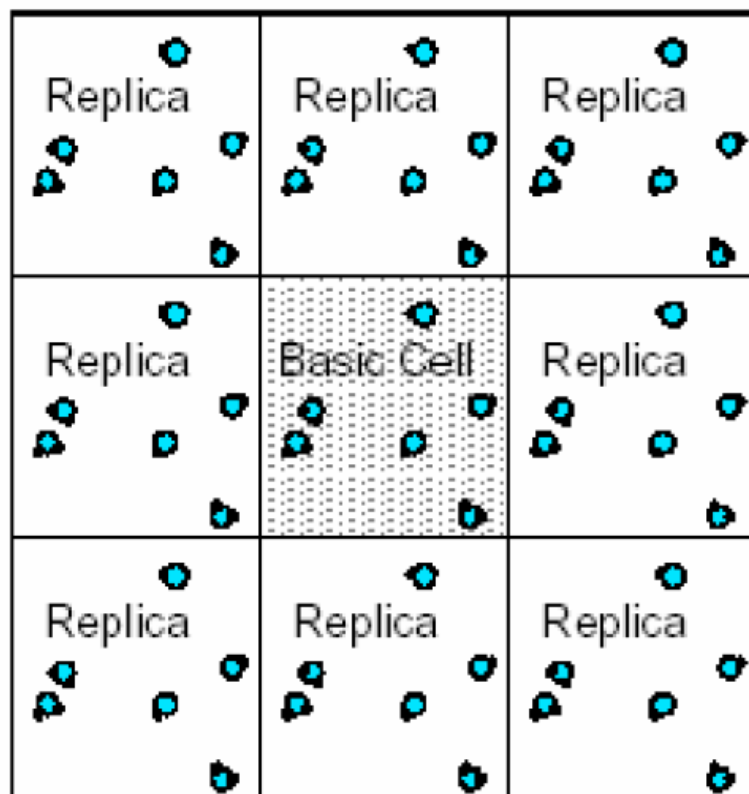
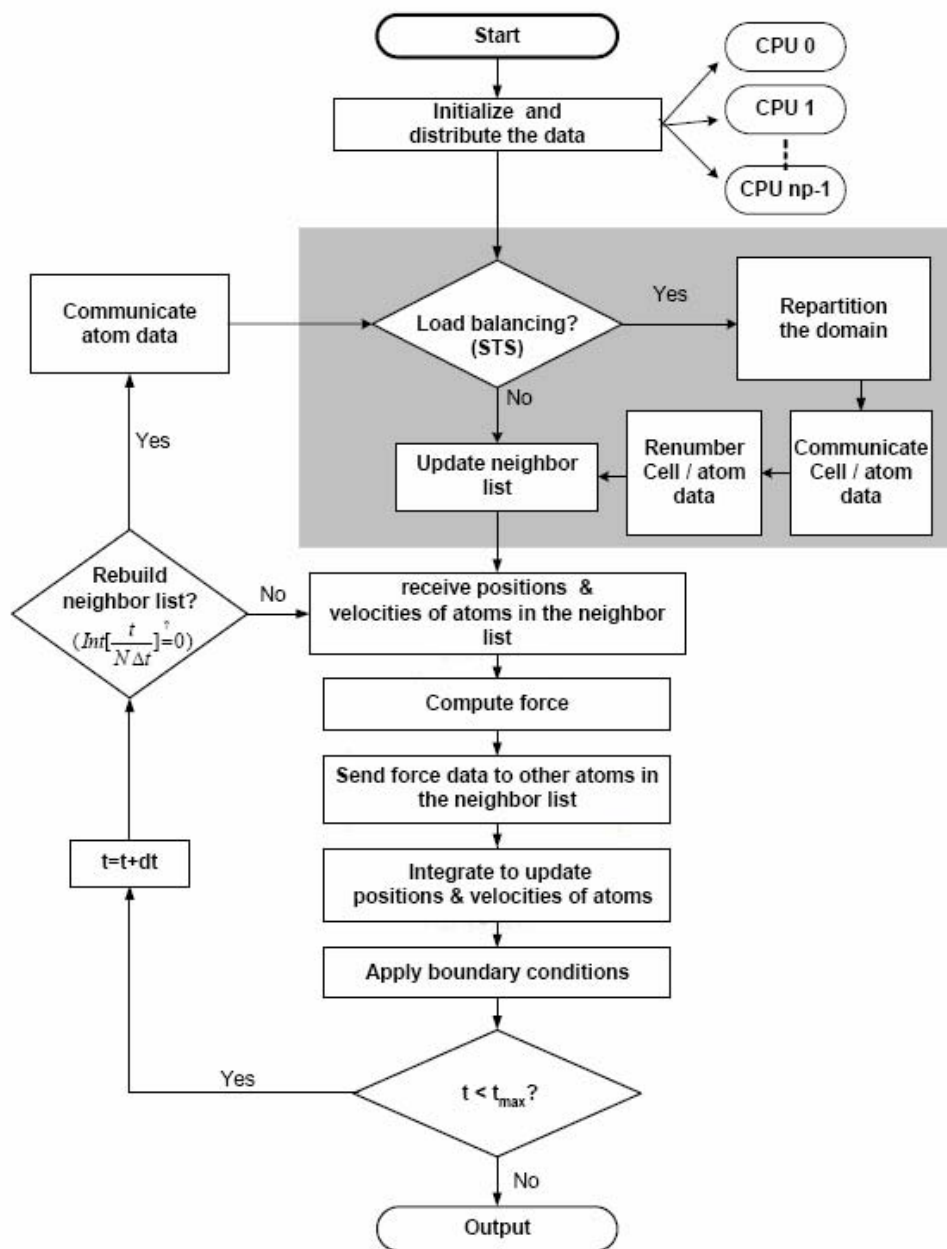
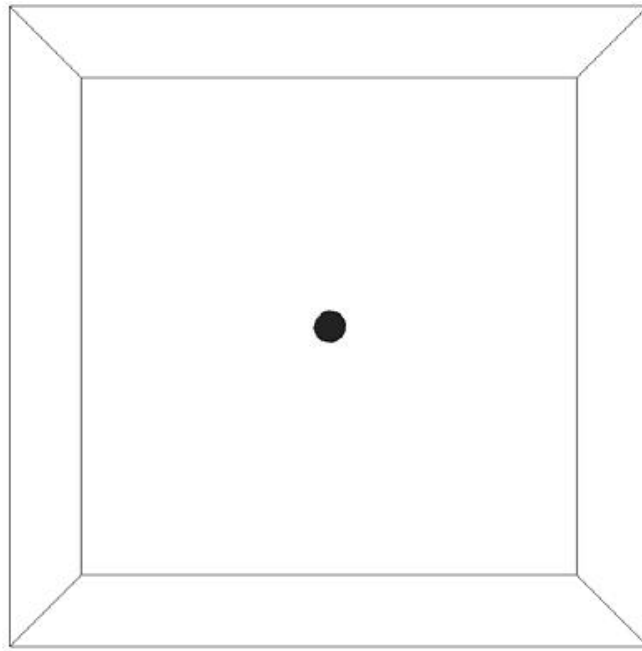


Fig. 2. 7 Periodic boundary conditions



**Fig. 2. 8 Proposed flow chart for parallel molecular dynamics simulation using dynamic domain decomposition.**



**Fig. 3. 1** Head-on ( $b= 0$ ) droplets pair collision initial setup on y-z plane.

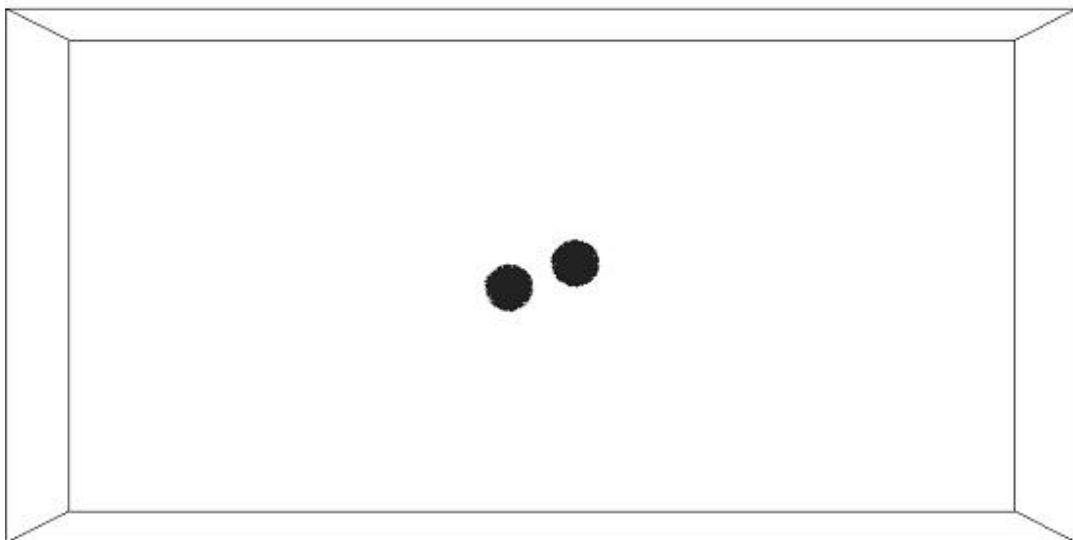


**Fig. 3. 2** Non-head-on (ex:  $b= 5nm$ ) droplets pair collision initial setup on x-y plane.



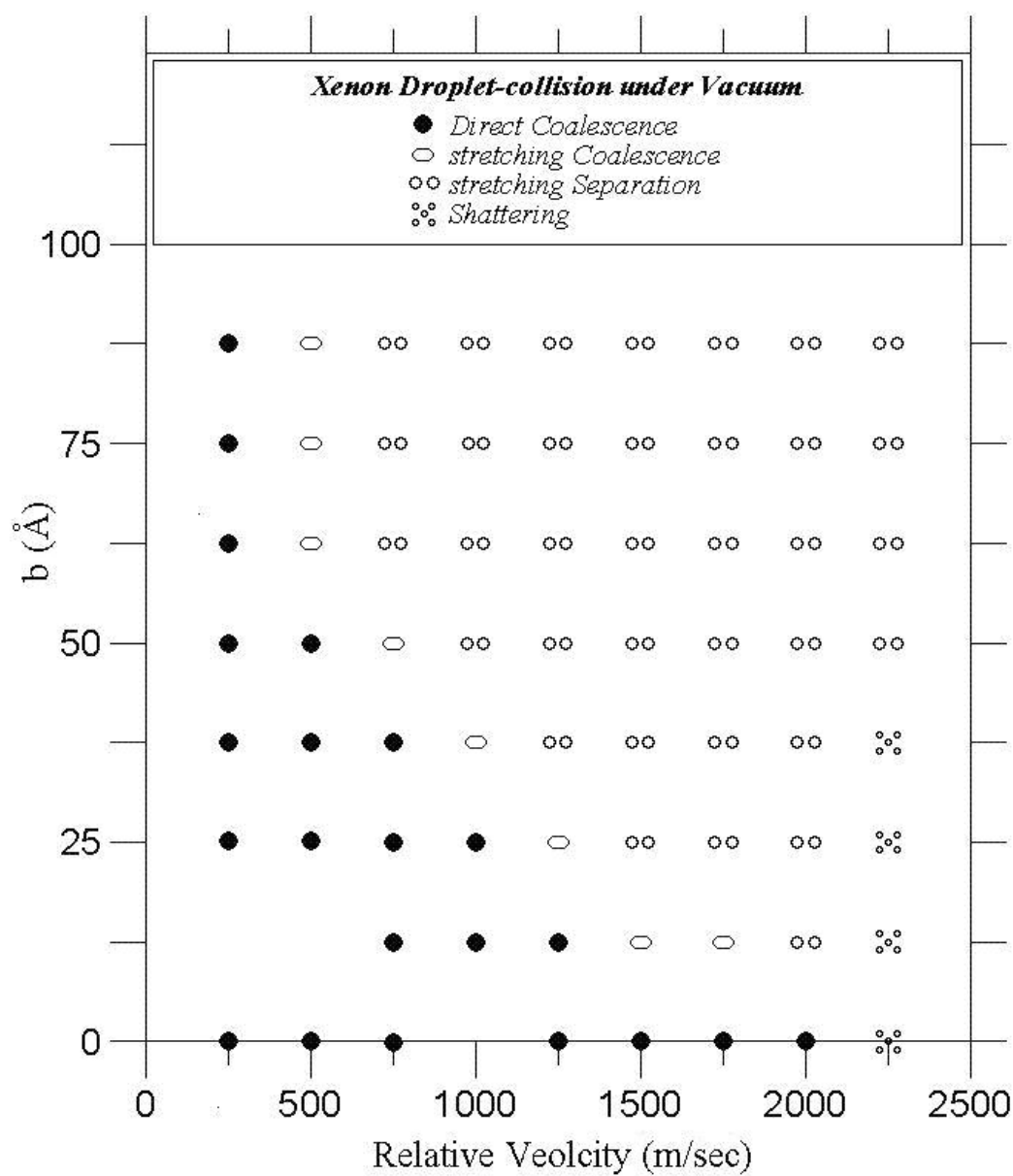


**Fig. 3.3** Distribution map of various regimes of Xenon droplet-collision.

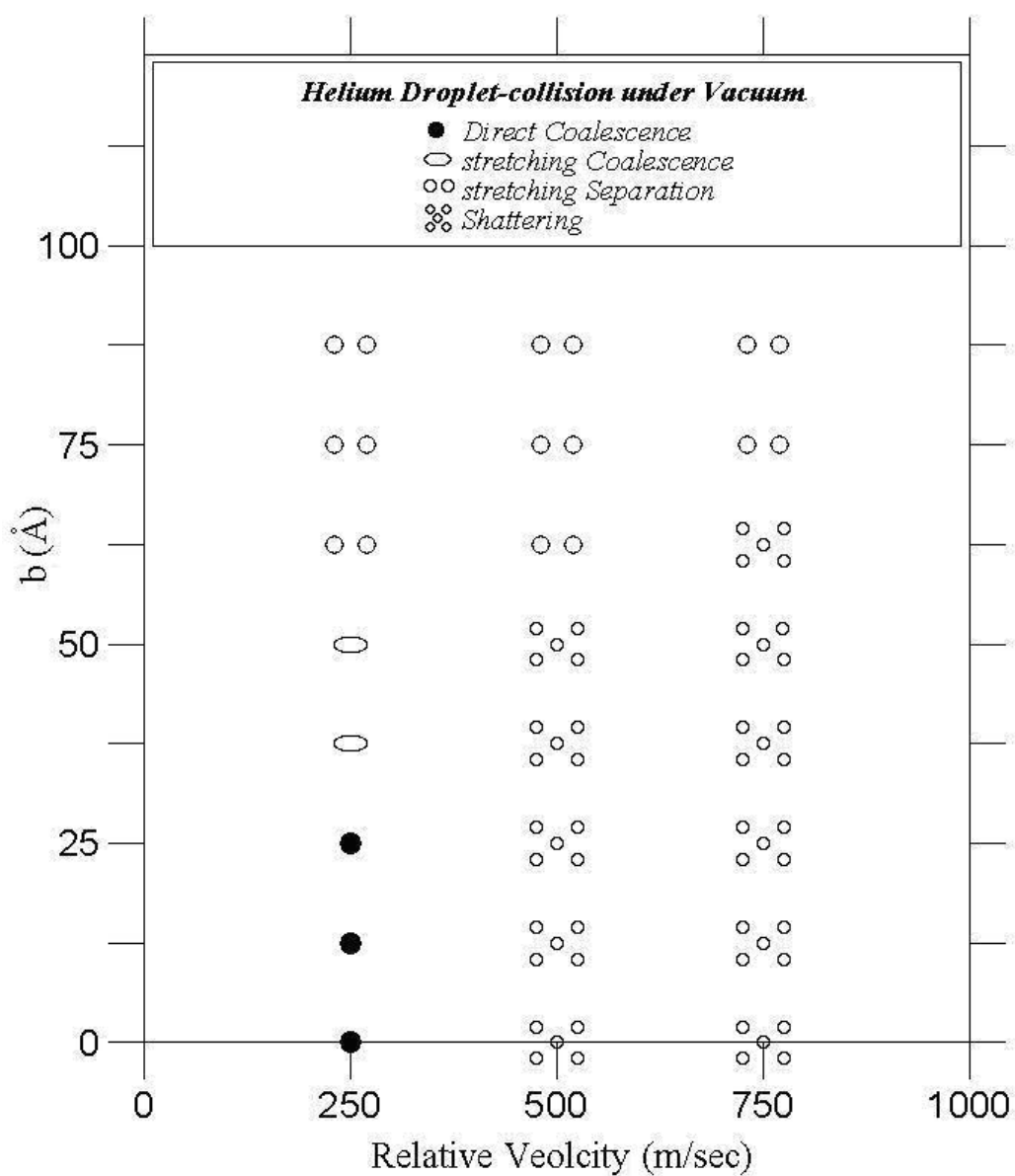


**Fig. 3. 4** Distribution map of various regimes of Helium droplet-collision.

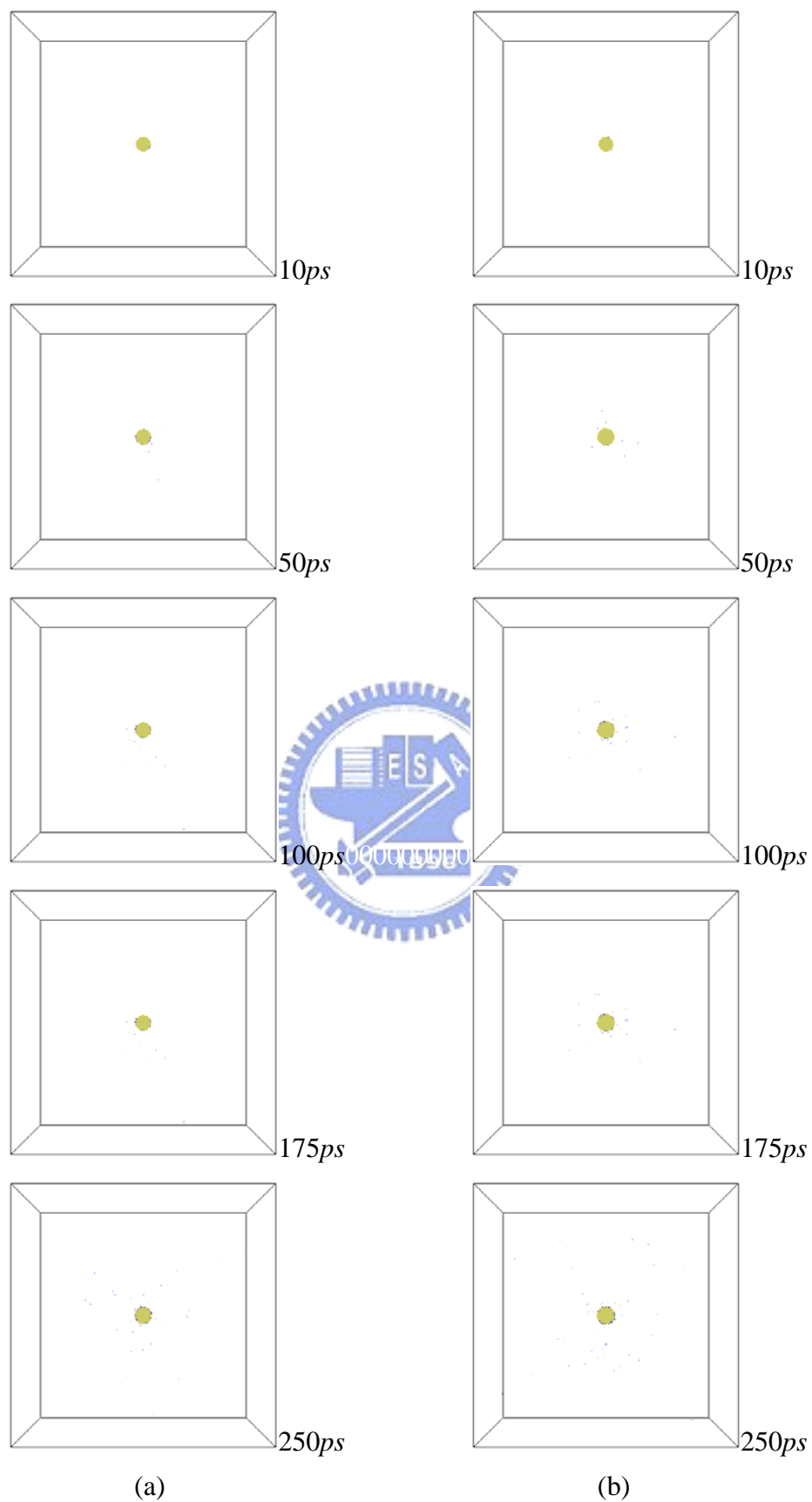


**Fig. 3. 5** Snapshot of Xenon droplet pair collision under vacuum, at (a)  $b=0, V=250\text{m/s}$ , (b)  $b=0, V=500\text{m/s}$ .

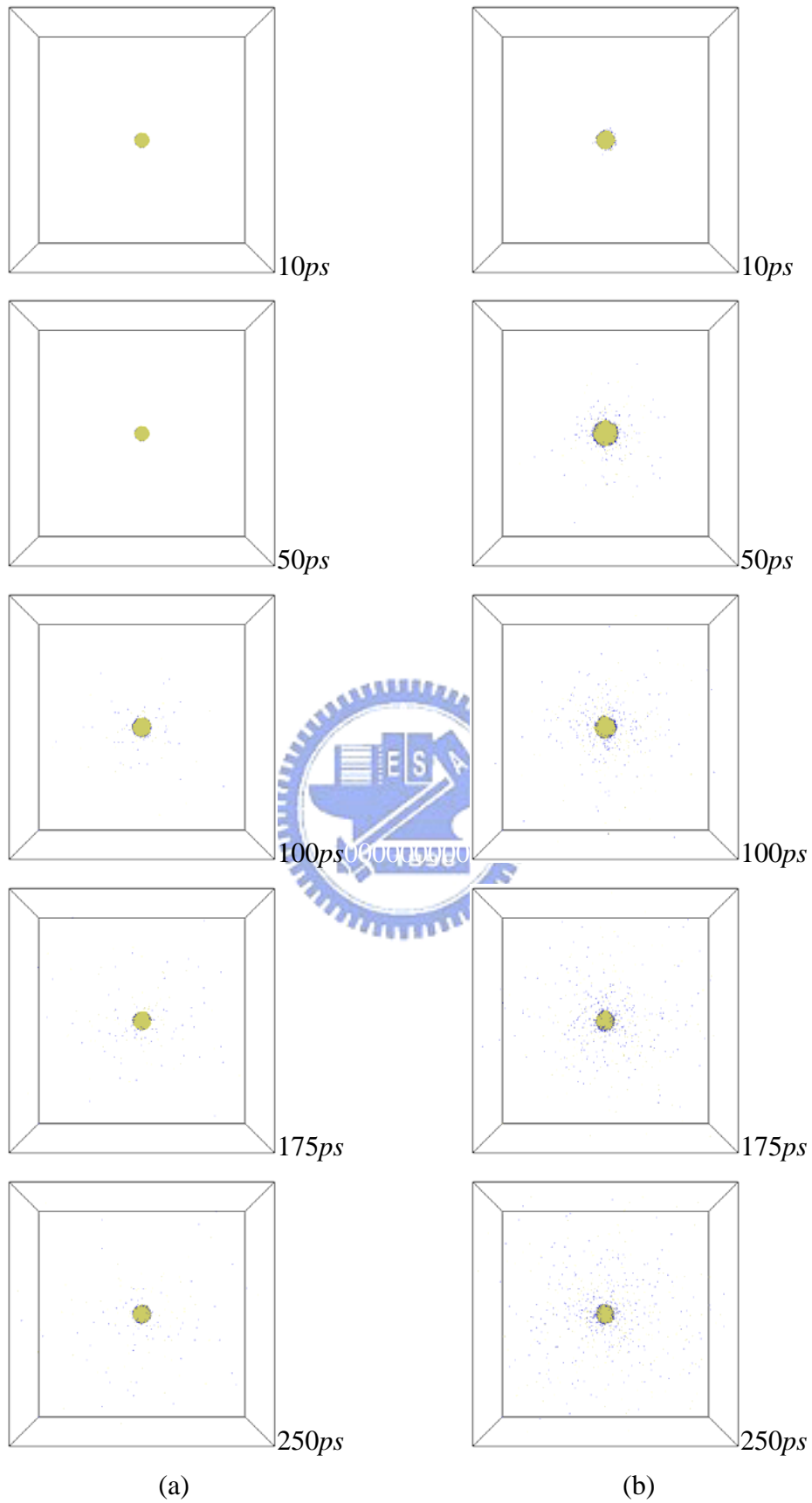


**Fig. 3. 6 Snapshot of Xenon droplet pair collision under vacuum, at (a)  $b=0$ ,  $V=750\text{m/s}$ , (b)  $b=0$ ,  $V=1250\text{m/s}$ .**

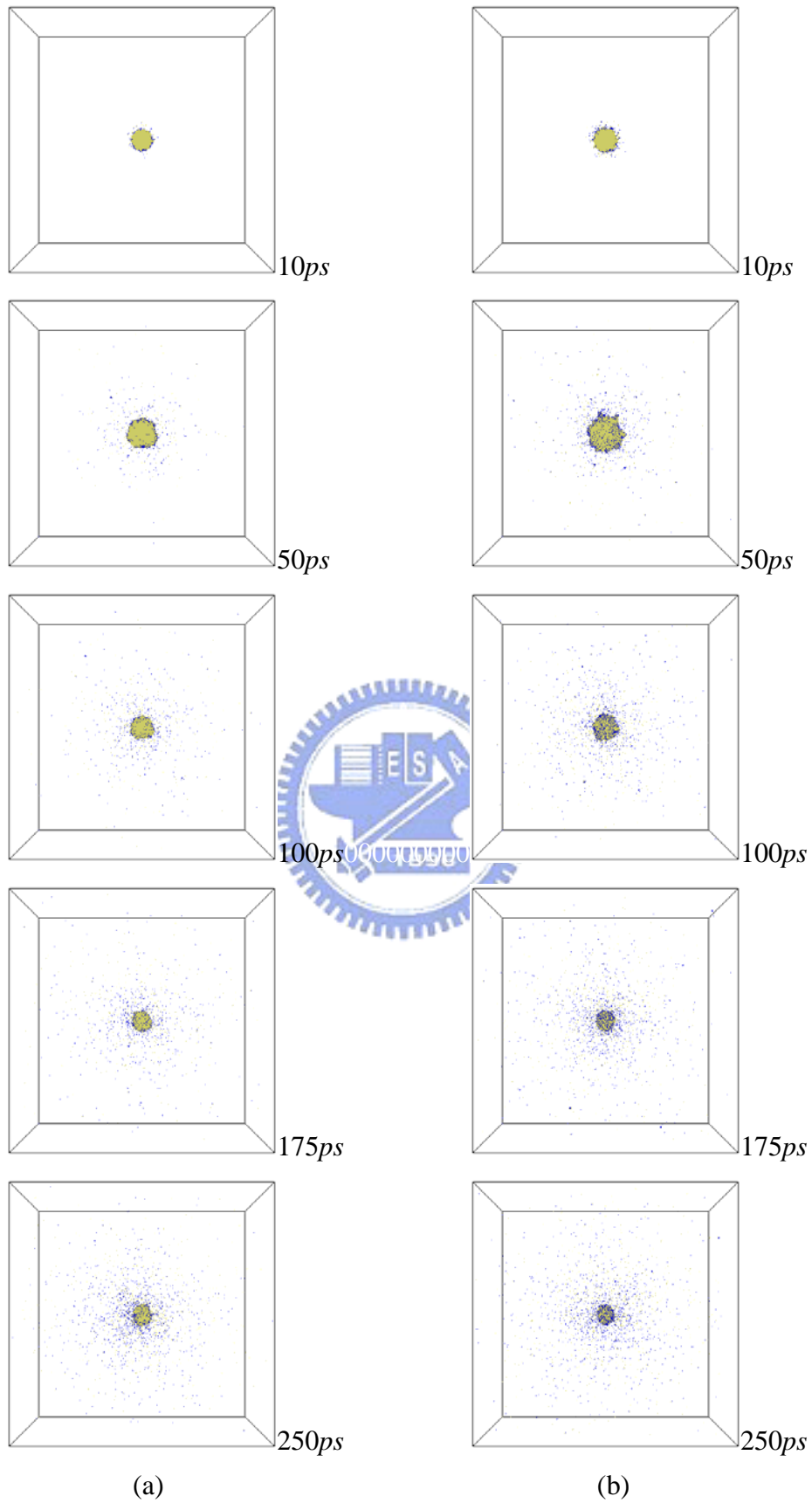


**Fig. 3. 7 Snapshot of Xenon droplet pair collision under vacuum, at (a)  $b=0$ ,  $V=1500m/s$ , (b)  $b=0$ ,  $V=1750m/s$ .**

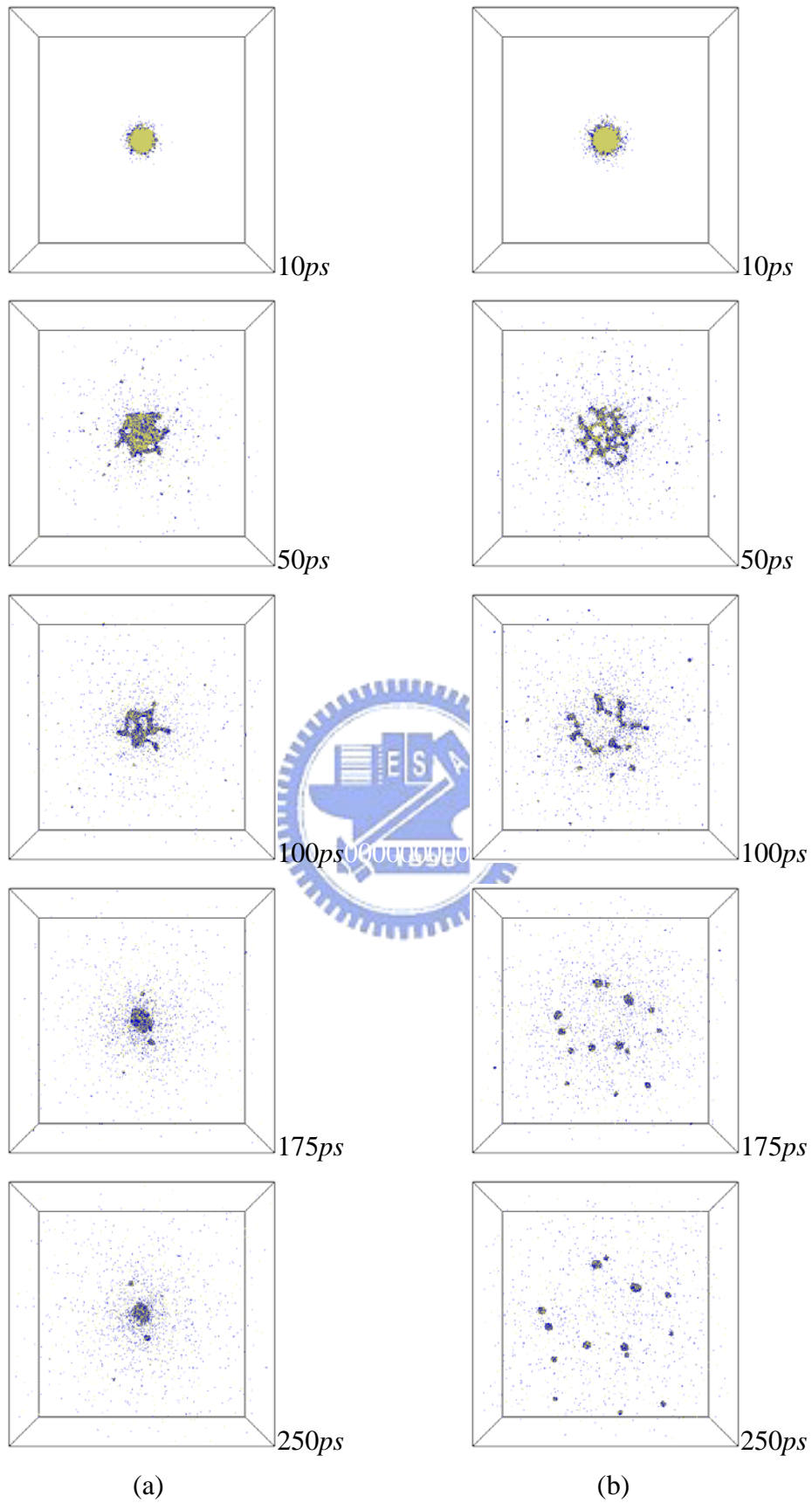


**Fig. 3. 8** Snapshot of Xenon droplet pair collision under vacuum, at (a)  $b=0$ ,  $V=2000\text{m/s}$ , (b)  $b=0$ ,  $V=2250\text{m/s}$ .

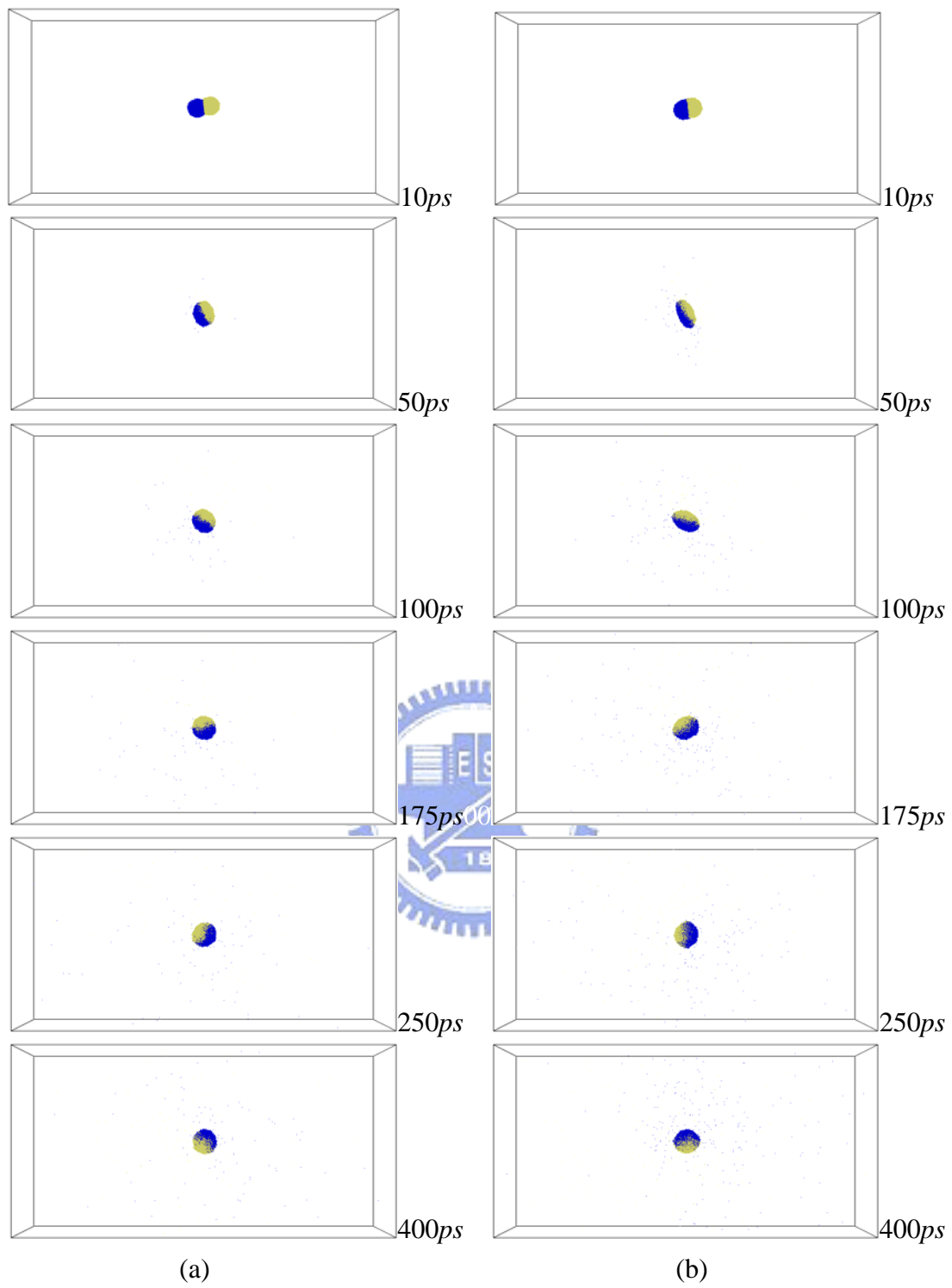


**Fig. 3. 9** Snapshot of xenon droplet pair collision under vacuum, at (a)  $b=1.25nm$ ,  $V=750m/s$ , (b)  $b=1.25nm$ ,  $V=1000m/s$ .

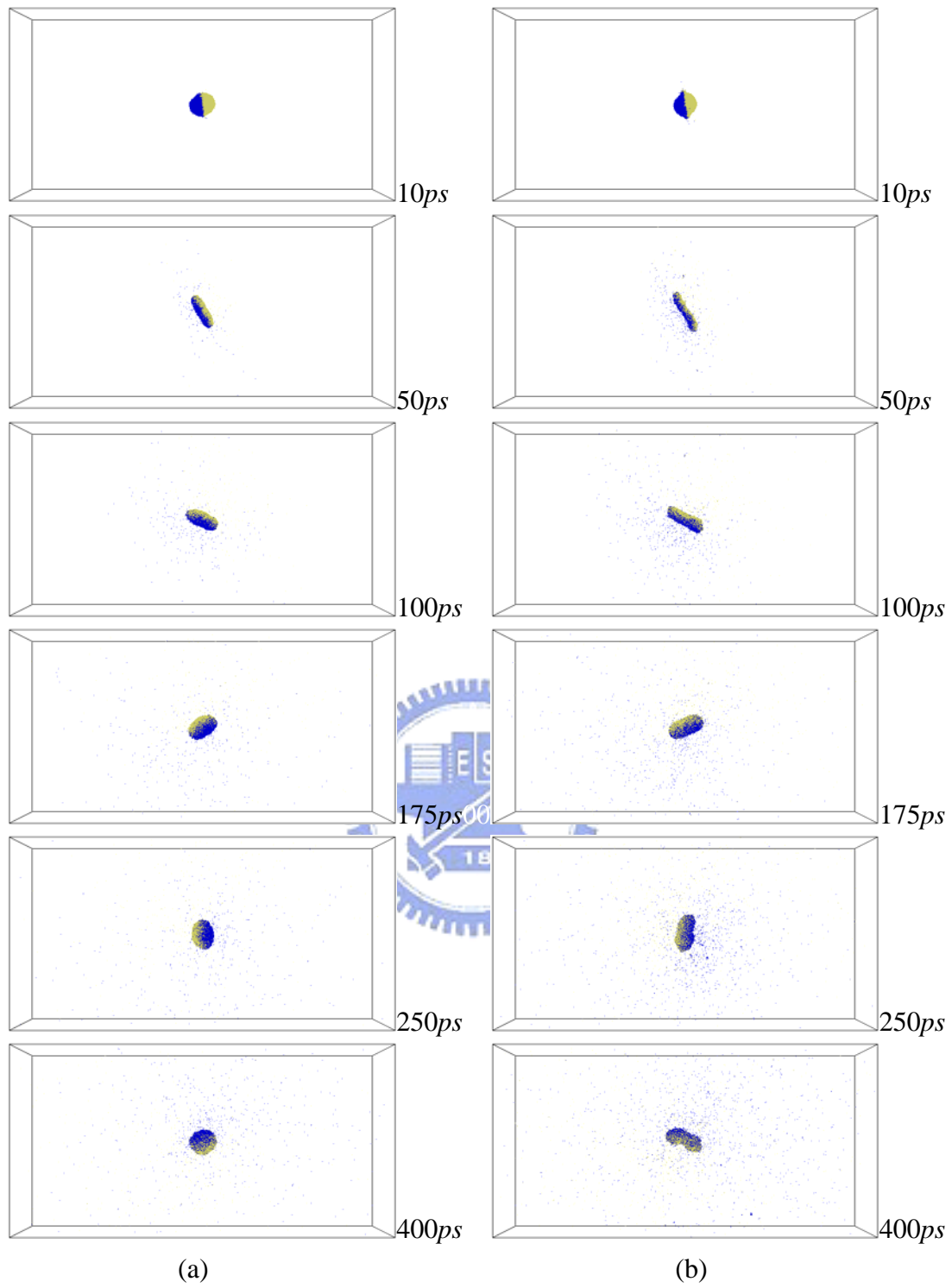


**Fig. 3. 10** Snapshot of xenon droplet pair collision under vacuum, at (a)  $b=1.25\text{nm}$ ,  $V=1250\text{m/s}$ , (b)  $b=1.25\text{nm}$ ,  $V=1500\text{m/s}$ .



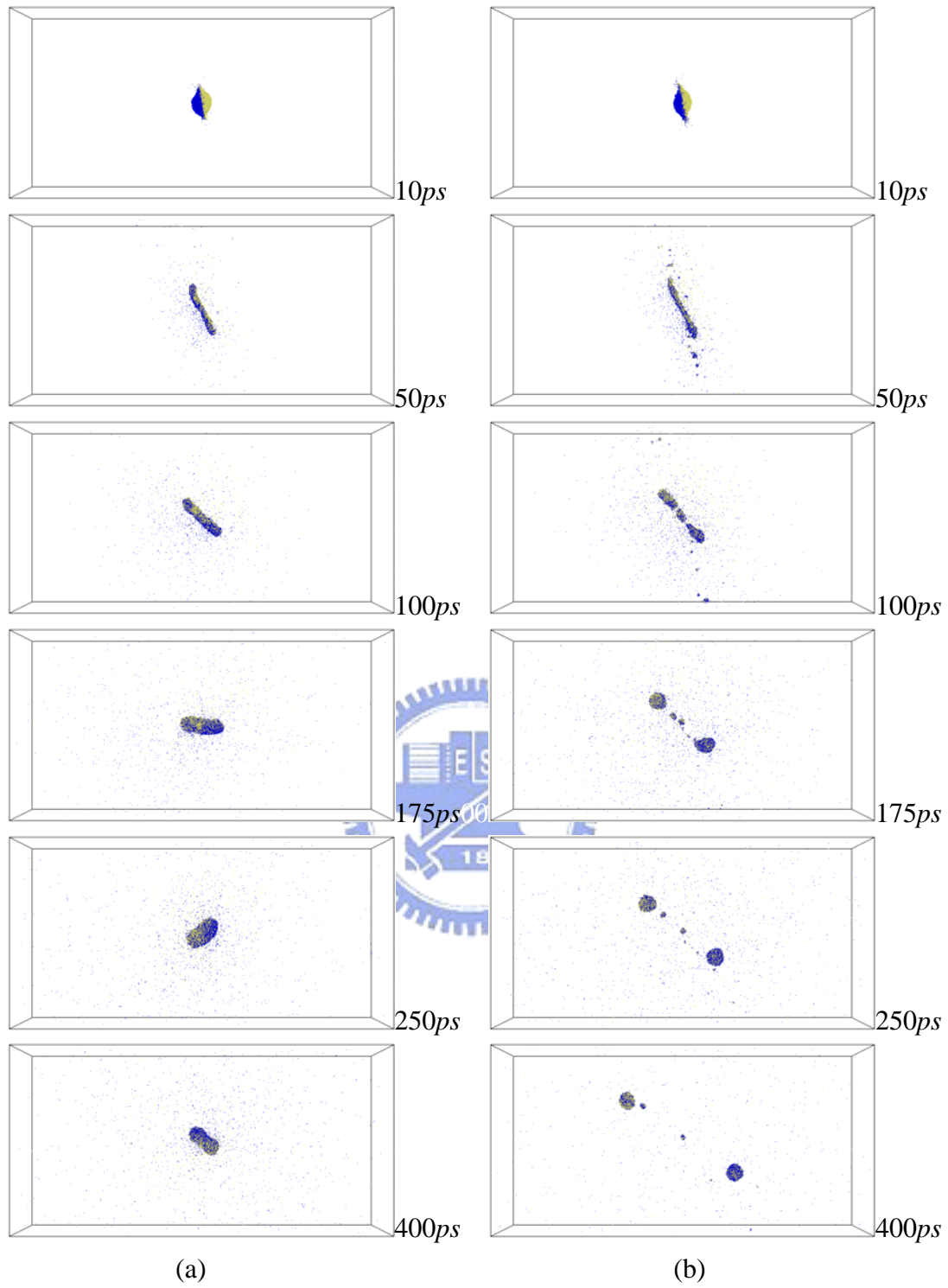


**Fig. 3. 11 Snapshot of xenon droplet pair collision under vacuum, at (a)  $b=1.25\text{nm}$ ,  $V=1750\text{m/s}$ , (b)  $b=1.25\text{nm}$ ,  $V=2000\text{m/s}$ .**

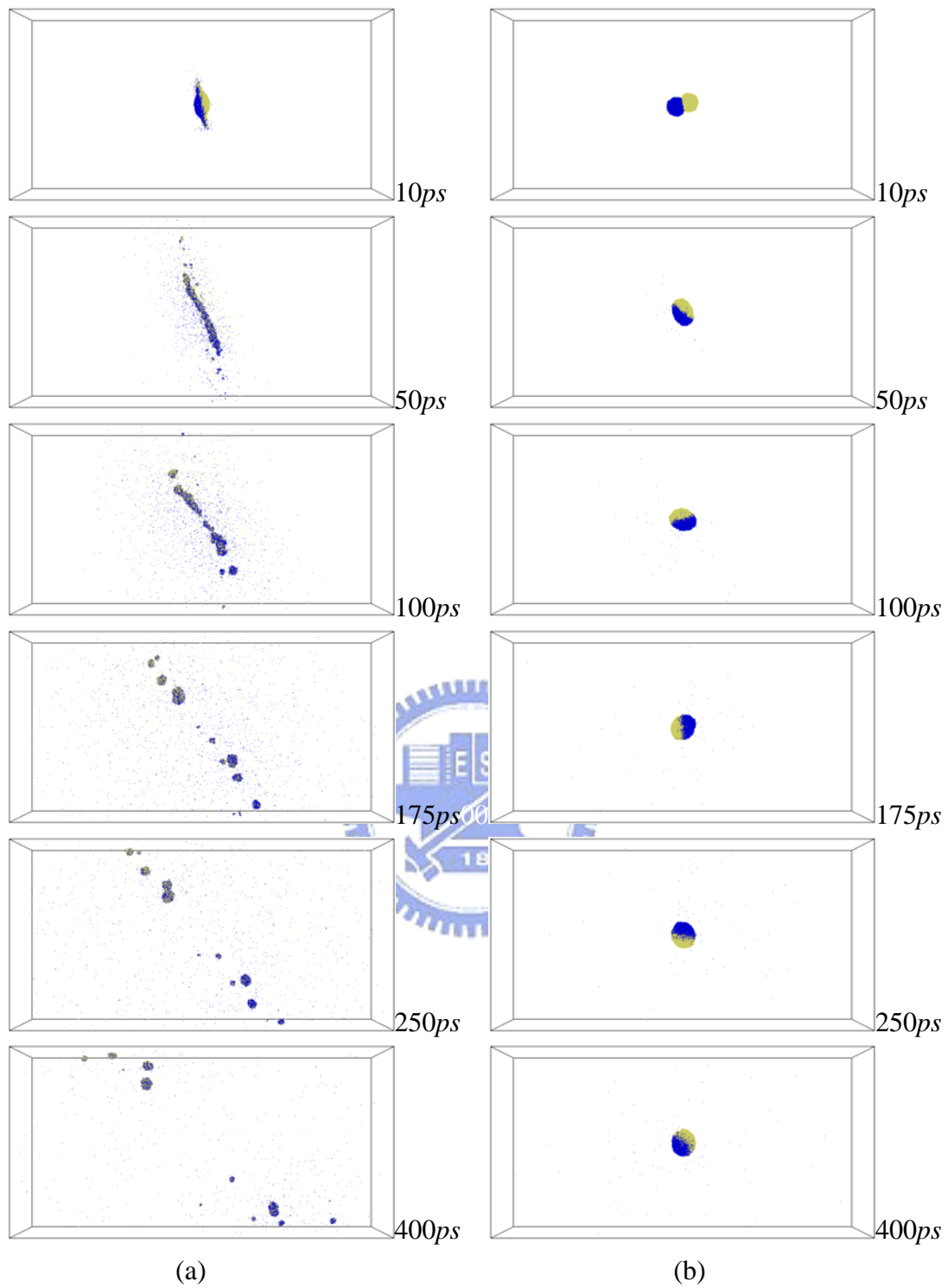


**Fig. 3. 12 Snapshot of xenon droplet pair collision under vacuum, at (a)  $b=1.25\text{nm}$ ,  $V=2250\text{m/s}$ , (b)  $b=2.5\text{nm}$ ,  $V=750\text{m/s}$ .**

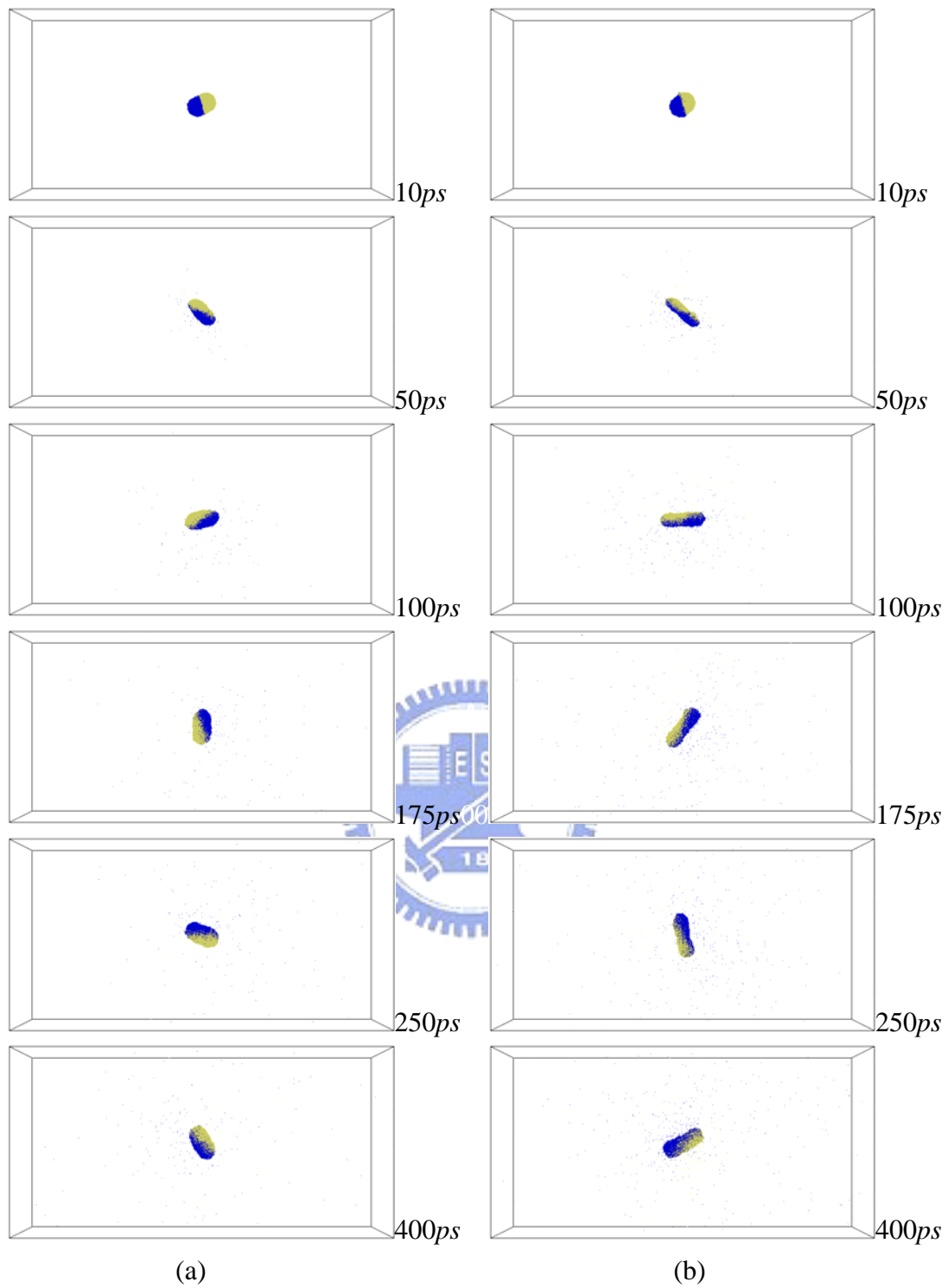


**Fig. 3. 13** Snapshot of xenon droplet pair collision under vacuum, at (a)  $b=2.5nm$ ,  $V=1000m/s$ , (b)  $b=2.5nm$ ,  $V=1250m/s$ .

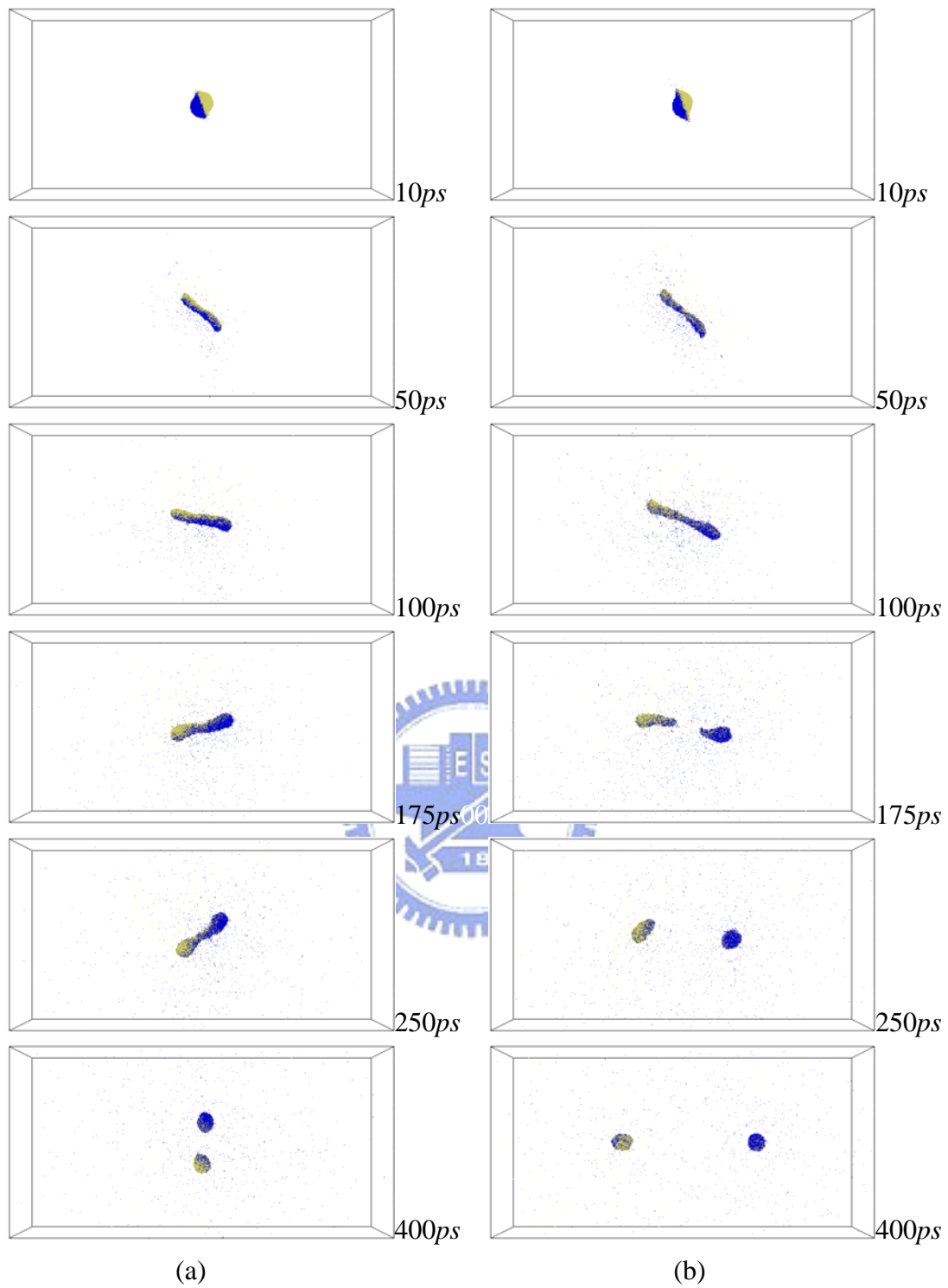


**Fig. 3. 14** Snapshot of xenon droplet pair collision under vacuum, at (a)  $b=2.5\text{nm}$ ,  $V=1500\text{m/s}$ , (b)  $b=2.5\text{nm}$ ,  $V=1750\text{m/s}$ .

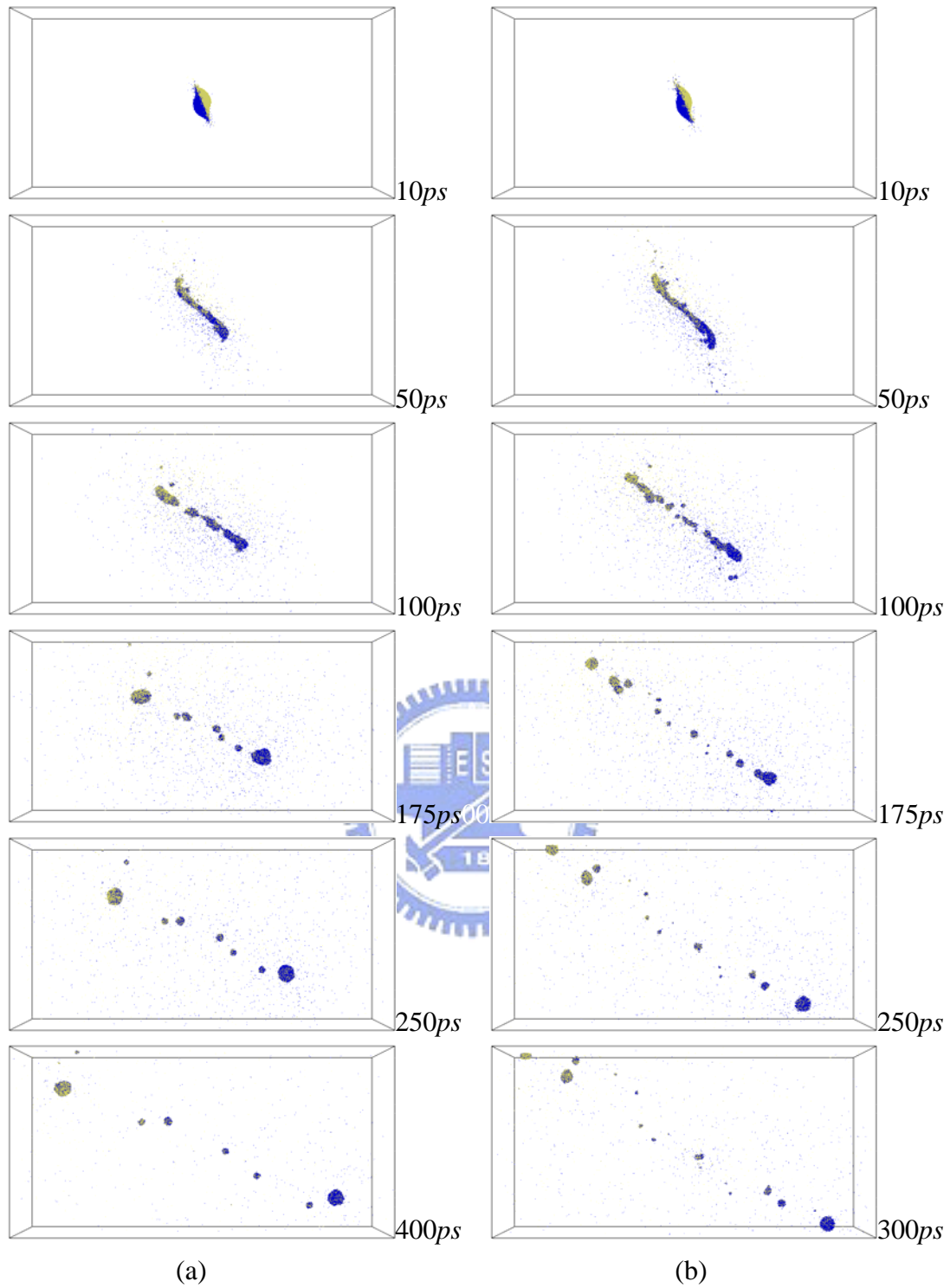


**Fig. 3. 15** Snapshot of xenon droplet pair collision under vacuum, at (a)  $b=2.5nm$ ,  $V=2000m/s$ , (b)  $b=2.5nm$ ,  $V=2250m/s$ .

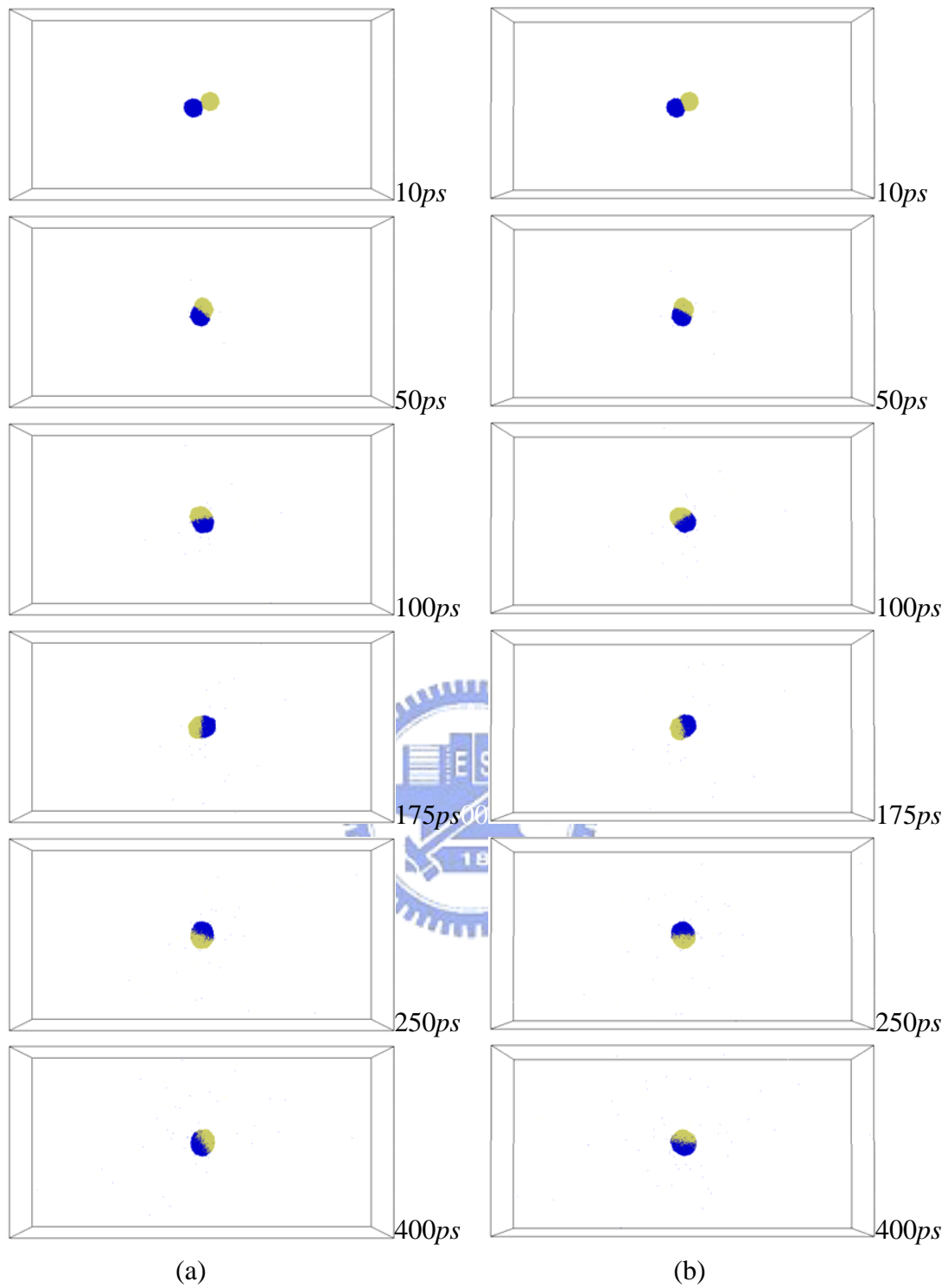


**Fig. 3. 16** Snapshot of xenon droplet pair collision under vacuum, at (a)  $b=3.75nm$ ,  $V=250m/s$ , (b)  $b=3.75nm$ ,  $V=500m/s$ .

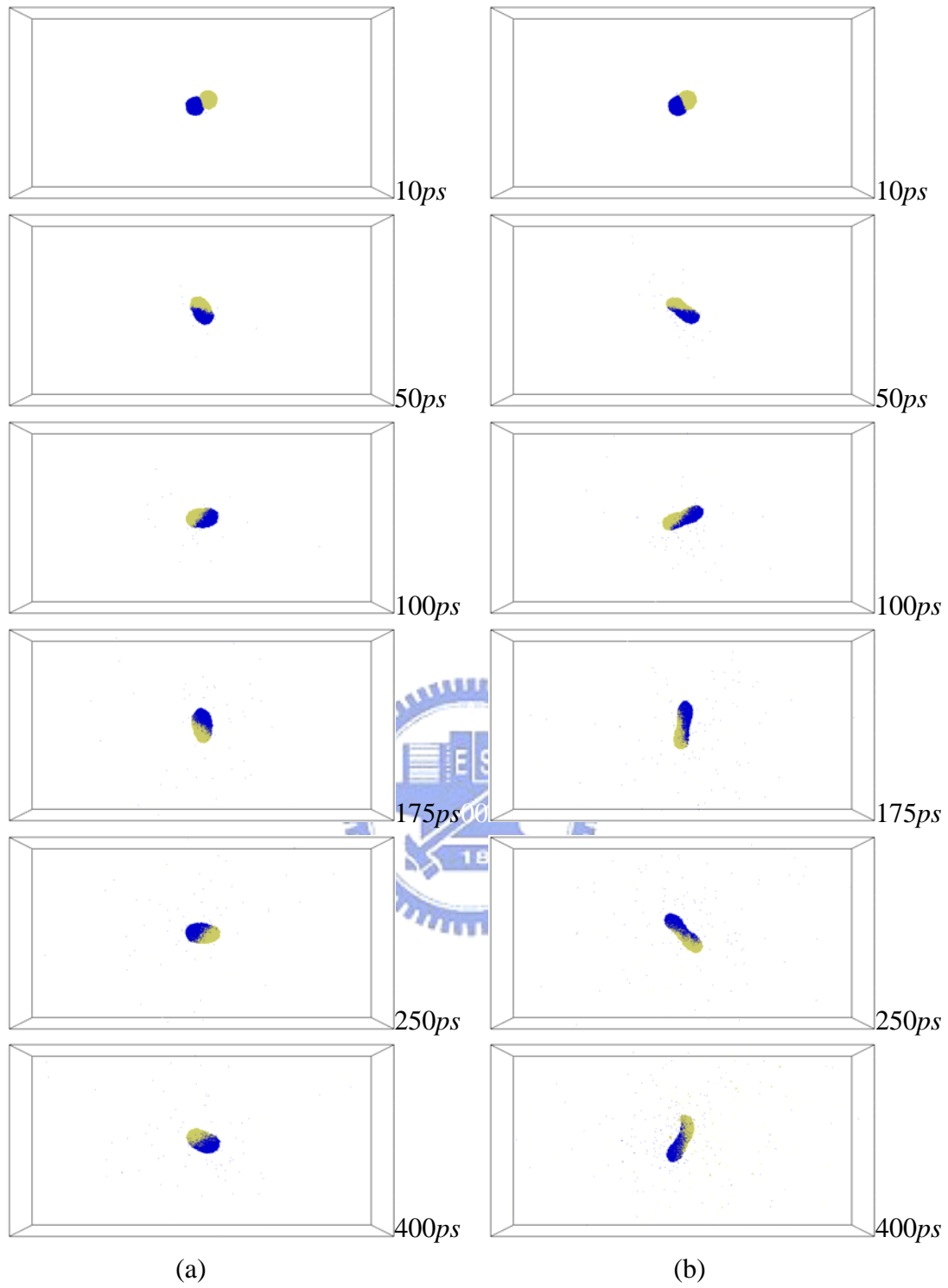


**Fig. 3. 17** Snapshot of xenon droplet pair collision under vacuum, at (a)  $b=3.75nm$ ,  $V=750m/s$ , (b)  $b=3.75nm$ ,  $V=1000m/s$ .

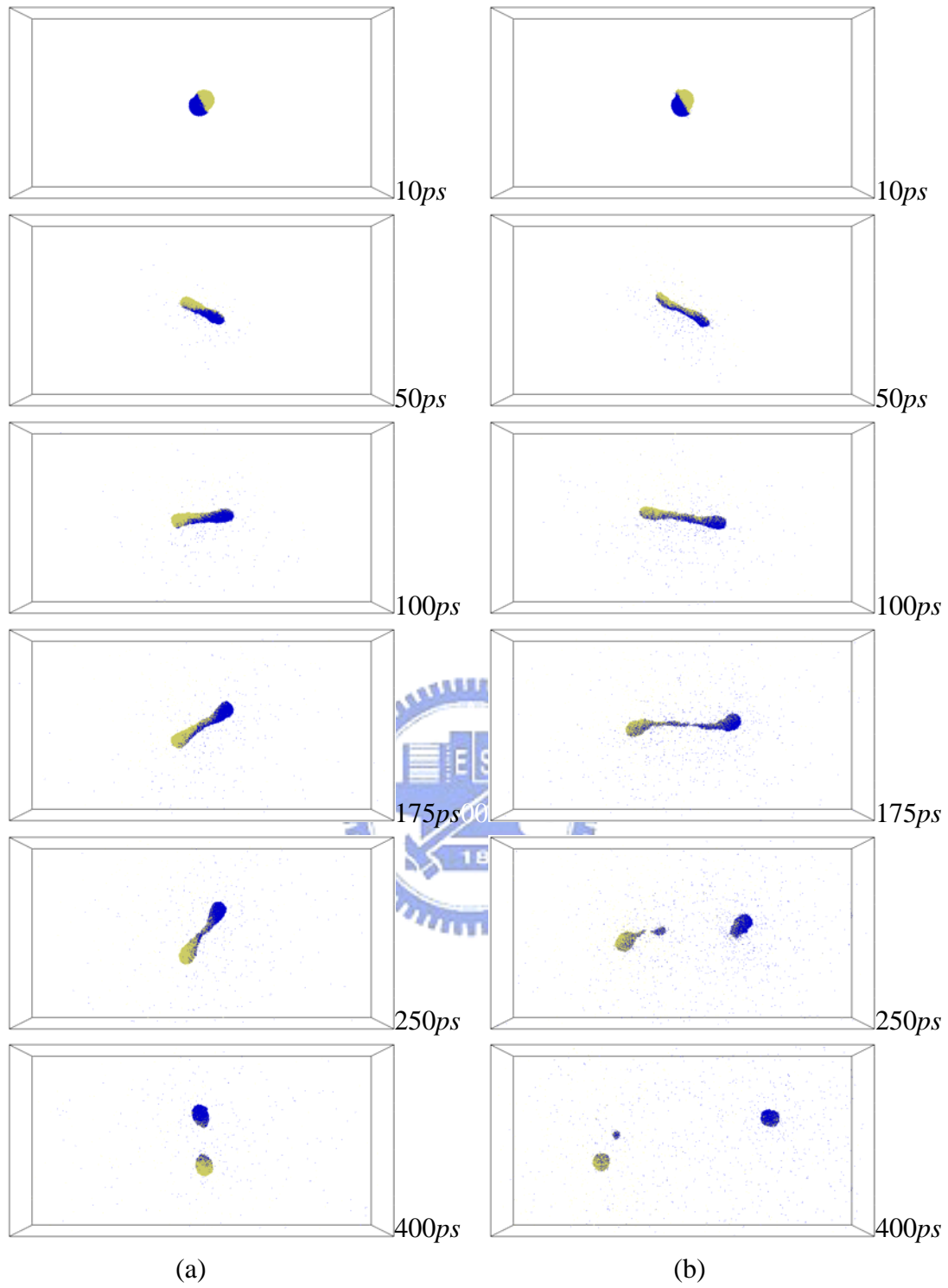


**Fig. 3. 18 Snapshot of xenon droplet pair collision under vacuum, at (a)  $b=3.75\text{nm}$ ,  $V=1250\text{m/s}$ , (b)  $b=3.75\text{nm}$ ,  $V=1500\text{m/s}$ .**



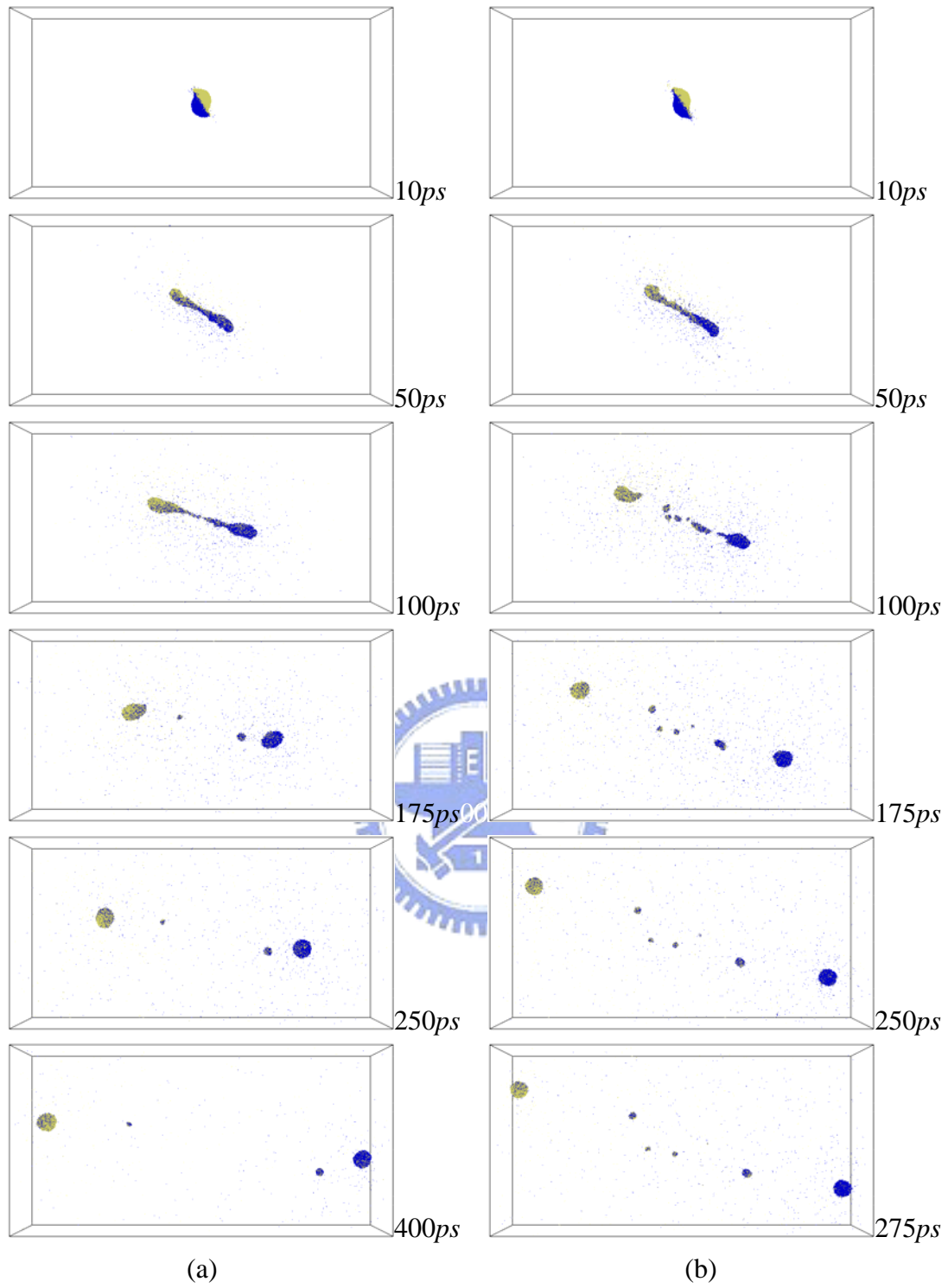


**Fig. 3. 19** Snapshot of xenon droplet pair collision under vacuum, at (a)  $b=3.75nm$ ,  $V=1750m/s$ , (b)  $b=3.75nm$ ,  $V=2000m/s$ .

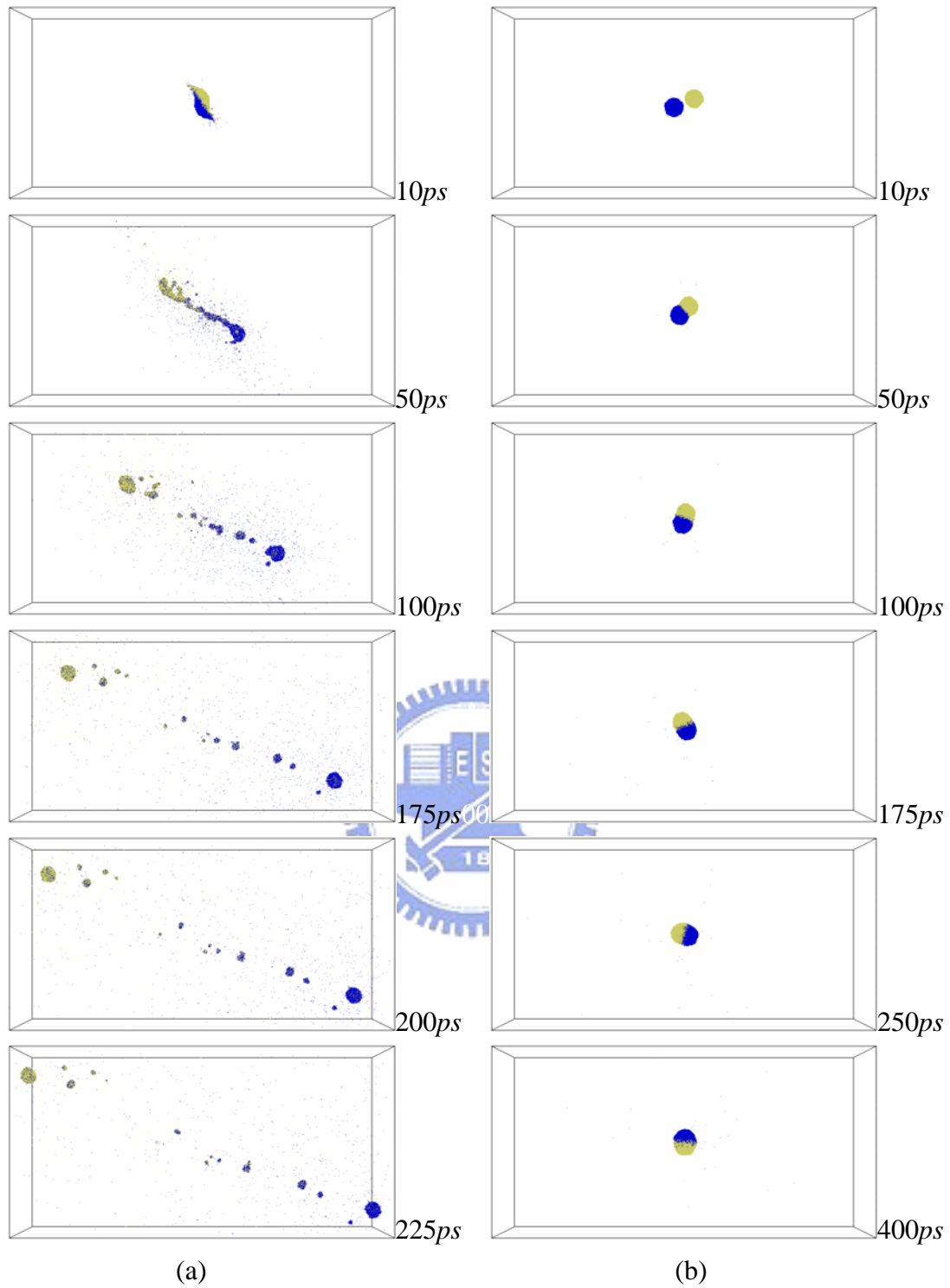


**Fig. 3. 20** Snapshot of xenon droplet pair collision under vacuum, at (a)  $b=3.75nm$ ,  $V=2250m/s$ , (b)  $b=5nm$ ,  $V=250m/s$ .

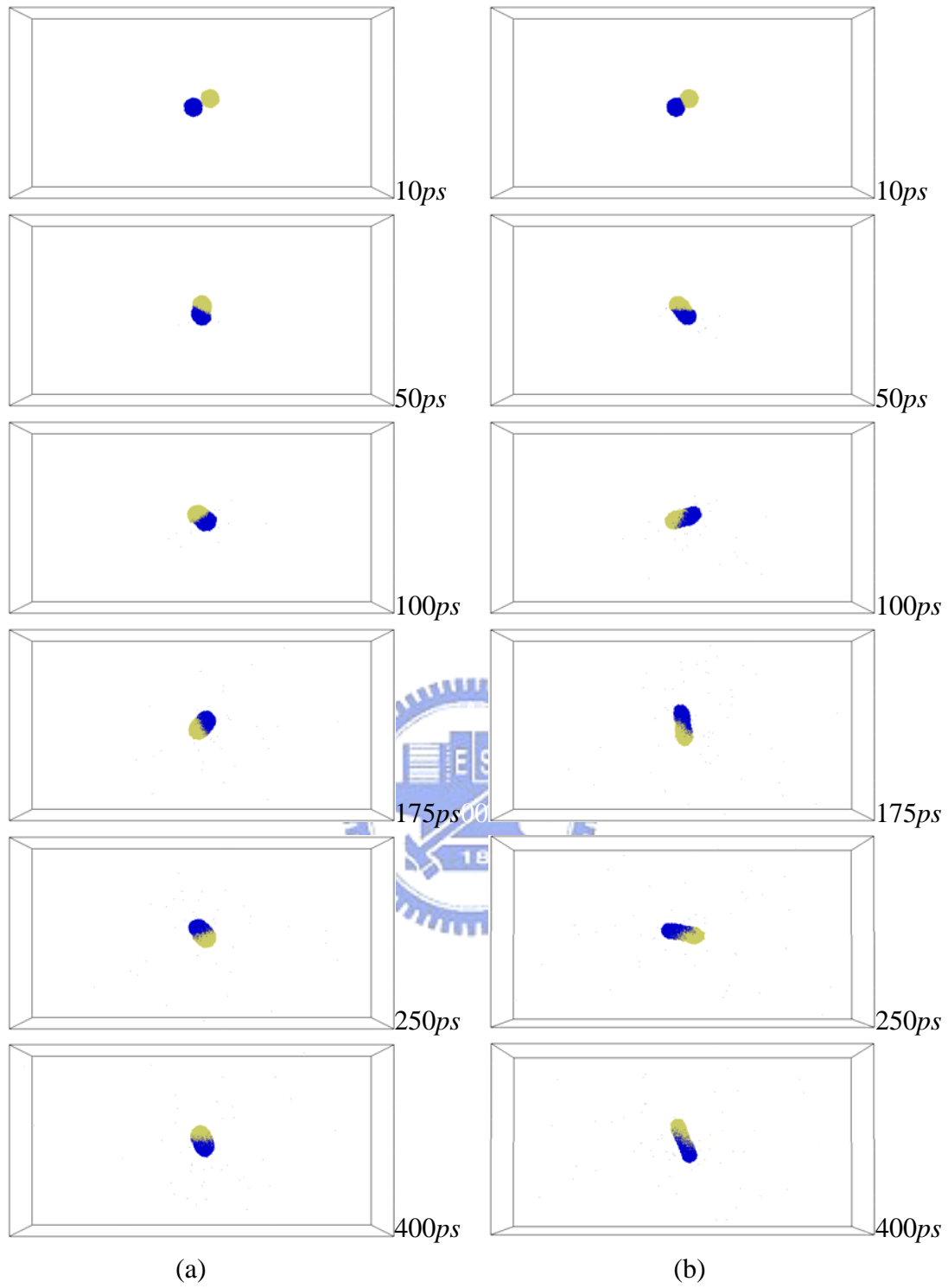


**Fig. 3. 21 Snapshot of xenon droplet pair collision under vacuum, at (a)  $b=5\text{nm}$ ,  $V=500\text{m/s}$ , (b)  $b=5\text{nm}$ ,  $V=750\text{m/s}$ .**

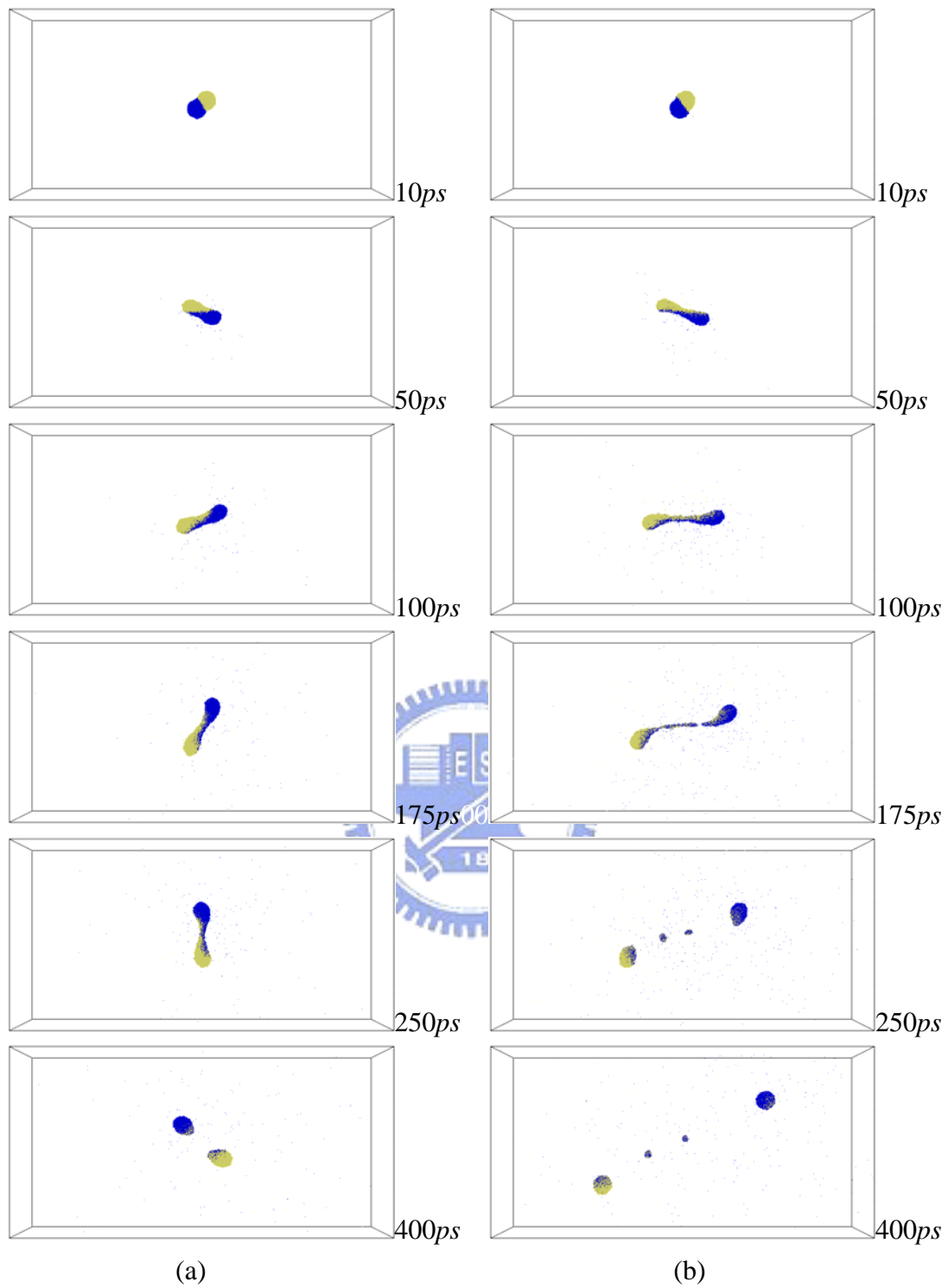


**Fig. 3. 22 Snapshot of xenon droplet pair collision under vacuum, at (a)  $b=5\text{nm}$ ,  $V=1000\text{m/s}$ , (b)  $b=5\text{nm}$ ,  $V=1250\text{m/s}$ ..**

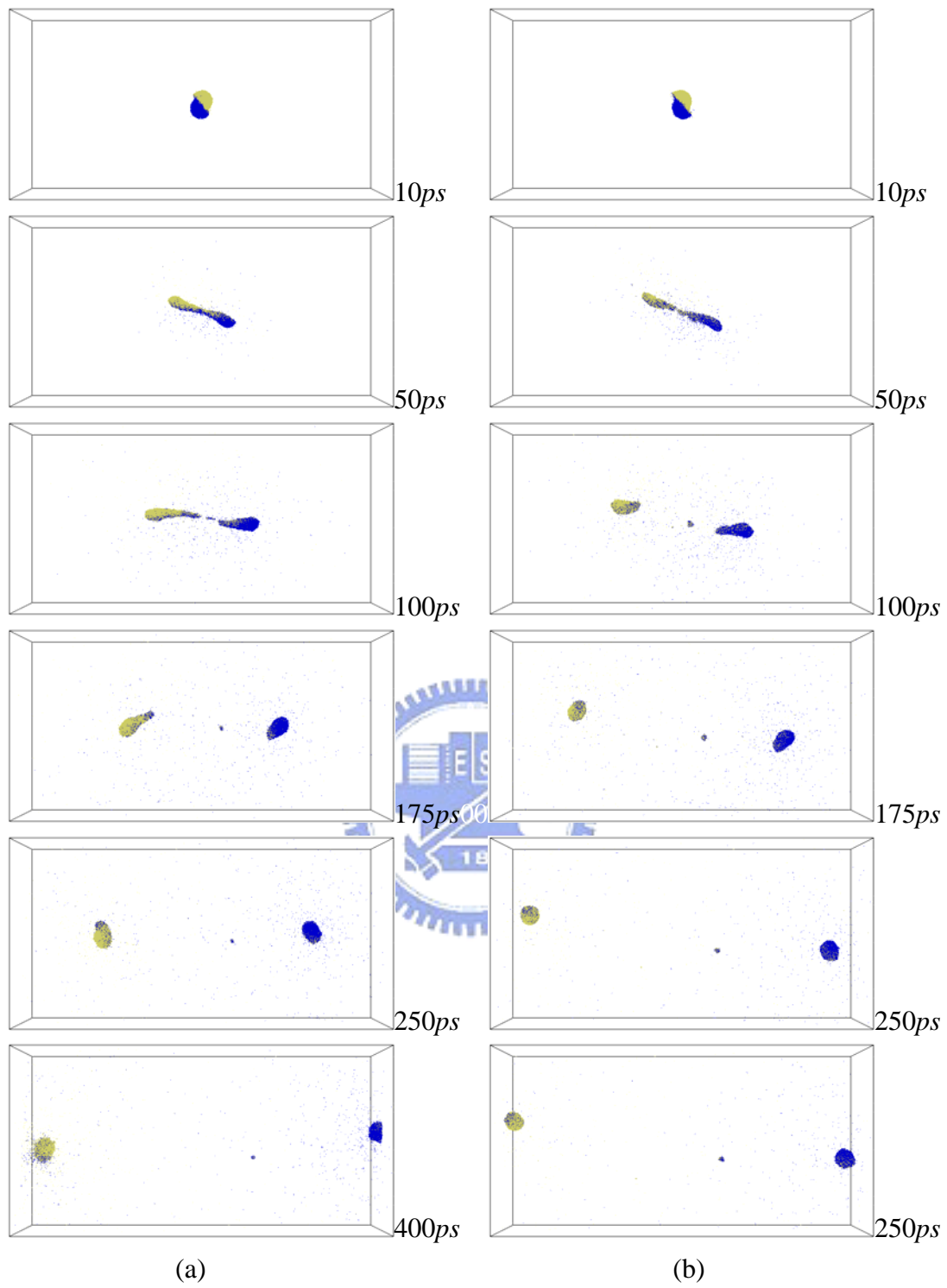


**Fig. 3. 23 Snapshot of xenon droplet pair collision under vacuum, at (a)  $b=5nm$ ,  $V=1500m/s$ , (b)  $b=5nm$ ,  $V=1750m/s$ .**

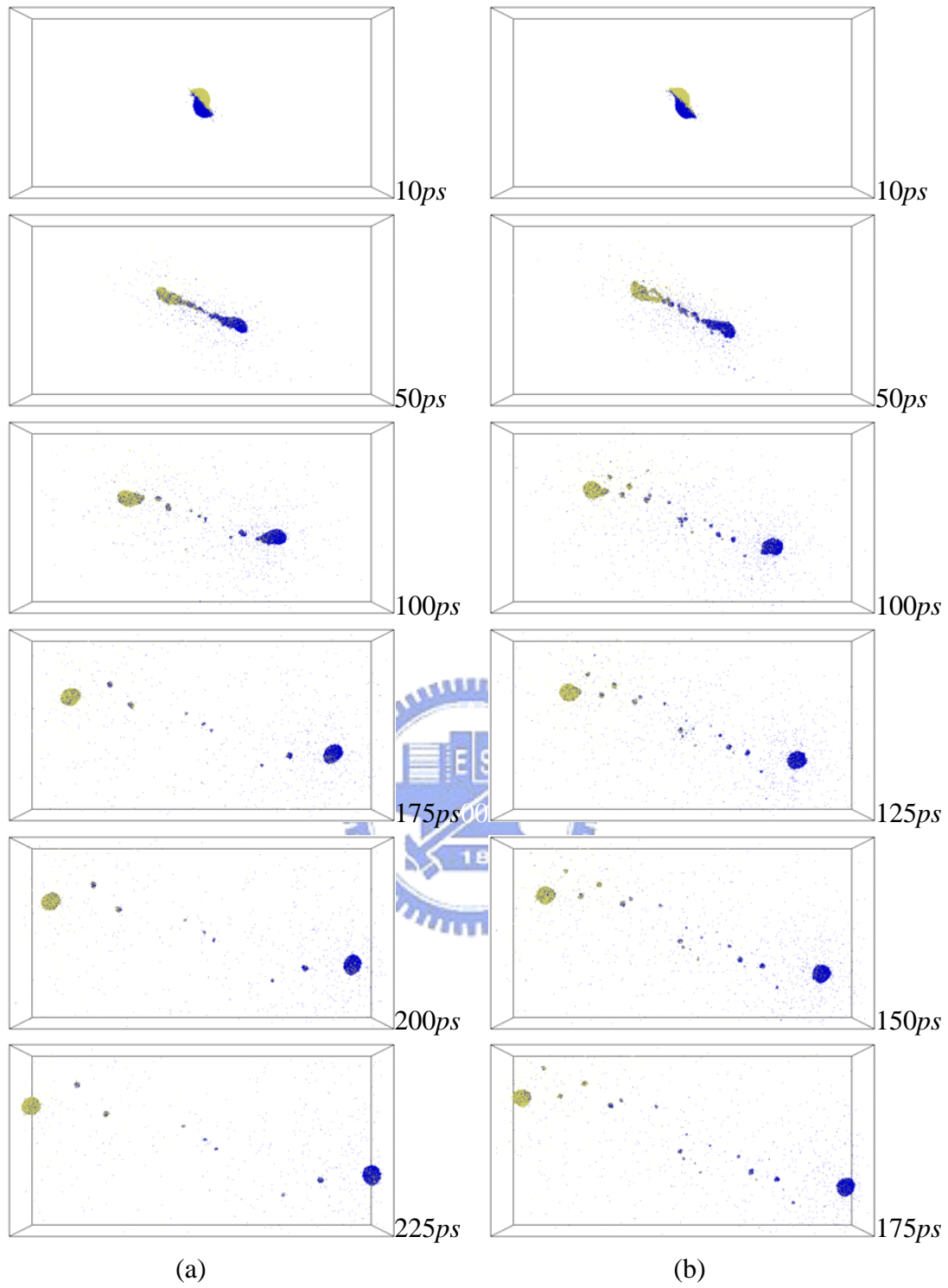


**Fig. 3. 24** Snapshot of xenon droplet pair collision under vacuum, at (a)  $b=5\text{ nm}$ ,  $V=2000\text{ m/s}$ , (b)  $b=5\text{ nm}$ ,  $V=2250\text{ m/s}$ .

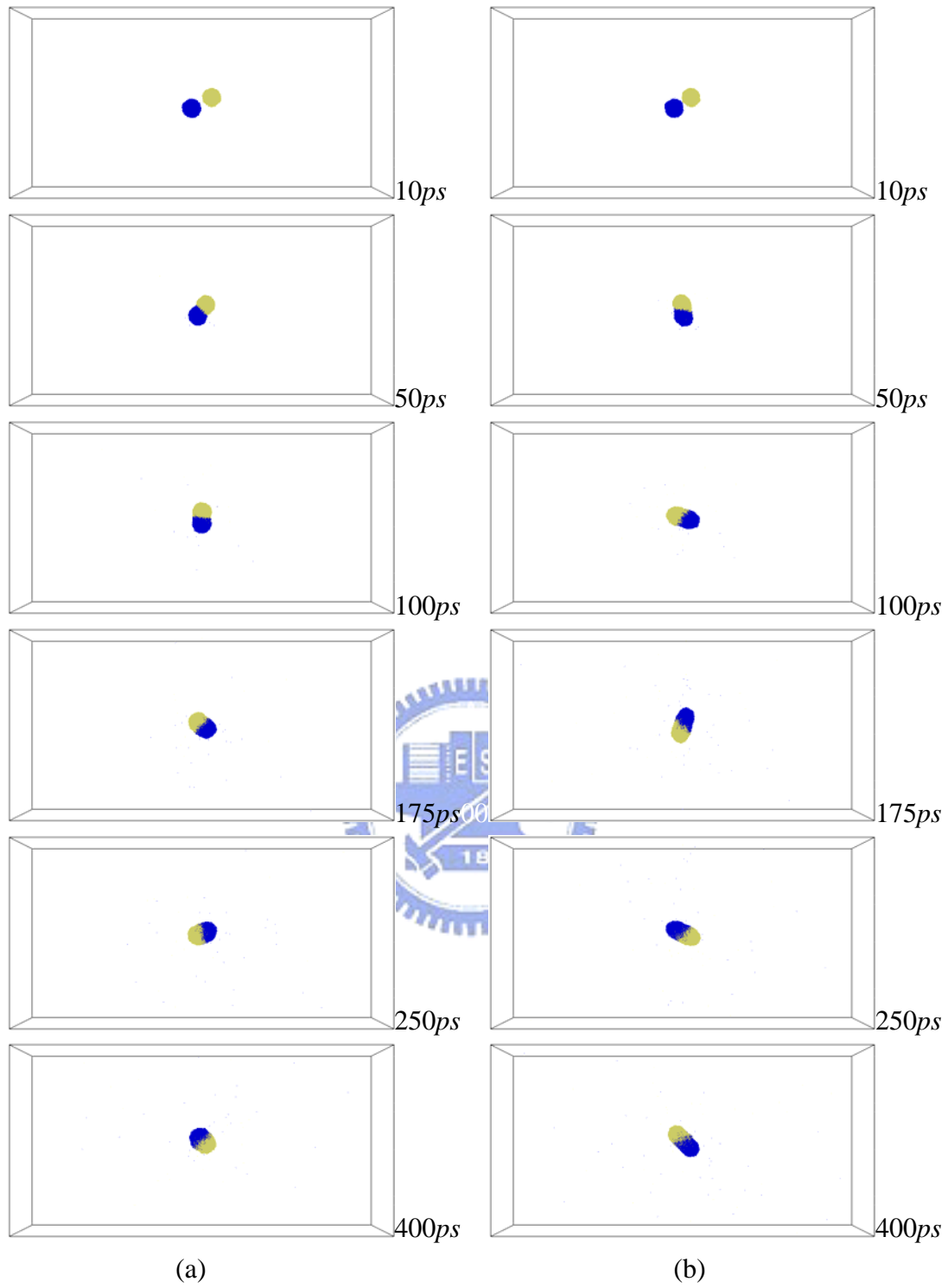


**Fig. 3. 25 Snapshot of xenon droplet pair collision under vacuum, at (a)  $b=6.25nm$ ,  $V=250m/s$ , (b)  $b=6.25nm$ ,  $V=500m/s$ .**

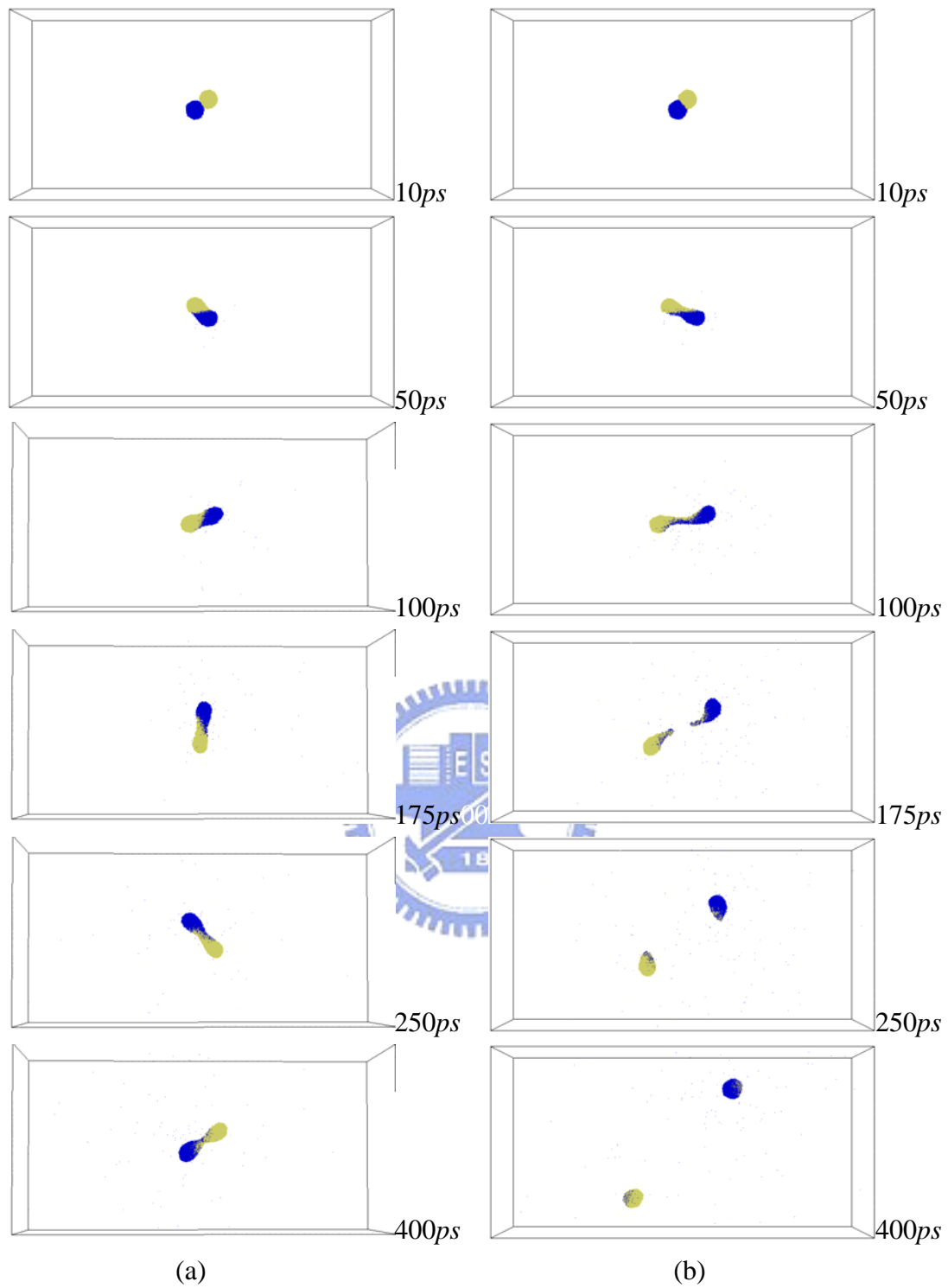


**Fig. 3. 26 Snapshot of xenon droplet pair collision under vacuum, at (a)  $b=6.25\text{nm}$ ,  $V=750\text{m/s}$ , (b)  $b=6.25\text{nm}$ ,  $V=1000\text{m/s}$ .**



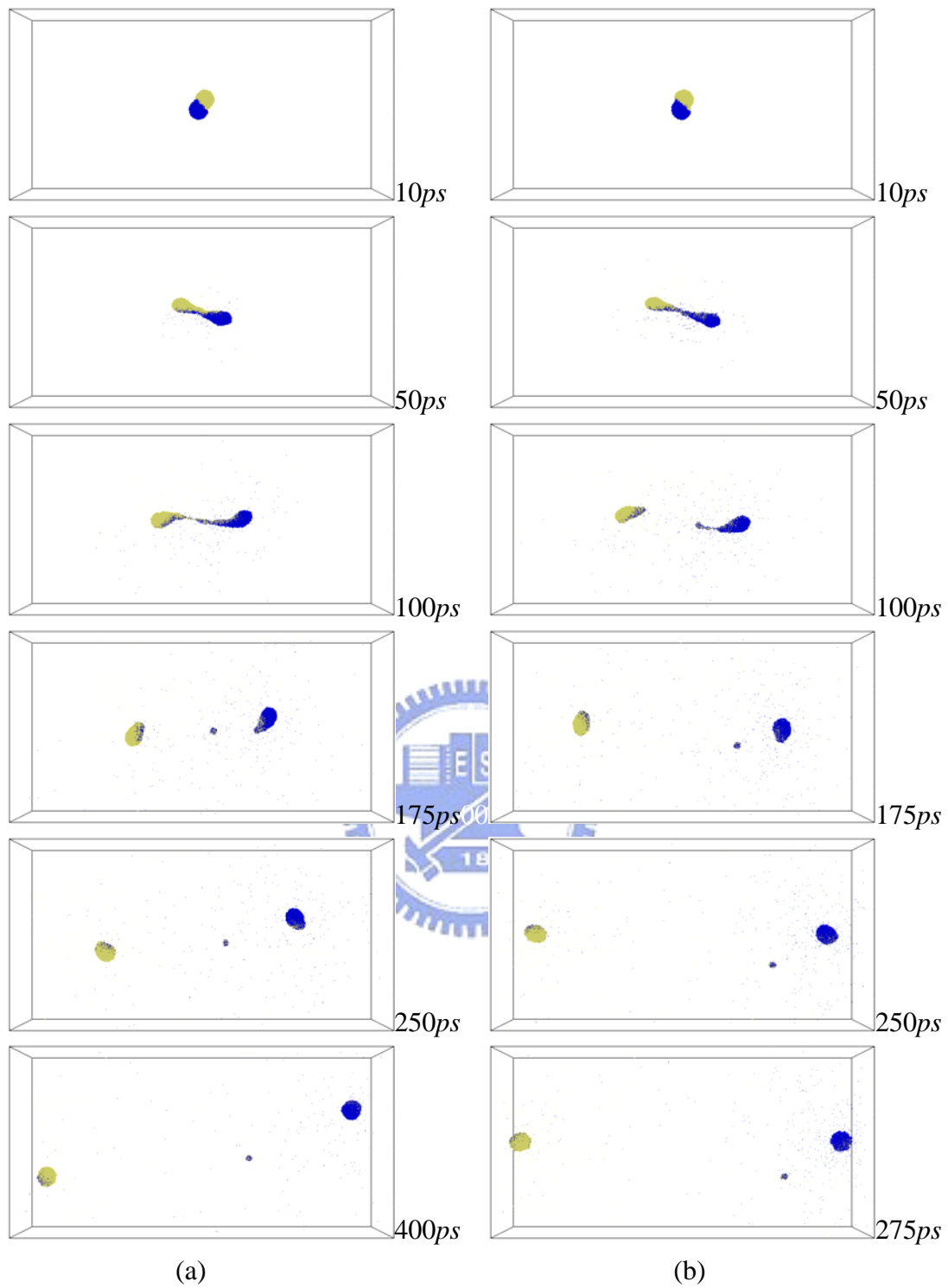


**Fig. 3. 27 Snapshot of xenon droplet pair collision under vacuum, at (a)  $b=6.25nm$ ,  $V=1250m/s$ , (b)  $b=6.25nm$ ,  $V=1500m/s$ ..**

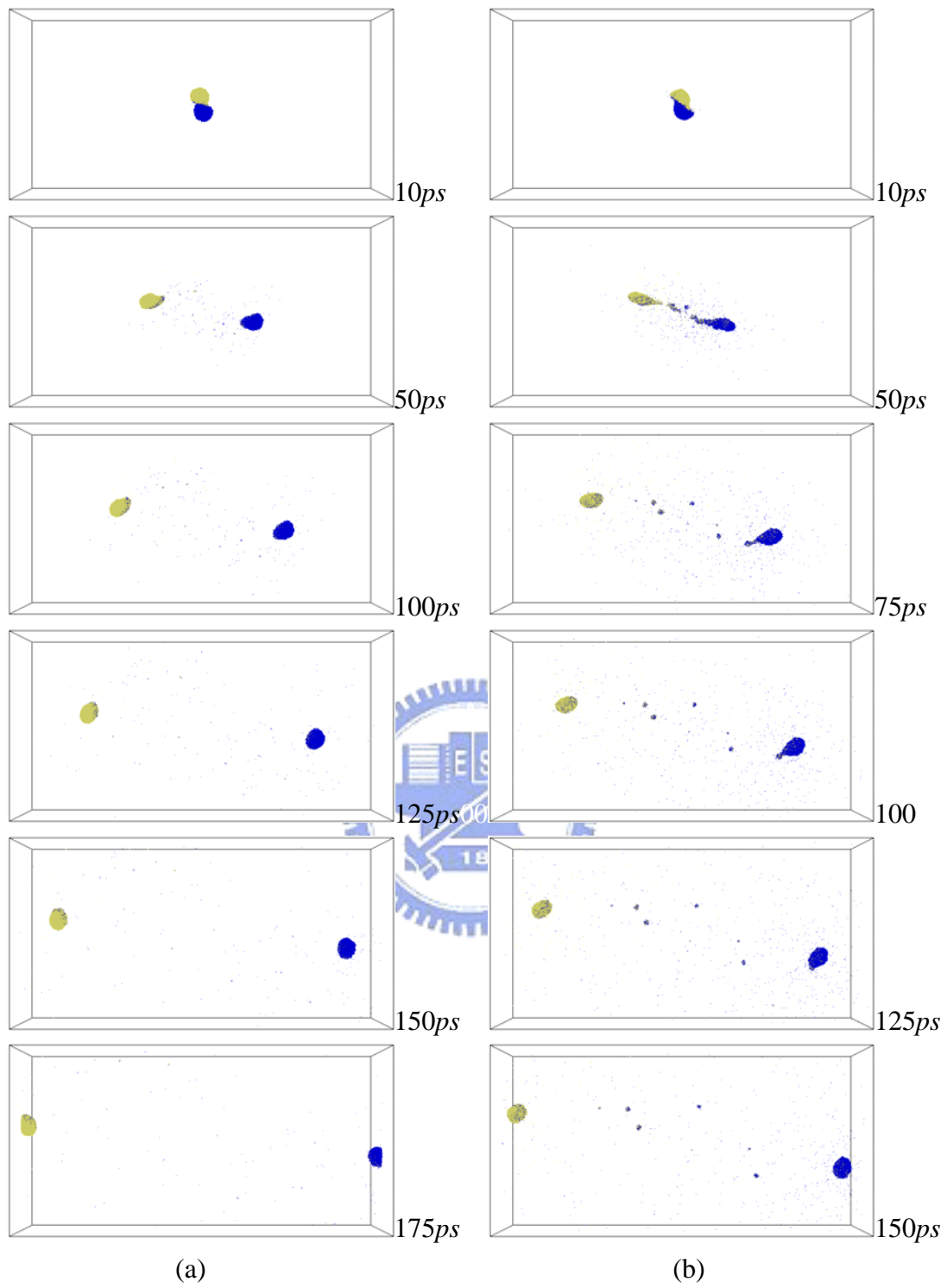


**Fig. 3. 28 Snapshot of xenon droplet pair collision under vacuum, at (a)  $b=6.25nm$ ,  $V=1750m/s$ , (b)  $b=6.25nm$ ,  $V=2000m/s$ .**

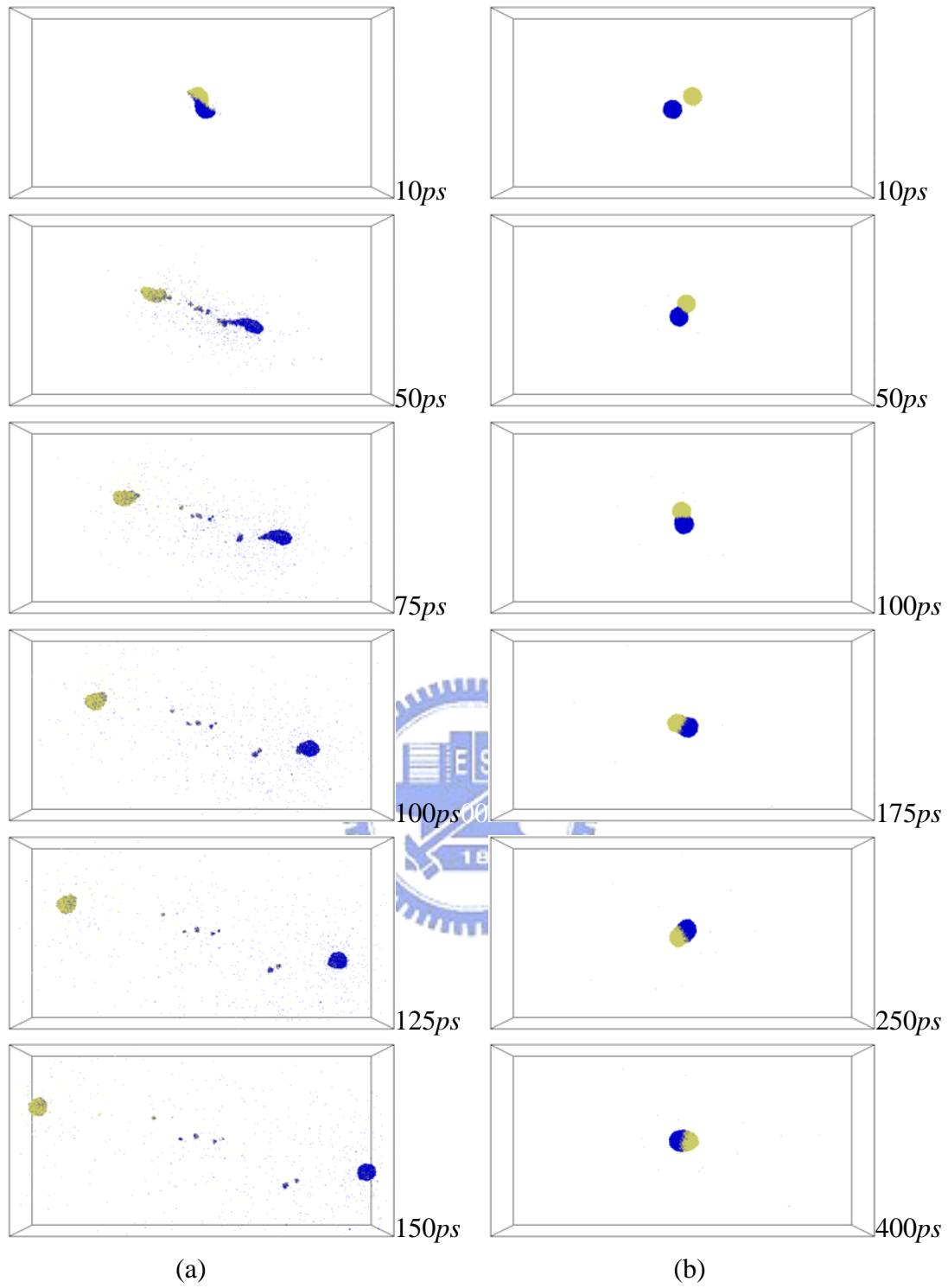


**Fig. 3. 29** Snapshot of xenon droplet pair collision under vacuum, at (a)  $b=6.25nm$ ,  $V=2250m/s$ , (b)  $b=7.5nm$ ,  $V=250m/s$ .

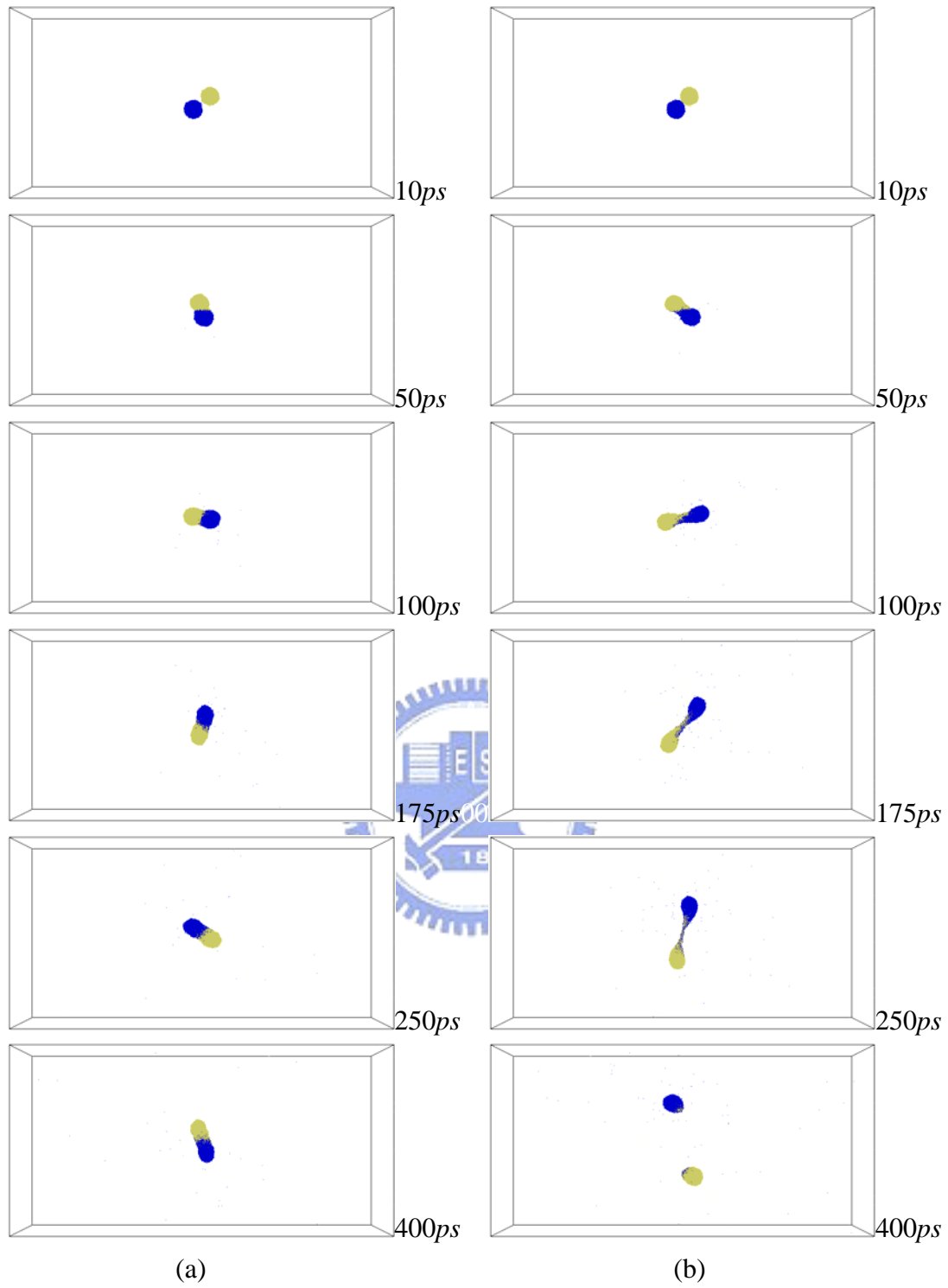


**Fig. 3. 30** Snapshot of xenon droplet pair collision under vacuum, at (a)  $b=7.5nm$ ,  $V=500m/s$ , (b)  $b=7.5nm$ ,  $V=750m/s$ .

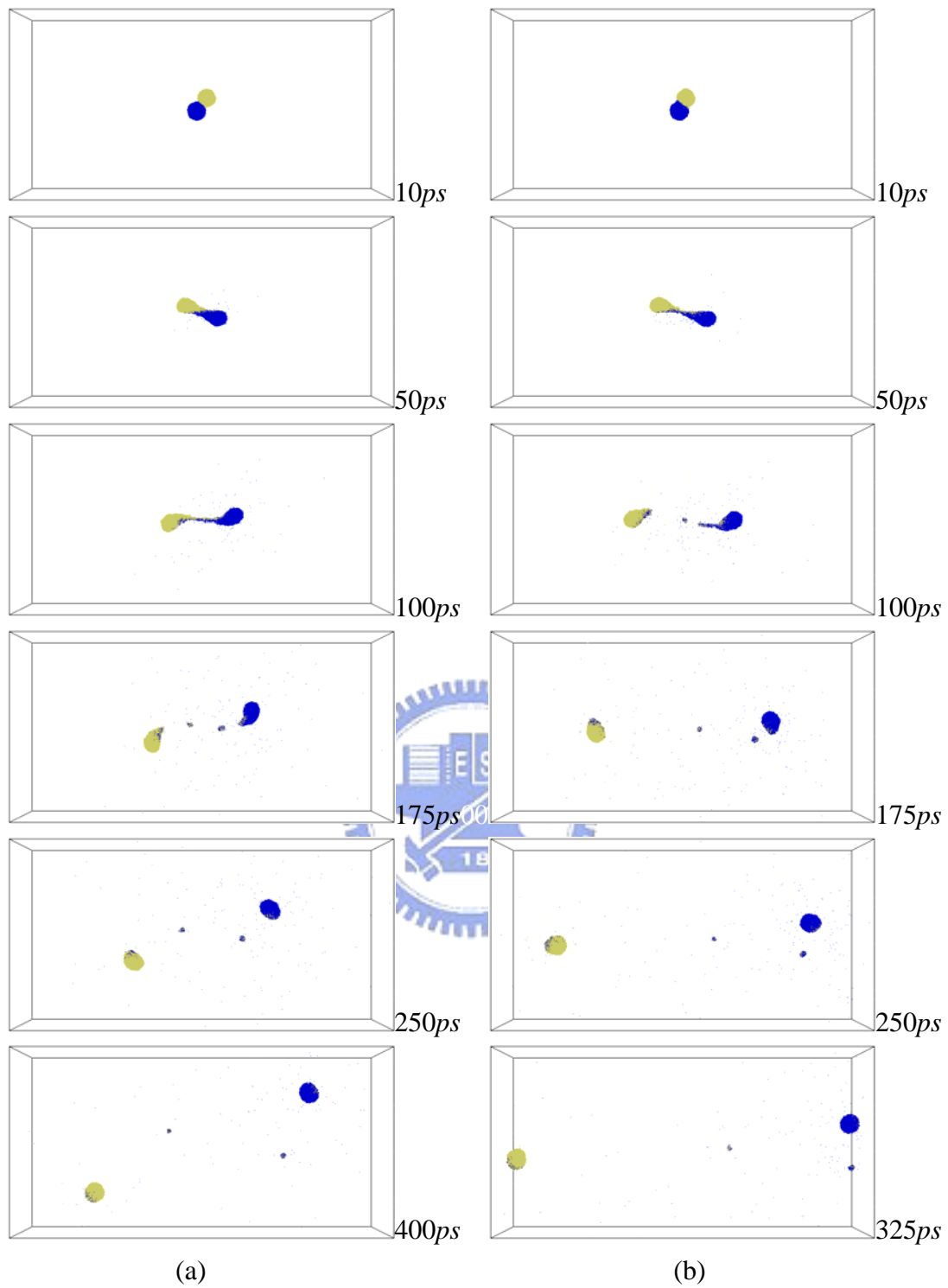


**Fig. 3. 31 Snapshot of xenon droplet pair collision under vacuum, at (a)  $b=7.5nm$ ,  $V=1000m/s$ , (b)  $b=7.5nm$ ,  $V=1250m/s$ ..**

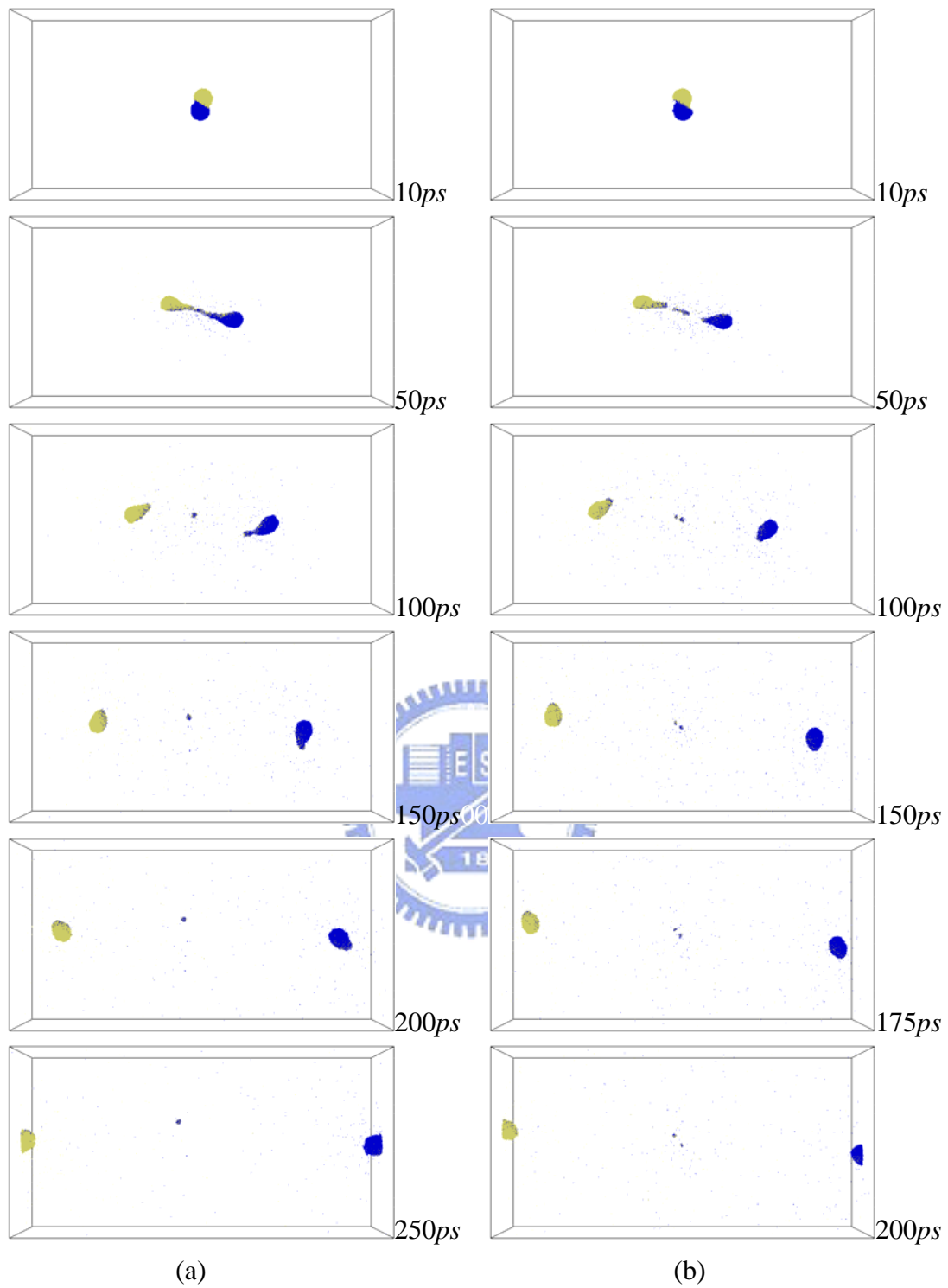


**Fig. 3. 32 Snapshot of xenon droplet pair collision under vacuum, at (a)  $b=7.5nm$ ,  $V=1500m/s$ , (b)  $b=7.5nm$ ,  $V=1750m/s$ .**

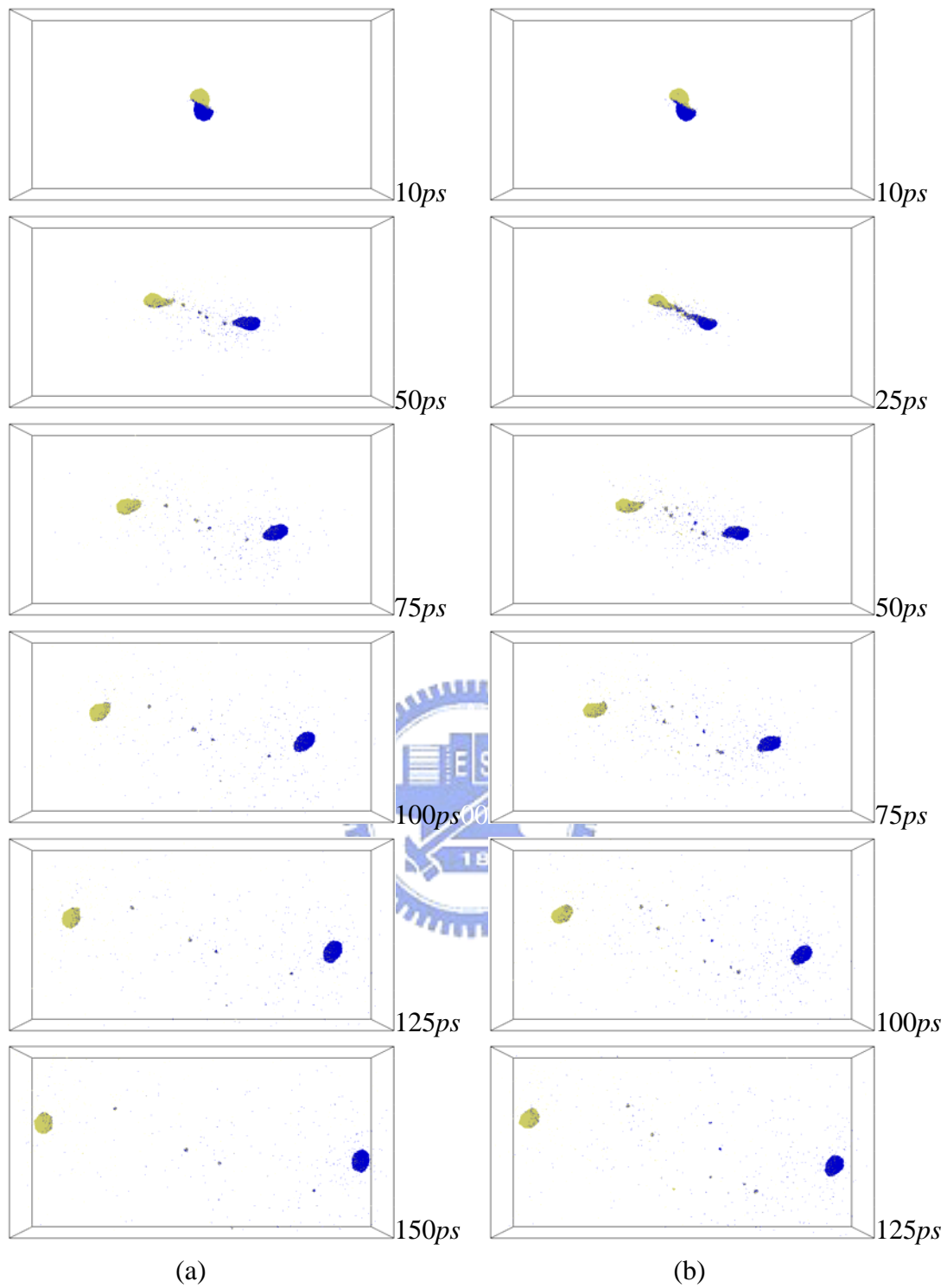


**Fig. 3. 33 Snapshot of xenon droplet pair collision under vacuum, at (a)  $b=7.5nm$ ,  $V=2000m/s$ , (b)  $b=7.5nm$ ,  $V=2250m/s$ .**

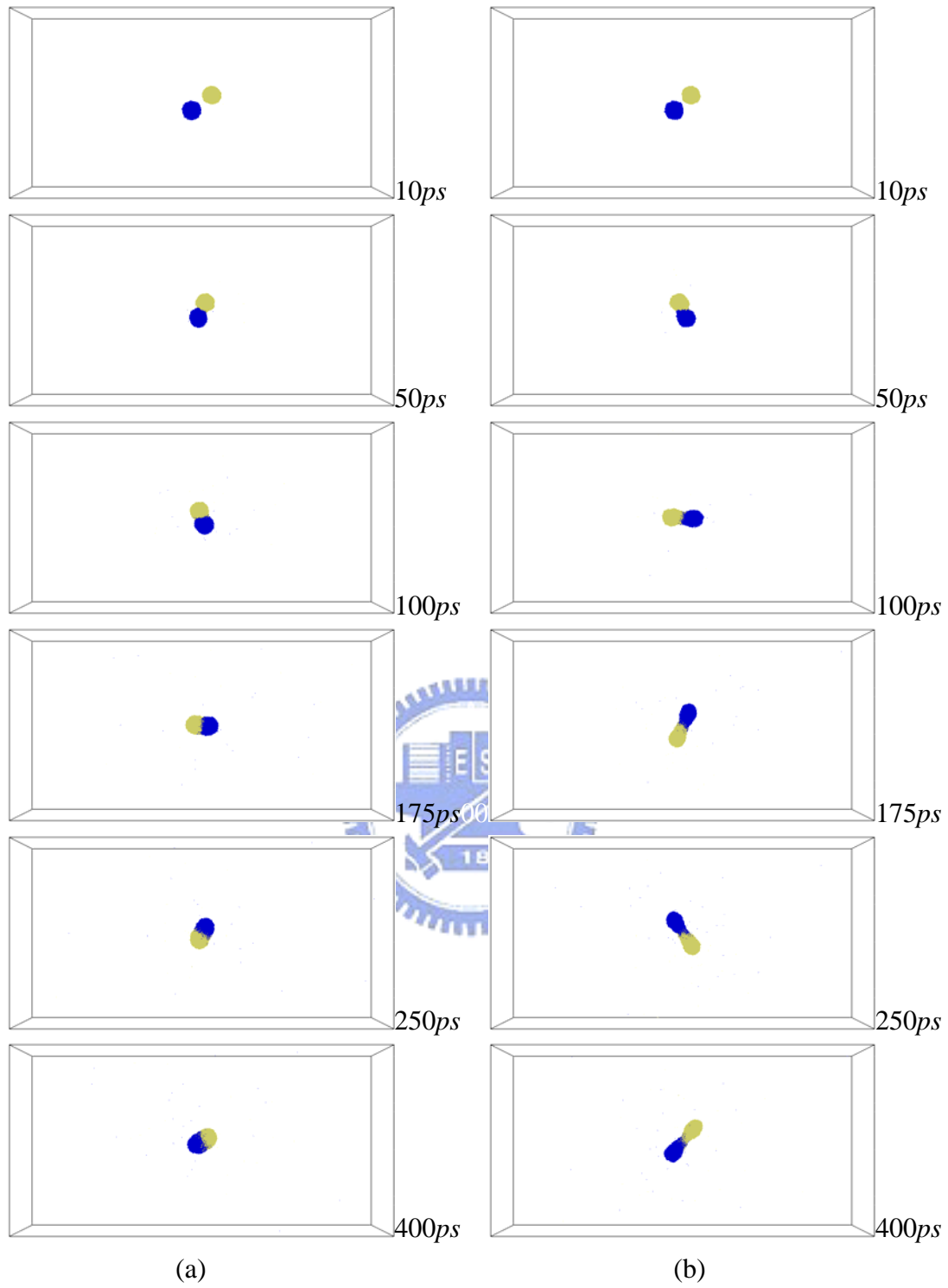


**Fig. 3. 34 Snapshot of xenon droplet pair collision under vacuum, at (a)  $b=8.75 \text{ nm}$ ,  $V=250 \text{ m/s}$ , (b)  $b=8.75$ ,  $V=500 \text{ m/s}$ .**



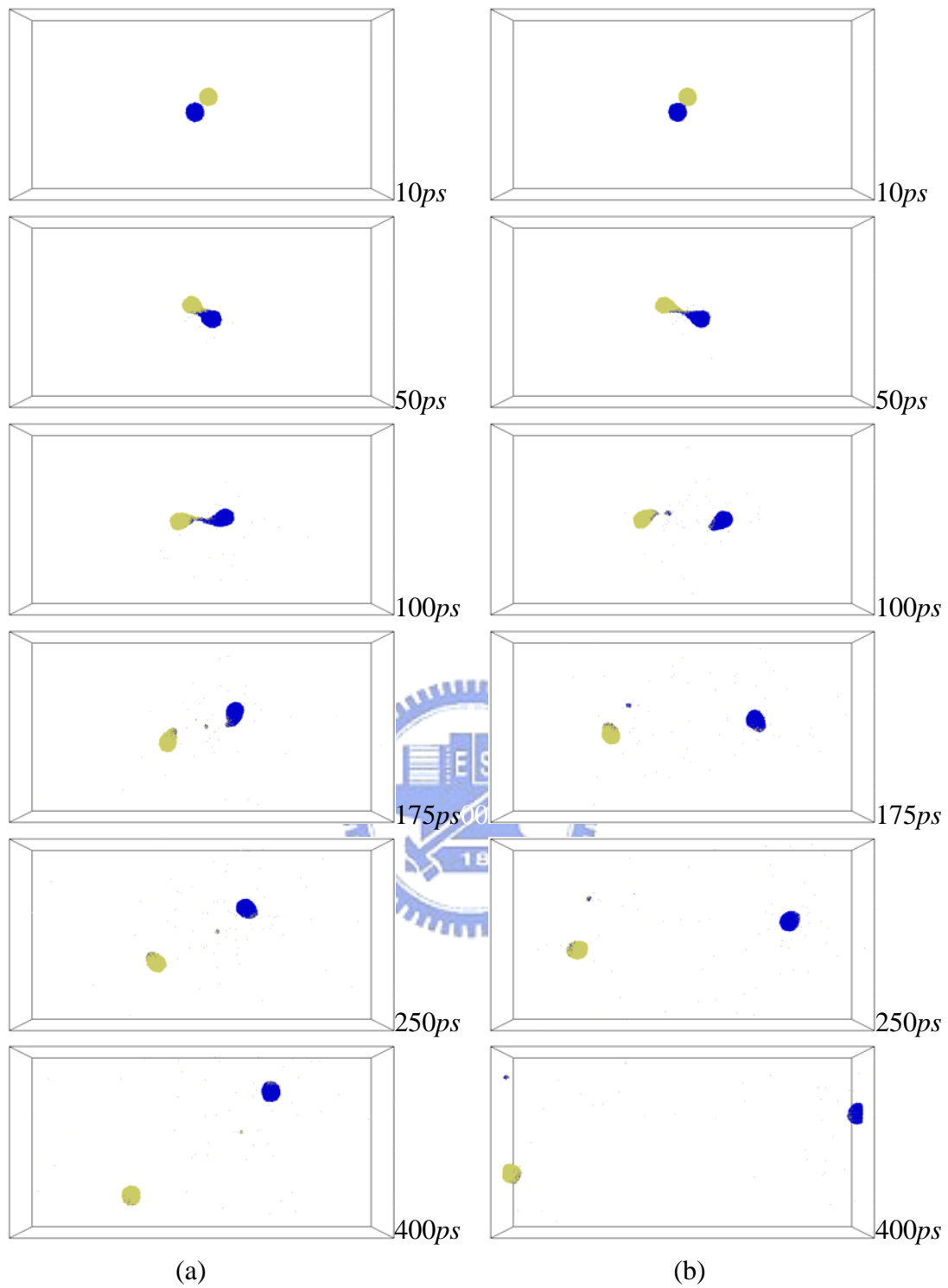


**Fig. 3. 35 Snapshot of xenon droplet pair collision under vacuum, at (a)  $b=8.75nm$ ,  $V=750m/s$ , (b)  $b=8.75$ ,  $V=1000m/s$ .**

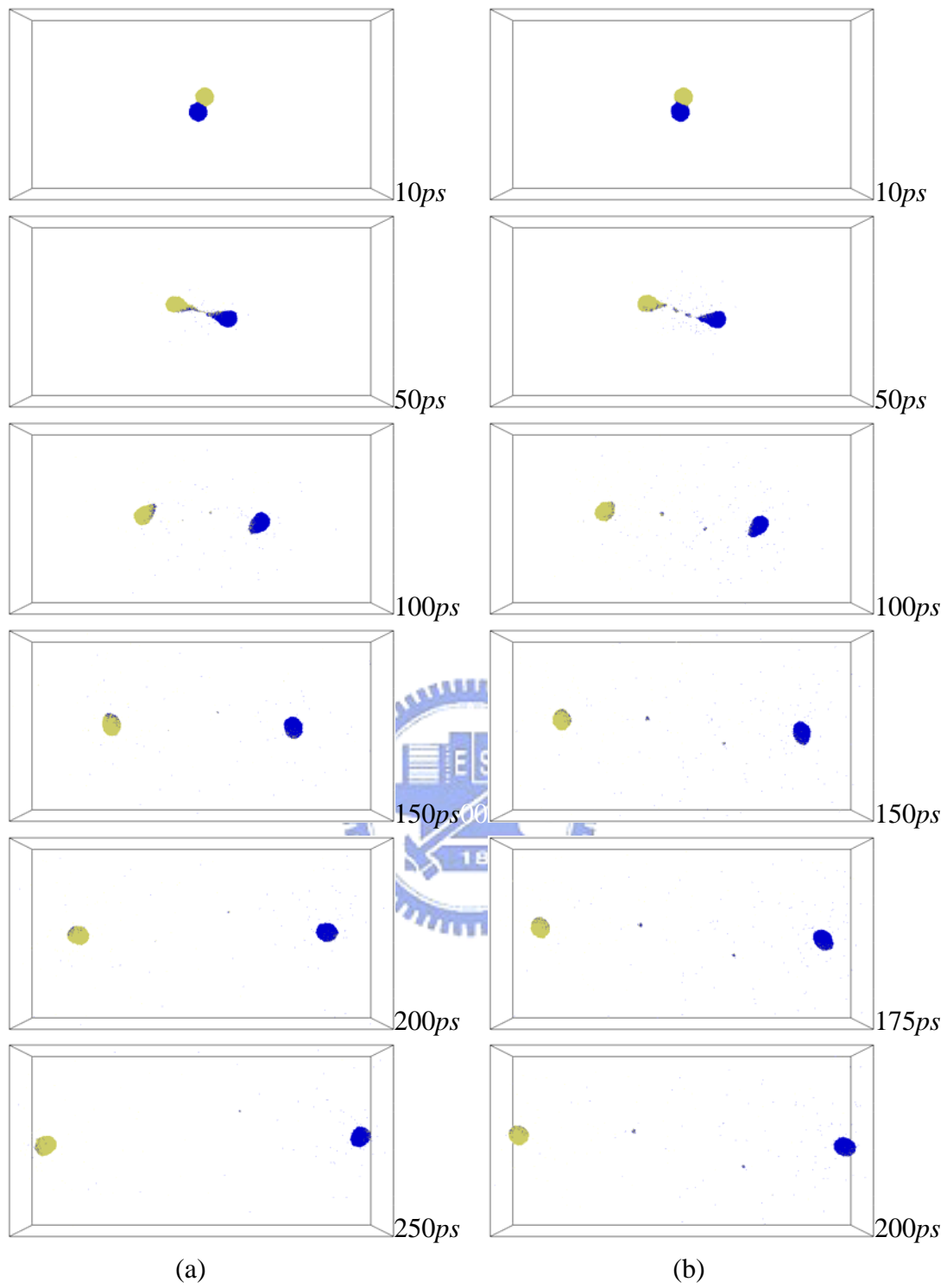


**Fig. 3. 36 Snapshot of xenon droplet pair collision under vacuum, at (a)  $b=8.75nm$ ,  $V=1250m/s$ , (b)  $b=8.75$ ,  $V=1500m/s$ .**

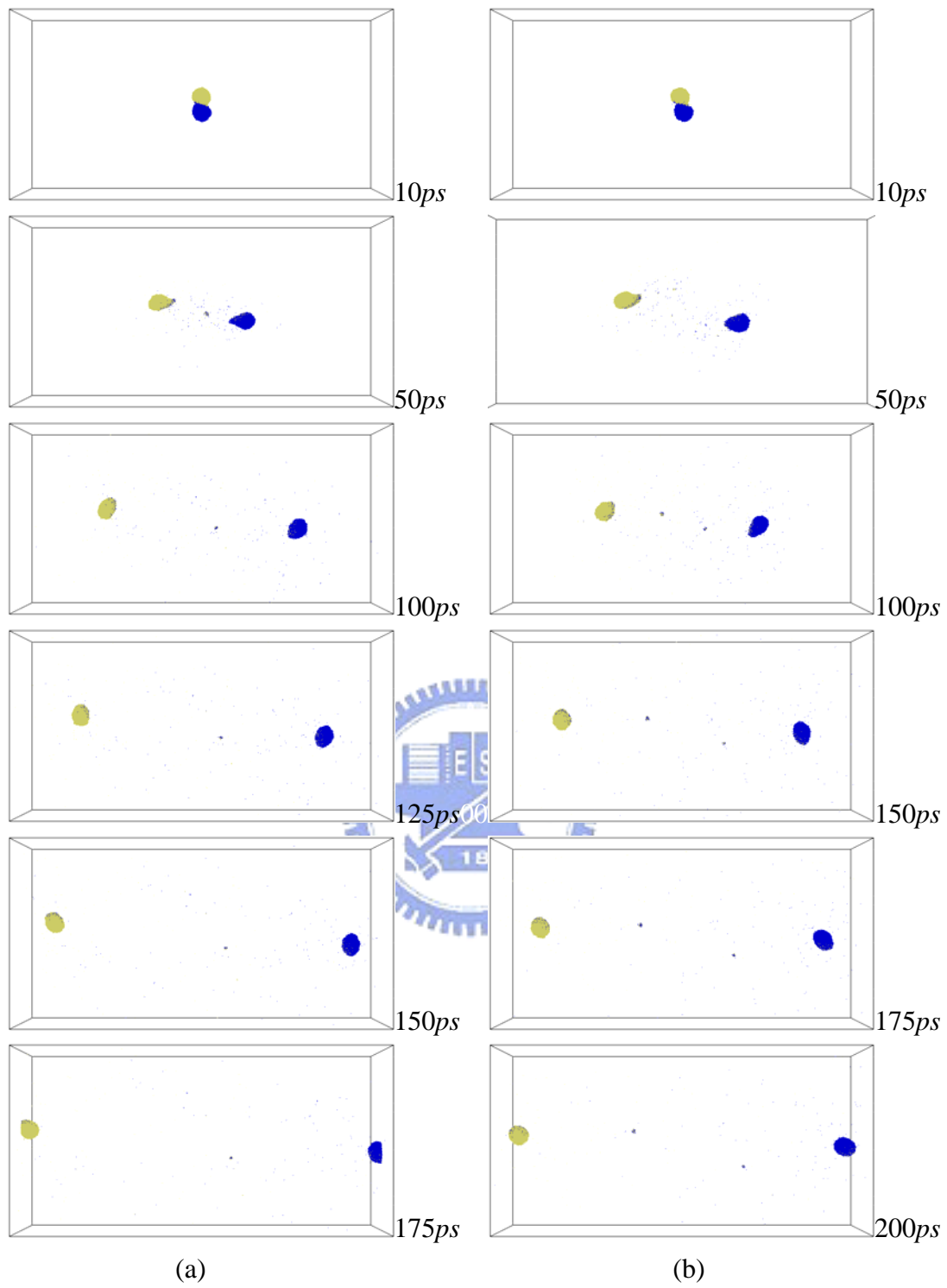


**Fig. 3. 37 Snapshot of xenon droplet pair collision under vacuum, at (a)  $b=8.75nm$ ,  $V=1750m/s$ , (b)  $b=8.75nm$ ,  $V=2000m/s$ .**

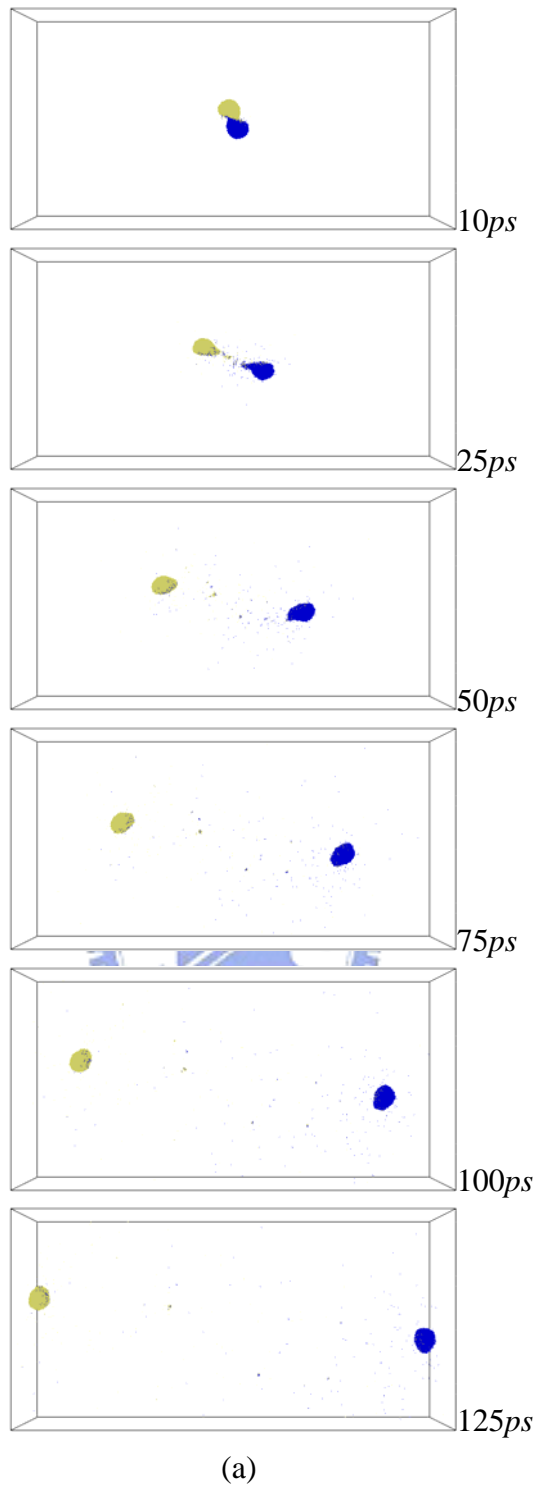


**Fig. 3. 38** Snapshot of xenon droplet pair collision under vacuum, at (a)  $b=8.75nm$ ,  $V=2550m/s$ .

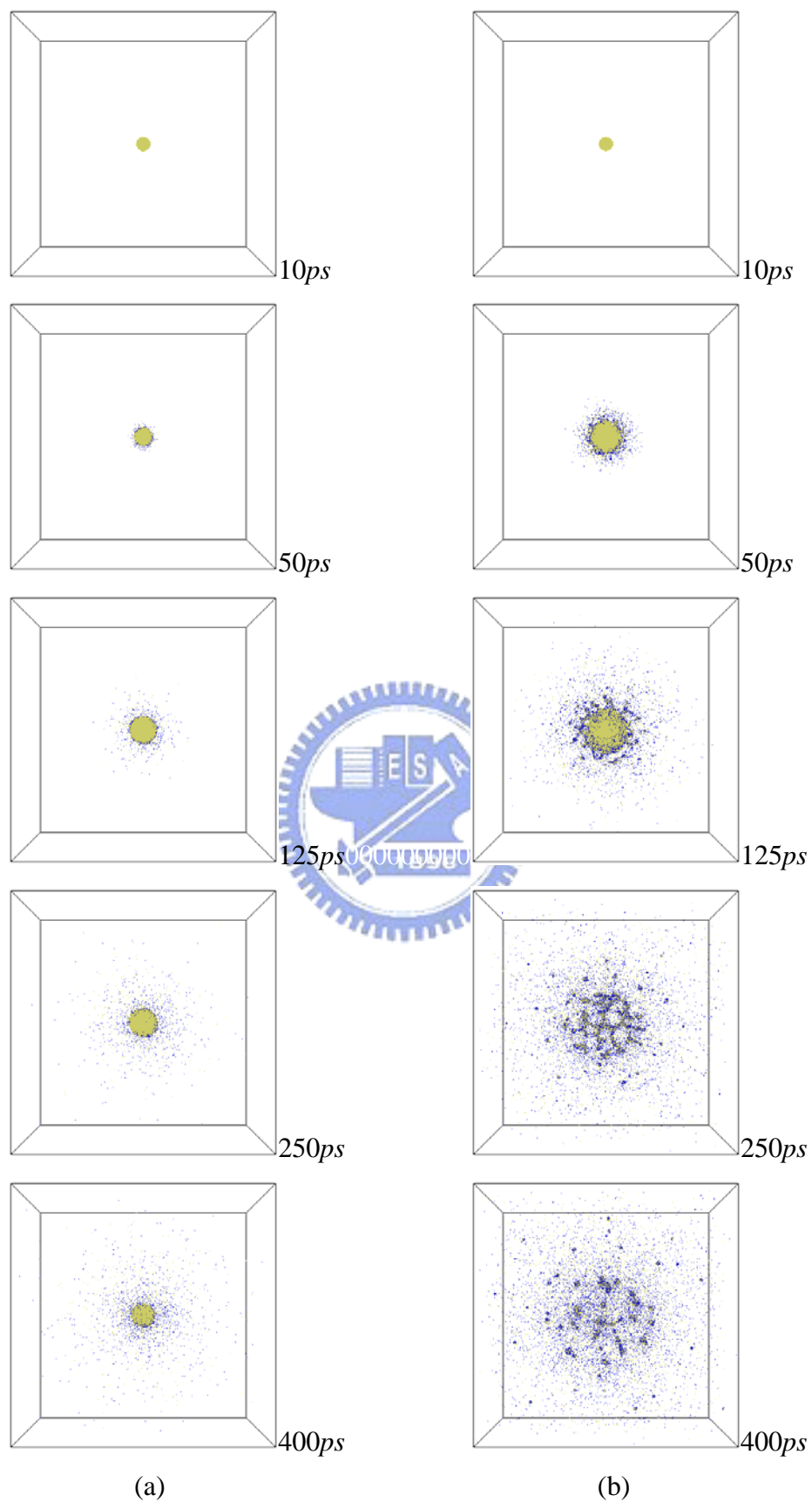
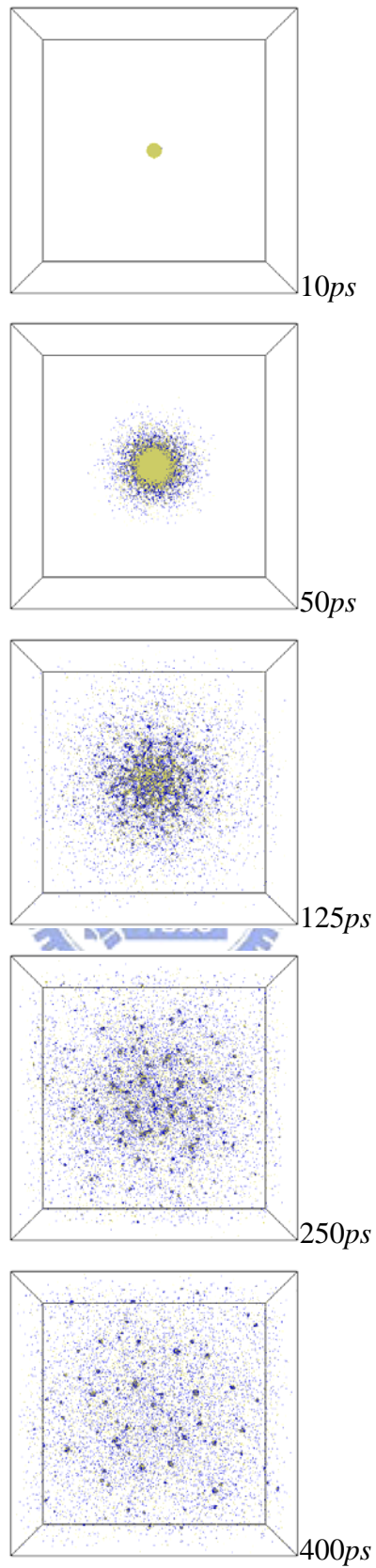


**Fig. 3. 39 Snapshot of helium droplet pair collision under vacuum, at (a)  $b=0$ ,  $V=250\text{m/s}$ , (b)  $b=0$ ,  $V=500\text{m/s}$ .**



(a)

**Fig. 3. 40** Snapshot of helium droplet pair collision under vacuum, at (a)  $b=0$ ,  $V=750m/s$ .

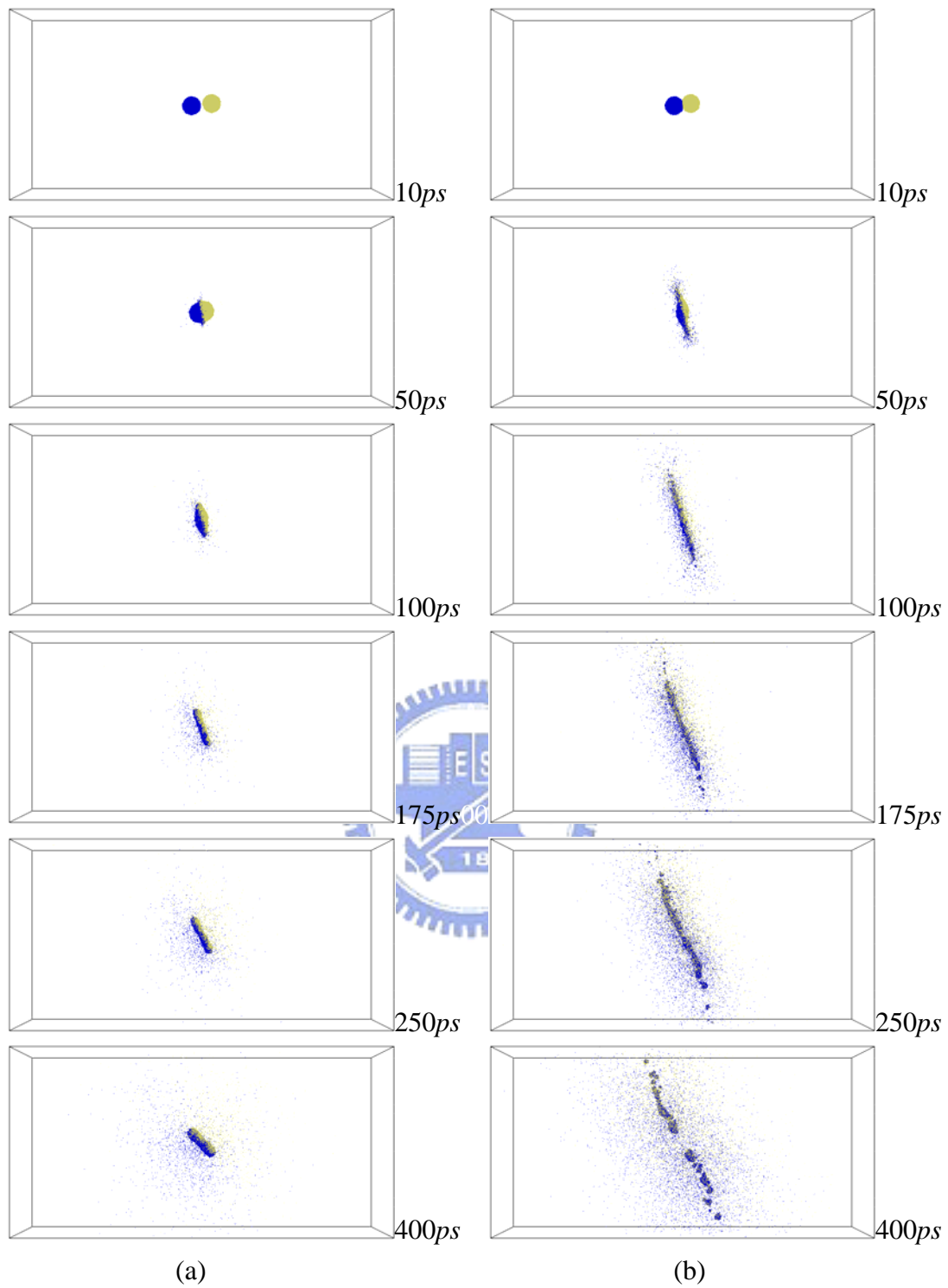


**Fig. 3. 41 Snapshot of helium droplet pair collision under vacuum, at (a)  $b=1.25\text{nm}$ ,  $V=250\text{m/s}$ , (b)  $b=1.25\text{nm}$ ,  $V=500\text{m/s}$ .**

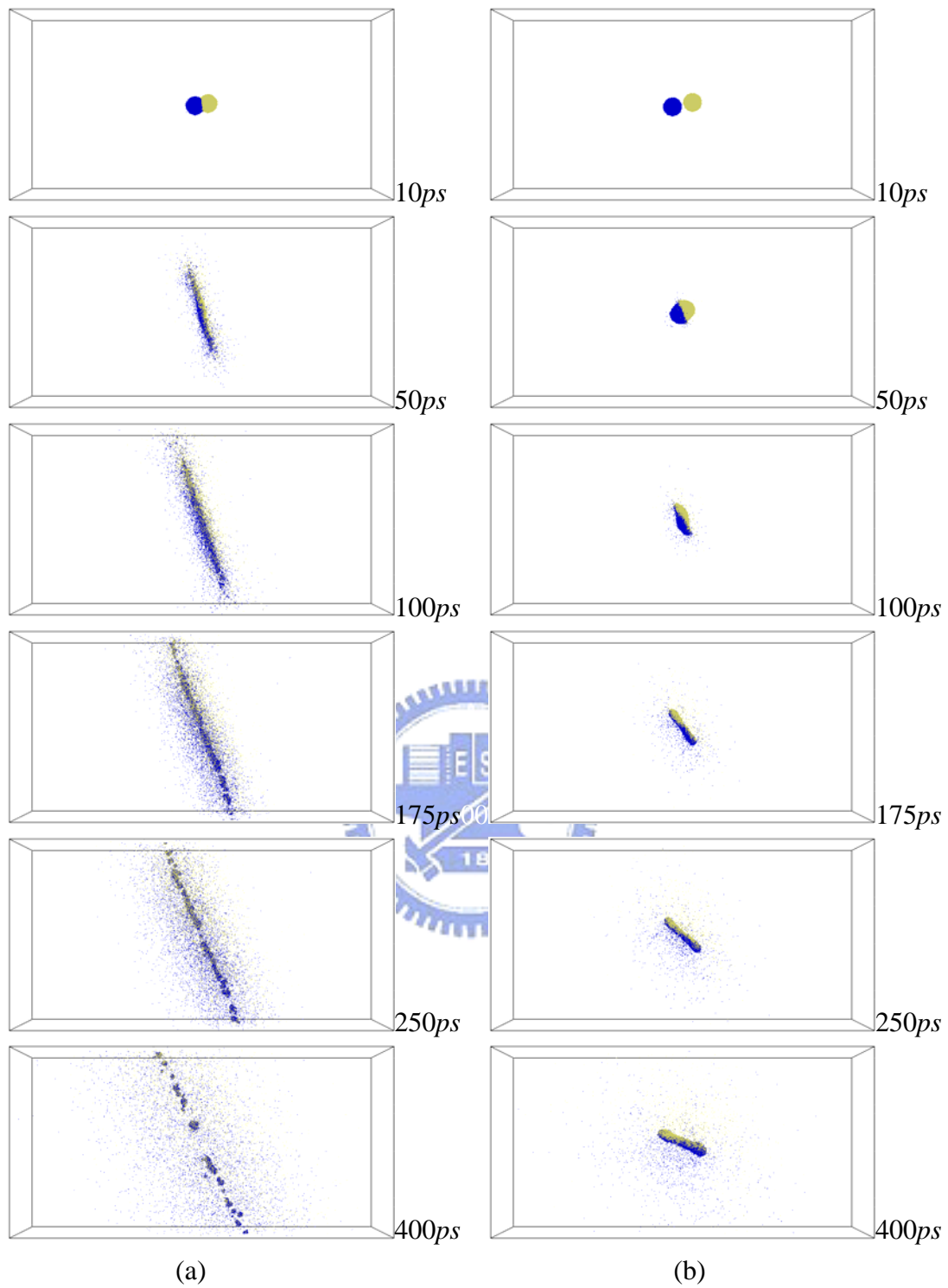


**Fig. 3. 42** Snapshot of helium droplet pair collision under vacuum, at (a)  $b=1.25nm$ ,  $V=750m/s$ , (b)  $b=2.5nm$ ,  $V=250m/s$ .



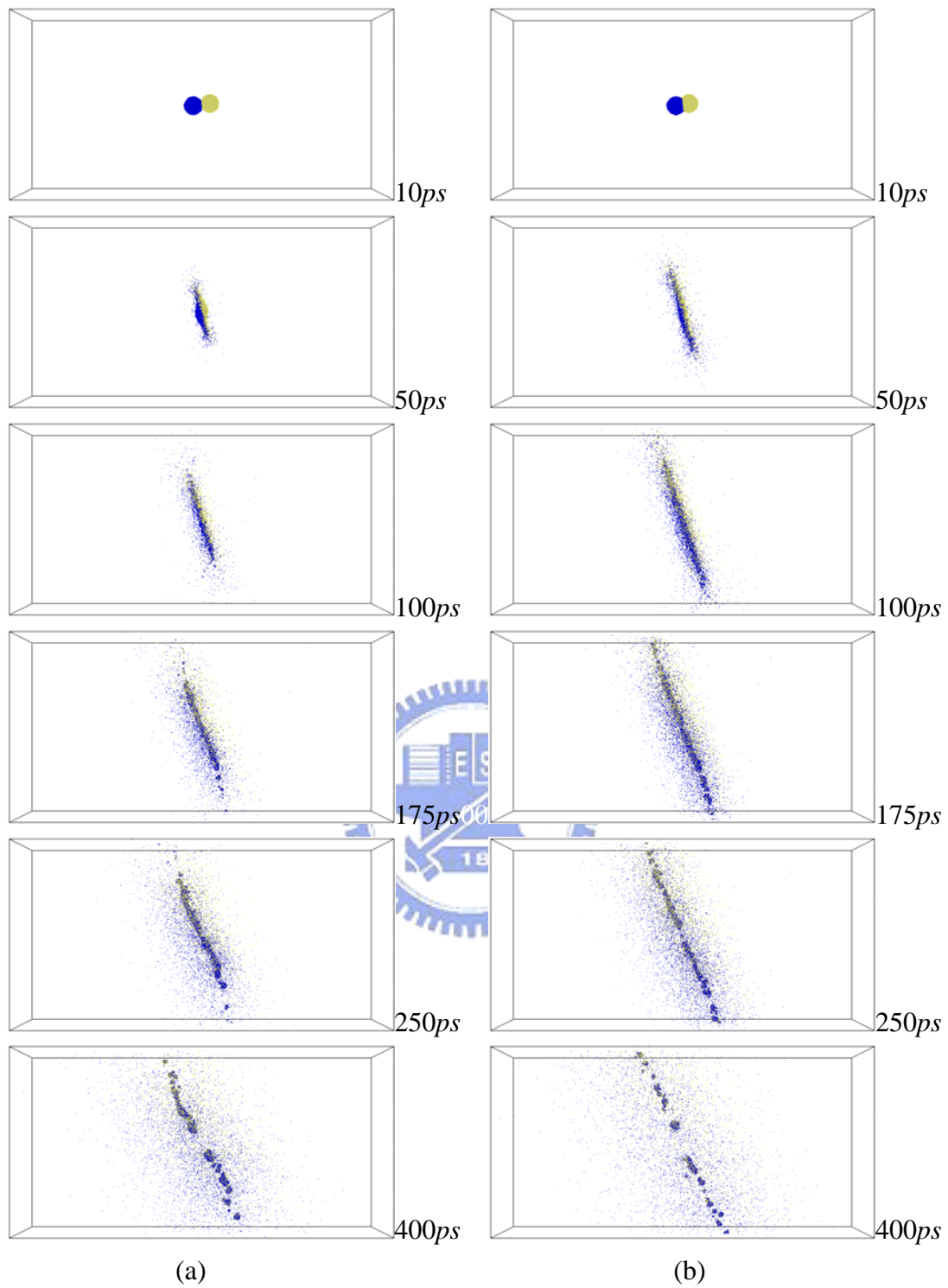


**Fig. 3.43** Snapshot of helium droplet pair collision under vacuum, at (a)  $b=1.25\text{nm}$ ,  $V=500\text{m/s}$ , (b)  $b=1.25\text{nm}$ ,  $V=750\text{m/s}$ .

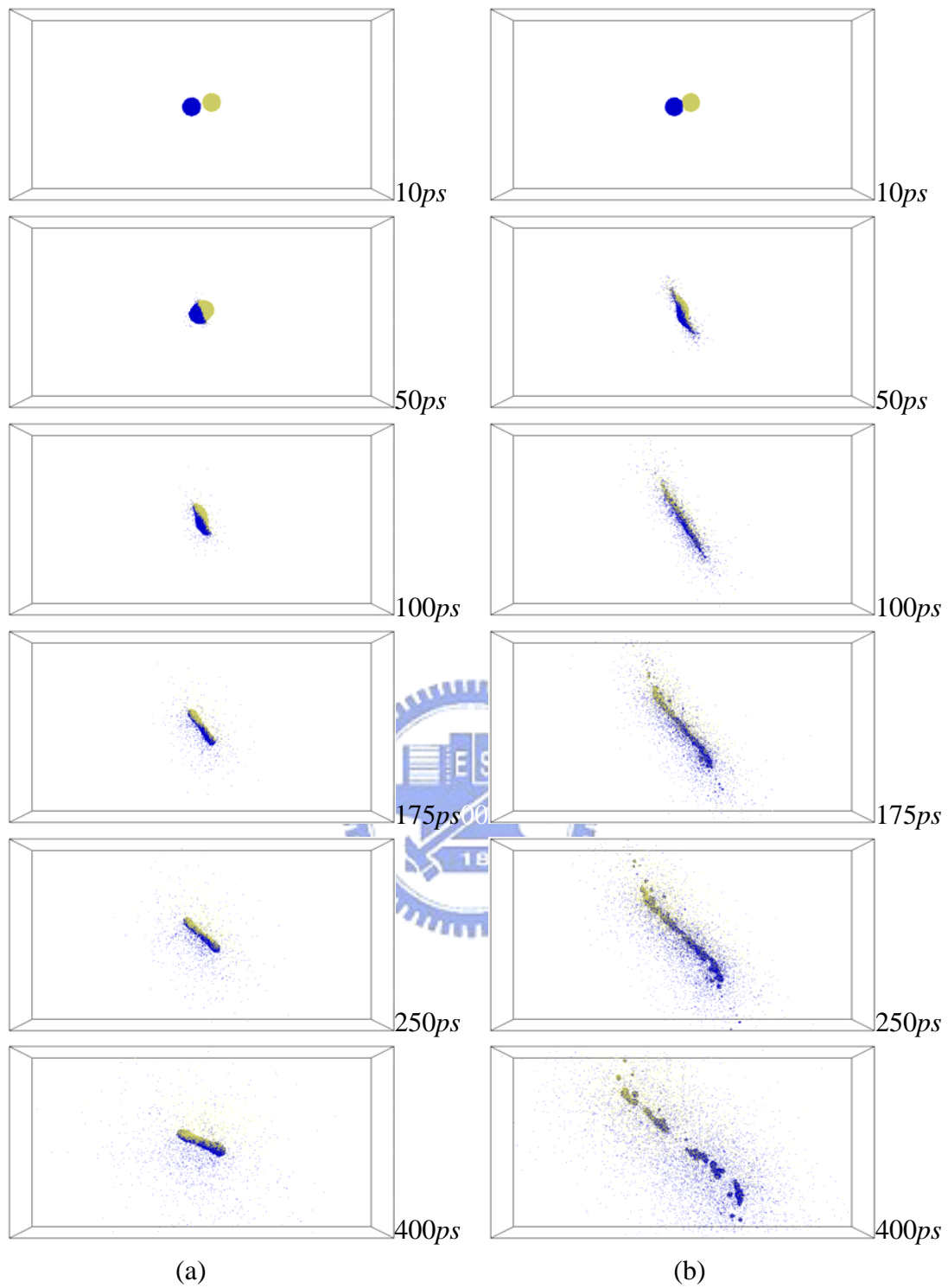


**Fig. 3. 44 Snapshot of helium droplet pair collision under vacuum, at (a)  $b=2.5\text{ nm}$ ,  $V=250\text{ m/s}$ , (b)  $b=2.5\text{ nm}$ ,  $V=500\text{ m/s}$ .**

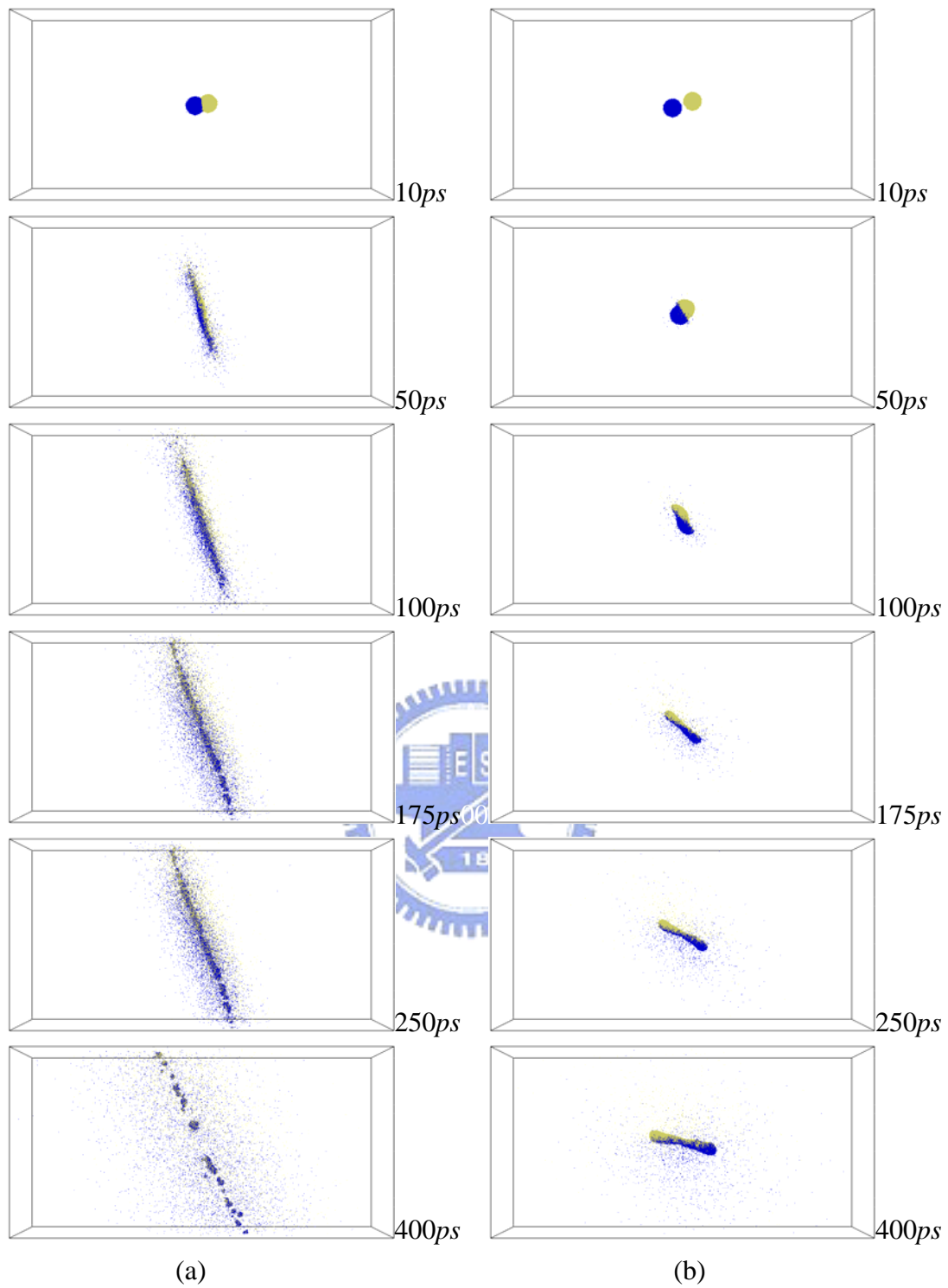


**Fig. 3.45** Snapshot of helium droplet pair collision under vacuum, at (a)  $b=2.5\text{nm}$ ,  $V=750\text{m/s}$ , (b)  $b=3.75\text{nm}$ ,  $V=250\text{m/s}$ .

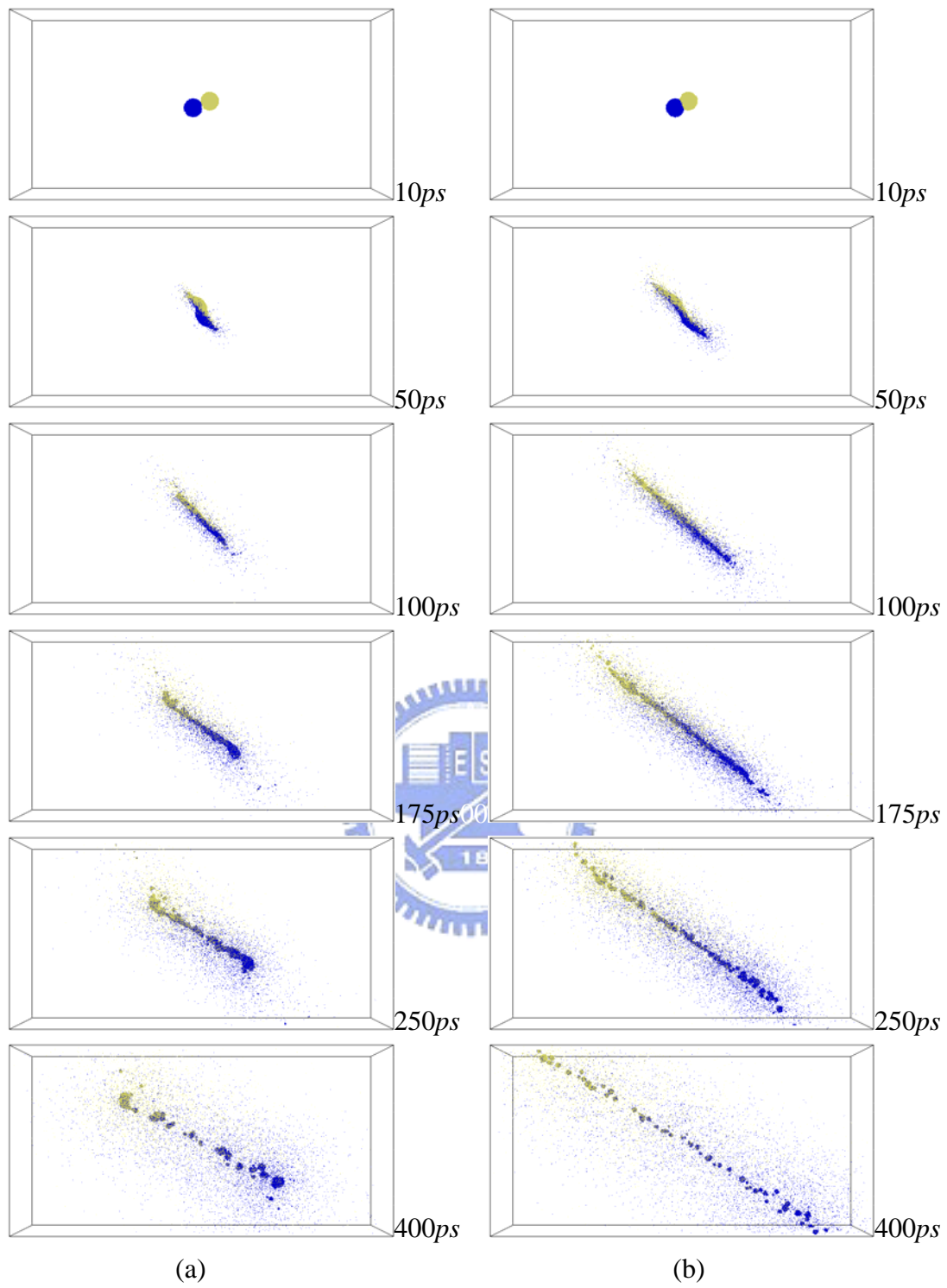


**Fig. 3. 46 Snapshot of helium droplet pair collision under vacuum, at (a)  $b=3.75nm$ ,  $V=500m/s$ , (b)  $b=3.75nm$ ,  $V=750m/s$ .**

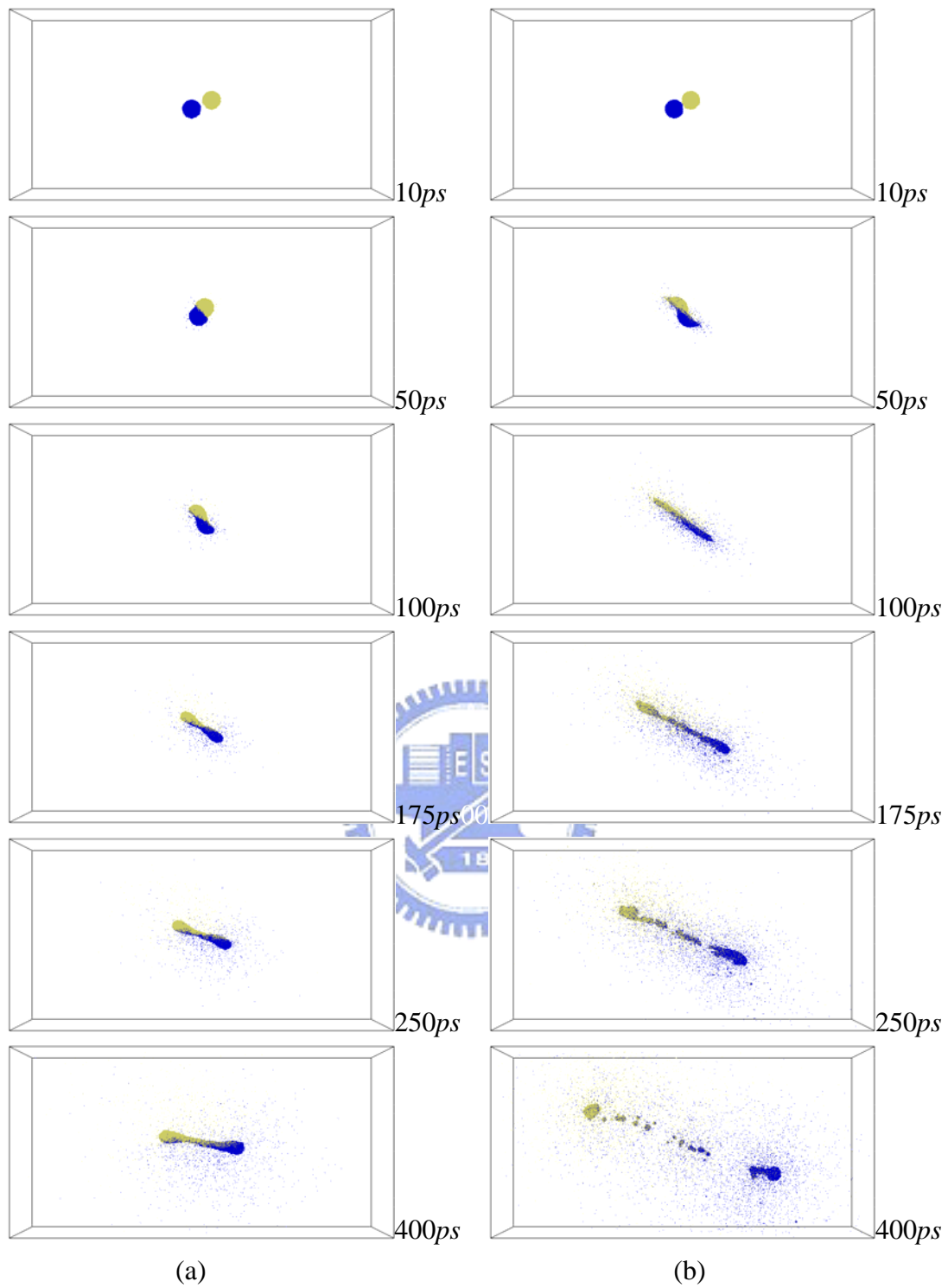


**Fig. 3. 47** Snapshot of helium droplet pair collision under vacuum, at (a)  $b=5\text{nm}$ ,  $V=250\text{m/s}$ , (b)  $b=5\text{nm}$ ,  $V=500\text{m/s}$ .

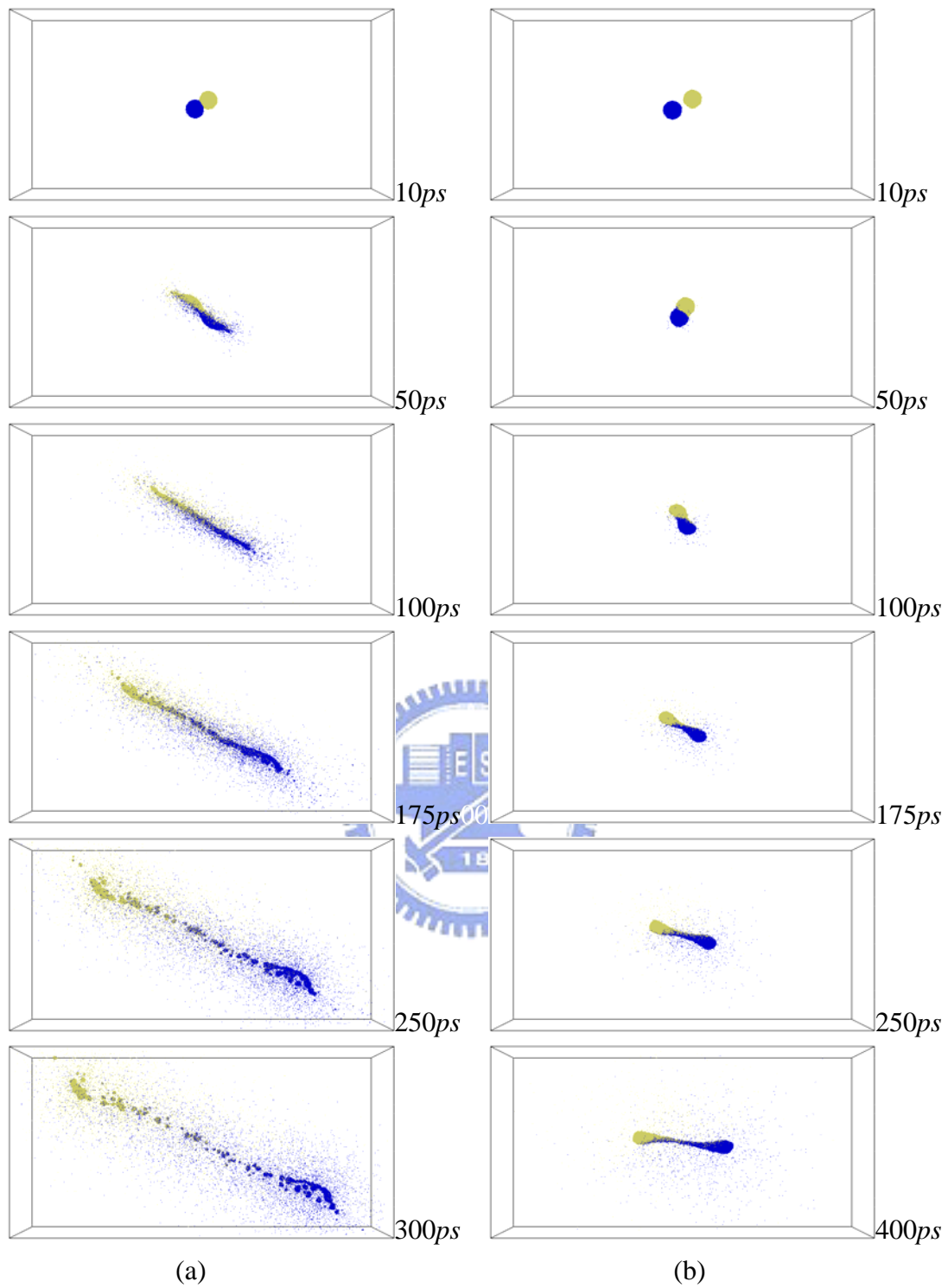


**Fig. 3. 48** Snapshot of helium droplet pair collision under vacuum, at (a)  $b=5nm$ ,  $V=750m/s$ , (b)  $b=6.25nm$ ,  $V=250m/s$ .

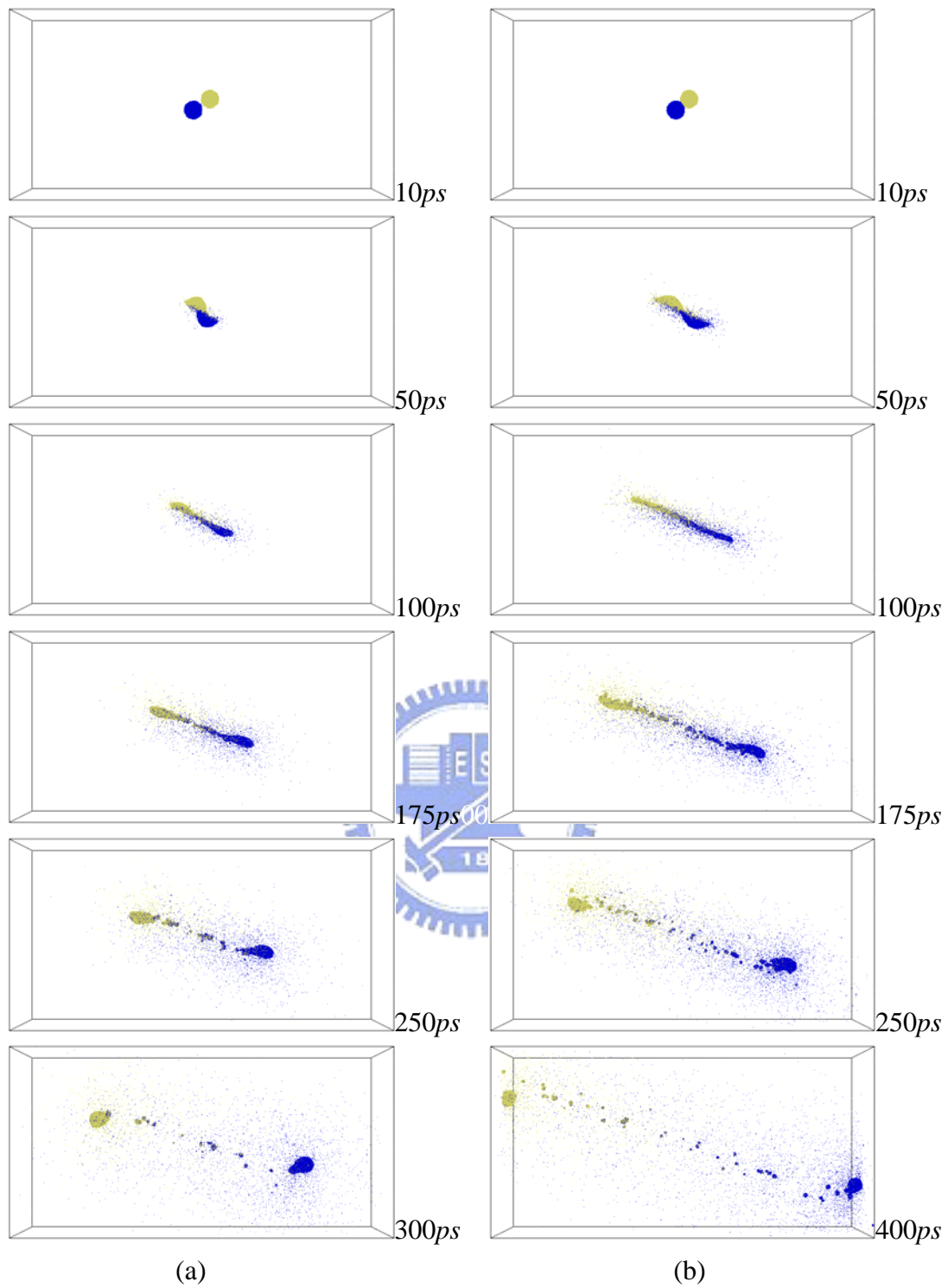


**Fig. 3. 49** Snapshot of helium droplet pair collision under vacuum, at (a)  $b=6.25nm$ ,  $V=500m/s$ , (b)  $b=6.25nm$ ,  $V=750m/s$ .

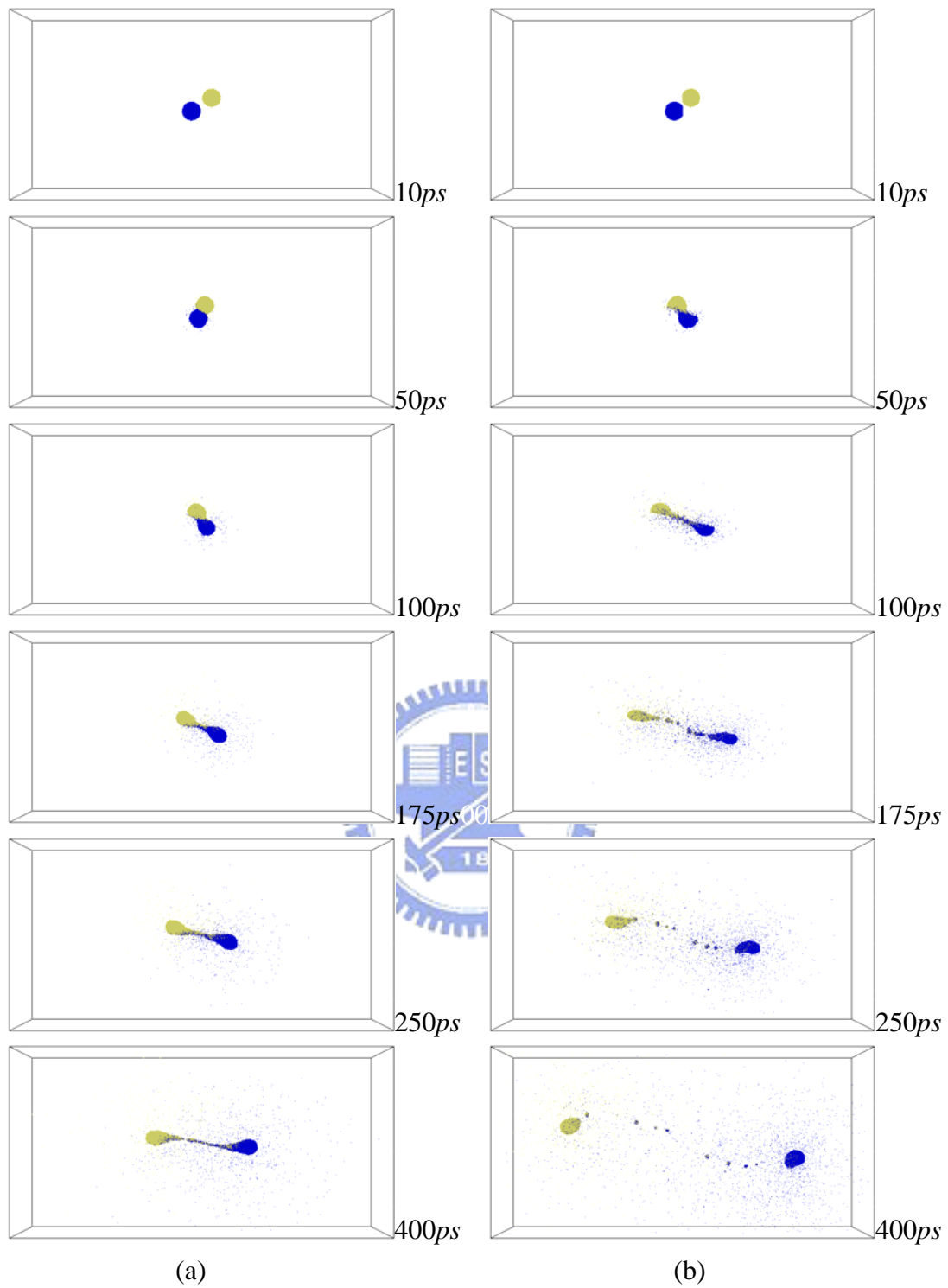


**Fig. 3. 50** Snapshot of helium droplet pair collision under vacuum, at (a)  $b=7.5\text{nm}$ ,  $V=250\text{m/s}$ , (b)  $b=7.5\text{nm}$ ,  $V=500\text{m/s}$ .



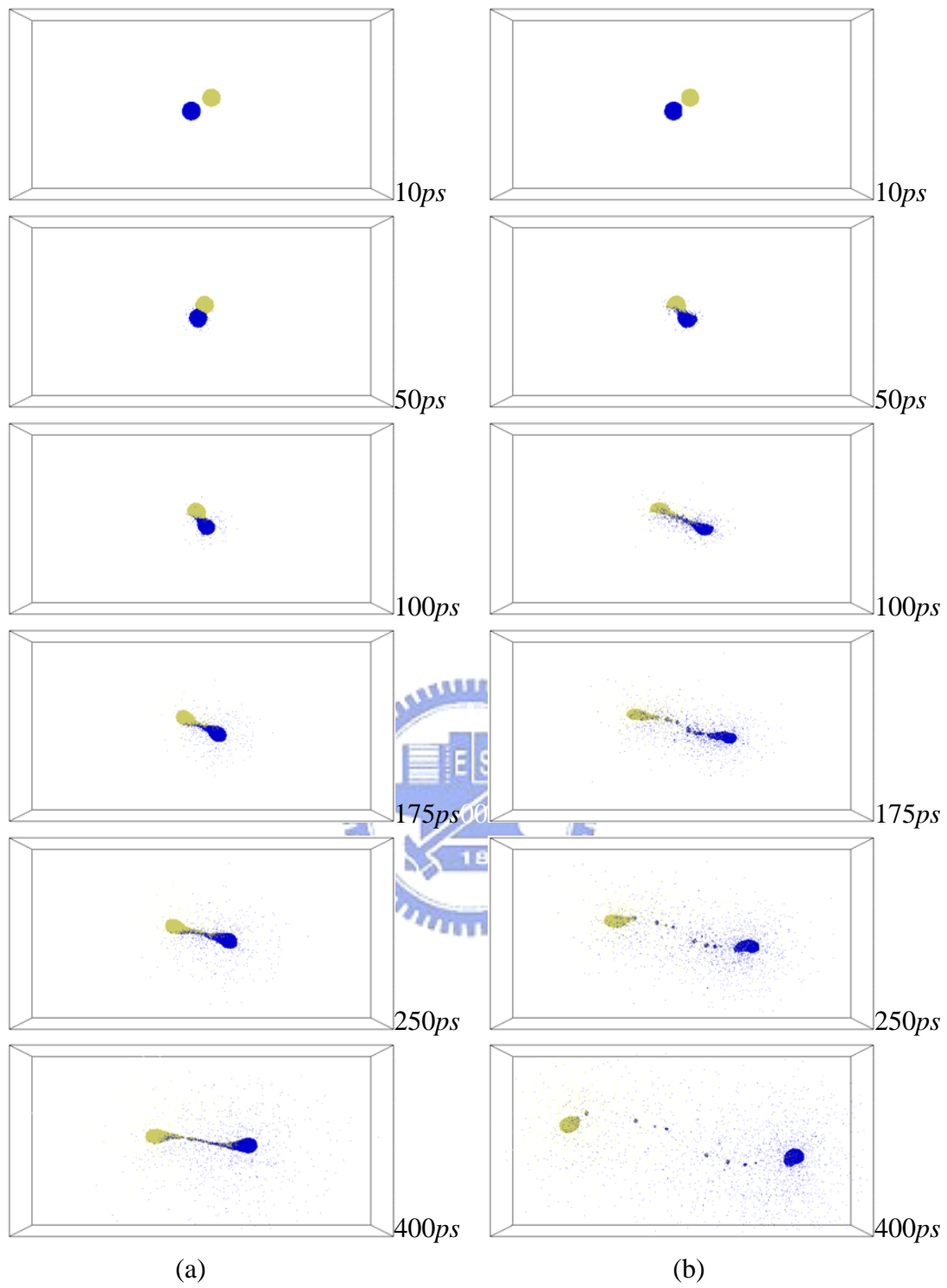


**Fig. 3. 51 Snapshot of helium droplet pair collision under vacuum, at (a)  $b=7.5nm$ ,  $V=750m/s$ , (b)  $b=8.75nm$ ,  $V=250m/s$ .**

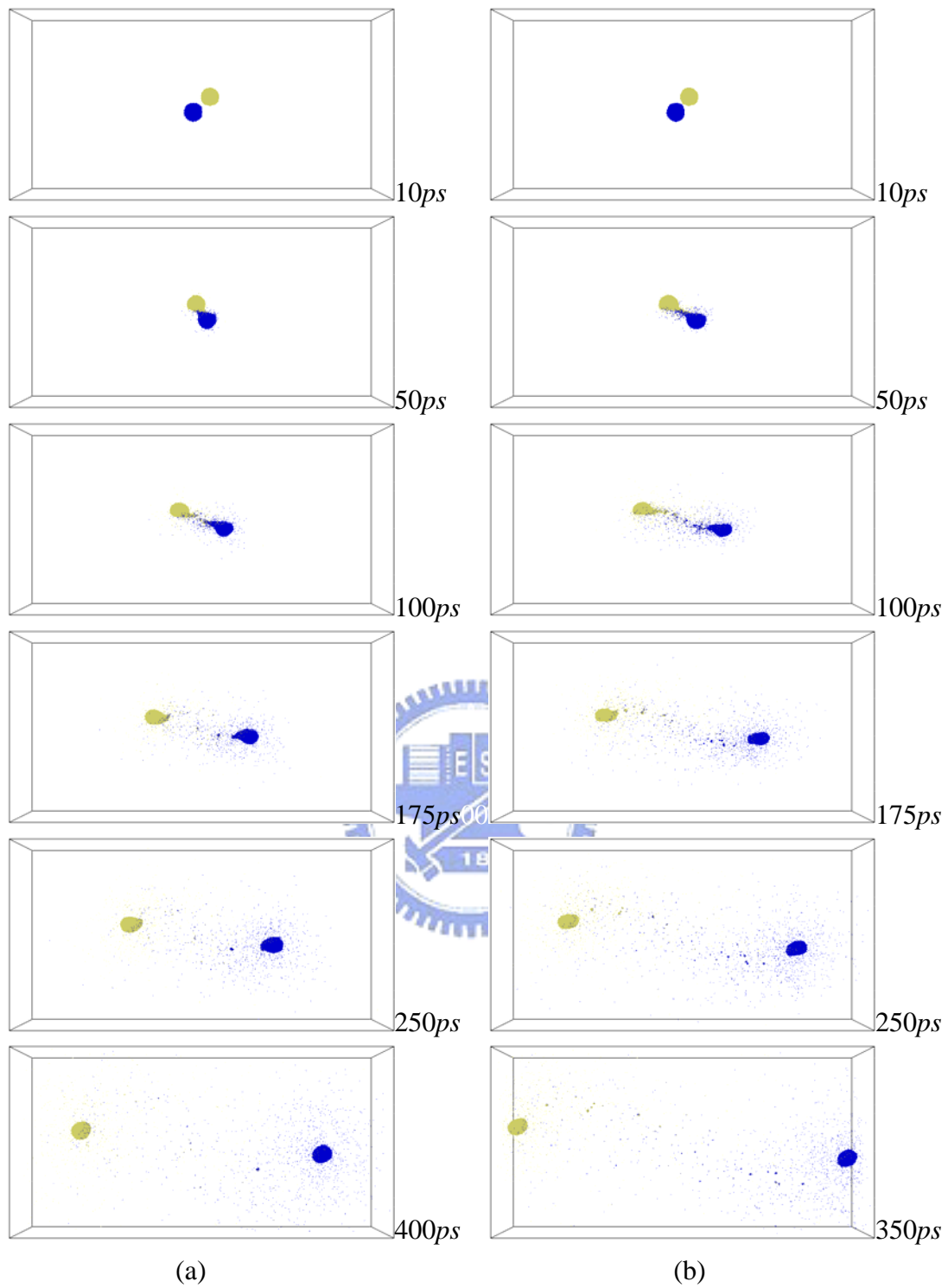
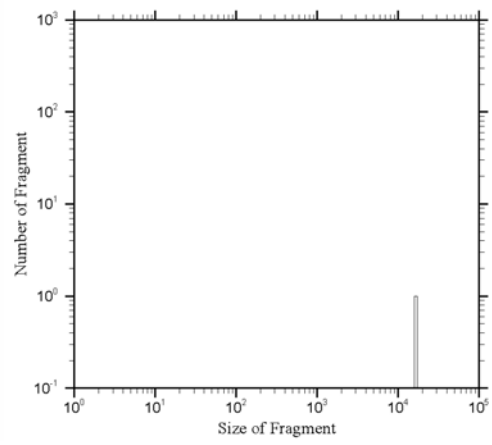
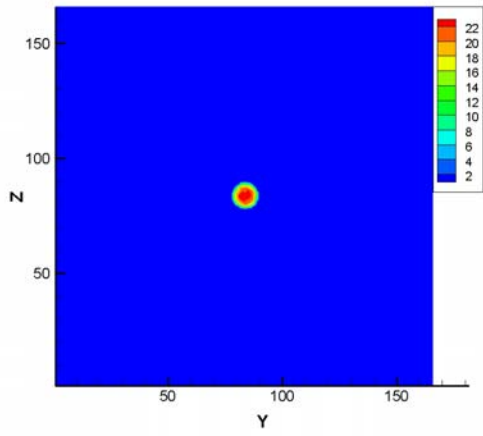
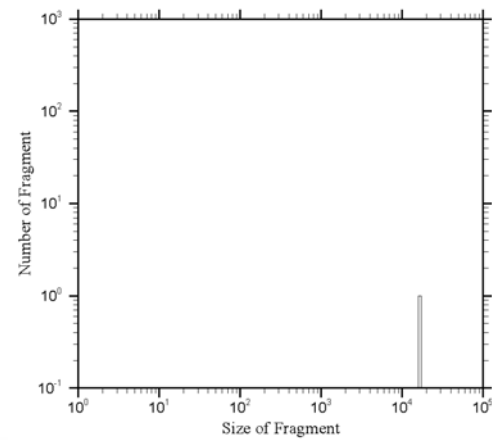
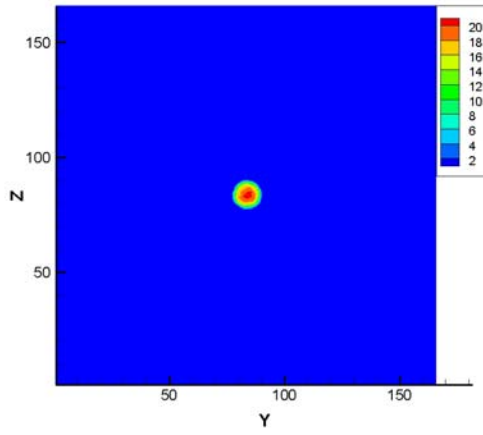


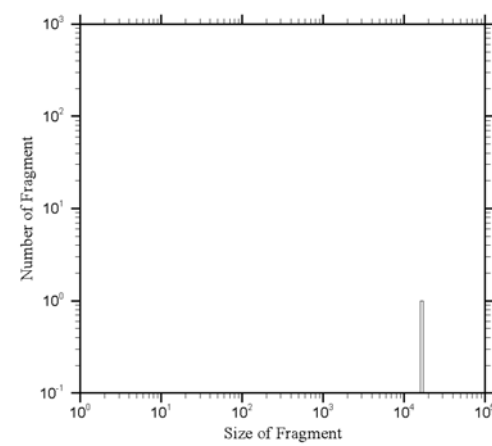
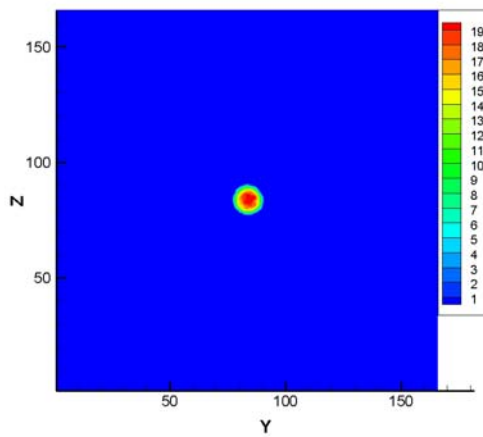
**Fig. 3. 52 Snapshot of helium droplet pair collision under vacuum, at (a)  $b=8.75nm$ ,  $V=500m/s$ , (b)  $b=8.75nm$ ,  $V=750m/s$ .**



(a)

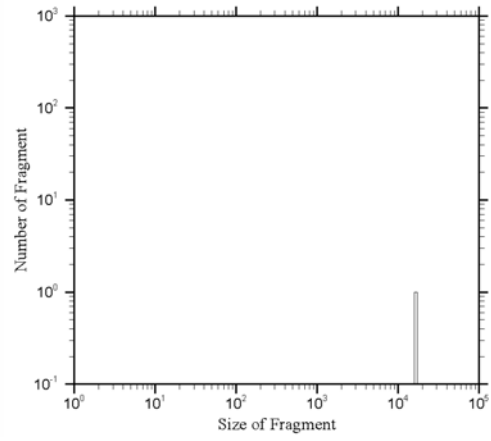
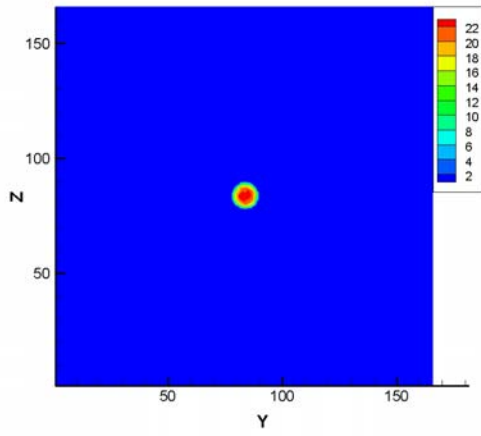


(b)

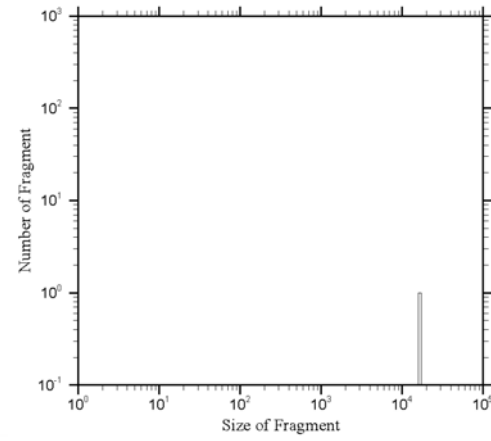
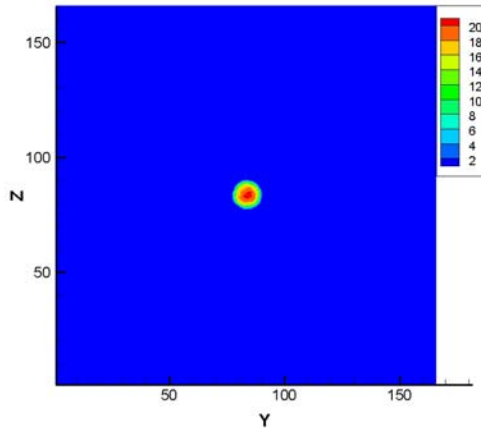


(c)

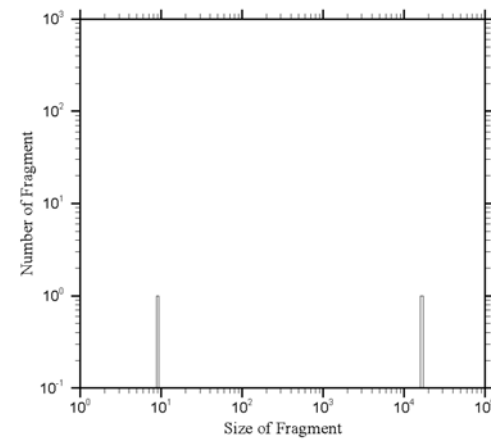
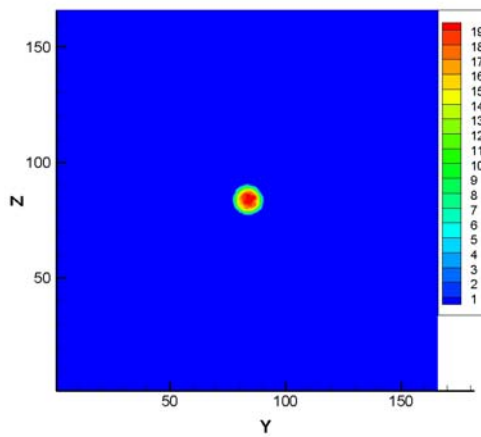
**Fig. 3. 53 Snapshot of density contour and clusters size distribution of Xenon droplets collision,  $b=0$ ,  $V=250m/s$ , at (a)  $25ps$ , (b)  $75ps$ , (c)  $150ps$ .**



(a)

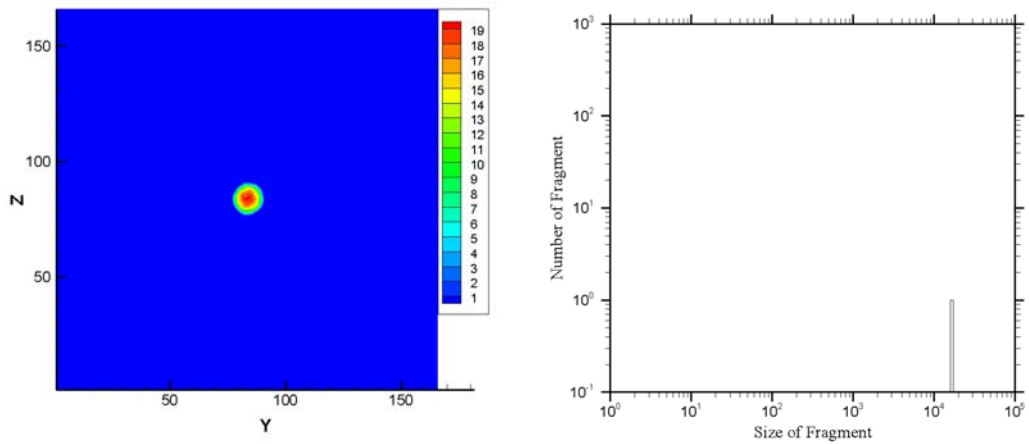


(b)

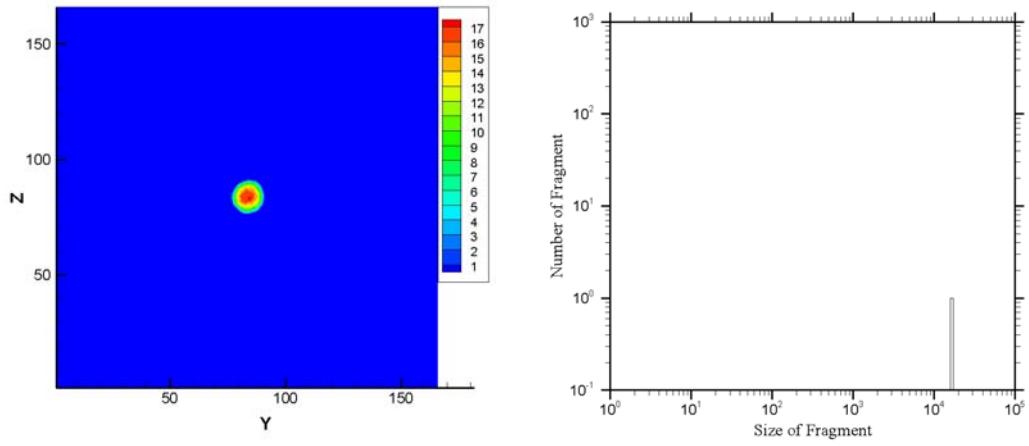


(c)

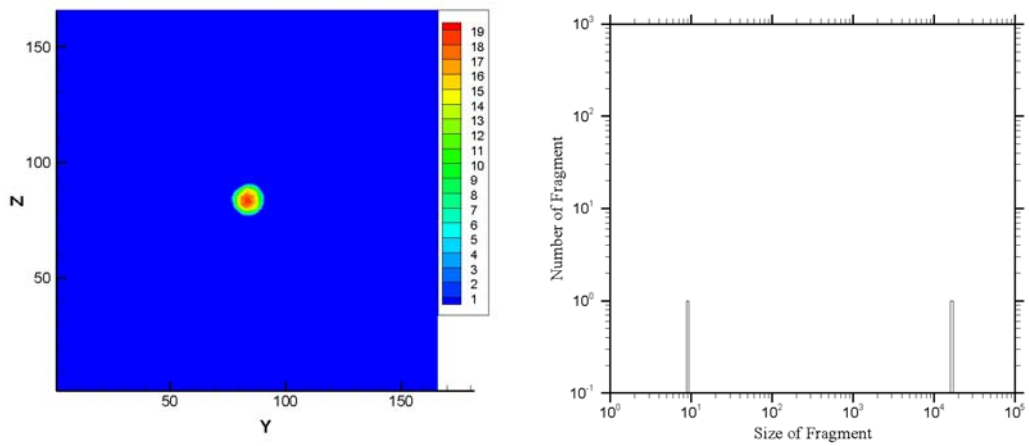
**Fig. 3. 54 Snapshot of density contour and clusters size distribution of Xenon droplets collision,  $b=0$ ,  $V=500m/s$ , at (a)  $25ps$ , (b)  $75ps$ , (c)  $150ps$ .**



(a)

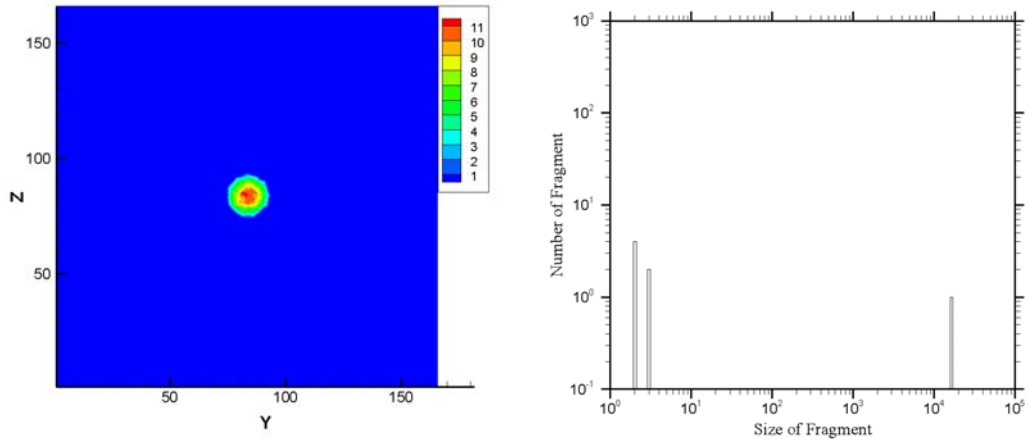


(b)

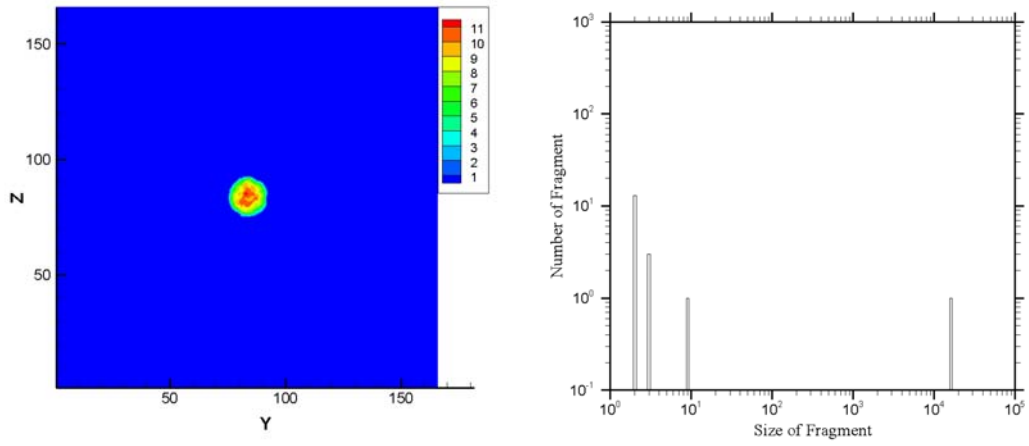


(c)

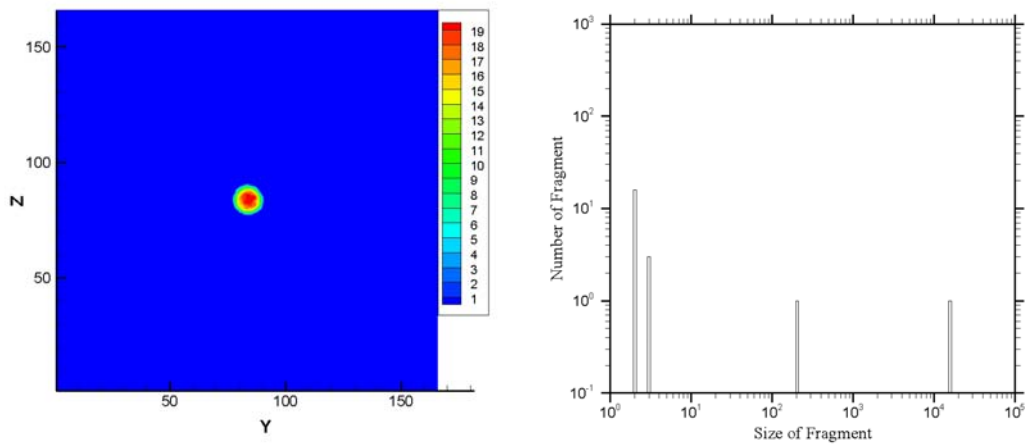
**Fig. 3. 55 Snapshot of density contour and clusters size distribution of Xenon droplets collision,  $b=0$ ,  $V=750m/s$ , at (a) 25ps, (b) 75ps, (c) 150ps.**



(a)

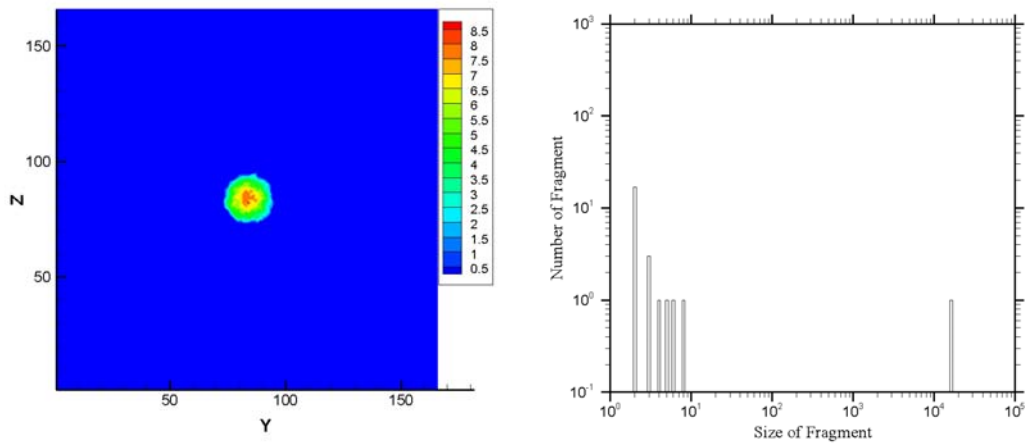


(b)

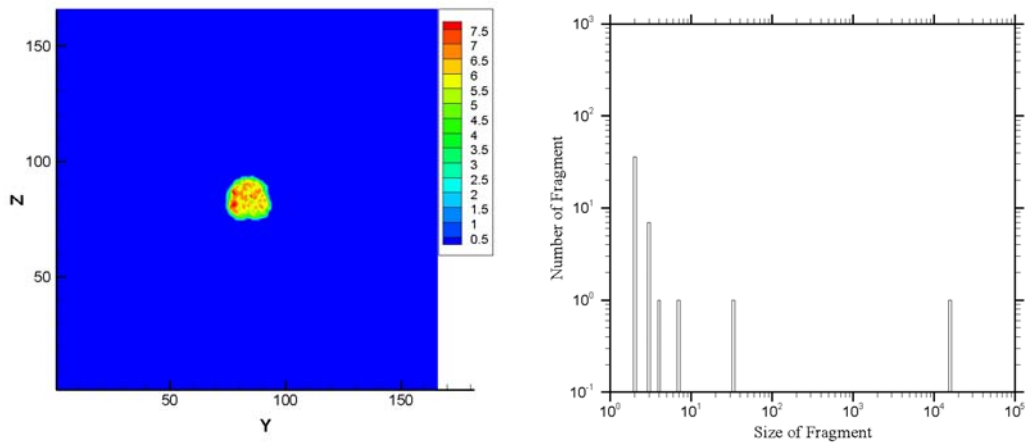


(c)

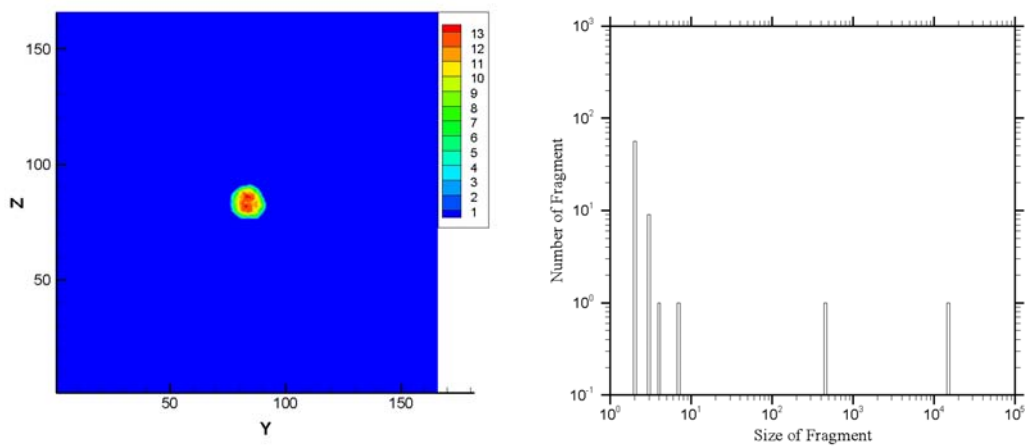
**Fig. 3.56 Snapshot of density contour and clusters size distribution of Xenon droplets collision,  $b=0$ ,  $V=1250m/s$ , at (a) 25ps, (b) 75ps, (c) 150ps.**



(a)

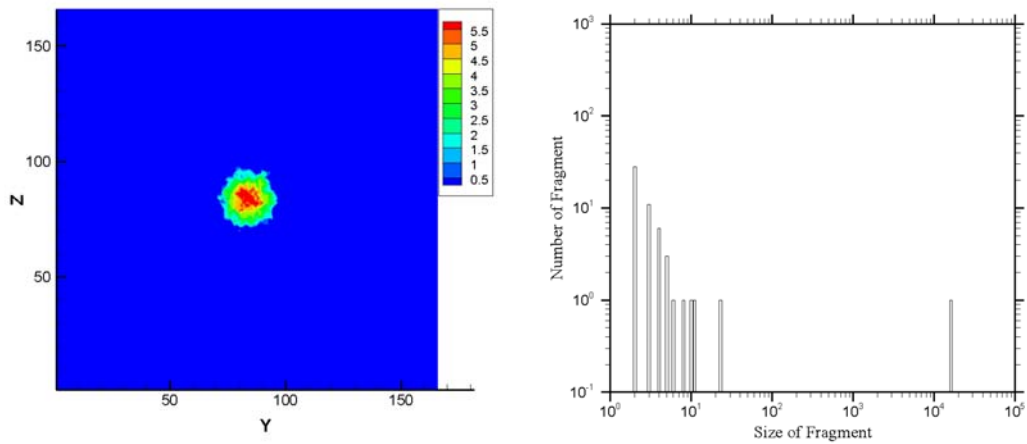


(b)

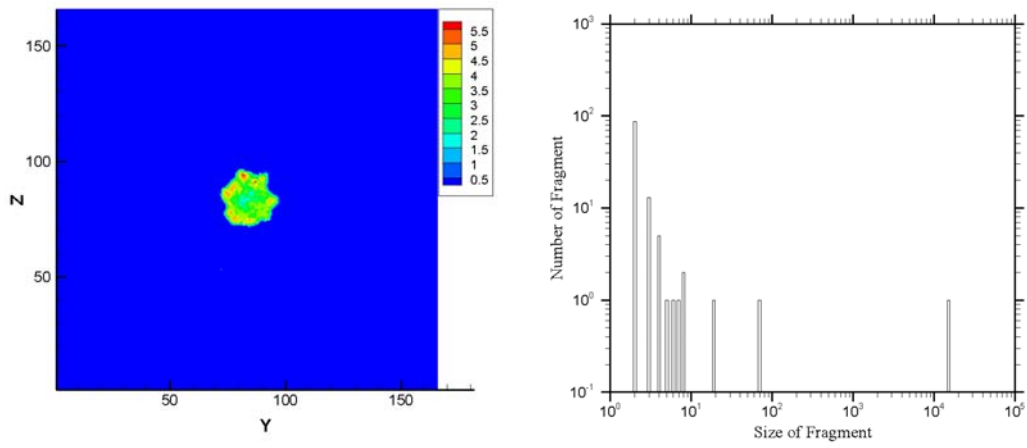


(c)

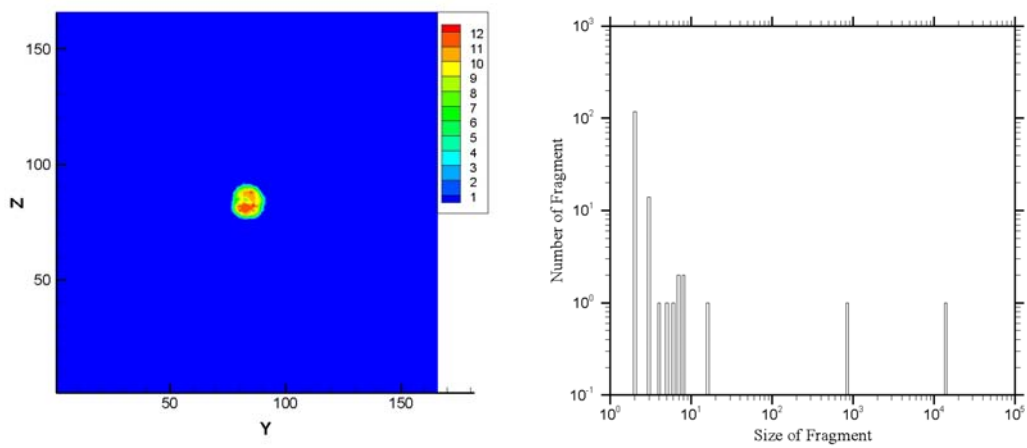
**Fig. 3. 57 Snapshot of density contour and clusters size distribution of Xenon droplets collision,  $b=0$ ,  $V=1500m/s$ , at (a)  $25ps$ , (b)  $75ps$ , (c)  $150ps$ .**



(a)



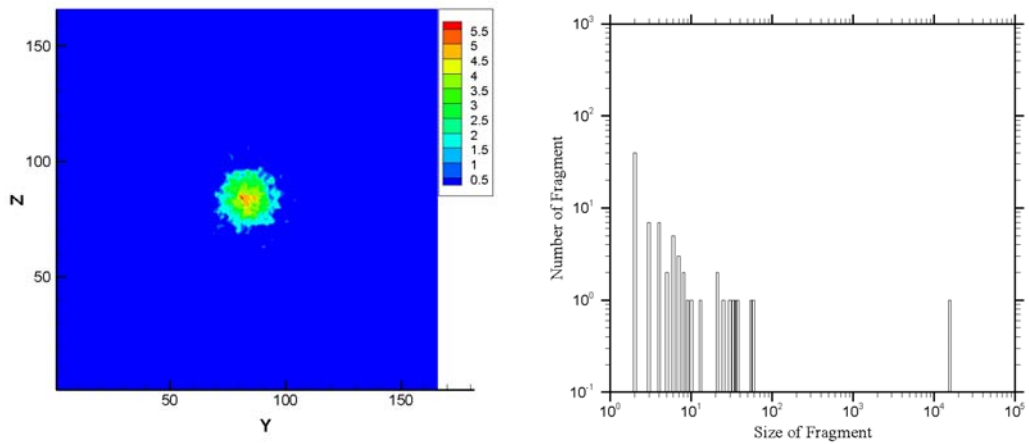
(b)



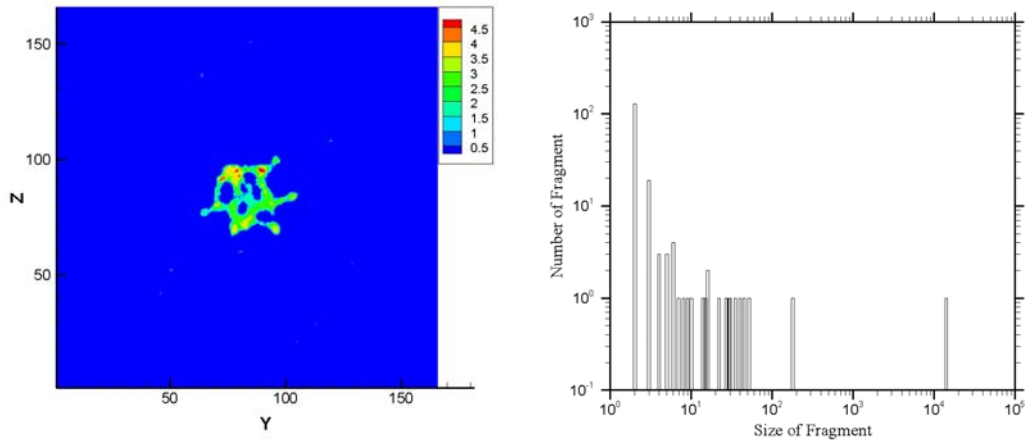
(c)

**Fig. 3. 58 Snapshot of density contour and clusters size distribution of Xenon droplets collision,  $b=0$ ,  $V=1750m/s$ , at (a)  $25ps$ , (b)  $75ps$ , (c)  $150ps$ .**

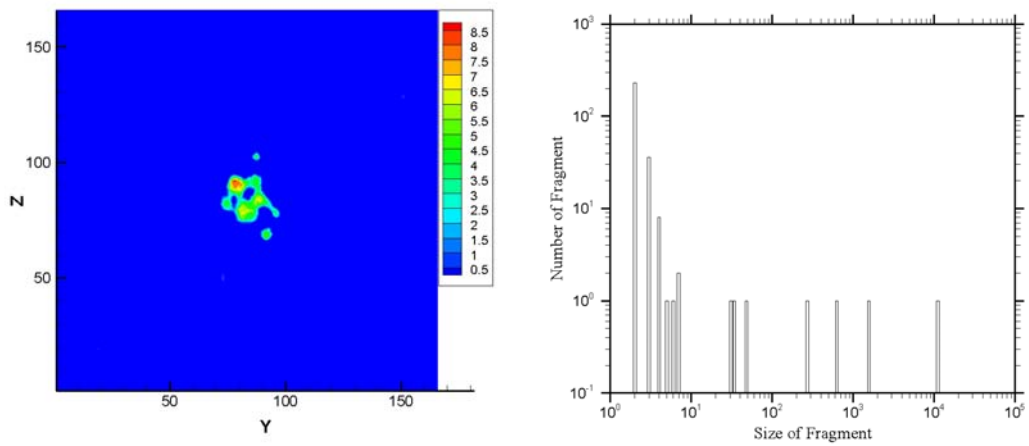




(a)

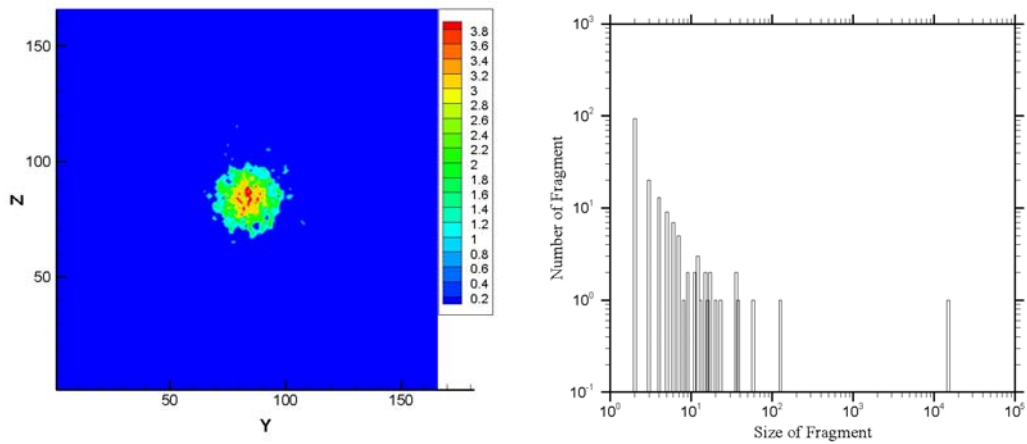


(b)

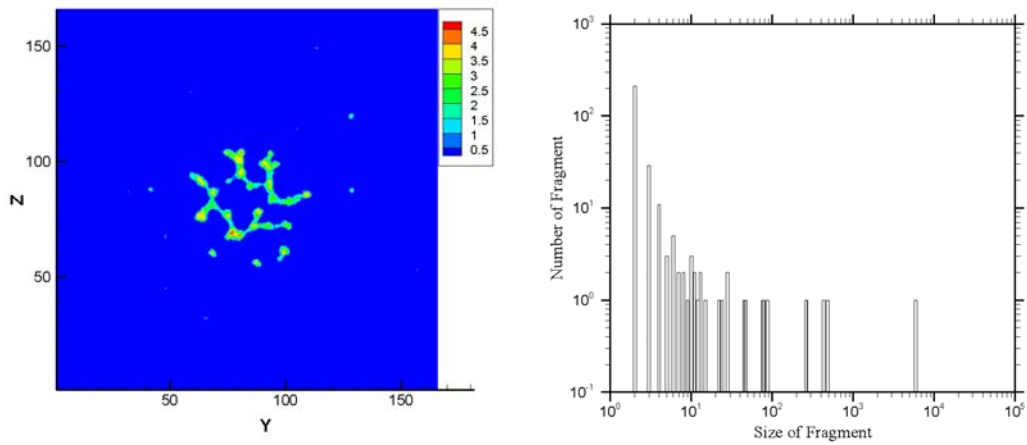


(c)

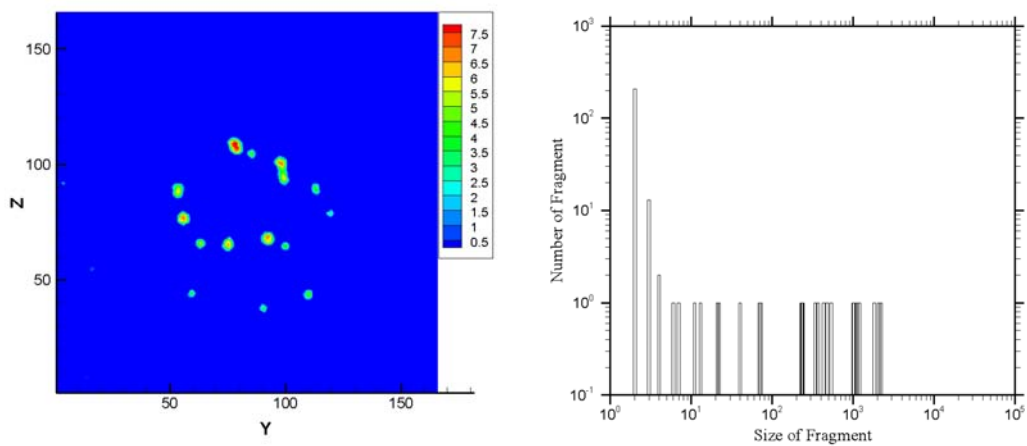
**Fig. 3.59 Snapshot of density contour and clusters size distribution of Xenon droplets collision,  $b=0$ ,  $V=2000m/s$ , at (a)  $25ps$ , (b)  $75ps$ , (c)  $150ps$ .**



(a)

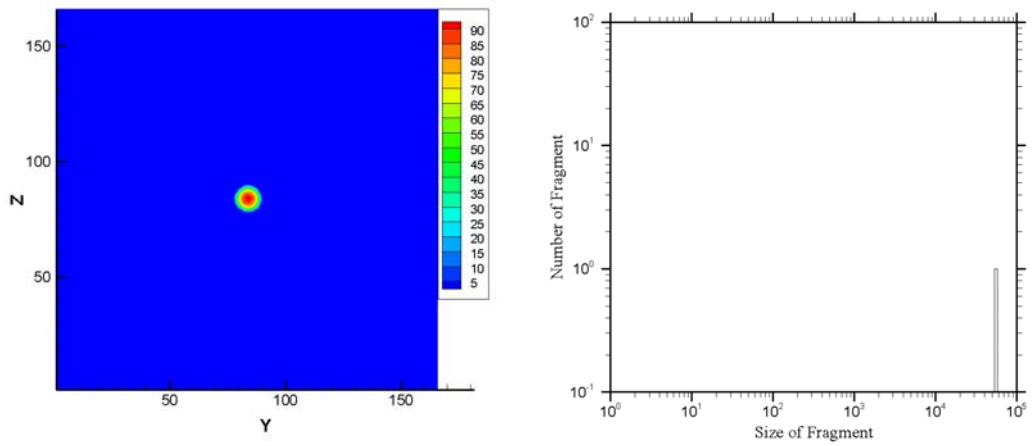


(b)

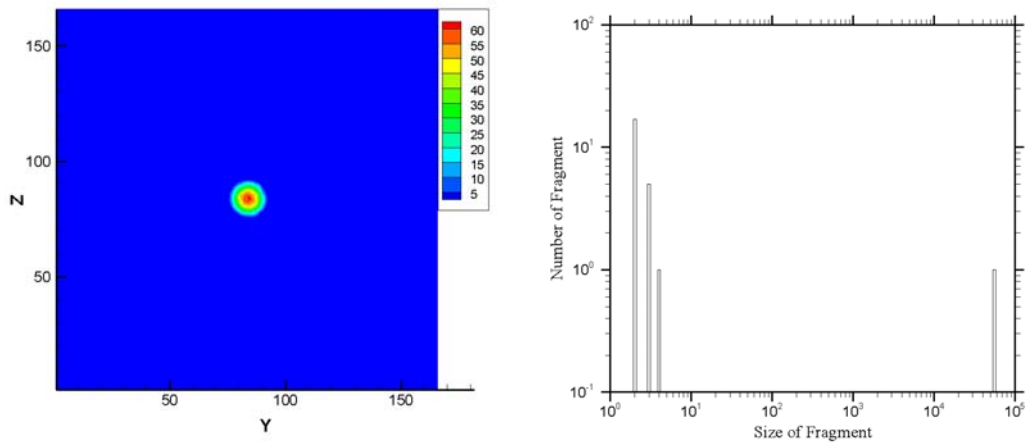


(c)

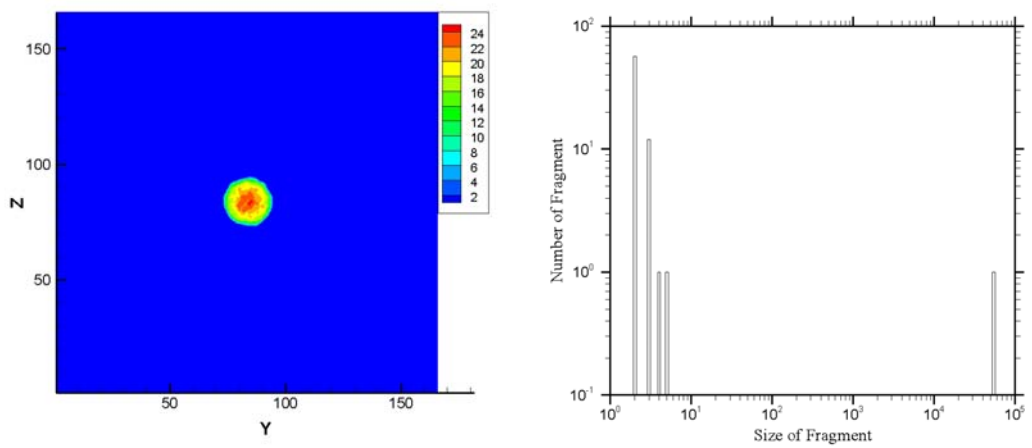
**Fig. 3. 60 Snapshot of density contour and clusters size distribution of Xenon droplets collision,  $b=0$ ,  $V=2250m/s$ , at (a)  $25ps$ , (b)  $75ps$ , (c)  $150ps$ .**



(a)

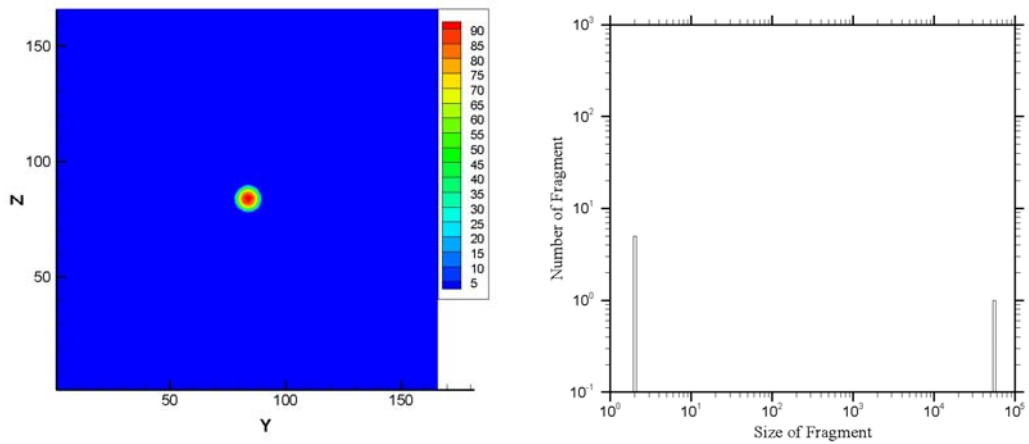


(b)

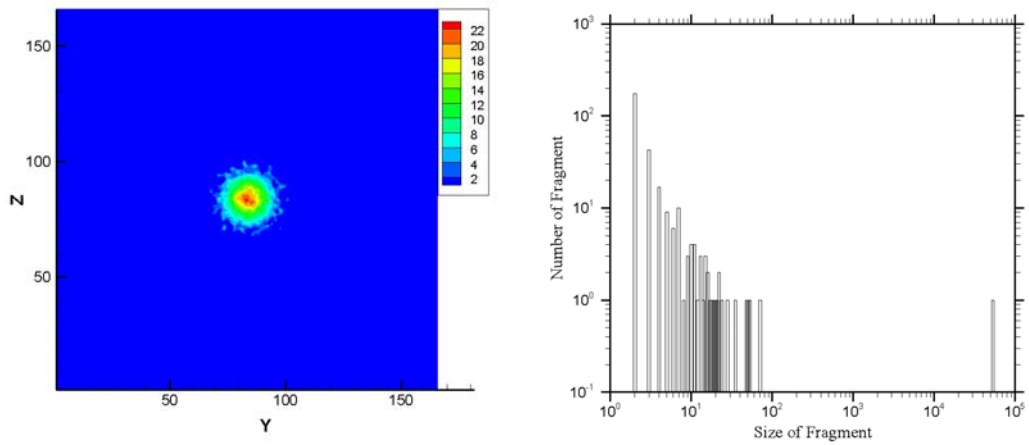


(c)

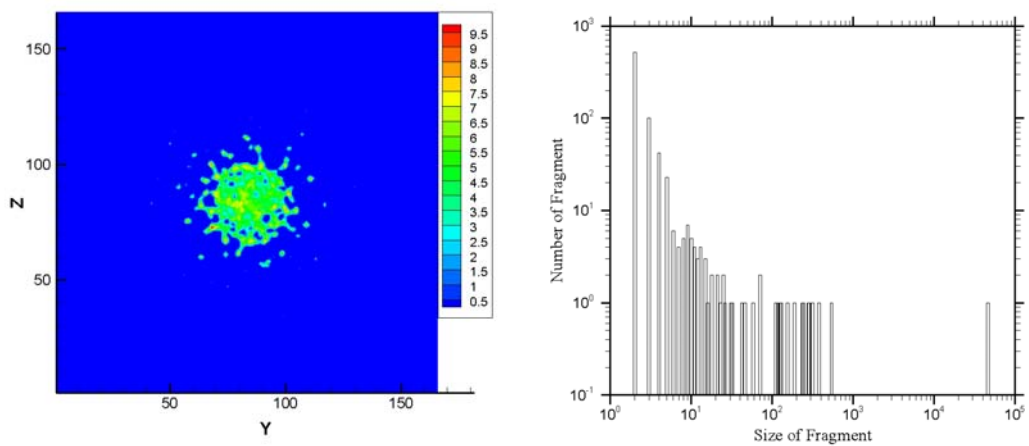
**Fig. 3. 61 Snapshot of density contour and clusters size distribution of Helium droplets collision,  $b=0$ ,  $V=250m/s$ , at (a)  $25ps$ , (b)  $75ps$ , (c)  $150ps$ .**



(a)

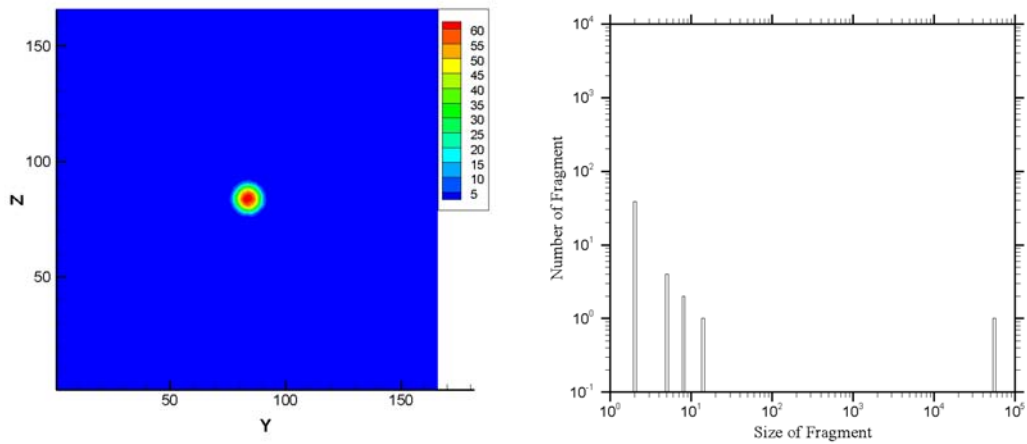


(b)

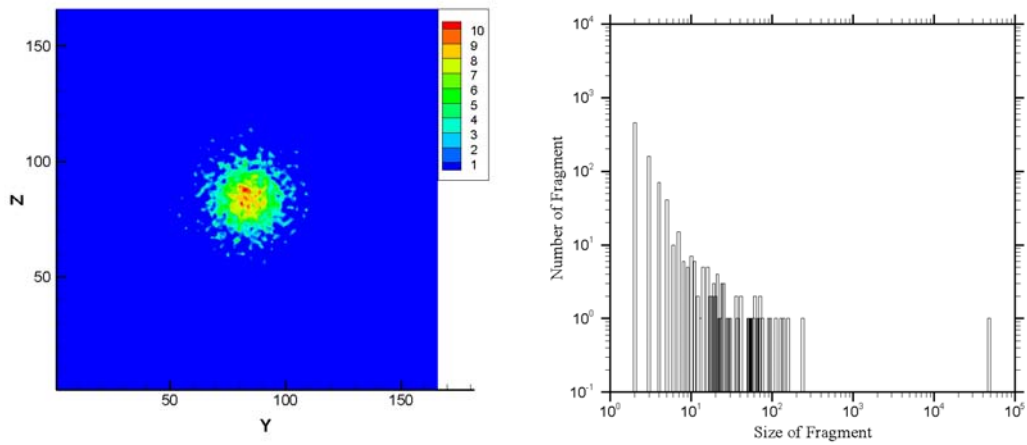


(c)

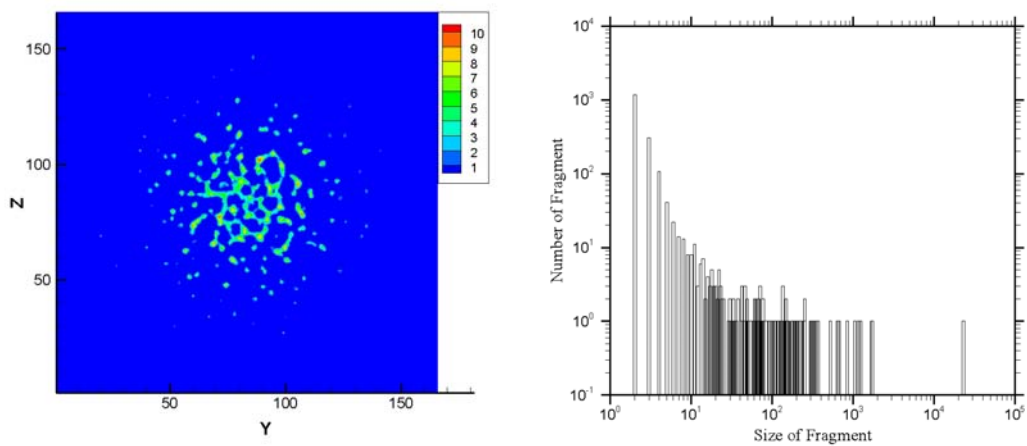
**Fig. 3. 62 Snapshot of density contour and clusters size distribution of Helium droplets collision,  $b=0$ ,  $V=500m/s$ , at (a)  $25ps$ , (b)  $75ps$ , (c)  $150ps$ .**



(a)



(b)



(c)

**Fig. 3. 63 Snapshot of density contour and clusters size distribution of Helium droplets collision,  $b=0$ ,  $V=750m/s$ , at (a)  $25ps$ , (b)  $75ps$ , (c)  $150ps$ .**

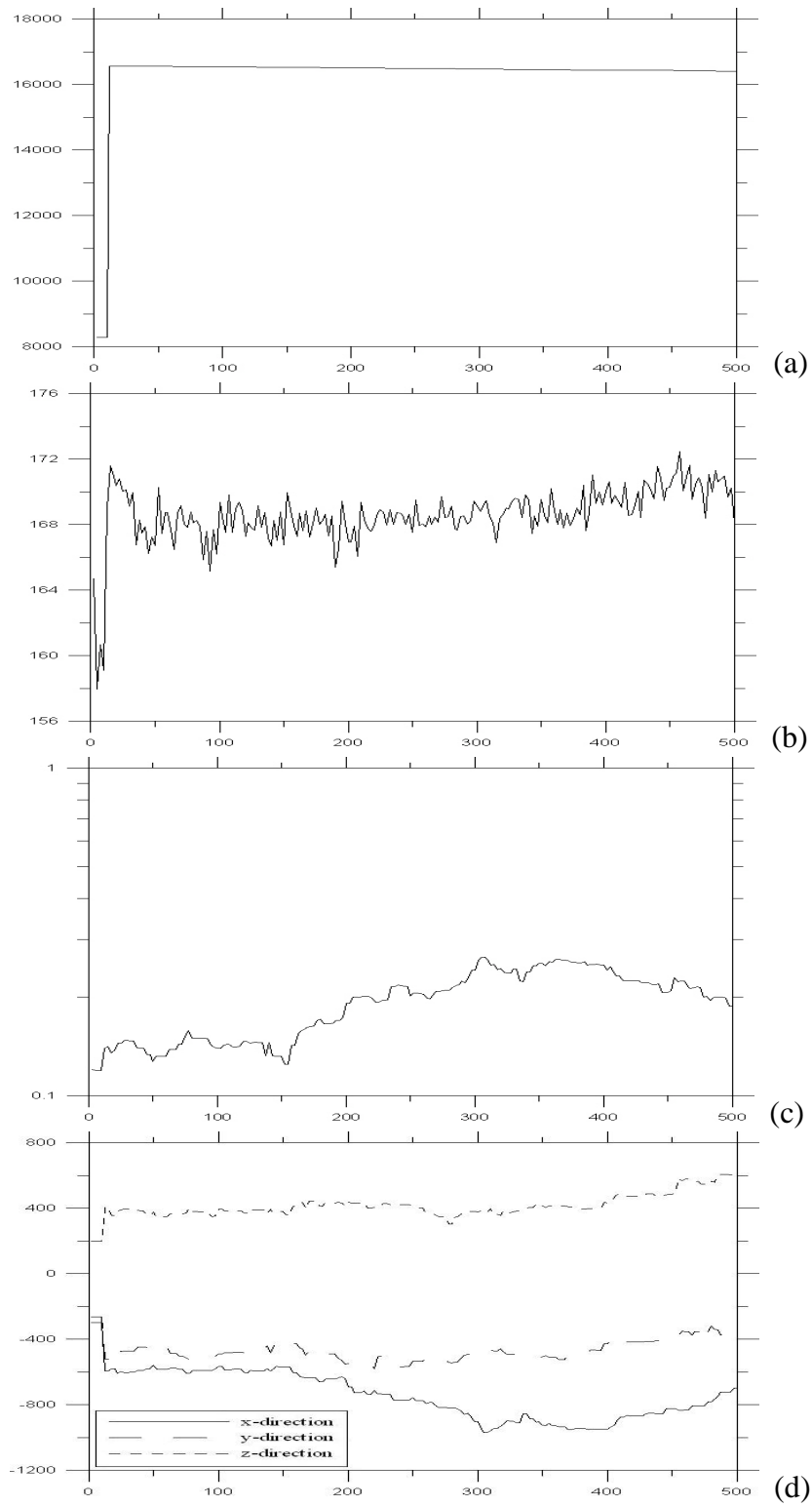


**Fig. 3. 64** Measurements of largest fragment of Xenon droplet pair collision,  $b=0$ ,  $V=250m/s$ , (a) Number of atoms, (b) Vibration temperature (k), (c) Rotation energy, (d) Angular momentum, respectively.

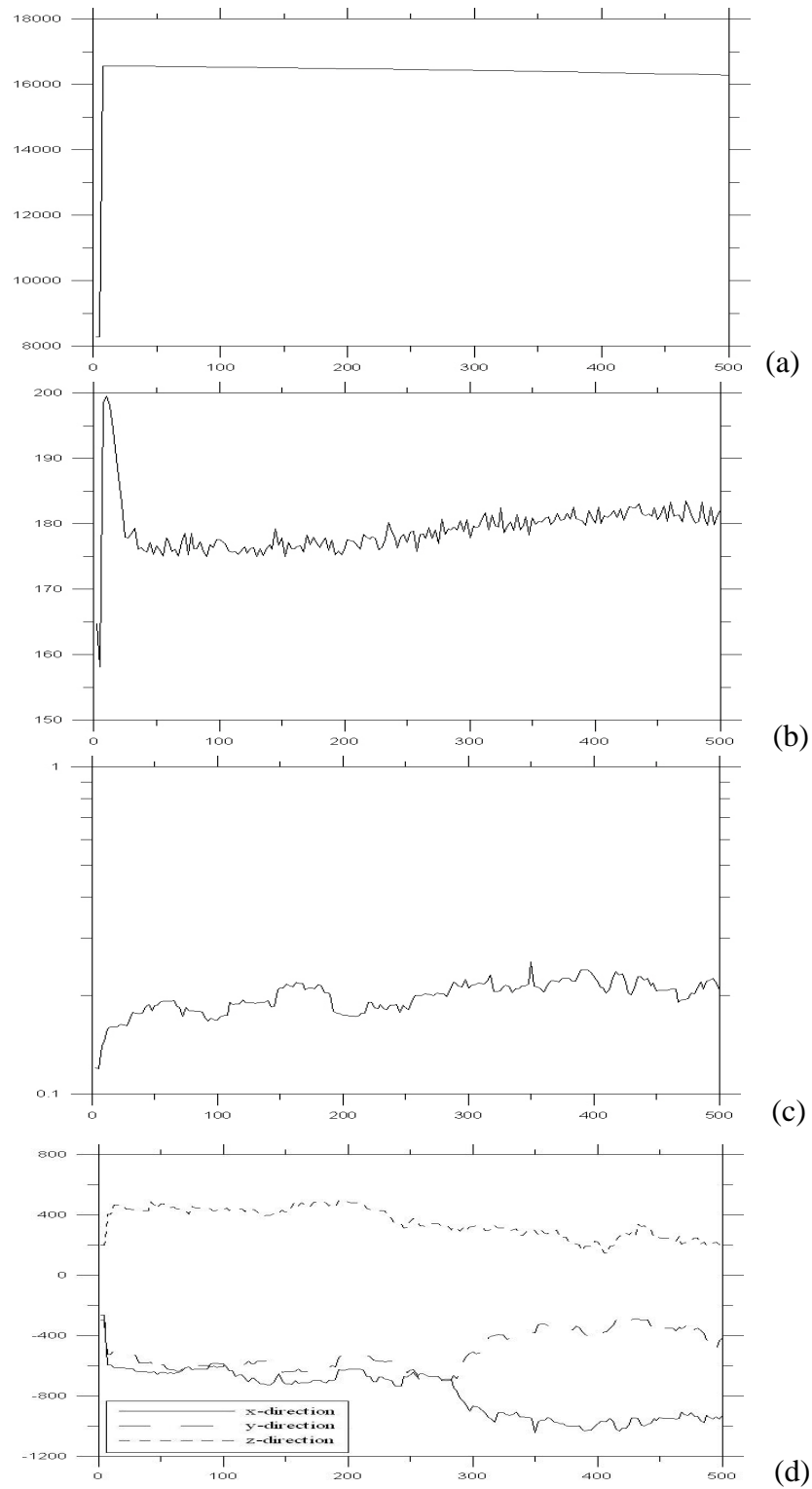


**Fig. 3. 65 Measurements of largest fragment of Xenon droplet pair collision,  $b=0$ ,  $V=500m/s$ , (a) Number of atoms, (b) Vibration temperature (k), (c) Rotation energy, (d) Angular momentum, respectively.**

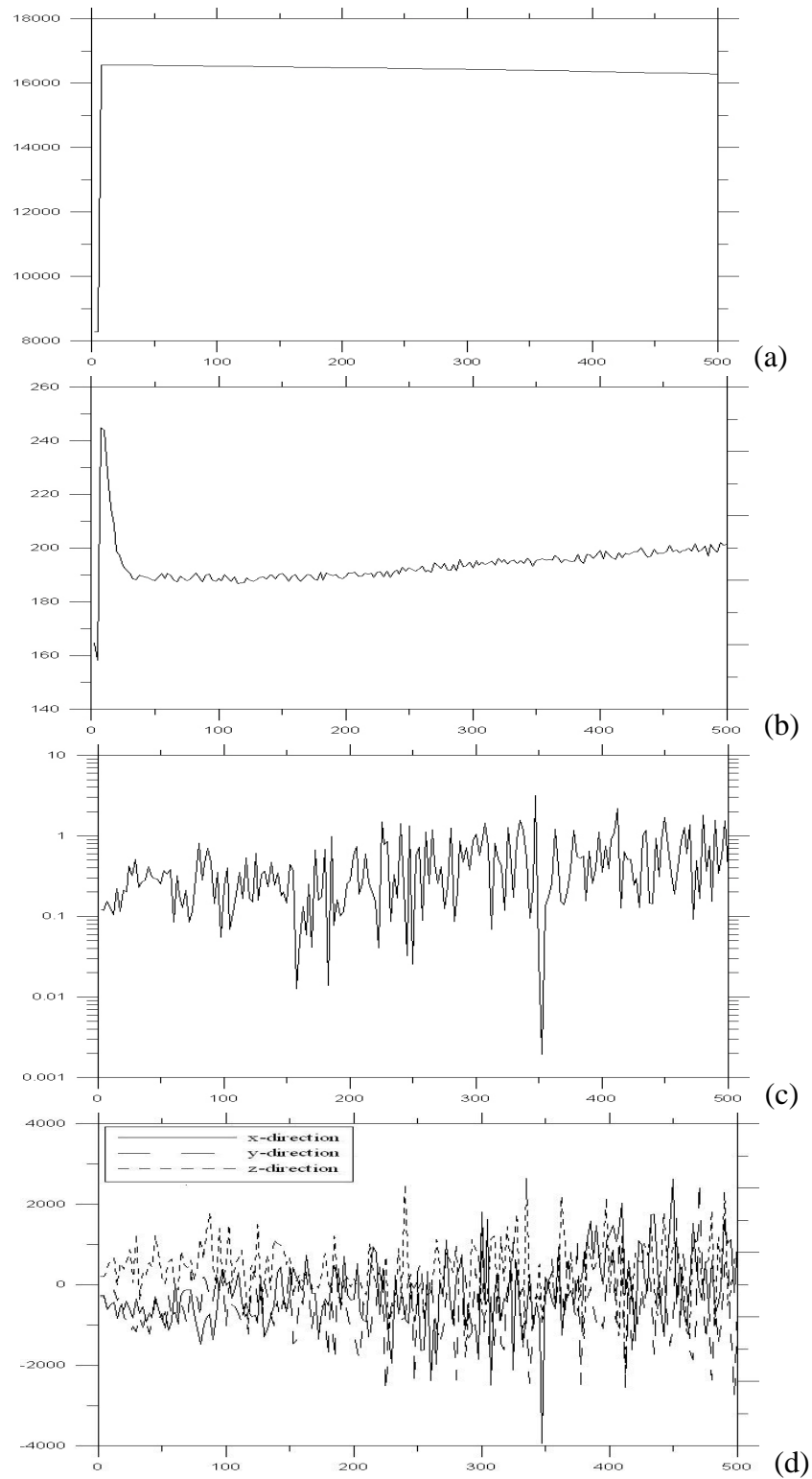


**Fig. 3. 66 Measurements of largest fragment of Xenon droplet pair collision,  $b=0$ ,  $V=750m/s$ , (a) Number of atoms, (b) Vibration temperature (k), (c) Rotation energy, (d) Angular momentum, respectively.**



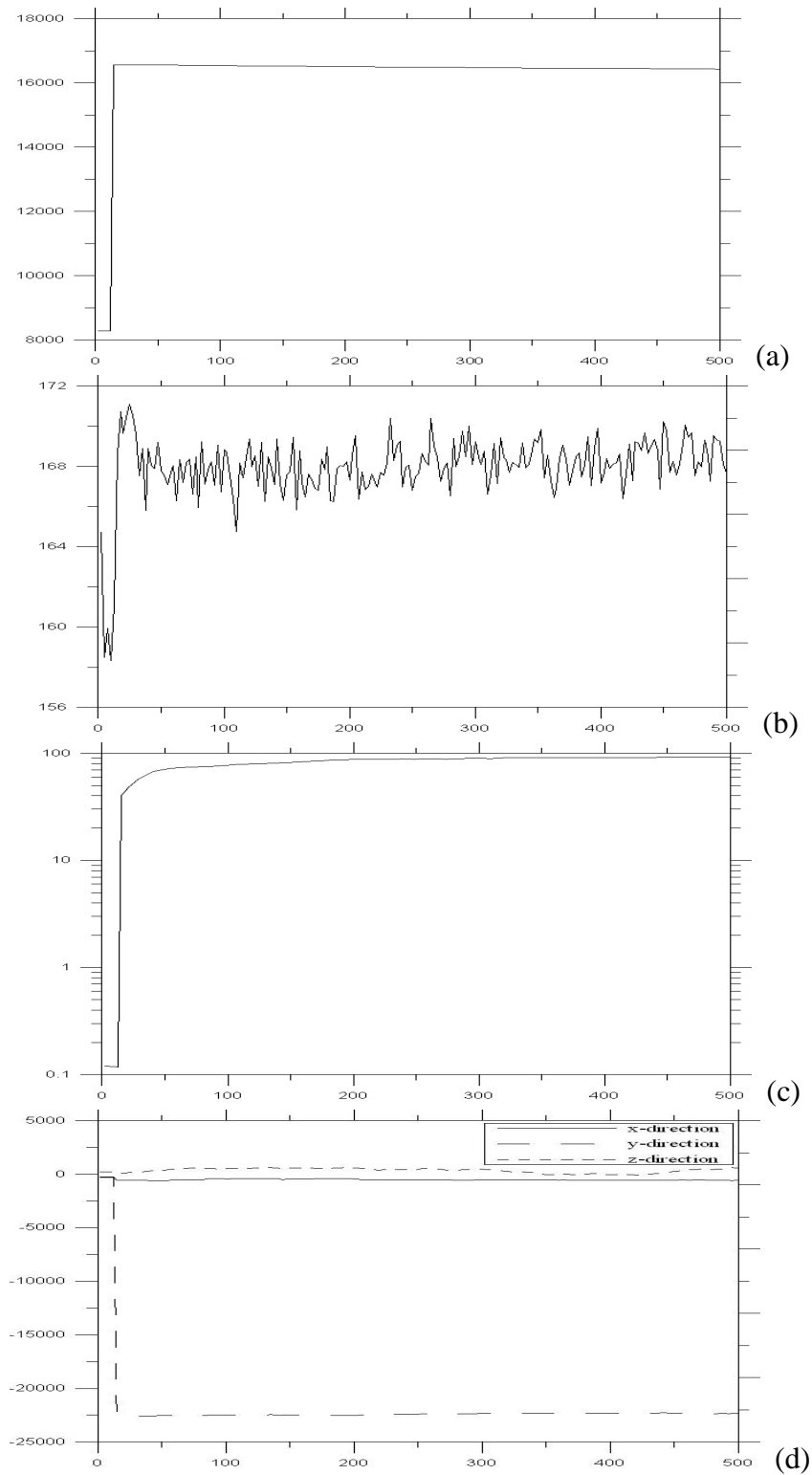


**Fig. 3. 67 Measurements of largest fragment of Xenon droplet pair collision,  $b=2.5nm$ ,  $V=250m/s$ , (a) Number of atoms, (b) Vibration temperature (k), (c) Rotation energy, (d) Angular momentum, respectively.**

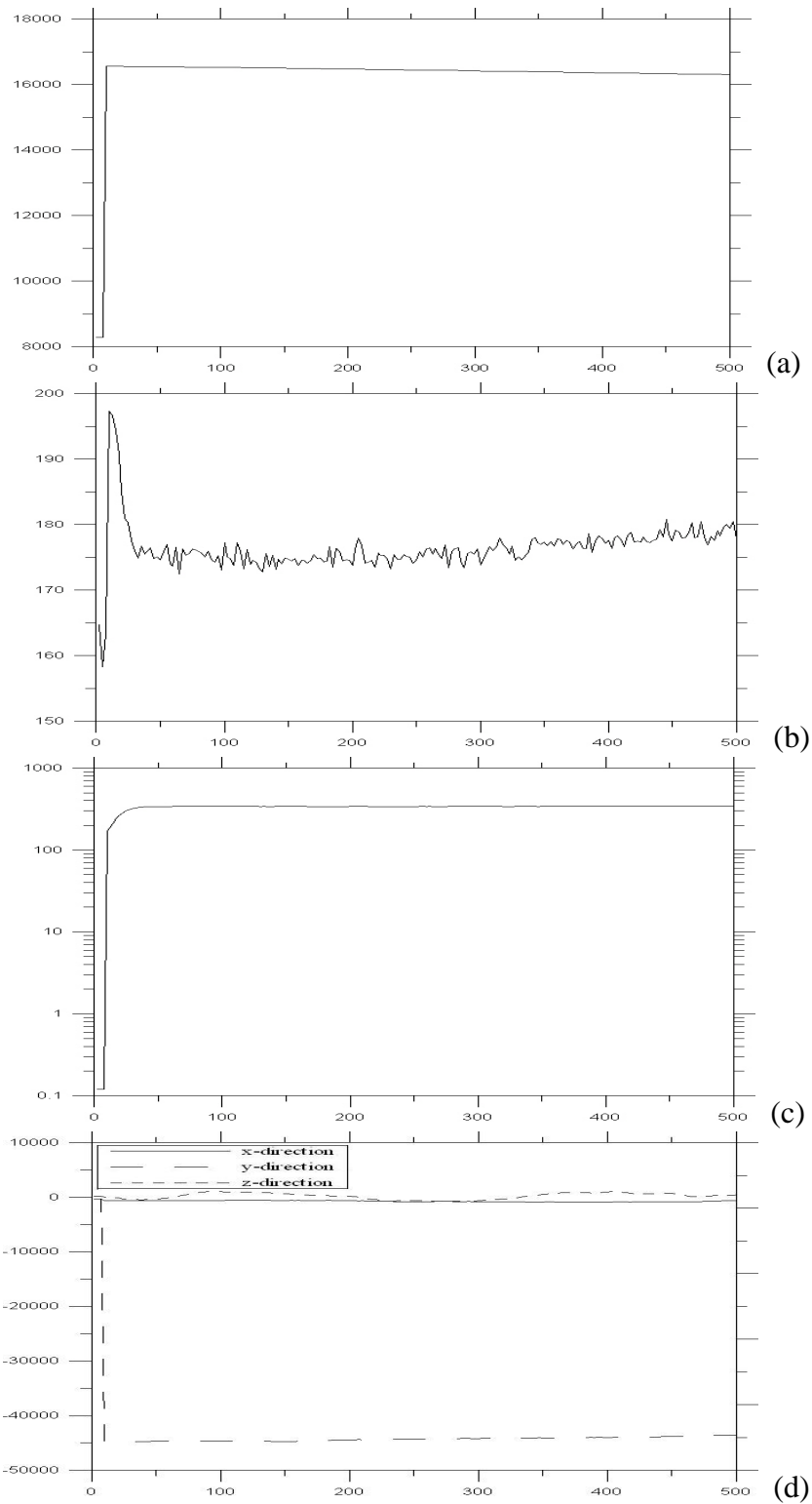


**Fig. 3. 68 Measurements of largest fragment of Xenon droplet pair collision,  $b=2.5nm$ ,  $V=500m/s$ , (a) Number of atoms, (b) Vibration temperature (k), (c) Rotation energy, (d) Angular momentum, respectively.**

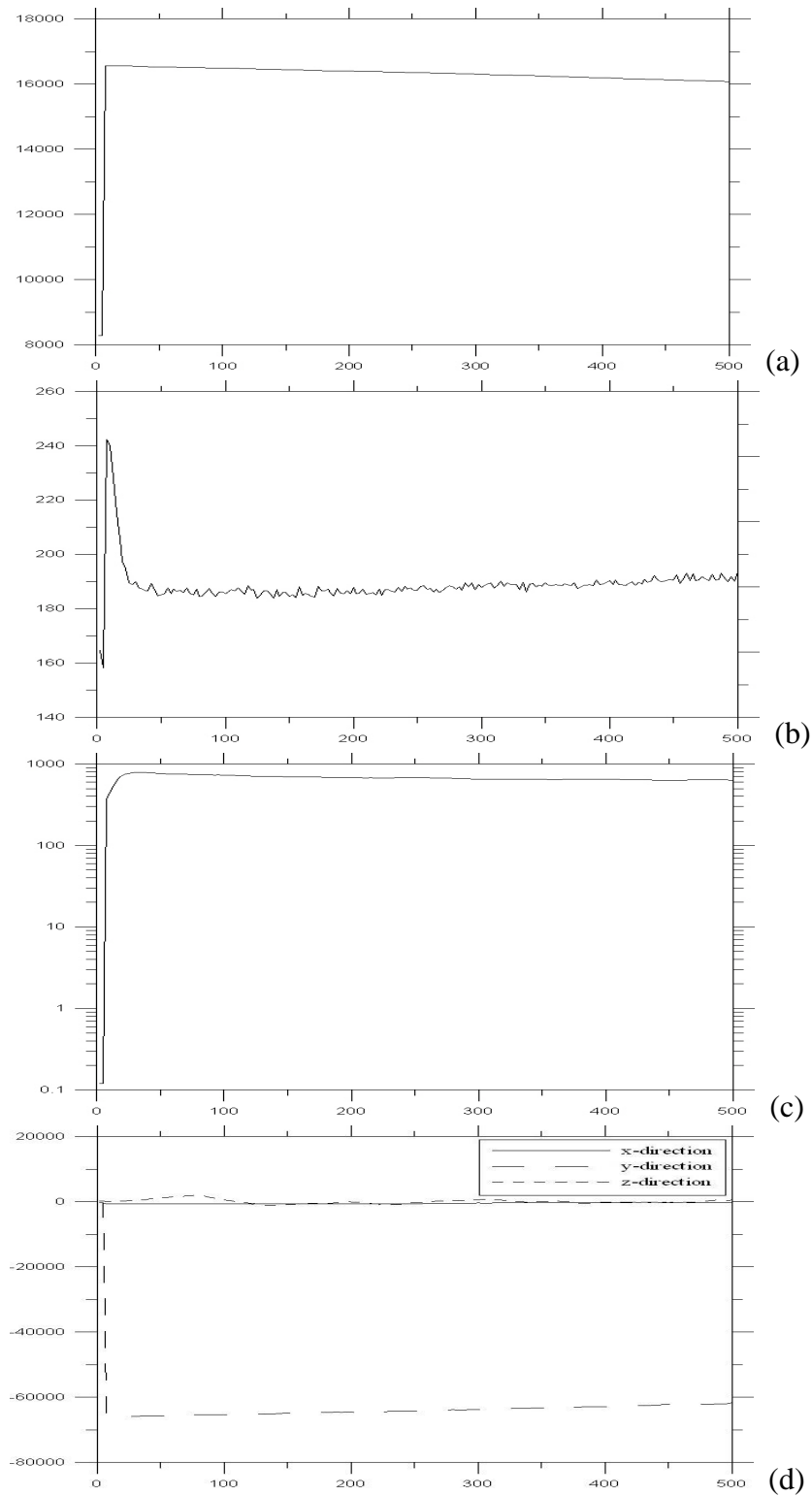


**Fig. 3. 69** Measurements of largest fragment of Xenon droplet pair collision,  $b=2.5nm$ ,  $V=750m/s$ , (a) Number of atoms, (b) Vibration temperature (k), (c) Rotation energy, (d) Angular momentum, respectively.

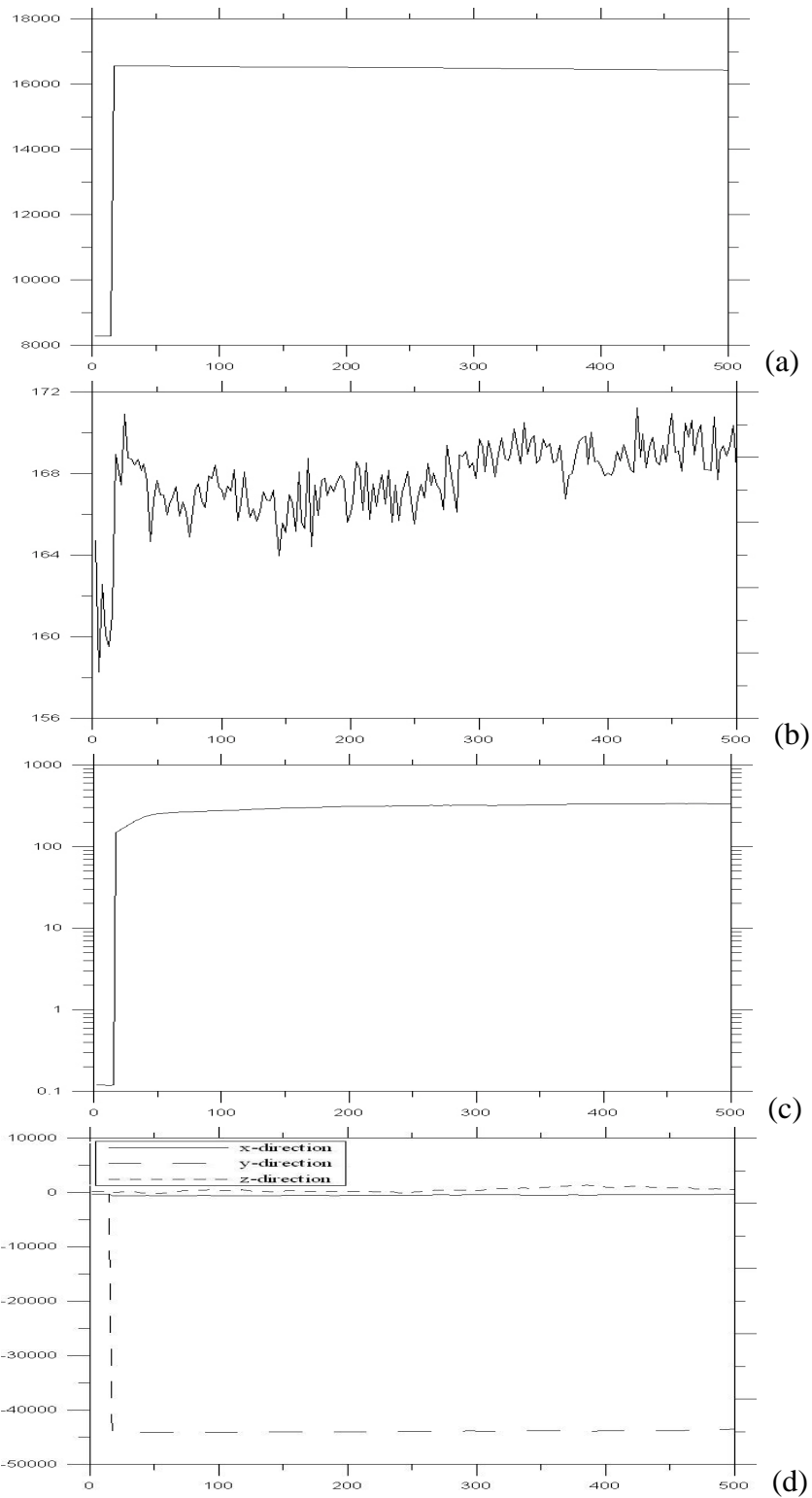


**Fig. 3. 70** Measurements of largest fragment of Xenon droplet pair collision,  $b=5nm$ ,  $V=250 m/s$ , (a) Number of atoms, (b) Vibration temperature (k), (c) Rotation energy, (d) Angular momentum, respectively.

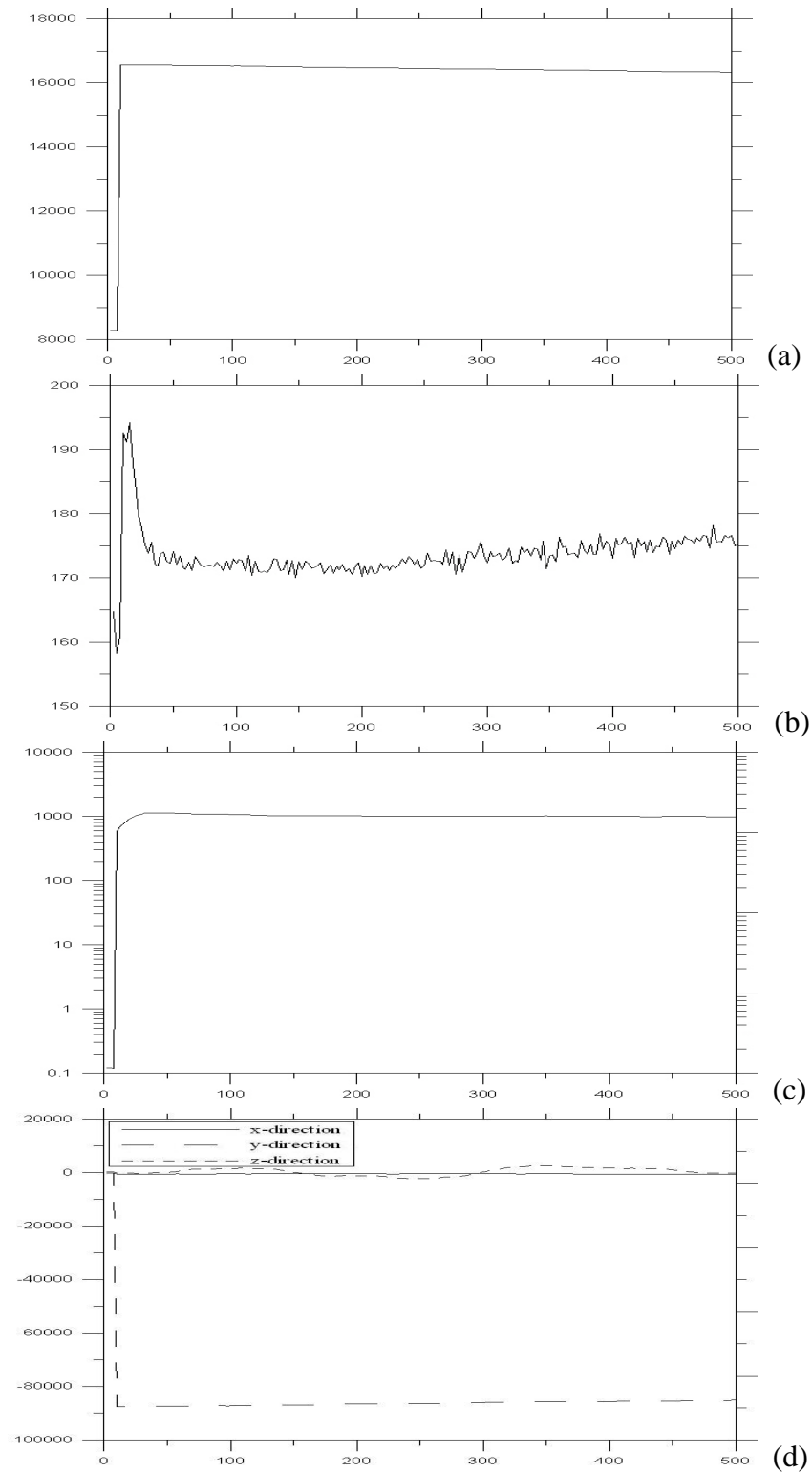


**Fig. 3. 71** Measurements of largest fragment of Xenon droplet pair collision,  $b=5nm$ ,  $V=500m/s$ , (a) Number of atoms, (b) Vibration temperature (k), (c) Rotation energy, (d) Angular momentum, respectively.

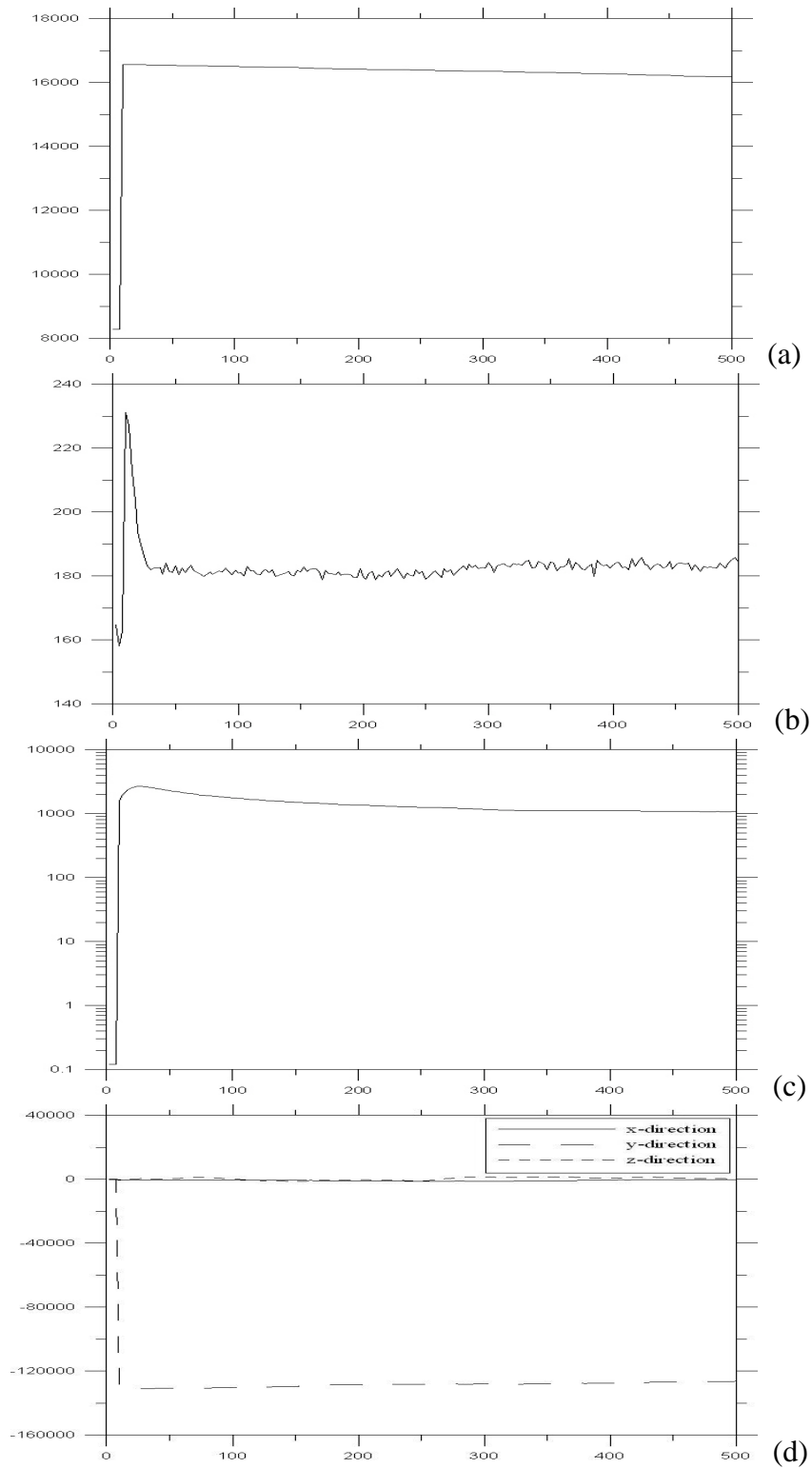


**Fig. 3. 72 Measurements of largest fragment of Xenon droplet pair collision,  $b=5nm$ ,  $V=750m/s$ , (a) Number of atoms, (b) Vibration temperature (k), (c) Rotation energy, (d) Angular momentum, respectively.**

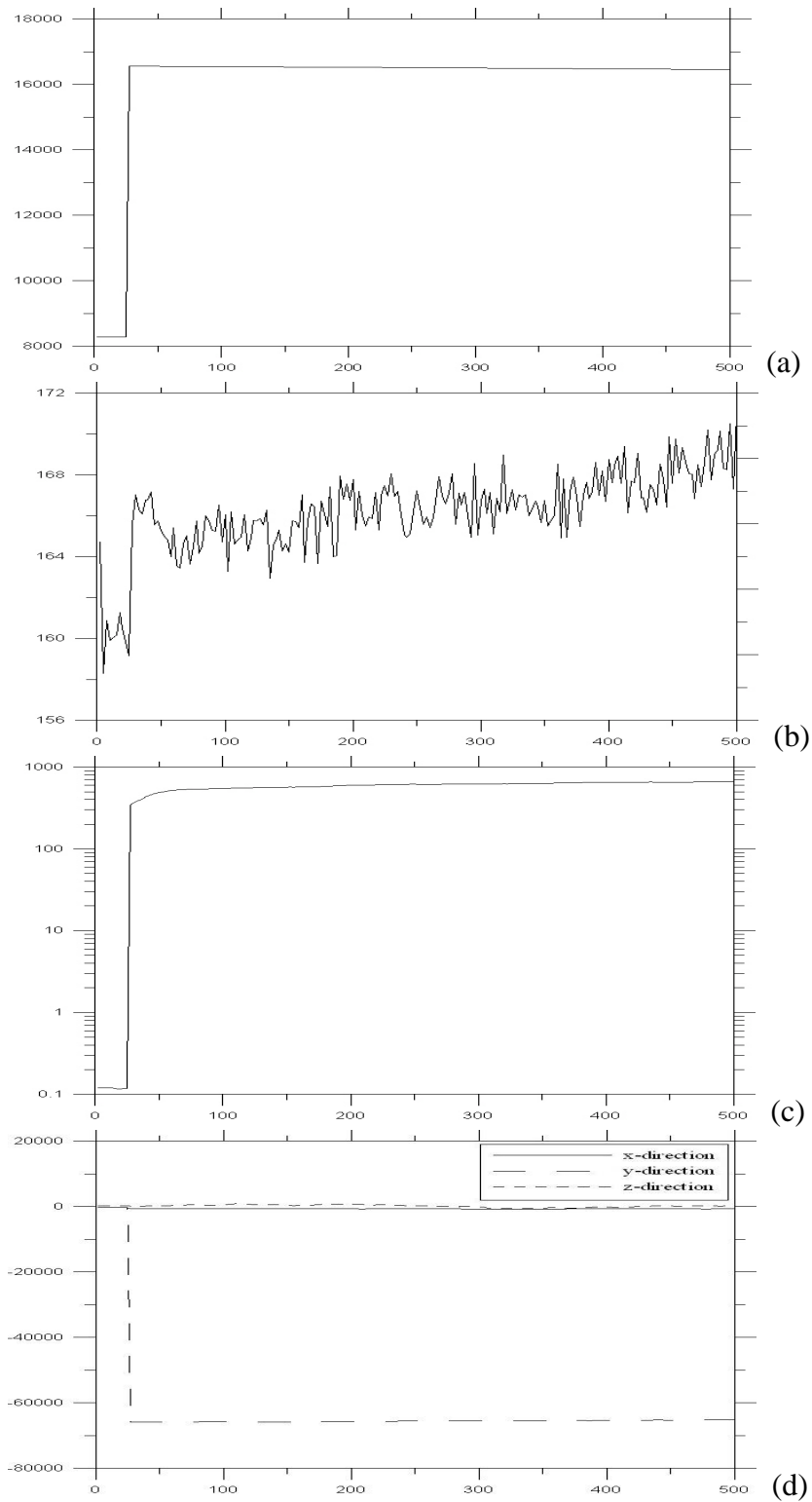


**Fig. 3. 73** Measurements of largest fragment of Xenon droplet pair collision,  $b=7.5nm$ ,  $V=250m/s$ , (a) Number of atoms, (b) Vibration temperature (k), (c) Rotation energy, (d) Angular momentum, respectively.

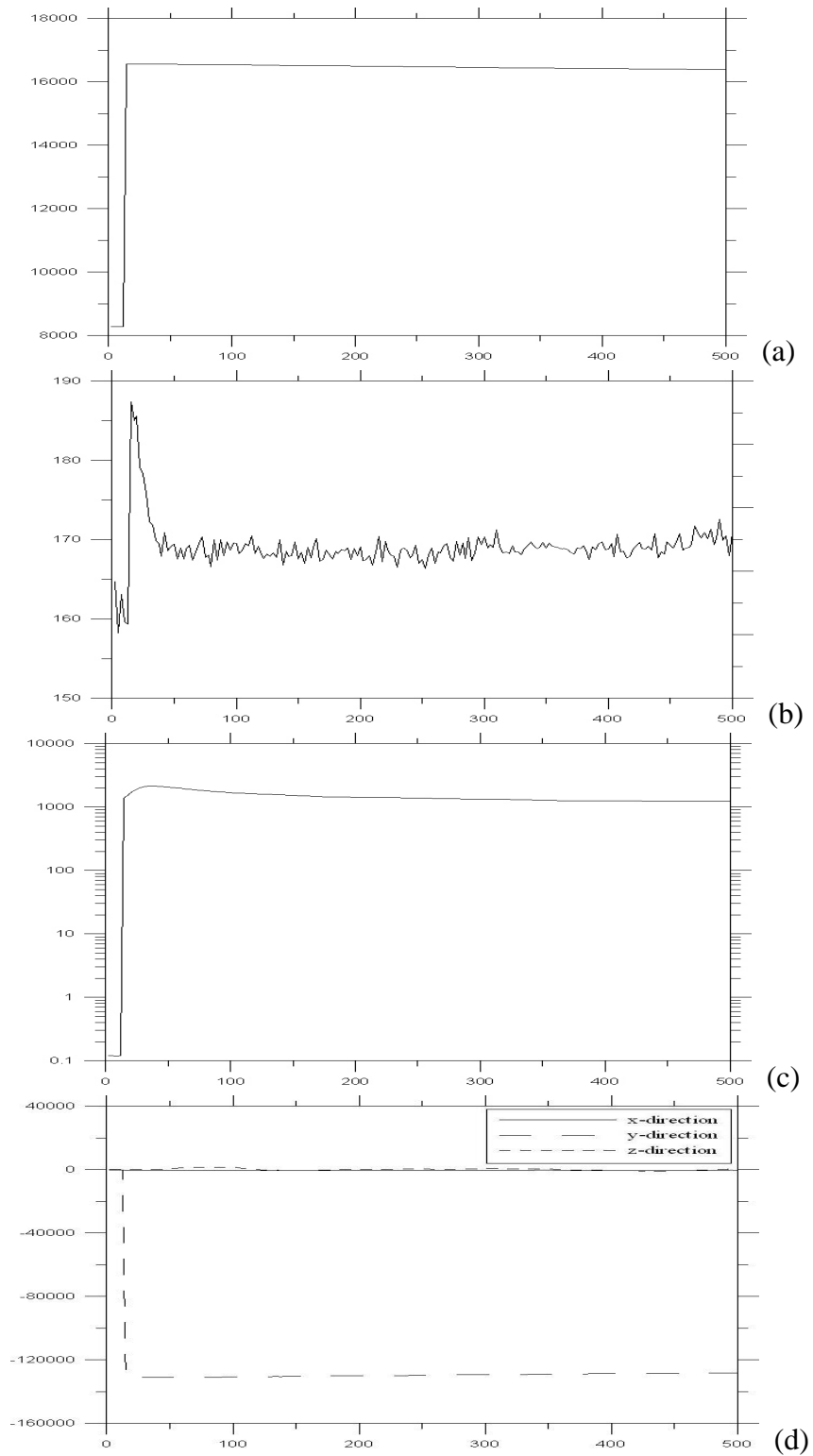


**Fig. 3. 74 Measurements of largest fragment of Xenon droplet pair collision,  $b=7.5nm$ ,  $V=500m/s$ , (a) Number of atoms, (b) Vibration temperature (k), (c) Rotation energy, (d) Angular momentum, respectively.**



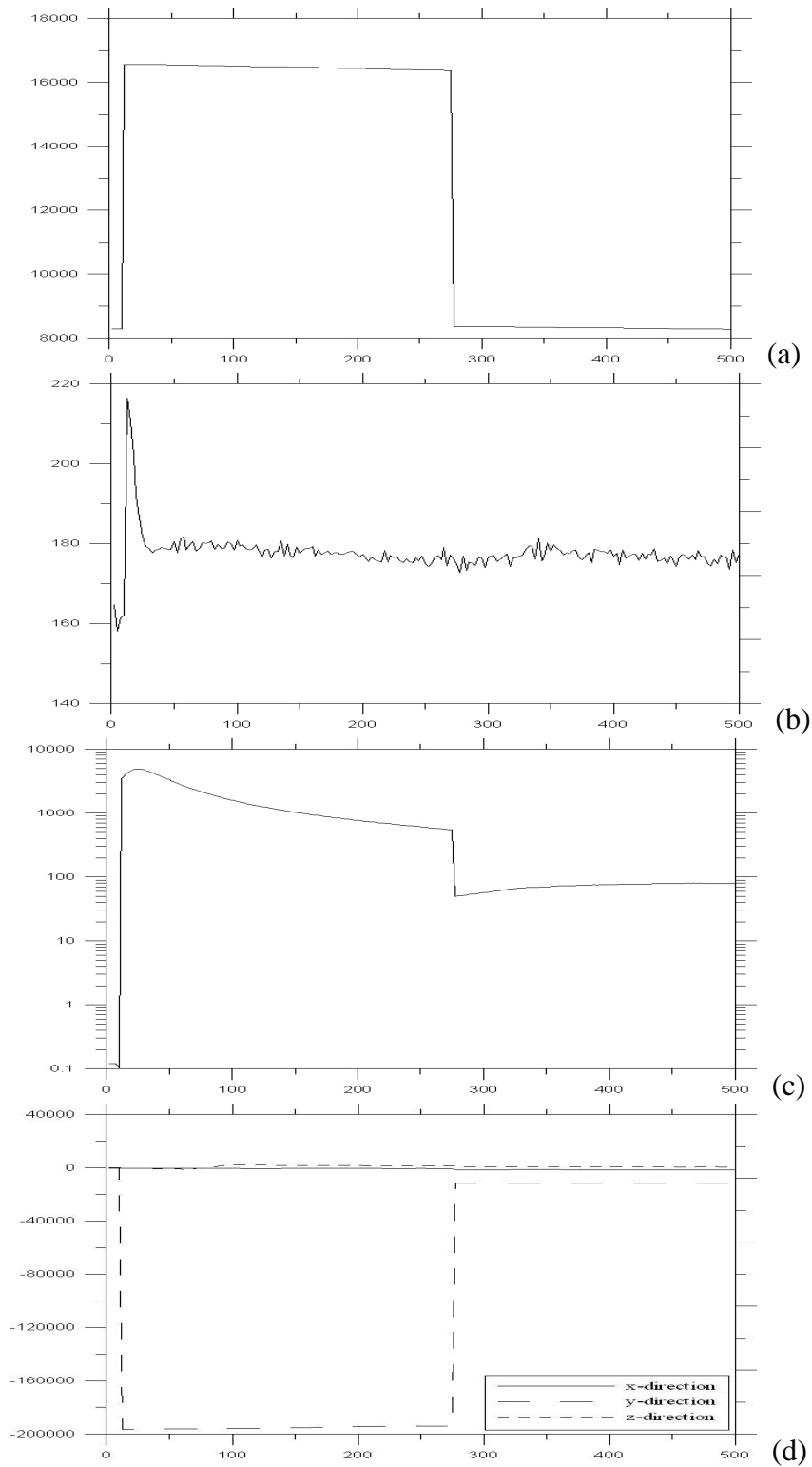


**Fig. 3. 75 Measurements of largest fragment of Xenon droplet pair collision,  $b=7.5nm$ ,  $V=750m/s$ , (a) Number of atoms, (b) Vibration temperature (k), (c) Rotation energy, (d) Angular momentum, respectively.**

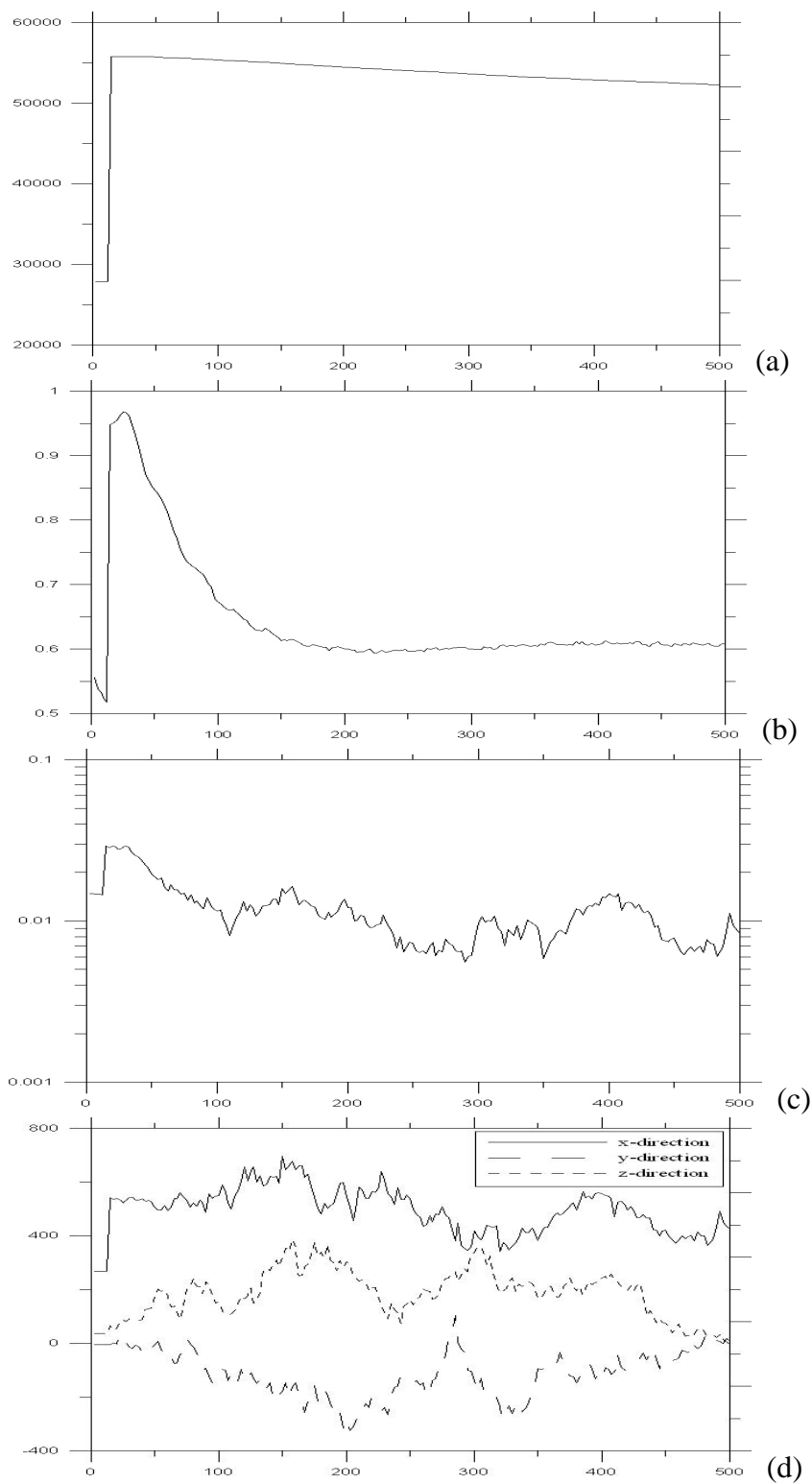


**Fig. 3. 76 Measurements of largest fragment of Helium droplet pair collision,  $b=0$ ,  $V=250m/s$ , (a) Number of atoms, (b) Vibration temperature (k), (c) Rotation energy, (d) Angular momentum, respectively.**

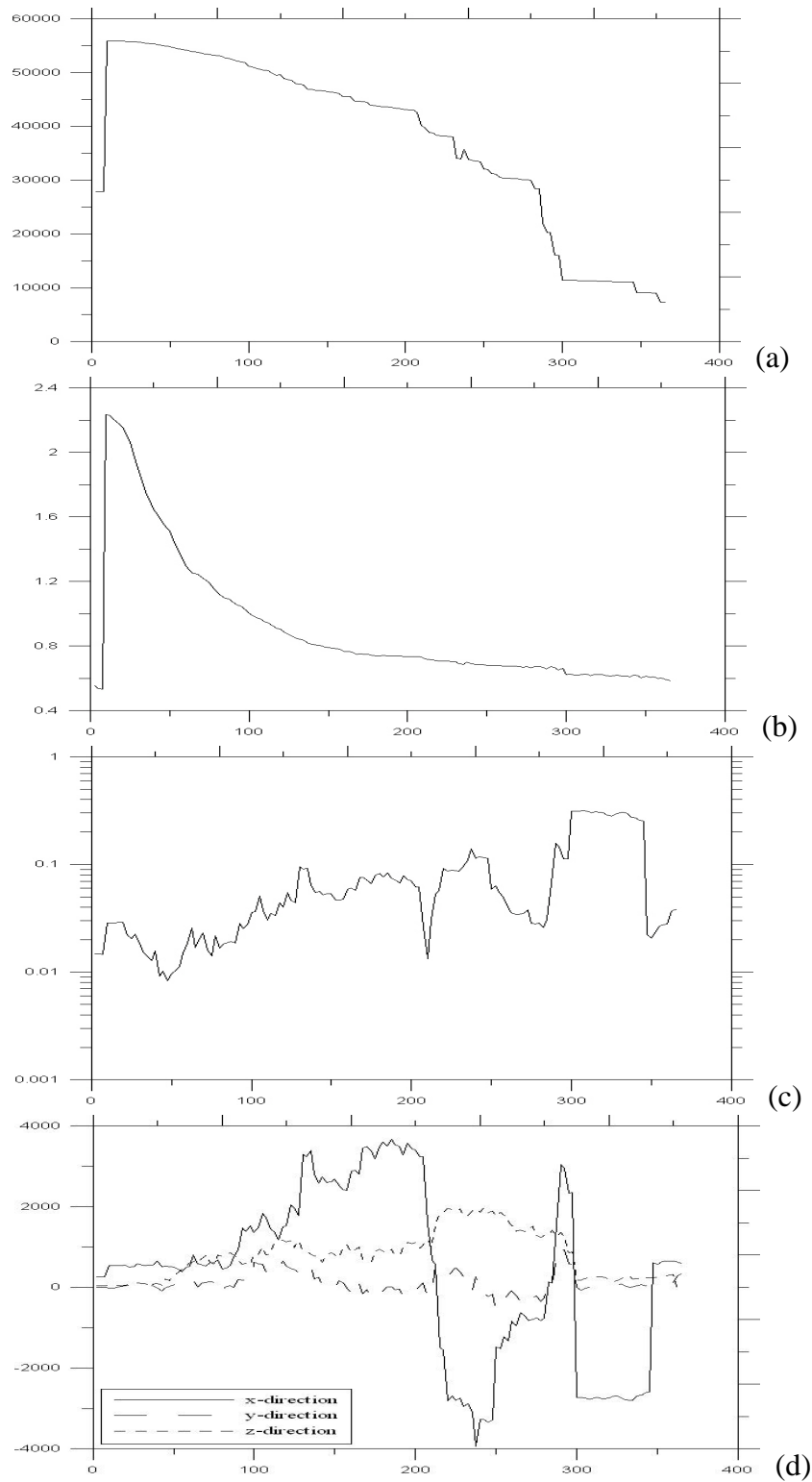


**Fig. 3.77** Measurements of largest fragment of Helium droplet pair collision,  $b=0$ ,  $V=500m/s$ , (a) Number of atoms, (b) Vibration temperature (k), (c) Rotation energy, (d) Angular momentum, respectively.

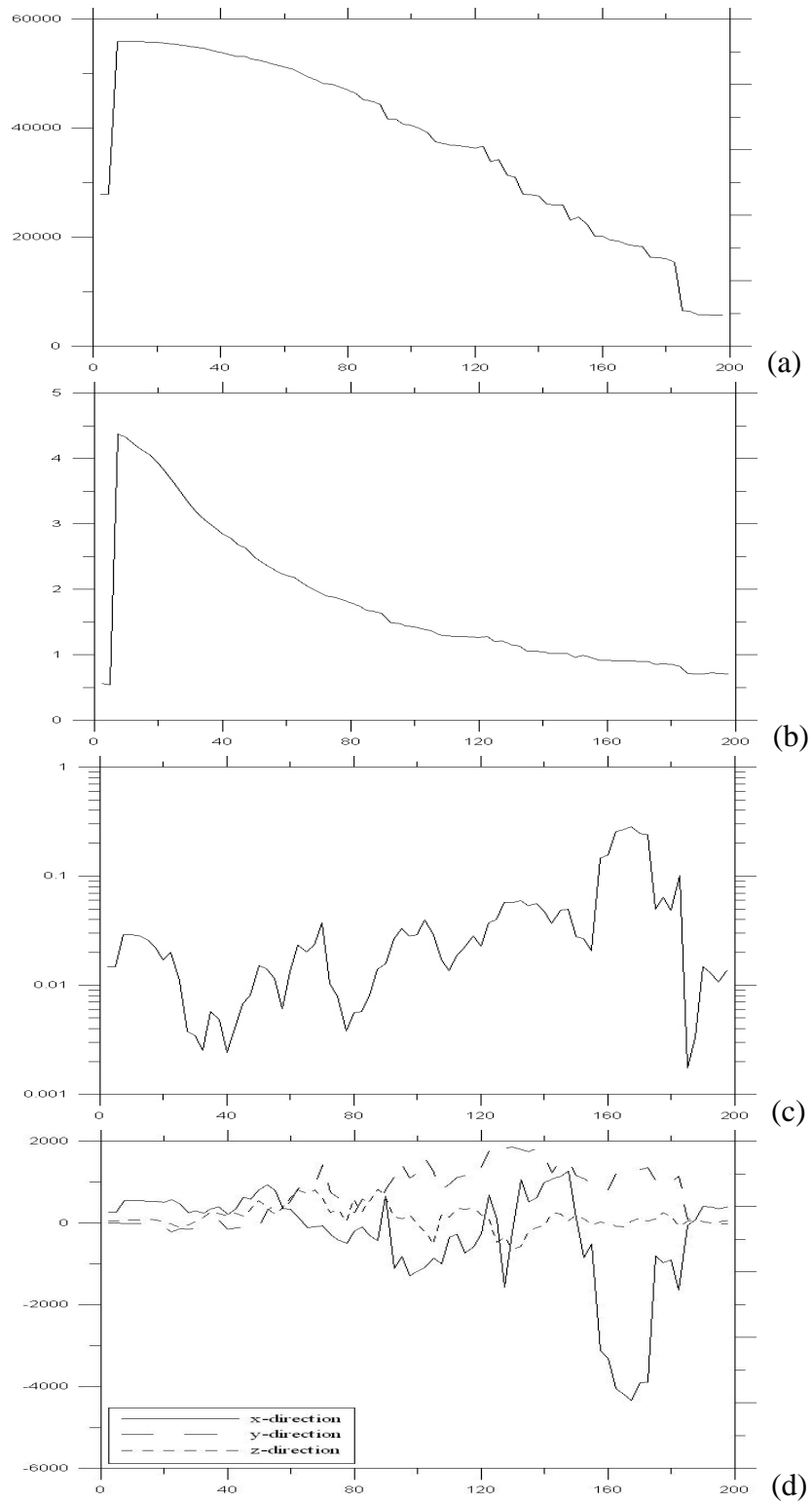


**Fig. 3. 78 Measurements of largest fragment of Helium droplet pair collision,  $b=0$ ,  $V=750m/s$ , (a) Number of atoms, (b) Vibration temperature (k), (c) Rotation energy, (d) Angular momentum, respectively.**

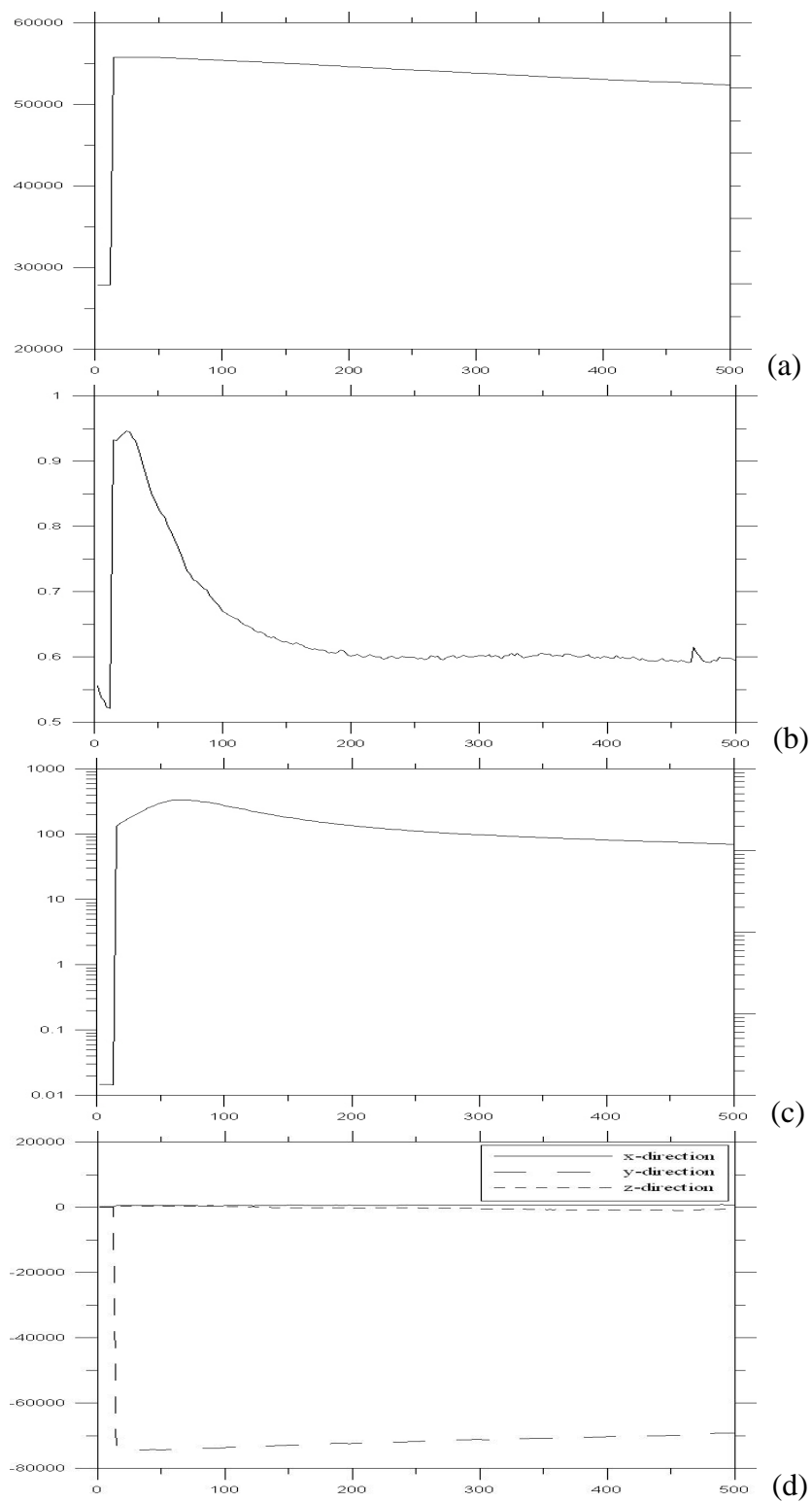


**Fig. 3. 79** Measurements of largest fragment of Helium droplet pair collision,  $b=2.5nm$ ,  $V=250m/s$ , (a) Number of atoms, (b) Vibration temperature (k), (c) Rotation energy, (d) Angular momentum, respectively.

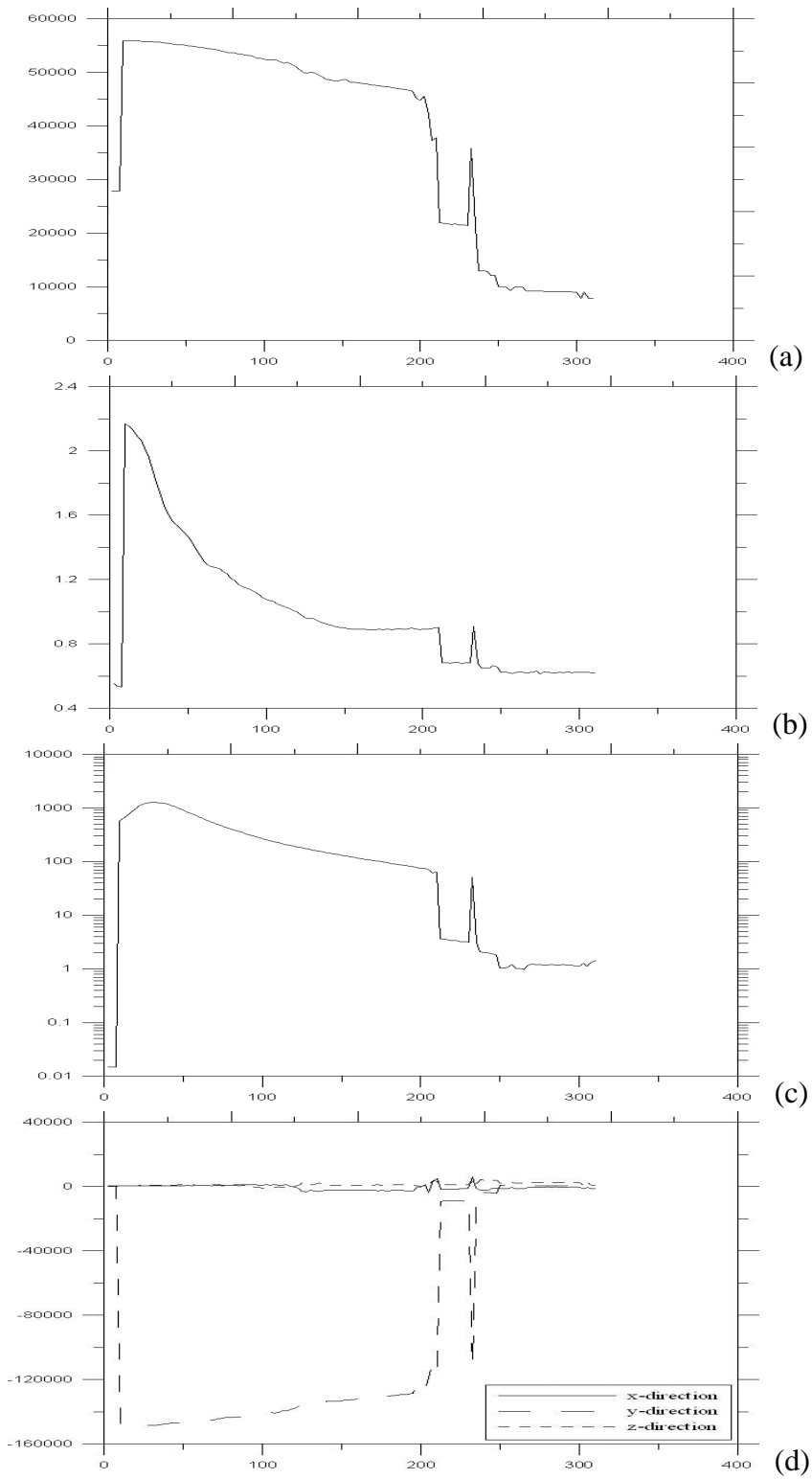


**Fig. 3. 80** Measurements of largest fragment of Helium droplet pair collision,  $b=2.5nm$ ,  $V=500m/s$ , (a) Number of atoms, (b) Vibration temperature (k), (c) Rotation energy, (d) Angular momentum, respectively.

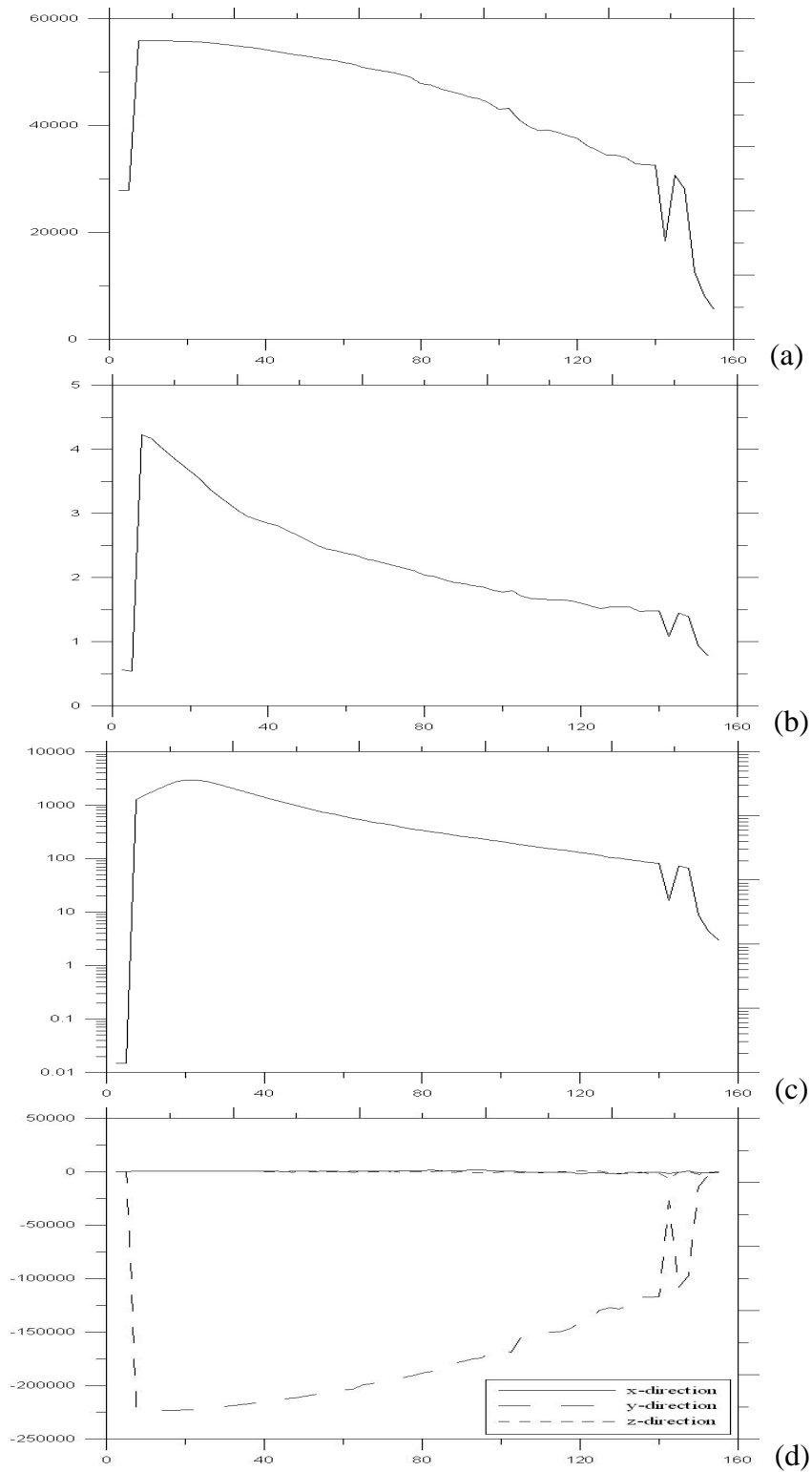


**Fig. 3. 81 Measurements of largest fragment of Helium droplet pair collision,  $b=2.5nm$ ,  $V=750m/s$ , (a) Number of atoms, (b) Vibration temperature (k), (c) Rotation energy, (d) Angular momentum, respectively.**

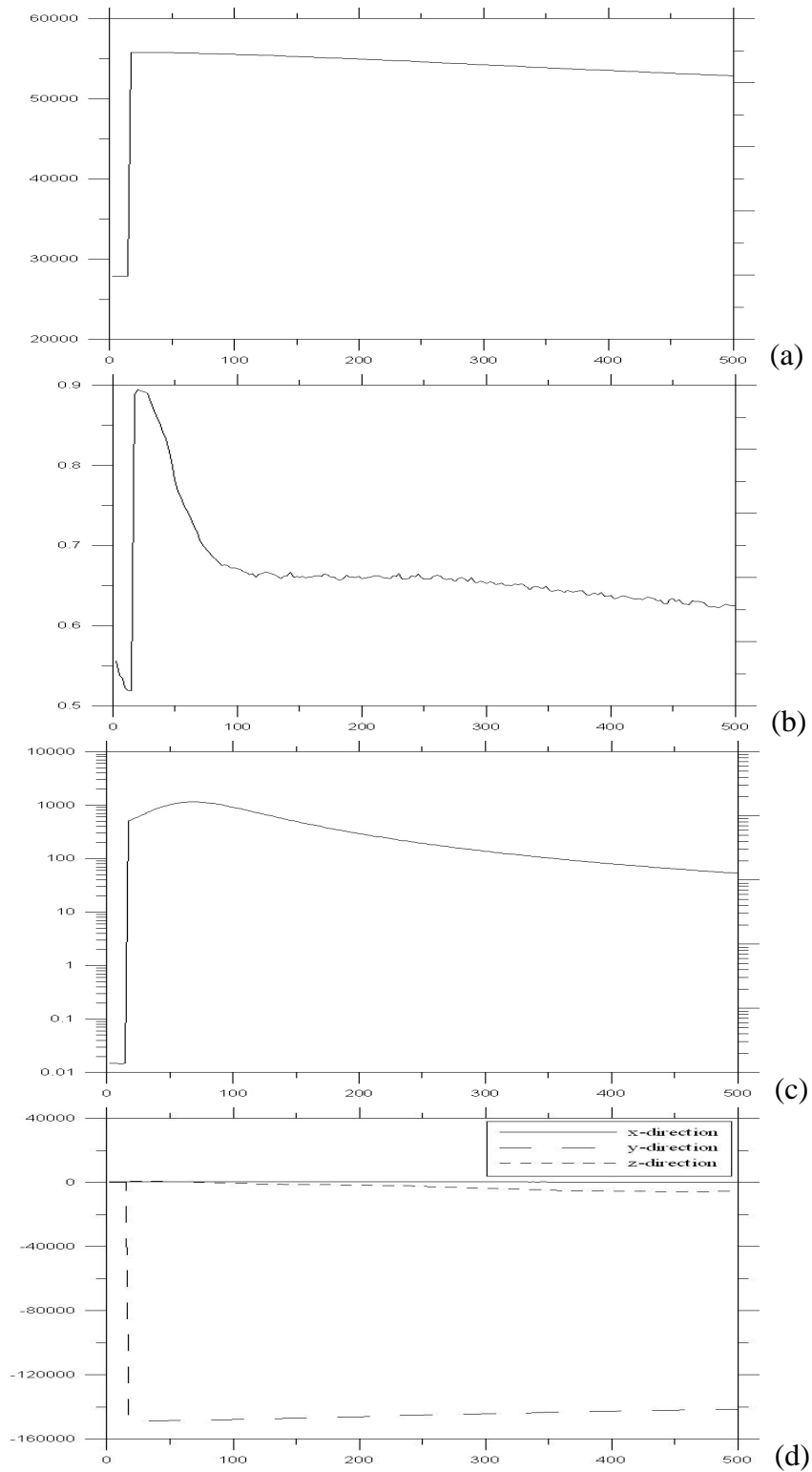


**Fig. 3. 82 Measurements of largest fragment of Helium droplet pair collision,  $b=5nm$ ,  $V=250m/s$ , (a) Number of atoms, (b) Vibration temperature (k), (c) Rotation energy, (d) Angular momentum, respectively.**



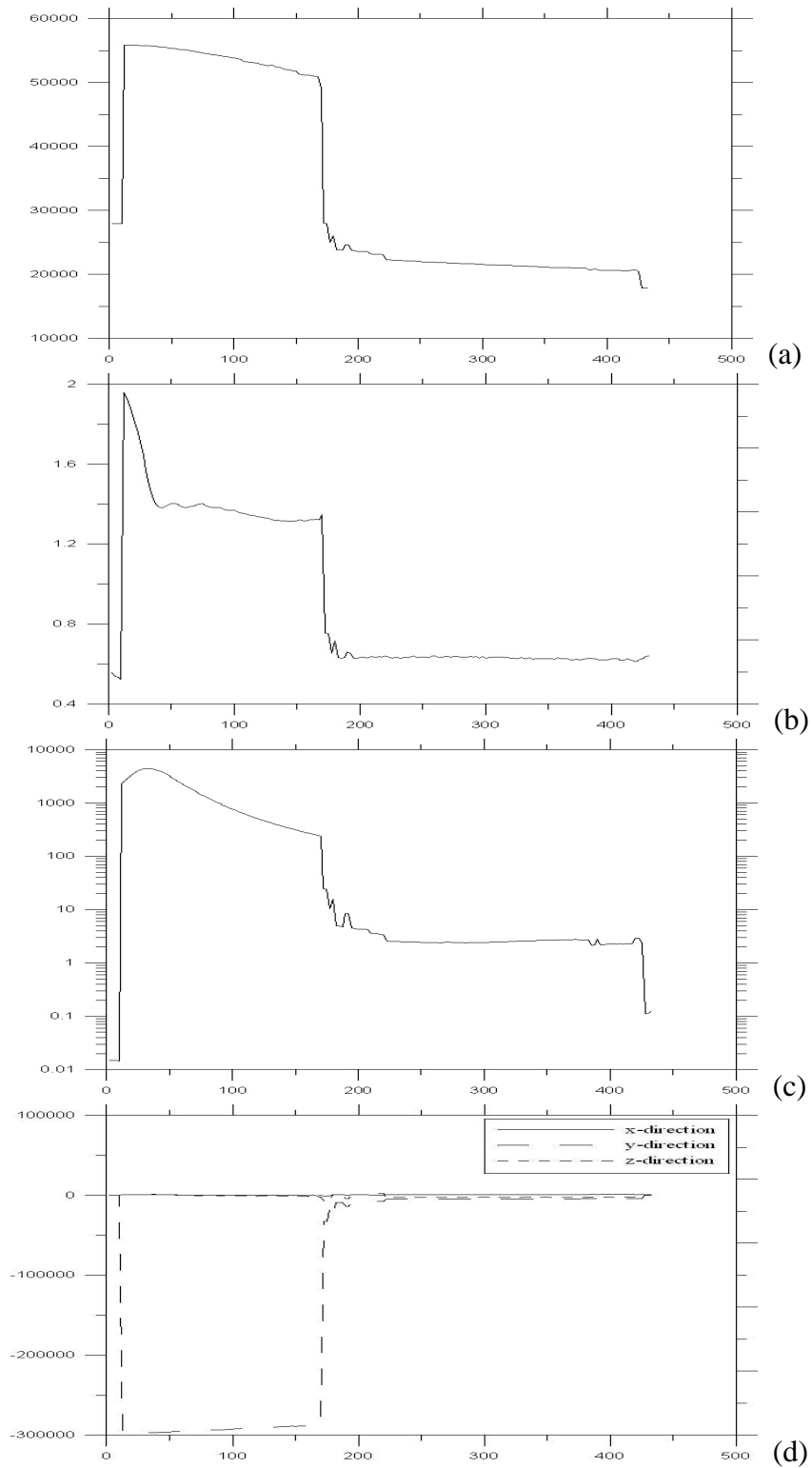


**Fig. 3. 83 Measurements of largest fragment of Helium droplet pair collision,  $b=5nm$ ,  $V=500m/s$ , (a) Number of atoms, (b) Vibration temperature (k), (c) Rotation energy, (d) Angular momentum, respectively.**

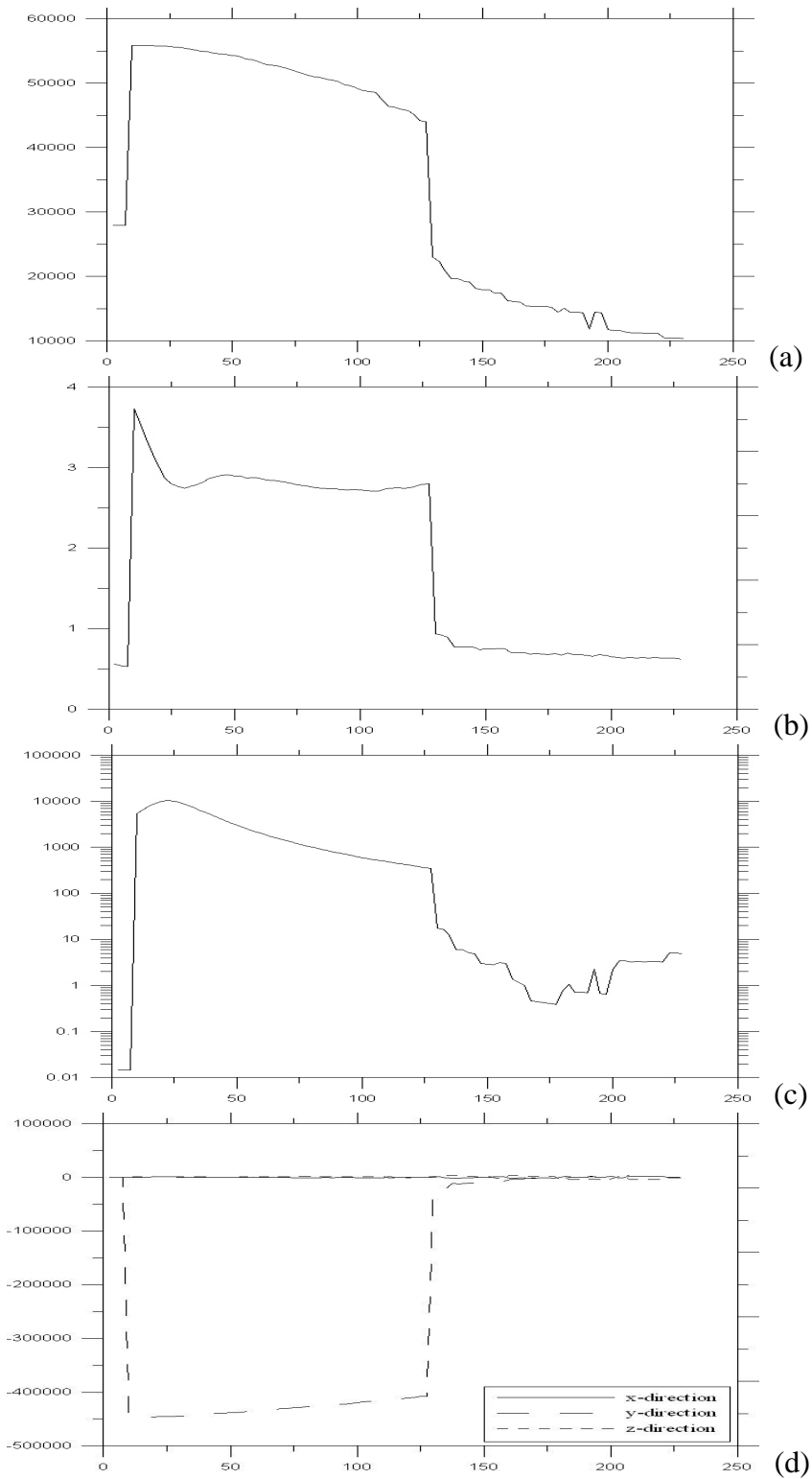


**Fig. 3. 84 Measurements of largest fragment of Helium droplet pair collision,  $b=5nm$ ,  $V=750m/s$ , (a) Number of atoms, (b) Vibration temperature (k), (c) Rotation energy, (d) Angular momentum, respectively.**

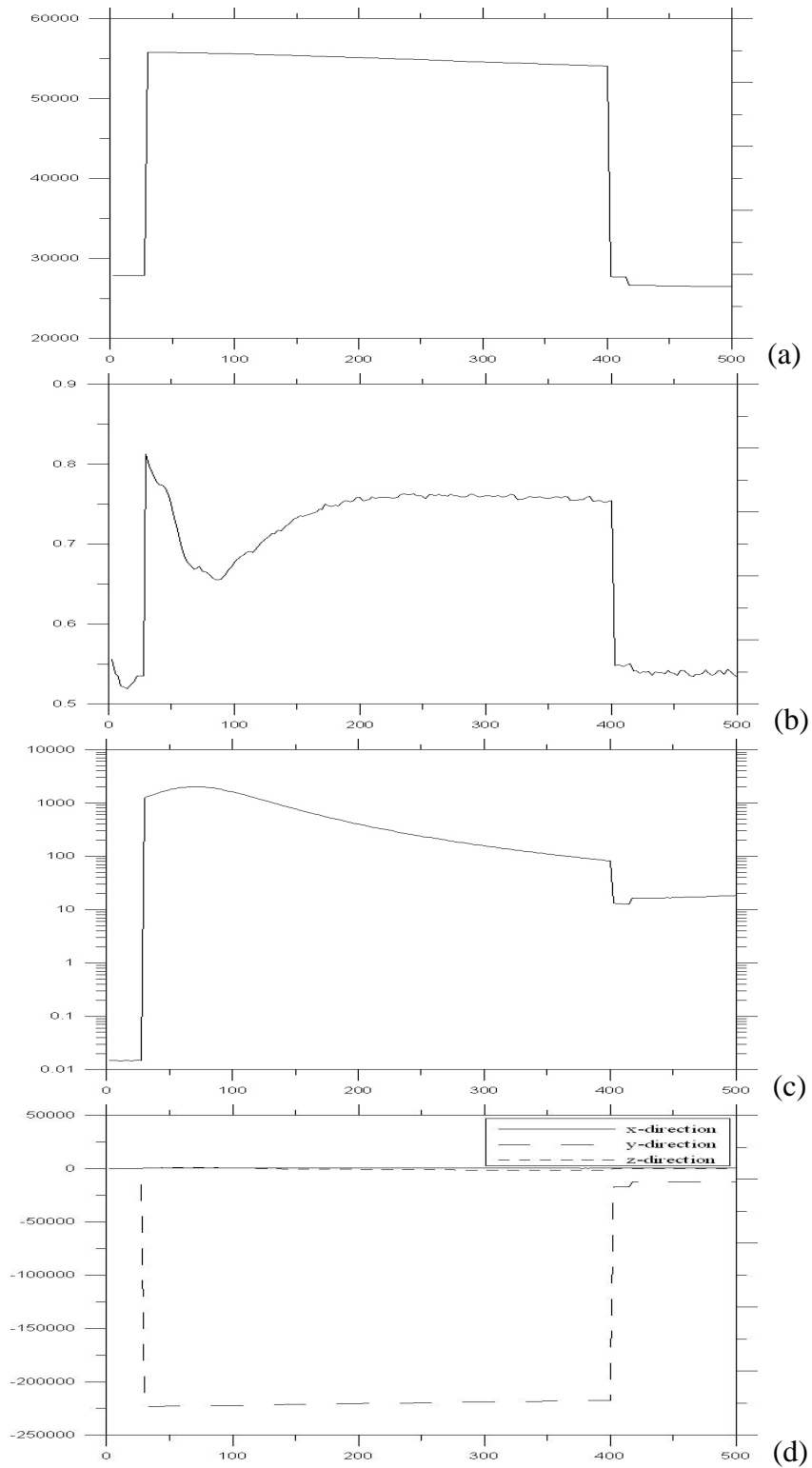


**Fig. 3. 85 Measurements of largest fragment of Helium droplet pair collision,  $b=7.5nm$ ,  $V=250m/s$ , (a) Number of atoms, (b) Vibration temperature (k), (c) Rotation energy, (d) Angular momentum, respectively.**

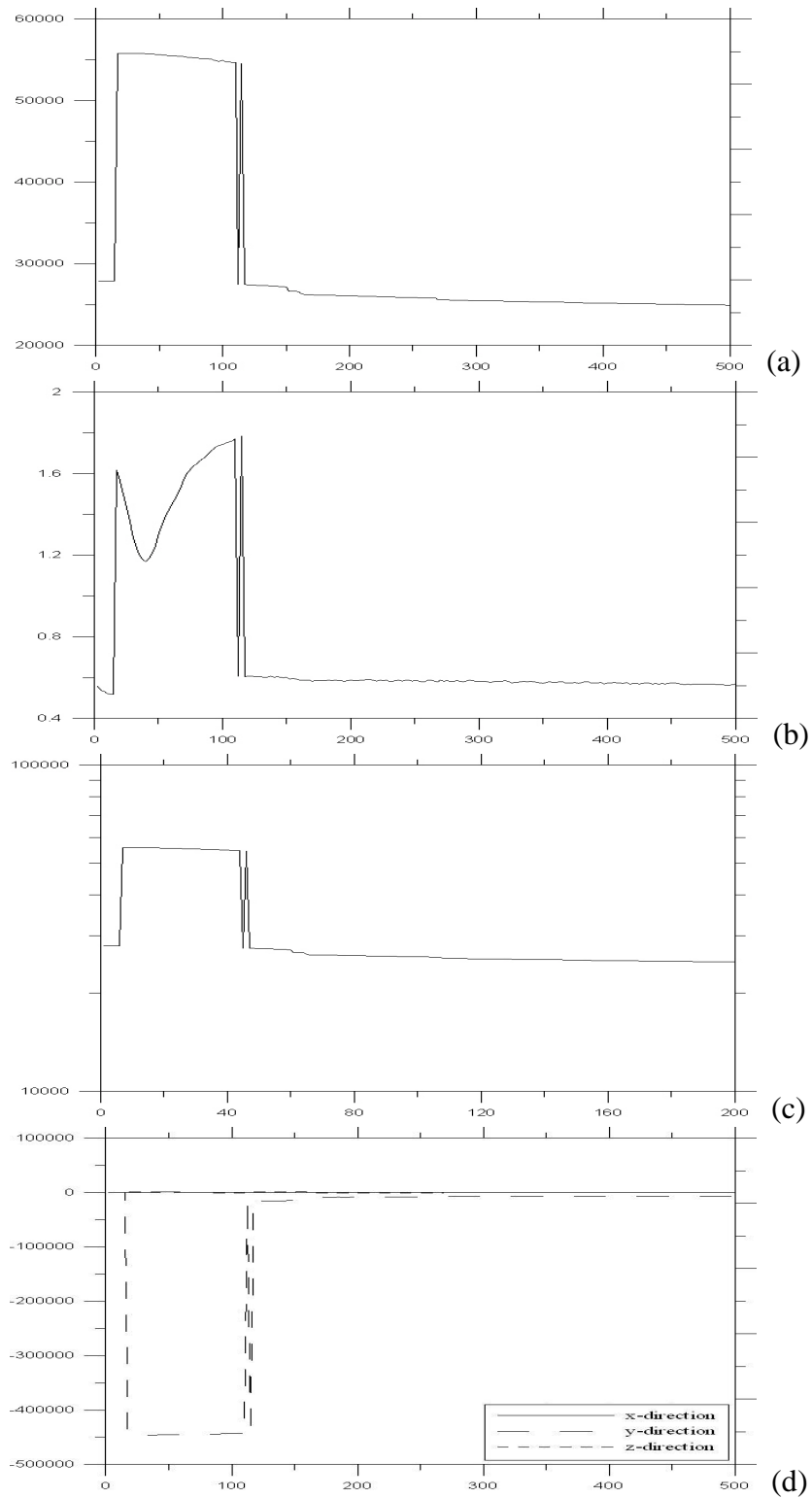


**Fig. 3. 86 Measurements of largest fragment of Helium droplet pair collision,  $b=7.5nm$ ,  $V=500m/s$ , (a) Number of atoms, (b) Vibration temperature (k), (c) Rotation energy, (d) Angular momentum, respectively.**

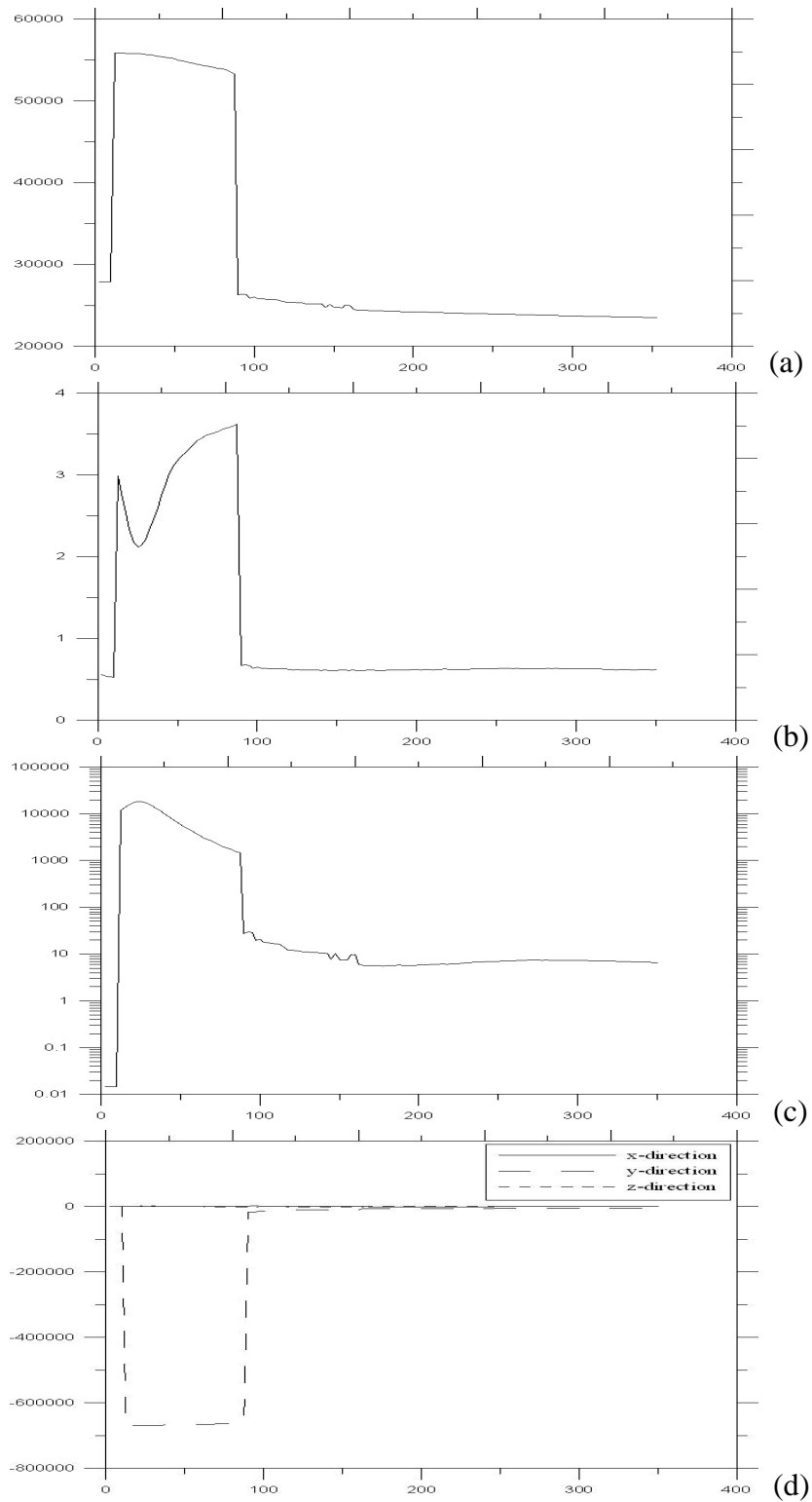


**Fig. 3. 87 Measurements of largest fragment of Helium droplet pair collision,  $b=7.5nm$ ,  $V=750m/s$ , (a) Number of atoms, (b) Vibration temperature (k), (c) Rotation energy, (d) Angular momentum, respectively.**

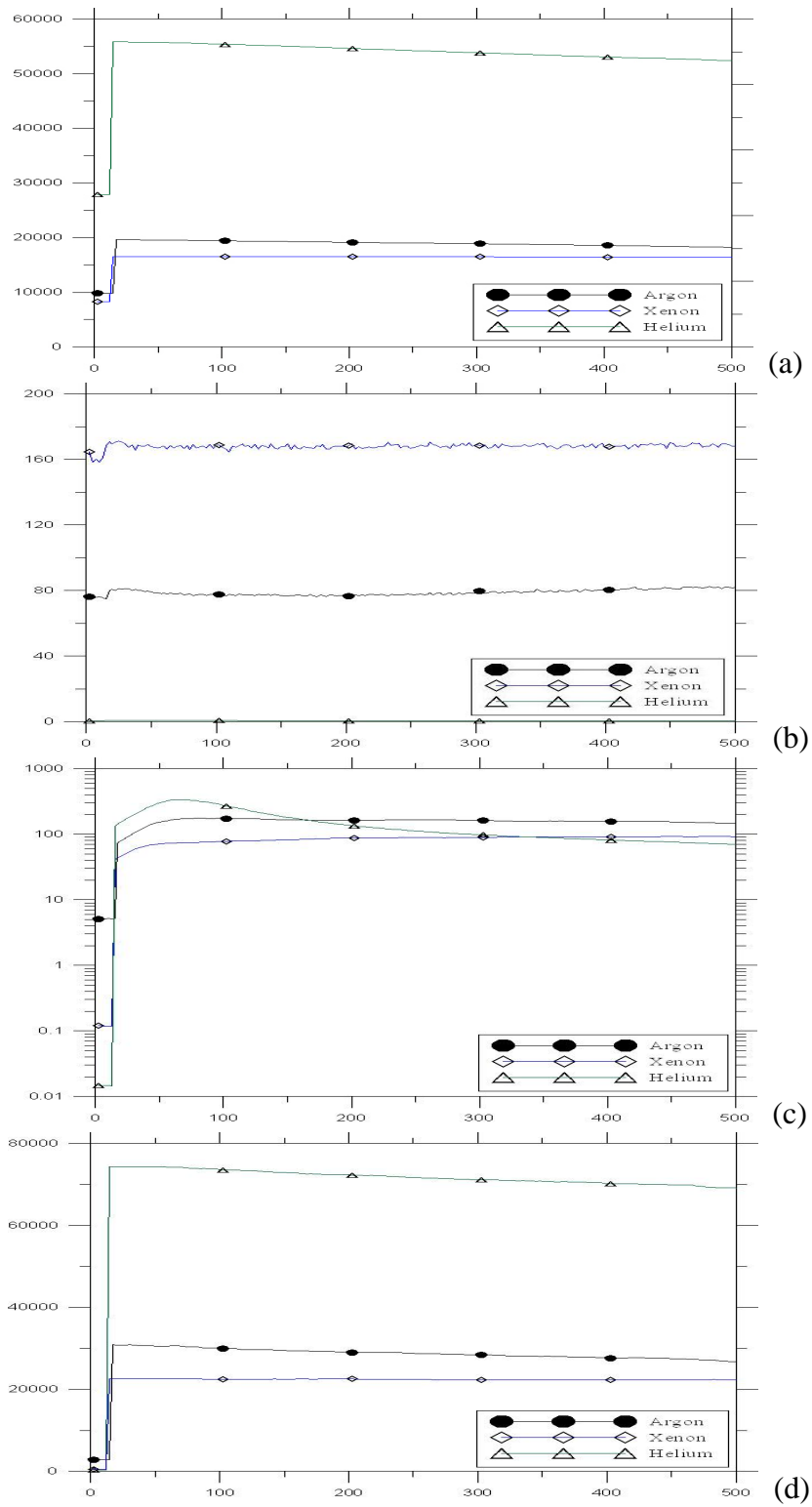


**Fig. 3. 88 Measurements of largest fragment of Helium droplet pair collision,  $b=2.5nm$ ,  $V=250m/s$ , (a) Number of atoms, (b) Vibration temperature (k), (c) Rotation energy, (d) Angular momentum, respectively.**

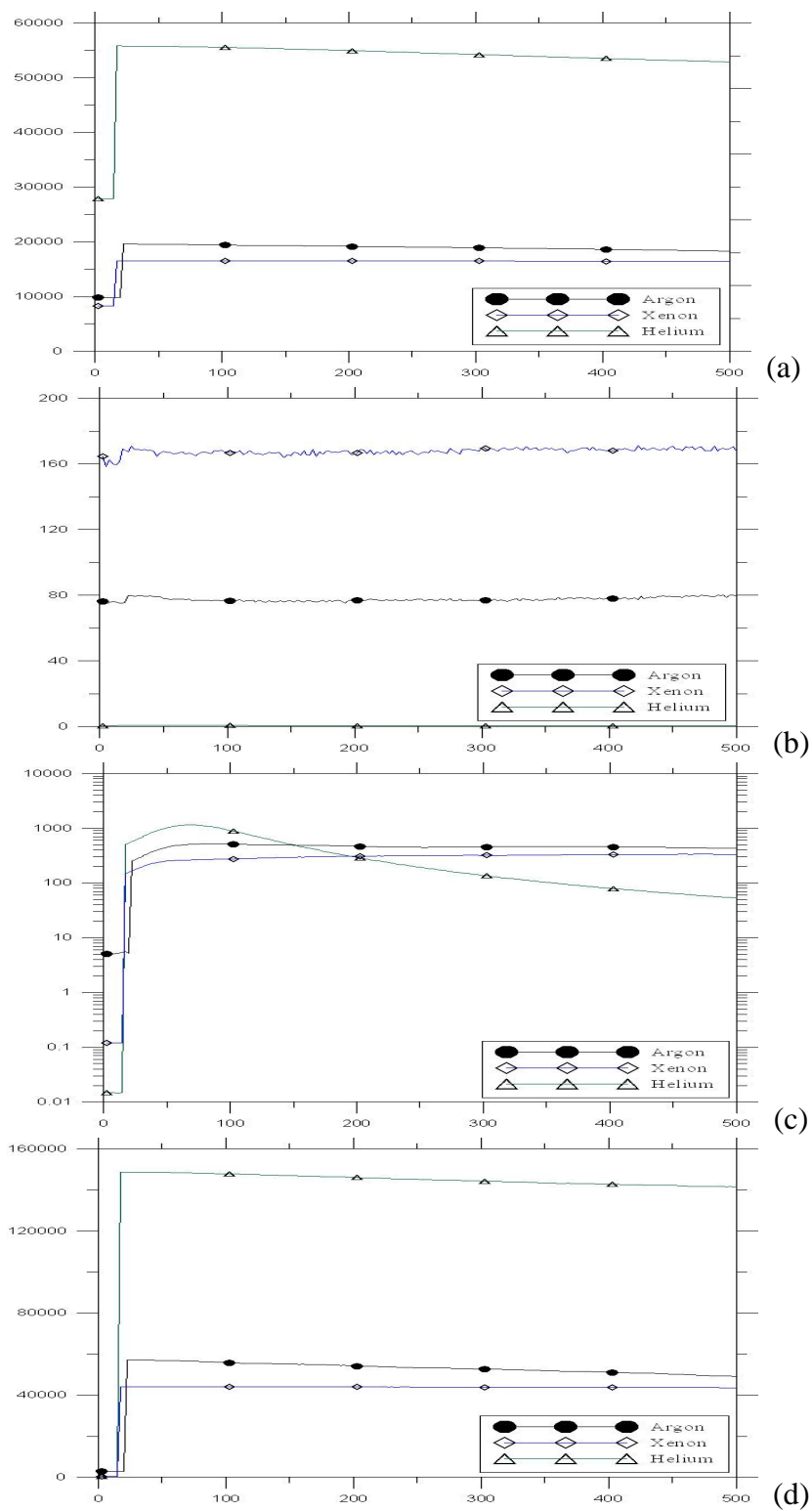


**Fig. 3. 89** Measurements of largest fragment of Helium droplet pair collision,  $b=5nm$ ,  $V=250m/s$ , (a) Number of atoms, (b) Vibration temperature (k), (c) Rotation energy, (d) Angular momentum, respectively.

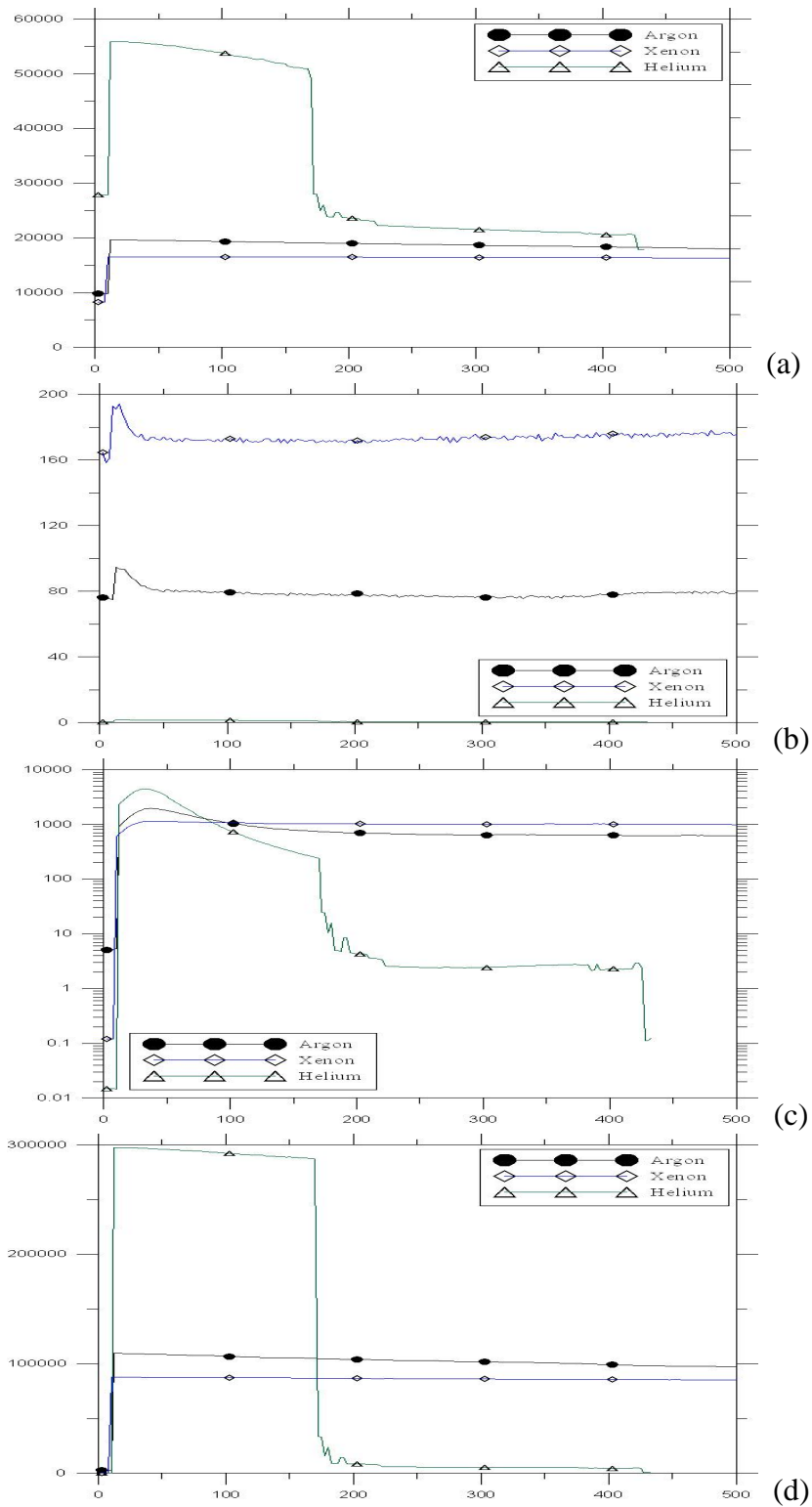


**Fig. 3.90** Measurements of largest fragment of Helium droplet pair collision,  $b=5nm$ ,  $V=500m/s$ , (a) Number of atoms, (b) Vibration temperature (k), (c) Rotation energy, (d) Angular momentum, respectively.



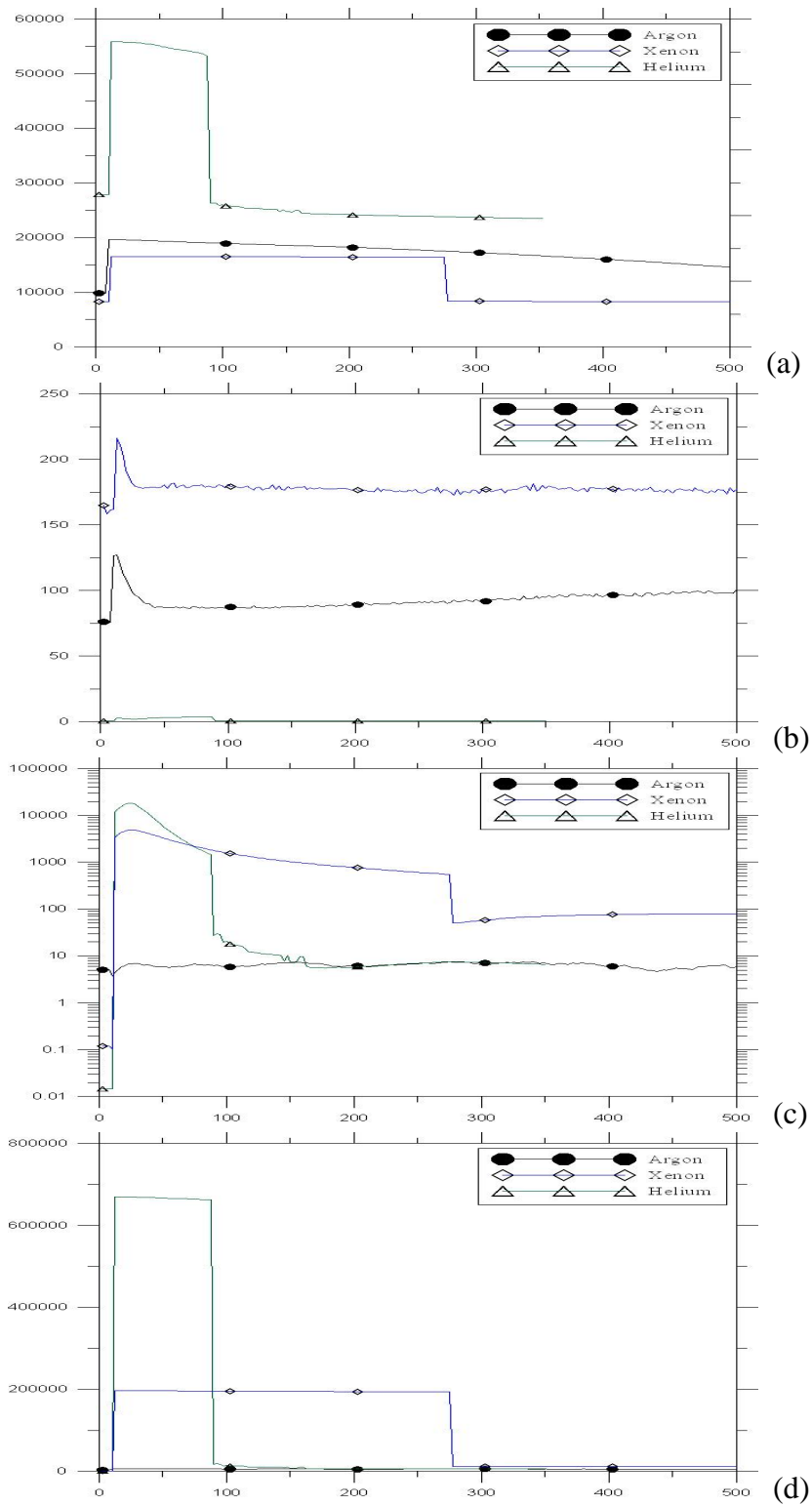


**Fig. 3. 91 Measurements of largest fragment of Helium droplet pair collision,  $b=7.5nm$ ,  $V=750m/s$ , (a) Number of atoms, (b) Vibration temperature (k), (c) Rotation energy, (d) Angular momentum, respectively.**

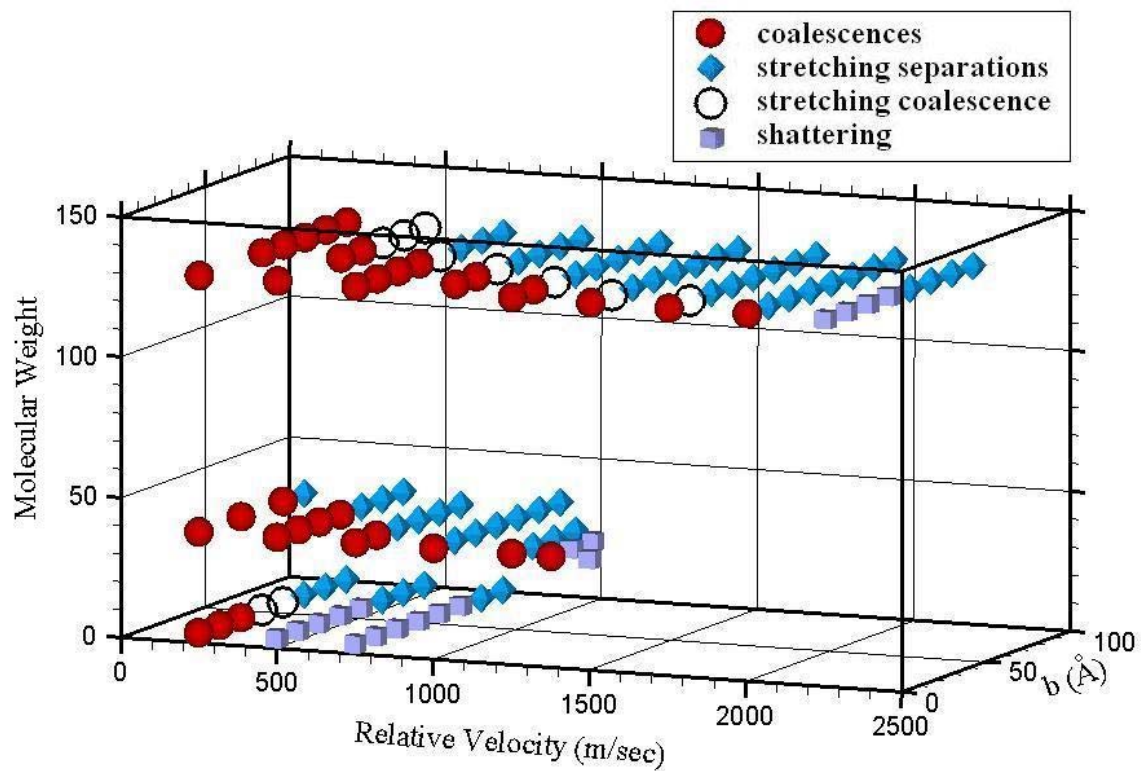


**Fig. 3. 92** Distribution map of various regimes of Xenon, Argon, and Helium droplet pair collision.